University of Alberta

Performance Improvement of Stirred Tank Reactors With Surface Feed

by

Sujit Bhattacharya ©

A thesis submitted to the Faculty of Graduate Studies and Research
in partial fulfillment of the requirements for the degree of
Doctor of Philosophy

in

Chemical Engineering

Department of Chemical and Materials Engineering

Edmonton, Alberta

Fall 2005

Library and
Archives Canada

Published Heritage
Branch

395 Wellington Street
Ottawa ON K1A 0N4
Canada

Bibliothèque et
Archives Canada

Direction du
Patrimoine de l'édition

395, rue Wellington
Ottawa ON K1A 0N4
Canada

0-494-08614-9

Your file Votre référence
ISBN:
Our file Notre reference
ISBN:

NOTICE:
The author has granted a non-exclusive license allowing Library and Archives Canada to reproduce, publish, archive, preserve, conserve, communicate to the public by telecommunication or on the Internet, loan, distribute and sell theses worldwide, for commercial or non-commercial purposes, in microform, paper, electronic and/or any other formats.

The author retains copyright ownership and moral rights in this thesis. Neither the thesis nor substantial extracts from it may be printed or otherwise reproduced without the author's permission.

AVIS:
L'auteur a accordé une licence non exclusive permettant à la Bibliothèque et Archives Canada de reproduire, publier, archiver, sauvegarder, conserver, transmettre au public par télécommunication ou par l'Internet, prêter, distribuer et vendre des thèses partout dans le monde, à des fins commerciales ou autres, sur support microforme, papier, électronique et/ou autres formats.

L'auteur conserve la propriété du droit d'auteur et des droits moraux qui protège cette thèse. Ni la thèse ni des extraits substantiels de celle-ci ne doivent être imprimés ou autrement reproduits sans son autorisation.

In compliance with the Canadian Privacy Act some supporting forms may have been removed from this thesis.

While these forms may be included in the document page count, their removal does not represent any loss of content from the thesis.

Conformément à la loi canadienne sur la protection de la vie privée, quelques formulaires secondaires ont été enlevés de cette thèse.

Bien que ces formulaires aient inclus dans la pagination, il n'y aura aucun contenu manquant.

Canada

Abstract

Current best mixing practice requires sub-surface feed of reagents into the turbulent impeller region of stirred reactors to suppress mixing limitations and to minimize byproduct formation. Dip tubes; however, can cause many operational problems. In this thesis alternate surface feed strategies were explored using the third Bourne reaction.

Initial experiments were conducted with the Rushton turbine and the down-pumping pitched blade turbine (PBTD) to establish base case performance. In the first modified configuration the impeller was unchanged but the feed was added at a high velocity to generate additional turbulence, enhance mixing, and transport reagents rapidly to the turbulent impeller region. This strategy failed, since it was very difficult to generate a fully turbulent feed jet and operation was very unstable. Sufficient improvement in performance could also not be achieved due to the macro-scale convective stoichiometric limitations. An analysis of these limitations showed that they are general limitations and this strategy is difficult to implement.

In the second configuration, feed was added slowly at the surface with an up-pumping pitched blade turbine (PBTU). Operation was greatly improved and continued to improve with increasing impeller speed. At very high impeller speeds air bubbles were entrained into the tank. The impeller speed at the onset of air entrainment, N_E, gives the upper limit of operation of the PBTU. Reactive experiments showed that the product

quality for a PBTU operated close to N_E matched the results obtained with dip tubes irrespective of impeller submergence. The up-pumping impeller was identified as a stable and robust impeller configuration suitable for surface feed.

Air entrainment is a result of subtle interactions between subsurface turbulence and the liquid surface. In this investigation a two-step mechanism of air entrainment is proposed: bubbles first form at the surface and are then dragged into the tank by the mean velocity. To validate this model, turbulent (RMS) and mean velocities were measured near the liquid surface with a Laser Doppler Velocimeter (LDV) at $N = 0.98N_E$. The model is able to predict air entrainment using conditions at the surface. The complex relationship between the impeller variables and the turbulent flow-field near the surface; however, is best address through full computational simulations.

Acknowledgements

Firstly, I want to thank my supervisor, Dr Suzanne Kresta, for the exceptional guidance, help and support she has provided me. Her knowledge, wisdom and the ability to get quickly to the key issues are things I sincerely hope to emulate. I will also always cherish her awesome warmth and kindness.

I am where I am because of my parents, brother and sister. They have stood resolutely behind me and given me strength when I needed it most.

I received great support from the departmental staff. I want to thank Andrée for her immense and uncomplaining help, as also Walter, Richard and Les from the electronic shop and Bob Scott, James (thanks bud!), Bob Smith, Clark and Dave from the machine shop. Marilee, Jaleen, Ann Marie and Kathy helped me cope with the various requirements of the department and the university. Thanks! I always thought computer administrators were grumpy, bureaucratic characters. Bob Barton and Jack changed that forever! Outside the department, Gerry from the glassblowing shop and Tony Selinger from the Department of Environmental Health and Safety were of the greatest help.

Heartfelt thanks to my colleagues in the mixing group, especially Vesselina and Gary, for making office a fun and stimulating place to be in and David who spent long strenuous hours in the laboratory helping me out with my air entrainment experiments.

I also want to thank Raghu, Praveen, Arvind, Hari, Vinay, Dalton, Shakir and all my other friends in Edmonton who made it the most enjoyable place to be in.

And finally there are the persons who can not be thanked enough for the support they gave me through some of my darkest hours; but thanks anyways Pauline, Errol, Ravi and Sandeep. And Joe you are one of the most positive, cheerful and helpful persons I have known!

Table of Contents

Chapter 1 *Introduction* *1*

Chapter 2 *Literature Review* *4*

2.1. Definitions of Mixing 4

2.2. Mixing and Reactions 6
  2.2.1. Relative Rates of Mixing and Reaction - the Damköhler number 6
  2.2.2. Reactive Mixing Experiments 8
    2.2.2.1. Kinetics of the Third Bourne Reaction 13
    2.2.2.2. Effect of Reactant Concentrations 14
    2.2.2.3. Effect of Feed Sequence 17
    2.2.2.4. Effect of Feed Time 18
    2.2.2.5. Effect of Feed Pipe Diameter 21
    2.2.2.6. Effect of Feed Location 22
    2.2.2.7. Effect of Multiple Nozzles 26
    2.2.2.8. Effect of Tank Scale, Impeller Speed and Geometry 27

2.3. Flow and Turbulence in a Stirred tank 28
  2.3.1. Flow-Field in a Stirred Tank 28
  2.3.2. Rushton Turbine (RT) 33
  2.3.3. Down-pumping Pitched Blade Turbine (PBTD) 39
  2.3.4. Up-pumping Pitched Blade Turbine (PBTU) 44

2.4. Turbulent Mixing 48
  2.4.1. Turbulence 49
    2.4.1.1. Definitions 49
    2.4.1.2. The Rate of Dissipation of Turbulent Kinetic Energy (ε) 50
    2.4.1.3. The Energy and Concentration Spectrums 52
    2.4.1.4. Commonly Used Simplifications 55
  2.4.2. Scales of Mixing 59
  2.4.3. Micromixing – Mechanisms and Models 65
    2.4.3.1. Engulfment, deformation, and diffusion (EDD) model 66
    2.4.3.2. Engulfment model 68
  2.4.4. Mesomixing – Mechanisms and Models 69
    2.4.4.1. Turbulent dispersion 71
    2.4.4.2. Inertial-convective disintegration 72
  2.4.5. Hierarchy of Time Scales in Reactive Mixing 75
  2.4.6. Sample Calculations Using Characteristic Mixing Time Scales 76
    2.4.6.1. Estimation of the Controlling Mechanism as a Function of t_f .. 76
    2.4.6.2. Estimation of the Functional Relationship Between t_{crit} and D 76

2.5. Concluding Remarks 77

Chapter 3 Surface Feed at High Velocity with PBTD *79*

3.1. Introduction **79**

3.2. Theory and Analysis **80**
- *3.2.1. Effect of Feed Time* *80*
- *3.2.2. Turbulent Axisymmetric Jets* *81*
- *3.2.3. Operational Limits for High Velocity Surface Feed* *87*

3.3. Experimental **97**
- *3.3.1. Determination of Byproduct Yield* *97*
- *3.3.2. Determination of Chemical Concentration* *98*
- *3.3.3. Experimental Procedure* *101*
- *3.3.4. Experimental Conditions Studied* *106*

3.4. Results and Discussions **107**
- *3.4.1. Effect of nozzle size and feed time on byproduct yield* *107*
- *3.4.2. Effect of impeller speed (N) on byproduct yield* *112*
- *3.4.3. Plunging Jet* *115*

3.5. Conclusions **118**

Chapter 4 Surface Feed at Normal Velocity with PBTU *121*

4.1. Introduction **121**

4.2. Experimental **121**
- *4.2.1. Measurement of Mixing Characteristics* *121*
- *4.2.2. Measurement of Flow Characteristics* *125*

4.3. Results and Discussions **136**
- *4.3.1. Submerged feed* *137*
- *4.3.2. Surface feed* *139*
  - 4.3.2.1. Single PBTD 139
  - 4.3.2.2. PBTU and PBTD combination 139
  - 4.3.2.3. Single PBTU 143
- *4.3.3. Air entrainment and critical Froude number* *144*
- *4.3.4. Optimized operation* *145*

4.4. Conclusions **148**

Chapter 5 Air Entrainment in Baffled Stirred Tanks *151*

5.1. Introduction **151**
- *5.1.1. Studies on Gas Entrainment in Baffled Vessels* *153*
- *5.1.2. Studies on Gas Entrainment in Fast Moving Bodies of Liquid* *159*
- *5.1.3. Interactions Between Turbulence and the Open Surface* *161*

5.2. Model of turbulence-surface interactions **164**

5.2.1. Bubble Formation *164*
5.2.2. Bubble Retention *166*

5.3. Experimental procedure for measurement of N_E 168

5.4. Experimental Details 172
5.4.1. Air Entrainment Into Un-baffled Vessel *174*
5.4.2. Air Entrainment with non-Standard Baffles *174*
5.4.3. Air Entrainment with Standard Baffles *174*

5.5. Results and Discussion 175
5.5.1. Air Entrainment in Un-baffled Tank *175*
5.5.2. Air Entrainment in a Baffled Tank *180*
5.5.2.1. Effect of Baffle Geometry on Air Entrainment 180
5.5.2.2. Air Entrainment with Standard Baffles 180
5.5.3. Velocity field in a Baffled Tank with PBTU *186*
5.5.3.1. Mean Flow 186
5.5.3.2. Root Mean Square Velocity 188

5.6. Analysis of Theoretical versus Measured Velocity Field 192

5.7. Conclusions 196

Chapter 6 Conclusions 199

6.1. Summary of Investigation 199

6.2. Observations 200

Bibliography 202

Appendix A Mean Flow Characteristics in a Stirred Tank 213

A.1. Rushton Turbine (RT) 213

A.2. Pitched Blade Turbine (PBT) 214

Appendix B Fully Turbulent Flows 218

B.1. Length Scales in Turbulent Mixing 222

B.2. Time Scales in Turbulent Mixing 226

Appendix C Models for Turbulent Mixing 229

C.1. Micromixing – EDD model: **229**

C.2. Micromixing – E model **230**

C.3. Mesomixing – Mechanisms and Models **231**

C.3.1. Model based on turbulent dispersion: *231*

C.3.2. Model based on inertial-convective disintegration: *232*

Appendix D Velocity and Scalar Profiles in a Round Jet ***235***

D.1. Boundary layer equations **235**

D.2. Axisymmetric jet in a co-flowing stream **239**

D.2.1. Momentum flux: *239*

D.2.2. Scalar flux *241*

D.3. Similarity Solutions - Velocity **242**

D.4. Similarity Solutions - Scalar **250**

D.5. Arguments against universal solution **254**

Appendix E Data from Reactive Experiments ***257***

Appendix F Vortex Data In Un-Baffled Vessel ***267***

Appendix G Data from Air Entrainment Experiments ***269***

Appendix H Experimental Data From LDV Measurements ***273***

Appendix I Byproduct Yield as a Function of RMS Velocity ***292***

List of Tables

Table 2.1 Details of reaction schemes commonly used in experiments on mixing limited reactions. 11

Table 2.2 Geometric details of a stirred tank and impellers 29

Table 2.3 Distribution of the rate of dissipation of turbulent kinetic energy per unit mass in various regions of a tank stirred with a Rushton turbine (Adapted from Ng and Yianneskis, 2000) 37

Table 2.4 Characteristic Length Scales in Turbulent Mixing 60

Table 2.5 Characteristic Time Scales in Turbulent Mixing 61

Table 3.1 Summary of axisymmetric jet experiments reported in the literature. 84

Table 3.2 Experimental conditions 94

Table 3.3 Sample calculation for high velocity feed. In these calculations d_f, t_f and N are estimated so that Constraints 1 to 4 are all satisfied. Conditions as in Table 3.2. 95

Table 3.4 Variability in the results when byproduct yield is calculated in terms of the amount of ethanol formed or the amount of ester reacted for the case of PBTD with feed at the surface with a 3mm nozzle and N = 252 rpm. 99

Table 3.5 Parameter settings and conditions used for the gas chromatograph. 99

Table 3.6 Chemical used for calibration and in the reactive experiments. 100

Table 3.7 Dimensionless numbers for plunging jet 117

Table 4.1 Details of Feed and Impeller configurations. The nozzle diameter was d = 3 mm for all cases. A smaller nozzle diameter of d = 0.762 mm was also tested for Case 4. 124

Table 4.2 Parameters of Aerometrics LDV system used in this work 129

Table 5.1 Minimum impeller speeds for the onset of surface aeration. The nomenclature for impeller speed is adopted from the parent reference. They are all roughly equivalent to the minimum impeller speed for air entrainment, N_E, used in the present study. 156

Table 5.2 Physical Properties of fluids measured @ 23°C 173

Table 5.3 Overview of Experiments 173

Table 5.4 Results with un-baffled vessel. The reported values are from the literature, the experiments (Expts) column is from this study. 177

Table 5.5 Impeller speed for air entrainment with impeller types other than PBTU 182

Table E.1 Experimental Data for PBTD. Feed is through a 3mm nozzle placed at the surface. 2r/D = 1.75 and N = 252 rpm 257

Table E.2 Experimental Data for PBTD. Feed is through a 0.762 mm nozzle placed at the surface. 2r/D = 1.75 & N = 252 rpm 258

Table E.3 Experimental Data for PBTD with the feed stream added 1.4cm above the liquid surface to form a plunging jet. Feed is through a 3 mm nozzle. 2r/D = 1.75 and N = 252 rpm 259

Table E.4 Experimental Data for PBTD with the feed stream added 1.4cm above the liquid surface to form a plunging jet. Feed is through a 0.762 mm nozzle. 2r/D = 1.75 and N = 252 rpm 259

Table E.5 Experimental Data for PBTD with feed added at the surface. Feed is through a 3 mm nozzle. 2r/D = 1.75 and N = 375 rpm 260

Table E.6 Experimental Data for PBTD with feed added at the surface. Feed is through a 3 mm nozzle. 2r/D = 1.75 and N = 500 rpm 260

Table E.7 Experimental Data for PBTD with feed added 2.1cm above the nozzle with a dip tube. Feed is through a 3 mm nozzle. 2r/D = 0.8 and N = 252 rpm 261

Table E.8 Experimental Data for PBTD with feed added 2.1cm above the nozzle with a dip tube. Feed is through a 0.762 mm nozzle. 2r/D = 0.8 and N = 252 rpm 262

Table E.9 Experimental Data for a combination of PBTU and PBTD with feed at the surface. Feed is through a 3 mm nozzle. 2r/D = 0.8 and N = 252 rpm ... 263

Table E.10 Experimental Data for PBTU with feed at surface. Feed is through a 3 mm nozzle. 2r/D = 1.75 and N = 252 rpm 264

Table E.11 Experimental Data for PBTU with feed at surface. Feed is through a 3 mm nozzle. 2r/D = 0.8 and N = 252 rpm 265

Table E.12 Experimental Data for PBTU with feed at surface. Feed is through a 0.762mm nozzle. 2r/D = 0.8 and N = 252 rpm 266

Table E.13 Experimental Data for PBTU with different impeller positions. Feed is through a 3mm feed pipe at the surface of the tank at 2r/D = 0.8. 266

Table F.1 Vortex Data From an Un-Baffled Tank Stirred with a Rushton Turbine. Experimental Fluid was R.O. Water. 267

Table F.2 Vortex Data From an Un-Baffled Tank Stirred with a Down-Pumping Pitched Blade Turbine. Experimental Fluid was R.O. Water. 267

Table F.3 Vortex Data From an Un-Baffled Tank Stirred with an Up-Pumping Pitched Blade Turbine. Experimental Fluid was R.O. Water. 268

Table G.1 Impeller speed at the onset of air entrainment, N_E. Data is presented here for water for various baffle configurations. 269

Table G.2 Impeller speed at the onset of air entrainment, N_E. Data is presented here for triethylene glycol (TEG) for two baffle configurations. 270

Table G.3 Impeller speed at the onset of air entrainment, N_E. Data is presented here for Bayol-35 for two baffle configurations. 271

Table H.1a Velocity data for an up-pumping pitched blade turbine of size D = T/3 which was placed 8 cm below the surface and operated at $N = 0.98N_E$ (321 rpm). Velocity was measured 1.5 cm below the liquid level in a vertical plane 6 mm upstream of the baffle. The experimental fluid is water. 273

Table H.1b Velocity data for an up-pumping pitched blade turbine of size D = T/3 which was placed 7 cm below the surface and operated at $N = 0.98N_E$ (306 rpm). Velocity was measured 1.5 cm below the liquid level in a vertical plane 6 mm upstream of the baffle. The experimental fluid is water. 274

Table H.1c Velocity data for an up-pumping pitched blade turbine of size D = T/3 which was placed 6 cm below the surface and operated at $N = 0.98N_E$ (290 rpm). Velocity was measured 1.5 cm below the liquid level in a vertical plane 6 mm upstream of the baffle. The experimental fluid is water. 275

Table H.1d Velocity data for an up-pumping pitched blade turbine of size D = T/3 which was placed 5 cm below the surface and operated at $N = 0.98N_E$ (277 rpm). Velocity was measured 1.5 cm below the liquid level in a vertical plane 6 mm upstream of the baffle. The experimental fluid is water. 276

Table H.2a Velocity data for an up-pumping pitched blade turbine of size D = T/2 which was placed 8 cm below the surface and operated at $N = 0.98N_E$ (191 rpm). Velocity was measured 1.5 cm below the liquid level in a vertical plane 6 mm upstream of the baffle. The experimental fluid is water. 277

Table H.2b Velocity data for an up-pumping pitched blade turbine of size D = T/2 which was placed 7 cm below the surface and operated at $N = 0.98N_E$ (174 rpm). Velocity was measured 1.5 cm below the liquid level in a vertical plane 6 mm upstream of the baffle. The experimental fluid is water. 278

Table H.2c Velocity data for an up-pumping pitched blade turbine of size D = T/2 which was placed 6 cm below the surface and operated at $N = 0.98N_E$ (164 rpm). Velocity was measured 1.5 cm below the liquid level in a vertical plane 6 mm upstream of the baffle. The experimental fluid is water. 279

Table H.2d Velocity data for an up-pumping pitched blade turbine of size D = T/2 which was placed 5 cm below the surface and operated at $N = 0.98N_E$ (157 rpm). Velocity was measured 1.5 cm below the liquid level in a vertical plane 6 mm upstream of the baffle. The experimental fluid is water. 280

Table H.3a Repeatability of velocity data for a PBTU. Second set of data for a D = T/3 impeller operated at a submergence of 8 mm and a speed of 321 rpm. Velocity was measured in a vertical plane 6mm upstream of the baffle, 1.5 cm below the liquid surface. The experimental fluid is water. 281

Table H.3b Repeatability of velocity data for a PBTU. Third set of data for a D = T/3 impeller operated at a submergence of 8 mm and a speed of 321 rpm.

Velocity was measured in a vertical plane 6mm upstream of the baffle, 1.5 cm below the liquid surface. The experimental fluid is water. 282

Table H.4a Velocity data for an up-pumping pitched blade turbine. Measurements were made in a vertical mid-baffle plane. Velocity was measured 1.5 cm below the liquid surface for a D = T/3 impeller operated at a submergence of 8 mm and a speed of 321 rpm. The experimental fluid is water. 283

Table H.4b Velocity data for an up-pumping pitched blade turbine. Measurements were made in a vertical mid-baffle plane. Velocity was measured 1.5 cm below the liquid surface for a D = T/3 impeller operated at a submergence of 6 mm and a speed of 290 rpm. The experimental fluid is water. 284

Table H.5a Velocity data for an up-pumping pitched blade turbine of size D = T/3 which was placed 8 cm below the surface and operated at $N = 0.98N_E$ (265 rpm). Velocity was measured 1.5 cm below the liquid level in a vertical plane 6 mm upstream of the baffle. The experimental fluid is Bayol-35. 285

Table H.5b Velocity data for an up-pumping pitched blade turbine of size D = T/3 which was placed 7 cm below the surface and operated at $N = 0.98N_E$ (246 rpm). Velocity was measured 1.5 cm below the liquid level in a vertical plane 6 mm upstream of the baffle. The experimental fluid is Bayol-35. 286

Table H.5c Velocity data for an up-pumping pitched blade turbine of size D = T/3 which was placed 6 cm below the surface and operated at $N = 0.98N_E$ (234 rpm). Velocity was measured 1.5 cm below the liquid level in a vertical plane 6 mm upstream of the baffle. The experimental fluid is Bayol-35. 287

Table H.5d Velocity data for an up-pumping pitched blade turbine of size D = T/3 which was placed 5 cm below the surface and operated at $N = 0.98N_E$ (220 rpm). Velocity was measured 1.5 cm below the liquid level in a vertical plane 6 mm upstream of the baffle. The experimental fluid is Bayol-35. 288

Table H.6a First set of velocity data for a down-pumping pitched blade turbine. Velocity was measured 4 mm below the impeller (D = T/3) operated at a speed of 400 rpm in a vertical plane 6mm upstream of the baffle. The experimental fluid is water. 289

Table H.6b Second set of velocity data for a down-pumping pitched blade turbine. Velocity was measured 4 mm below the impeller (D = T/3) which was operated at a speed of 400 rpm. Measurements were made in a vertical plane 6mm upstream of the baffle. The experimental fluid is water. 290

Table H.6c Third set of velocity data for a down-pumping pitched blade turbine. Velocity was measured 4 mm below the impeller (D = T/3) which was operated at a speed of 400 rpm. Measurements were made in a vertical plane 6mm upstream of the baffle. The experimental fluid is water. 291

List of Figures

Figure 2.1 The effect of the variation of Damköhler number on product quality. The values are calculated for the Bourne 3rd Reaction (Table 2.2) using the micromixing model developed by Bourne et al. (Reproduced from Yu, 1993) 9

Figure 2.2 Optimum molar ratio for reactive mixing experiments (Reproduced from Figure 5.3, Yu, 1993) 16

Figure 2.3 Representative data from literature on the effect of feed time on byproduct yield. The data was taken in a 19 L reactor with a Rushton turbine and surface feed. Bourne 2nd Reaction was used to test mixing limitations with sodium hydroxide being added into a tank containing a mixture of hydrochloric acid and ethyl chloroacetate. The experimental conditions were: H = T, D/T = 0.33, N = 100 RPM (Reproduced from Bourne and Yu, 1994). 19

Figure 2.4 Effect of feed position on product distribution. The numbers shown are the selectivity to the undesirable byproduct for the feed location indicated by the position of the arrow. The first two figures show the results for a baffled tank with a radial and an axial impeller respectively, while the last figure is for an unbaffled tank. Feed in regions of low levels of turbulence cause more byproduct formation (Adapted from Patterson et al., 2004. The results are from Nienow and Inoue, 1993) 24

Figure 2.5 Effect of multiple feed pipes. Adapted from Figures 4 and 6 in Bourne and Hilber (1990) 25

Figure 2.6 (a) Schematic diagram of a typical stirred tank (b) Rushton turbine (RT) (c) Down-pumping pitched blade turbine (PBTD) (d) Up-pumping pitched blade turbine (PBTU) (Drawings of the impellers are modified forms of sketches downloaded from www.postmixing.com) 30

Figure 2.7 (a) Mean flow field of a Rushton Turbine (Schäffer et al., 1997). (b) Axial profile of mean radial velocity at different radial positions (Wu and Patterson, 1989). (c) Schematic diagram of a SRJ and the internal annular wall jet in a stirred tank with a Rushton turbine (Kresta et al., 2001) 34

Figure 2.8 Zonal Model for flow and dissipation in a stirred tank. The numerical values represent zones. The characteristic features of each zone are described in Table 1, Kresta et al. (2004). 36

Figure 2.9 Mean flow field from a PBT (a) at low clearance (b) at high clearance (Bhattacharya and Kresta, 2002) (c) Radial profile of mean velocity below impeller (Kresta and Wood, 1993) (d) Radial velocity profiles in a three dimensional wall jet (Bhattacharya and Kresta, 2000). 40

Figure 2.10 (a) Mean flow field generated from a PBTU (b) Mean flow field produced from a PBTD 45

Figure 2.10 (c) Axial RMS velocity, u/V_{Tip} for a PBTU (d) Radial RMS velocity v/V_{Tip} for a PBTU and (e) Tangential RMS velocity, w/V_{Tip} for a PBTU 46

Figure 2.10 (f) Axial RMS velocity, u/V_{Tip} for a PBTD (g) Radial RMS velocity v/V_{Tip} for a PBTD and (h) Tangential RMS velocity, w/V_{Tip} for a PBTD 46

Figure 2.11 An idealized scheme showing the production (at the rate, $\wp$), the transfer and the final dissipation (at the rate, ε) of turbulent kinetic energy. In this simplified scheme, approximate length scales are defined for the largest and the smallest eddies. ℓ represents the volume averaged size of the large eddies containing most of the energy, while λ represents the volume averaged size of the small eddies involved in the dissipation of the turbulent kinetic energy. In a more rigorous framework, Λ_g (Taylor's integral scale, 1935) and λ_g (Taylor's microscale, 1935) should be used. For the special case of isotropic turbulence ℓ can be defined in terms of Λ_g and λ in terms of λ_g. 51

Figure 2.12 Three-dimensional Energy Spectrum and Concentration Spectrum in turbulent flows with very high local Reynolds number (inertial subrange exists). 54

Figure 2.13 a) One-dimensional energy spectrum for a tank stirred with a Rushton turbine. (Reproduced from Wernersson, 1997). b) Trailing vortices attached to the blades of a Rushton turbine visualized through LES (Reproduced from Bakker and Oshinowo, 2004) c) Trailing vortex attached to the blade of a PBT. PIV measurements (Reproduced from Schäffer et al., 1998). 58

Figure 2.14 Schematic spectrums of concentration variance for fluids at very high Reynolds number. (a) The spectrum for a liquid with high Schmidt number and (b) the spectrum for a gas with low Schmidt number. Not to scale. 63

Figure 2.15 Schematic representation of (a) a Vortex tube (b) Formation of laminated structure by the action of vorticity (c) Engulfment of fluid from by the local environment due to the action of strain on the vortex tubes (d) Lamellar structure of the fluid in the vortex (A) and the fluid from the local environment (B) inside a vortex tube. Figures adapted from Figures 8.14, 8.13, 8.16 and 8.17 in Baldyga and Bourne (1999). 67

Figure 2.16 Schematic representation of the engulfment model. (a) shows the growth of the mixing volume (V_m) by engulfment from the surrounding (b) concentration profile of B for mixing without reaction (c) concentration profile of B with instantaneous reaction ($t_2 < t_1 < t_0$). Figure reproduced from Figure 8.22 in Baldyga and Bourne (1999). 70

Figure 2.17 Schematic representation of the mesomixing process by inertial-convective disintegration accompanied by micromic. A blob of fluid undergoes inertial-convective disintegration and distortion between times [t_o and t_1] and [t_2 and t_3]. Micromixing homogenizes the concentration between times [t_1 and t_2]. Note that inertial-convective disintegration and micromixing occur simultaneously and not in series. Reproduced from Figure 8.31, page 596, Baldyga and Bourne (1999) 70

Figure 2.18 A view of mesomixing: structure of partially segregated islands. The islands contain two regions: grey regions with only B and black micromixed regions where A, B and C are chemically homogeneous. The islands are immersed within the surrounding mixture (white) containing only A and C. 74

Figure 3.1 (a) Schematic of free, axisymmetric jet (b) Schematic of feed jet in stirred tank ($U_z = U_m$) (c) Self-similar profile of axial velocity in a fully turbulent axisymmetric jet (Equation 3.55) 82

Figure 3.2a Operating range for a fully turbulent feed jet 93

Figure 3.2b In the small scale it is difficult to operate the impeller while satisfying all constraints (T = 0.24m, D/T = 1/3). 96

Figure 3.3 Chromatograms of samples collected at various stages of an experiment (PBTU, d_f = 3mm, t_f = 2848s). Note the formation of a small amount of ethanol after addition of HCl and the larger amounts of ethanol in the final product. The peaks are truncated only in the recorded graphs. Calculation of area is not affected in the integrator. 102

Figure 3.4 Calibration curve for ethyl chloroacetate. The abscissa is the ratio of the retention area of the peak for ethyl chloroacetate to that for 2-butanone. The ordinate is the known concentration of the ester in the injected sample. 103

Figure 3.5 Schematic of feed assembly and tank. Sodium hydroxide (2) is fed through the nozzle (4) by a cavity style gear pump (3). The amount of feed added is measured by difference using a Mettler balance (1). 104

Figure 3.6 Effect of Re_f on byproduct yield. For the larger nozzle size, replicates are shown for various different feed times (see also Table 3.4). The solid line connects the averages of these replicates. 108

Figure 3.7 Effect of feed time on byproduct yield 111

Figure 3.8a Effect of impeller speed on byproduct yield 113

Figure 3.8b Effect of impeller speed and molar flow rates of A and B on the byproduct yield 114

Figure 3.9 Plunging Jet 116

Figure 4.1 Schematic of feed and impeller configurations: a) conventional submerged feed b) surface feed with up-pumping PBT. Table 4.1 gives full details of the feed and impeller geometry for all five cases considered. 123

Figure 4.2 (a) Aerometrics LDV setup used to measure instantaneous velocity. (b) Tank cross section. 127

Figure 4.3a Comparison of mean velocity data from present study with data from Kresta (1991). The data from Kresta (1991) are shown filled while the replicates from this investigation are shown hollow. Measurements are shown for a PBTD with D = T/3, located at an off-bottom clearance, C/D = 1. The measurement traverse is at a distance of 4 mm below the lower edge of the impeller. The impeller speed in Kresta (1991) was 450 rpm while the present data were collected at 400 rpm for similar tank sizes. 130

Figure 4.3b Comparison of RMS velocity data from present study with data from Kresta (1991). The data from Kresta (1991) are shown filled while all replicates from the present investigation are shown hollow. Measurement conditions are the same as in Figure 4.3a. 131

Figure 4.4a Reproducibility of velocity measurements. Axial mean velocity data is shown for the up-pumping pitched blade turbine (D = T/3) with the impeller operated at S/D = 1 and a speed equal to 98% of the speed at which air bubbles are entrained into the tank ($0.98N_E$). The first and the last set of data shown in this figure were collected over a period separated by more than 12 months. 132

Figure 4.4b Reproducibility of RMS velocity measurements. Data is shown conditions similar to that in Figure 4.4a. 133

Figure 4.5 Radial profiles of the axial velocity, at a location 1.5cm below the quiescent surface is shown for two planes: mid-baffle and at a plane located with an offset of 6mm from the baffle. 134

Figure 4.6 Radial profiles of the axial velocity, at a location 1.5cm below the quiescent surface is shown for two planes: mid-baffle and at a plane located with an offset of 6mm from the baffle. 135

Figure 4.7 Effect of feed time on byproduct yield for submerged feed. Results are shown here for the base case configurations (Cases 1 and 2). For Case 2, the PBTD, the feed pipe is located at two heights above the impeller to illustrate the sensitivity of byproduct yield to feed location. 138

Figure 4.8 Effect of feed time on byproduct yield for surface feed configurations: Cases 3, 4 and 5. A PBTU dramatically improves performance relative to a conventional PBTD (dotted line), but does not quite attain the performance of the submerged feed at small h/D unless the impeller is operated at Fr'_{crit}. The up-pumping configuration shows little effect of geometry on byproduct yield. See an expanded scale of the mesomixing range in Figure 4.9. 140

Figure 4.9 Expanded Figure 4.8 showing the effect of feed time on byproduct yield in the mesomixing regime. A small, but significant effect of feed location (2%) and nozzle diameter (up to 10%) is evident for very short feed times. 142

Figure 4.10 Critical Froude number (N_E^2S/g) for the up-pumping impeller as a function of impeller submergence, S. When the impeller is operated above the critical Froude number, air bubbles are entrained into the tank. Since the curves for the two impeller sizes do not collapse, the Froude number does not completely capture the physics of air entrainment at the surface. 146

Figure 4.11 Best performance near ($0.96Fr_{crit}$) the critical Froude number. When the up-pumping impeller is operated close to the critical Froude number, the byproduct yield is minimized and is comparable to the best possible performance obtained with a submerged feed pipe, shown as a triangle. Near the critical Froude number, the byproduct yield is independent of submergence, suggesting that air entrainment is a function of surface turbulence rather than of Froude number.......... 147

Figure 4.12 RMS velocity measured close to the surface for PBTD and PBTU. At Fr'_{crit} the turbulence levels at the surface are similar irrespective of the submergence or impeller type. These results indicate that the onset of air entrainment occurs when surface turbulence levels reach a critical value. 149

Figure 5.1 Comparison of experimental results from the present study with parametric models from previous studies. Empirical correlations are not applicable outside the conditions for which they are developed. 158

Figure 5.2 Regions characterizing the effect of turbulence on a free surface (Brochinni and Peregrine, 2001). In the shaded region interaction between turbulence and the surface increases from gentle surface undulations at the lower limit to surface breakage at the upper. Four limiting regions are shown by the dotted lines at the We and Fr limits. The dashed line is for Re = 100. The filled and hollow symbols represent the maximum and the minimum RMS velocities measured at the surface of the tank. The characteristic length scale for these symbols is the diameter of the entrained bubbles. 162

Figure 5.3 Proposed mechanism for air entrainment. Bubbles are formed at the interface when the turbulent kinetic energy is strong enough to break the stabilizing effects of surface tension and gravity. The newly formed bubbles are pulled into the tank by the mean down-flow. 165

Figure 5.4 Experimental configurations: (a) Vortex formation in un-baffled tank (b) Standard baffles and PBTU (c) Short baffles and PBTU (c) Notched baffles and PBTU.......... 169

Figure 5.5 Qualitative description of the surface of the tank when the impeller speed is below, at and above N_E. 170

Figure 5.6 Parity plot of h_l/D from experiments in an un-baffled tank in this study and previously reported parametric models. Good agreement is obtained in the data from three different laboratories.......... 176

Figure 5.7 Critical impeller speed for air entrainment (N_E) for a PBTU ($D = T/3$) with different fluids and baffle geometries. While fluid properties affect N_E, baffle geometry does not. Note also the increasing N_E with deeper submergence for all fluids. 179

Figure 5.8a Raw data showing the critical impeller speed required for air entrainment (N_E) at different submergences for a PBTU at two impeller sizes ($D = T/3$ and $D = T/2$) with standard baffles. N_E increases with increasing impeller submergence. Fluid properties (ρ, σ and ν, see Table 5.2) also affect N_E. 181

Figure 5.8b The impeller Froude number required for air entrainment for a small diameter PBTU ($D = T/3$). 184

Figure 5.8c The Froude number required for air entrainment for a large diameter PBTU ($D = T/2$). Note that air entrainment starts at much smaller impeller speeds for the larger impeller and the change in axes scales. 184

Figure 5.8d Parity plot of the impeller speed at the onset of air entrainment for a PBTU. Experimental data from the present study are compared with the only available parametric model for a PBTU (Tanaka and Izumi, 1987). 185

Figure 5.9 Radial profiles of the vertical component of mean velocity when the impeller speed is close to N_E. Beyond $r \sim 0.08$m the flow is downwards. The downward moving fluid pulls any bubbles formed at the surface downwards into the tank. This is the region of air entrainment. (a) Comparison of profiles with water for two impeller sizes (b) Comparison for water and Bayol-35 for D = 80 mm. 187

Figure 5.10a The axial component of the root mean square fluctuation (RMS) velocity when the impeller speed is $0.97N_E$. The turbulence in the outer part of the tank scales with the impeller speed and diameter. 189

Figure 5.10b The axial and radial components of the RMS velocity near the surface are equal in the region of air entrainment. 190

Figure 5.10c The absolute value of the RMS velocity is nearly constant in the region of air entrainment. There is a requirement for a minimum level of turbulence near the surface for air entrainment to occur. Once entrainment has occurred, mean down flow is necessary to pull the bubble into the tank. The amount of turbulence required however depends on the fluid properties. 191

Figure 5.11 Comparison of the constant of proportionality in Equations 5.11 and 5.16 for Bayol-35 and Water. In the region of air entrainment, where the downward mean flow is fully formed and unaffected by the wall ($2.2 < 2r/D < 2.5$) the data collapse for both water and Bayol-35. The critical value of the constant $[u\,(|U|/\phi)^{0.25}]$ is between 0.075 and 0.15. 193

Figure 5.12a Relation between the RMS and mean velocity at the surface at critical and sub critical conditions. For the PBTU, the velocity data comes from

Figures 5.9 and 5.10c in the air entrainment region (shown in Figure 5.11). The data is for a PBTU with D = T/3 and includes all submergences (S = 4 to 8cm). The functional relation between u/U and $[Re/We^2Fr]^{0.25}$ is different for the sub critical condition ($N < N_E$) than for the onset of air entrainment ($N \sim N_E$). 194

Figure 5.12b u/U calculated using Equation 5.20 is compared to the values measured with LDV. 195

Nomenclature

A	Dimensional constant in Equation (2.13a), -
A_f	Cross-sectional area of feed pipe, m^2
b	jet half-width, m
B	Parametric constant in Equation (3.56), -
B_l	constant in Reiger et al (1979) correlation for h_l in Equation (5.17)
C	Impeller clearance (Figure 2b), m
C_i	Concentration of species 'i', $kmol/m^3$
C_{io}	Intial concentration of species 'i' before reaction, mol/m^3
$\overline{C}_{io}$	Concentration of species 'i' obtained using the definition in Equation (2.3), mol/m^3
C_l	constant in Equation (5.3)
C'_l	constant in Equation (5.8)
C''	constant in Equation (5.16)
d_b	bubble diameter, m
d_f	Feed pipe diameter, m
d_{min}	Minimum feed pipe diameter given by Equation (3.67), m
d_{max}	Maximum feed pipe diameter, m
d_W	impeller width, m
D	Impeller diameter, m
$\mathcal{D}$	Diffusivity of fluid, m^2/s
$\mathcal{D}_T$	Diffusivity of fluid, m^2/s
Da	Damkoehler number defined in Equation (2.1), -
Da_{av}	Average Damkoehler number calculated using $\bar{\varepsilon}$, $Da_{av} = \frac{\bar{\tau}_{mixing}}{\tau_R}$ -
D(k)	Dissipation spectrum, m^3/s^2
E	Engulfment rate coefficient (Baldyga and Bourne, 1999), s^{-1}
E_T	Specific turbulent kinetic energy available at the surface, J/kg

E_S	Specific surface energy needed to deform the surface by overcoming surface tension, J/kg
E_P	Specific potential energy given by Equation 5.5, J/kg
$E(k)$	Three-dimensional energy spectrum, m^3/s^2
f	Frequency of signal, Hz
f_D	Frequency of Doppler shift caused by particle passing through the measuring volume, Hz
$f(\eta)$	Similarity profile of the axial velocity in a jet, -
Fr	Froude number given by Equation (5.1), -
Fr_f	Froude number at the feed pipe, $Fr_f = \frac{U_f}{\sqrt{gd_f}}$, -
Fr_I	Impeller Froude number at impeller speed of N, N^2D/g, -
Fr'_I	Modified impeller Froude number, N^2S/g, -
Fr_{crit}	The critical Froude number above which turbulence dominated over the stabilizing influence of gravity, see Brocchini and Peregrine (2001), -
$Fr'_{I,crit}$	Critical value of the modified impeller Froude number, $Fr'_{I,crit} = N_E^2 S/g$, -
Fr_{surf}	Froude number associated with the mean flow at the surface from Equation (5.15), -
g	Acceleration due to gravity, m/s^2
$G(k)$	Concentration spectrum, mol^2/m^5
Ga_I	Impeller Galileo number, Re_I^2/Fr_I, -
h	Height measured with respect to the upper surface of impeller, m
h_1	Height of vortex tip from impeller in an un-baffled tank, m
h_2	Height of the liquid at the tank wall in an un-baffled vessel, m
H	Liquid height in tank, m
J	Linear momentum of the fully turbulent jet, kg-m/s
k	Turbulent kinetic energy per unit mass, m^2/s^2. Note that the wave number is also represented by 'k' to maintain the notation used for this quantity in the literature.
k_i	Wave number vector, 1/m
k_K	Wave number corresponding to the Kolmogoroff scale, $k_K \sim 1/\eta$, 1/m

k_O	Wave number corresponding to the integral length scale $k_o \sim 1/\ell$, 1/m
k_R	Generic expression used for rate constant of a reaction, (variable units)
k_1, k_2	Rate constants in Equation (3.82), m^3/mol.s
K_L	Head-loss coefficient at contraction or expansion in Equation (3.66), -
K_l	Constant in Markopoulos and Kontogeorgaki (1995) correlation for h_l in Equation 5.18
ℓ	length scale of eddy, m
ℓ_{crit}	Length scale of eddies where the effect hydrostatic forces and surface tension become equal, m
L	Characteristic length scale in Figure (5.2), m
L_D	Characteristic length scale used in turbulent dispersion for determining whether the source of the feed is point or finite as defined in Equation (2.42), m
L_t	Distance from liquid surface to impeller (Figure 2b), m
L_X	Length scale characterizing the system or reactor e.g. tank diameter, m
m_{Tank}	Total mass of liquid in the stirred tank, kg
n_f	Number of feed pipes, -
n_i	Number of moles of component "i", mol
$\dot{n}_A$	Molar flow rate of reagent A coming to the reaction zone with the circulation, mol/s
$\dot{n}_B$	Molar flow rate of reagent B coming to the reaction zone with the feed, mol/s
$\dot{n}_{A,Imp}$	Molar pumping rate of reagent A at the impeller given by Equation (E.2), mol/s
n_{SAi}	i = 1, 2 or 3. Impeller speeds at which bubbles start forming at the surface, dispersing through the liquid and at which the impeller power draw reduces. Nomenclature from Heywood et al. (1985), rpm
N	Impeller speed, rpm
$N_{Constraint3}$	Impeller speed required to satisfy Constraint 3, rpm
$N_{Constraint3}$	Impeller speed required to satisfy Constraint 4, rpm
N_E	Impeller speed at which air bubbles are entrained and remain in the tank, rpm
N_{min}	Minimum impeller speed, rpm
N_{max}	maximum impeller speed, rpm

N_S	Another nomenclature for N_E used in literature, rpm
N_Q	flow number of impeller, -
P	Impeller power consumption, W
P_o	Power number of impeller, -
q	characteristic velocity scale in Figure (5.2). Brocchini and Peregrine, 2001 use a velocity scaling of $k = 1/2q^2$, m/s
Q	Pumping capacity of an impeller, Equation (2.11) m^3/s
Q_f	Volumetric flow rate of feed, m^3/s
$Q_{f,Nozzle}$	Volumetric flow rate of feed per nozzle when multiple nozzles are present, m^3/s
Q(z)	Flow rate of axisymmetric jet, m^3/s
Q_{ij}	Two-point correlation tensor defined in Appendix C, -
r	Radial distance, m
r_b	Radius of curvature of deformation or bubble radius, m
r_m	Separation vector between two spatial locations, m
r_α	Rate of reaction for species α, mol/m^3-s
r_{Umax}	Position along the radius of the tank with maximum mean velocity, m
R	Impeller radius, m
R_U	Parameter used to distinguish whether feed is finite and point source, Equation (2.43), -
R_{jet}	Radial extent of fully turbulent jet, m
Re_f	Reynolds number of feed defined in Equation (3.63), -
Re_I	impeller Reynolds number, ND^2/ν, -
Re_F	Reynolds number of feed stream, d_fU_f/ν, -
Re_{surf}	Reynolds number associated with the mean flow at the surface from Equation 5.13, -
s	Rate of strain or vortex deformation, see Equation (C.2), 1/s
S	Submergence below surface of an up-pumping impeller, m
Sl	Modified Strouhal number in the model of Sverak and Hrubý (1981), ND/v^*, -
t	time of operation, s
t_{crit}	Critical feed time below which operation moves from micromixing limited to a mesomixing limited regime, described in section (2.2.2.4), s

t_f	Feed time, s
t_{max}	Maximum feed time given by Equation (3.68), s
t_{min}	Minimum feed time given by Equation (3.69), s
T	Stirred tank diameter, m
u	Local rate of shrinkage of striations given by Equation (C.2), m/s
u'	Axial component of the root mean square velocity, m/s
u_S	Turbulent velocity scale in Equation (2.19), m/s
U	Axial component of velocity, m/s
U_{Core}	The core velocity in the three-dimensional wall jet, m/s
U_f	Velocity at the feed nozzle, m/s
U_m	Peak axial velocity in the radial profile of the jet at any z, m/s
U_s	Velocity at impeller suction (Equation 3.72), m/s
U_z	Peak velocity of jet near impeller suction, m/s
U_P	Velocity of seed particle added for LDV measurements, m/s
U_{tip}	Tangential velocity at impeller tip (πND), m/s
U_∞	Rise velocity of a bubble, m/s
$\overline{U}_C$	Average velocity of the stream in which velocity measurement probe is located, m/s
$\overline{U}$	Average velocity of the flow field surrounding the feed stream, m/s
v'	Radial component of fluctuation velocity, m/s
v^*	Suction velocity into the pipe at onset of gas entrainment in the model of Sverak and Hrubý (1981), m/s
V	Radial component of the mean velocity, m/s
V_f	Volume of feed, m^3
V_{Tank}	Volume of tank, m^3
V_{Tip}	Impeller tip speed, πND, m/s
V_m	Mixing or reaction volume in the E-model, m^3
W	Baffle width, m
We	Weber number given by Equation (5.2), -
We_f	Weber number at feed pipe, $We_f = \frac{\rho_f U_f^2 d_f}{\sigma}$, -

We_{crit}	The critical Weber number above which turbulence dominated over the stabilizing influence of surface tension, see Brocchini and Peregrine (2001), -
We_{surf}	Weber number associated with the mean flow at the surface from Equation (5.14), -
X_J	Yield of byproduct 'J'. The byproduct yield used for the third Bourne reaction is defined in Equation (3.84), -
y	depth of deformation from which a bubble is formed, m
y_m	apex of the bulge on the liquid surface when a turbulent eddy impinges on the surface, m
z	Distance from nozzle or height measured with respect to the tank bottom, m
z_o	Virtual origin of jet (Figure 3.1), m

Greek Symbols

α	Fraction of the impeller pumping molar flow rate of reagent A reaching the reaction zone with the circulation in the tank and defined by Equation (3.75), -
δ	Thickness of striation, boundary layer thickness, m
δ_ω	The size of vortex with maximum vorticity, $\delta_\omega = 11.5\eta$, m
ΔP_f	Pressured drop across nozzle, Pa or psi
ΔP_{pump}	Available pressure from pump, Pa or psi
β	Number of jet half-widths in the integration limit of Equation (3.58), -
ε	local rate of dissipation of turbulent kinetic energy per unit mass at any location (also denoted as ε_{local}), m^2/s^3
ε_C	The rate of dissipation of concentration fluctuations, mol/m^3-s
ε_{max}	Maximum rate of dissipation of turbulent kinetic energy, m^2/s^3
ε_{Total}	Total dissipation of power in a stirred tank, P/m_{Tank}, m^2/s^3
$\bar{\varepsilon}$	Average rate of dissipation of turbulent kinetic energy per unit mass, $\bar{\varepsilon} = \frac{P}{\rho V_{Tank}}$, m^2/s^3
φ	Constant in Equation (A.1), -
γ	Constant in Equation (A.1), -

η	Kolmogorov length scale, m
η_B	Batchelor length scale given in Table (), m
η_C	Corrisin length scale given in Table (), m
η_r	Dimensionless radial distance, $r/(z - z_o)$, -
ϕ	Parameter in Equation (3.55), -
θ	Blendtime (Grenville et al., 1995), s
θ_{LDV}	Angle between laser beams used for laser Doppler velocimetry, degrees
ρ	Fluid density, kg/m^3
ρ_g	density of air, kg/m^3
ρ_a	Density of air, kg/m^3
ρ_f	Density of feed, kg/m^3
ρ_T	Density of fluid in tank, kg/m^3
σ	Surface tension of fluid, N/m
Λ_g	Cross-stream integral length scale defined in Table 2.5, m
Λ_c	Integral length scale for concentration fluctuations defined in Table 2.5, m
Λ_{co}	Integral length scale for concentration fluctuations as it leaves the feed pipe, m
μ	dynamic viscosity, kg/m-s
ϕ	fluid property dependent parameter given by Equation (5.12), m^3/s^3
τ_C	Corrisin time scale given by Equation (B.38), s
τ_D	Characteristic mesomixing time due to turbulent dispersion, Equation (2.41), s
τ_{DI}	Characteristic time used to distinguish whether feed is finite or point source, Equation (2.44), s
τ_E	Micromixing time given by the Engulfment model, Equation (2.39), s
τ_{meso}	A generalized mesomixing time scale, s
τ_{mixing}	Characteristic mixing time calculated on the basis of local ε, s
$\bar{\tau}_{mixing}$	Characteristic mixing time calculated on the basis of $\bar{\varepsilon}$, s
τ_R	Characteristic reaction time, s
τ_S	Characteristic mesomixing time due to inertial-convective disintegration, Equation (2.45), s

ν	Kinematic viscosity, m^2/s
ν_f	Kinematic viscosity of fluid in feed, m/s^2
ν_T	Kinematic viscosity of fluid in tank, m/s^2
λ	Wavelength of the laser beam, m
λ_B	Batchelor scale, m

Chapter 1

Introduction

Mixing is ubiquitous, being present as the key step in innumerable man-made and natural operations. The breadth of applications and the intractable nature of turbulent mixing problems are well illustrated by Farge and Guyon (1999) in their musings on the philosophical and historical roots of turbulent mixing. Because of its universality, examples of mixing also abound, ranging from daily activities like the dissolution of sugar crystals into a cup by stirring; to industrial processes such as blending of pigments, paints and polymers; to large, global events like the mixing of the warm and cold water in the oceans which can trigger major climatic changes.

While mixing is encountered in numerous applications, its significance to the chemical industry is of particular interest to the present discussion. Industrial processes like fermentation, production of fine chemicals and pharmaceuticals, polymer processing, pulp and paper making invariably require mixing operations: blending and dispersion of liquids, dispersion of gases, suspension and distribution of solids in fluids and blending of solids. Identifying mixing problems and finding efficient solutions to them is therefore an important part of the optimal design and operation of chemical processes. Conversely, failure to provide proper mixing can lead to complete design failures and inability to achieve the requisite product quality on scale-up. According to some estimates up to 5% of the yield is lost in the chemical industry owing to to poor mixing alone (Paul et al. 2004). Identifying and solving mixing problems therefore continue to be an important aspect of chemical engineering research.

This work deals with one of the problems plaguing the mixing industry, namely the lack of sufficient mixing near the liquid surface in a stirred tank and the consequent drop in reactor performance when reagents are fed into this region. In many classes of competitive reactions, the product selectivity is best when reactants are fed close to the impeller (where turbulence is highest) with dip tubes. It worsens significantly when reagents are fed into a region of low turbulence, like the liquid surface, due to reduced mixing rates. Hence, the recommended practice is to feed close to the impeller using submerged feed pipes, or dip-tubes. Dip tubes are however, not always welcomed in the plant due to numerous problems associated with their use. First, there are mechanical issues related to the support and vibration of the tubes in tanks of commercial size. Second, submerged tubes require special materials for highly corrosive liquids. Third, the large residual reactant holdup in long feed pipes can lead to unwanted reactions at startup and shutdown, with the ultimate possibility of plugging of the line. Finally, at low feed rates backmixing can occur, moving the reaction from the turbulent region back into the relatively quiescent feed pipe. Surface feed may therefore be favoured from an operational point of view even when the requirements of reactive mixing, fluid mechanics and best mixing practice clearly point to a sub-surface feed. In order to make this feed configuration work, it is important to develop methods by which byproduct formation can be suppressed and product quality improved to the required levels. In this study, several alternate feed and impeller configurations are explored to find a simple, industrially feasible solution to the problems caused by surface feed of reagents.

Chapter 2 is a review of the issues determining product quality in a mixing sensitive reaction. When the reactor is operated in a fully turbulent regime, the interrelation between mixing rates and chemical kinetics quickly becomes complicated because of the multiscalar nature of the flow and scalar fields. The chapter reviews key concepts of turbulent mixing and outlines the important findings of various groups working in this area. Ultimately, it is the flow field in the reactor, which determines turbulence levels, and hence mixing rates. Earlier studies on the flow field generated by the various types of impeller used in this investigation are therefore also reviewed.

Previous studies show that an improvement in mixing rates and hence performance is directly linked to the turbulence levels in the zone of mixing. Hence, the key requirement is to produce a high local turbulent energy dissipation rate locally in the reaction zone near the surface. This can be done by either modifying the flow characteristics of the feed stream itself or by changing the ambient flow field around it.

Chapter 3 outlines the methods and the results obtained by modifying the feed stream. The feed velocity is increased many times over the traditional values in an attempt to enhance entrainment and mixing of ambient fluid into the feed stream and improves mixing characteristics. The results show that operation in this regime is extremely difficult and unstable. Chapter 4 deals with the second approach. Instead of employing sub-surface feed with the traditional impellers, surface feed is used with an up-pumping impeller. The turbulent discharge stream from the impeller is directed towards the surface thereby increasing turbulence in this region. Instead of feeding into the most turbulent region, the problem is inverted and a high level of turbulence is brought to the feed zone. Results show that operation in this mode provides much improved performance. Different feed and impeller geometries were used to determine the best configuration.

Any impeller can cause entrainment of air bubbles from the surface of the tank if it is operated at a high enough speed. This can become a problem for some industrial processes where air bubbles may be deleterious to process objectives. Up-pumping impellers entrain air bubbles at much lower speeds than the other kinds of impellers; hence the problem is all the more acute for this impeller. Chapter 5 deals with an extensive study, which was conducted to properly identify (i) the point of air entrainment and its dependence on various operating parameters and (ii) the mechanism of this process. Velocity measurements were also made close to the surface to allow a better fundamental understanding of this phenomenon.

Chapter 6 is a summary of ideas and highlights the key results obtained in this study on surface feed of reagents using the third Bourne reaction.

Chapter 2

Literature Review

Mixing can have a profound influence on product quality in complicated reactions. A good understanding of the interactions between mixing rates and reaction kinetics has developed through extensive investigations involving customized reaction schemes, judicious application of theories developed in associated areas like turbulent flows and numerical simulations. Important results from some of these investigations are reviewed in this chapter. The discussions are grouped into the following sections:

- First, results from previous experimental studies on reactive mixing are presented to highlight the key issues in the area.
- While the relative rates of mixing and reaction affect product quality directly, it is the flow-field and the local turbulence levels in the tank that ultimately determines the rate of mixing. This chapter, therefore, also includes a discussion on the turbulent flow field generated in a stirred tank.
- The last section is a summary of the theoretical aspects of turbulent mixing, its distinctive features and the methods used to characterize it. In a strictest sense, the present investigation does not involve the application of detailed mixing models. These models nonetheless provide a deeper insight into the phenomenon of turbulent mixing and have consequently been included in the discussion.

2.1. *Definitions of Mixing*

Mixing has many facets and a mixing problem can be approached from many different perspectives. The scale at which mixing occurs, the properties of the components, the nature of segregation or even the dominating forces involved in the process changes with each situation making it difficult to develop a general or universal theory of mixing (Hinch, 1999). It is nevertheless possible to formulate a generalized definition of the process by identifying its universal objectives. Paul et al. (2004) describe mixing as "the reduction in inhomogeneity in order to achieve a desired process result". The inhomogeneity or segregation can be one of concentration, phase or temperature.

Hence, phenomemologically mixing is a process, which promotes homogeneity by actively reducing segregation and associated heterogeneity or as stated by Kresta (2004), its main objective is the control of segregation. Although this definition captures the essence of the mixing process, another approach is often preferred when describing it for problem solving. This approach is necessitated by the virtual impossibility of being able to account for all nuances and contingencies of mixing problems and the consequent requirement for a case-by-case approach to solve individual problems. Thus, the 'definition' consists of a simple listing of the conditions under which the mixing problem exists, e.g. the classification from Yu (1993):

- The number of phases involved (gas, liquid or solid which can be miscible or immiscible),
- The flow regimes (laminar, transitional or turbulent)
- The fluid properties (Newtonian or non-Newtonian)
- Process objectives (reaction, dissolution, mass transfer, heat transfer)
- And the modes of operation (batch, semi-batch, continuous)

The approach is practical because it clearly identifies the immediate mixing objectives that need to be met but ultimately it is not very satisfying since it does not reveal the universal characteristics underlying the process.

From a chemical engineering perspective, it is possible to categorize further the role of mixing. Any chemical process can be broadly divided into three steps: blending of raw components, reaction between components and, finally, separation, purification and retrieval of the finished product. Mixing processes may exist in each of these steps. It is involved not only in the initial, macroscale blending of the raw material (gas, liquid or solid) but also in the smaller micro (Batchelor or Kolmogorov scales) and/or mesoscale mixing within the reactor leading finally to diffusion and reaction. Even in the separation and purification steps, which are generally purely physical processes, intermixing and backmixing of fluid streams occur because of which the desired results are affected. Apart from these mass transport related steps, there could also be requirement for convective mixing to accelerate the addition or removal of heat for non-isothermal reactions. The research outlined in this dissertation deals mainly with the problems arising out of insufficient micro and mesoscale mixing in the reaction step, identified here as the second step in the generalized scheme for chemical processes.

2.2. Mixing and Reactions

The influence of mixing on the yield and distribution of a reaction depends primarily on the reaction mechanism and the relative rates of the two processes. When the reaction in question is only a primary, single step process, the relative rates of reaction and mixing determine the reactor volume required. If the rate of mixing is slower than the reaction kinetics then the reactor volume is dependent solely on the former and vice-versa. However, when the reaction mechanism is complicated, involving multiple reaction steps, not only is the overall rate of reaction retarded by a slower mixing rate but more importantly, the yield and distribution of the products are also affected. The issues involved are complicated and the understanding of how they interact has developed only recently. Some of these aspects are described below, starting with the definition of the Damköhler number, a quantity commonly used for characterizing mixing limitations.

2.2.1. Relative Rates of Mixing and Reaction - the Damköhler number

The Damköhler number (Da) is named after a twentieth century German engineer, Gerhard von Damköhler, who studied the effects of turbulence on the propagation of flames. From its initial application to combustion engineering, Da has spread to numerous other fluid flow and diffusion problems involving reaction and/or heat transfer. Because of the variety of areas in which it is used, the definitions of Da have also become varied. In his compilation of physical laws and models, Hall (2000) lists five separate definitions of the Damköhler number, identified sequentially as the Damköhler first to the fifth numbers. While the first two Das' deal with the ratios of the rate of reaction to the flow rate of the fluid and the rate of mass transfer respectively, the third and fourth deal with the ratio of the heat liberated by a reaction to the heat transported by convection and conduction. The Damköhler fifth number is defined as the ratio of the inertial to the viscous forces and is essentially the same as the Reynolds number. The definition of the Damköhler number has therefore been adapted according to the necessities of the physical processes to which it is applied. Its general form however, continues to remain the ratio between the rate of generation or consumption of mass or heat to the rate at which it is transported.

When applied to the area of reactive mixing, the Damköhler number is defined as the ratio of the rate of reaction to the rate of mixing or equivalently as the ratio between the characteristic mixing time (τ_M) and the reaction time (τ_R):

$$Da = \frac{\tau_M}{\tau_R} \tag{2.1}$$

(This definition makes the mixing Damköhler number similar to the definition of the conventional Damköhler second number). Because turbulent mixing occurs in multiple length scales, τ_M is chosen as the characteristic time of mixing at the scale where it is rate controlling. The characteristics time scales in Equation (2.1) are usually estimated from local quantities in the reaction zone, e.g. τ_M is often calculated from the local rate of dissipation of turbulent kinetic energy per unit mass (ε). Where the local dissipation is unknown, or exact geometric similarity is enforced, the mixing time, τ_M, is sometimes also defined in terms of the rate of dissipation of turbulent kinetic energy averaged over the mass of the whole tank, $\bar{\varepsilon}$:

$$\bar{\varepsilon} = \frac{\rho P_o N^3 D^5}{\rho V_{Tank}} \tag{2.2}$$

The Damköhler number obtained using this definition of τ_M is the average Damköhler number, Da_{av}. The dependence of the characteristic mixing time on turbulence will be discussed in more details in later sections. The characteristic time for reaction is obtained from the kinetics of the slowest, rate controlling reaction step; e.g. for a second order rate controlling step with rate, $r = -k_R C_A C_B$ mol/m^{3}s, $\tau_R = (k_R C_{Bo})^{-1}$ s. Here C_{Bo} is the initial (or feed) concentration of the limiting reactant B. It is conventional (e.g. in combustion theory) to refer the Damköhler number not to the feed concentration (C_{Bo}) but rather to the concentration that B would have if it were mixed completely with the other reagent/s before reaction started ($\overline{C}_{Bo}$). Hence, τ_R is often represented as $\tau_R = (k_R \overline{C}_{Bo})^{-1}$ s (Baldyga and Bourne, 1989; Baldyga and Bourne, 1990; Baldyga and Bourne, 1992;

Baldyga et al., 1993; Bourne and Yu, 1994; Baldyga and Bourne, 1999). Note however, that

$$\overline{C}_{Bo} = \frac{C_{Bo}}{1+a} \qquad (2.3)$$

where a is the ratio of the feed volume to the initial tank volume. When the volume ratios are kept constant, Da definitions based on the two concentrations are numerically different but only by a fixed constant. Patterson et al. (2004) point out that it may be desirable to use C_{Bo} rather than $\overline{C}_{Bo}$ in estimating the reaction time to obtain the highest reaction rate and the worst-case mixing limitation.

Figure 2.1 shows the relation between the Damköhler number and the product quality for a typical reaction (the Bourne third reaction). When Da is very small, the rate of mixing is faster than the rate of reaction ($\tau_M < \tau_R$), molecules are transported to each other faster than the rate at which they can react and the product distribution is determined solely by reaction kinetics. On the other hand, when Da is large the reaction is very fast, molecules react as soon as they come in contact and the yield and selectivity of products are controlled by the rate at which the fluid elements are contacted in a microscopic scale. Mixing thus becomes important in determining the quality of products. The faster the reaction rate the greater is the deviation from kinetic predictions due to the increasing influence of mixing on yield and selectivity. The value of the Damköhler number that needs to be maintained for good reactor performance depends on the amount of byproduct that can be tolerated by the process. For example, in Figure 2.1 if 5% byproduct is tolerable, then Da (based on $\overline{C}_{Bo}$) for good performance is 0.025. This is equivalent to Da (based on C_{Bo}) of about 1.3 (from Equation 2.3) when a = 50.

2.2.2. Reactive Mixing Experiments

The fact that mixing can have a considerable influence on the yield and selectivity of reactions implies that product distribution can be altered not only by chemical but also by physical means. This underscores the importance of gaining a better understanding of the effects of mixing on complex reactions. Two kinds of reaction schemes have been used commonly for experiments (e.g. pages 38-47, Badyga and Bourne, 1999):

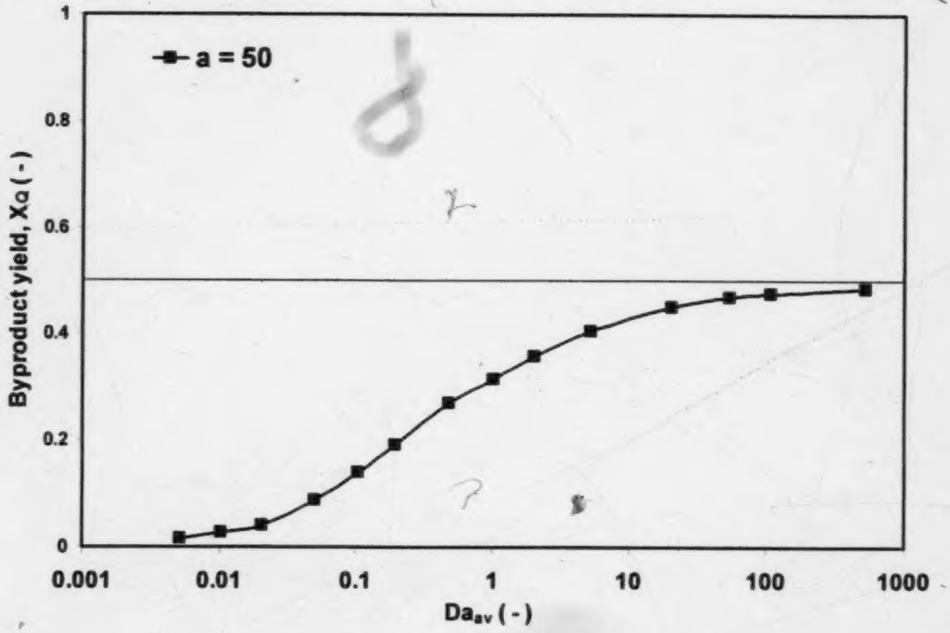

Figure 2.1 The effect of the variation of Damköhler number on product quality. The values are calculated for the Bourne 3rd Reaction (Table 2.2) using the micromixing model developed by Bourne et al. (Reproduced from Yu, 1993)

a) Competitive or Parallel Reactions:

$$A + B \xrightarrow{k_1} D + E$$

$$C + B \xrightarrow{k_2} F + G$$

Examples include:

- Nitration of benzene and toluene
- Reduction of Co(III) complexes by Cr(II) ions
- Simultaneous neutralization of acid and hydrolysis of ester by NaOH
- Diazo coupling with simultaneous reagent decomposition
- Iodate/iodine reaction with neutralization
- Acetal hydrolysis with simultaneous neutralization

b) Competitive-Consecutive or Parallel-series Reaction Schemes:

$$A + B \xrightarrow{k_1} C\,(\text{primary product})$$

$$C + D \xrightarrow{k_2} E\,(\text{byproduct})$$

Examples:

- Ethylene diamine with isocyanate or isothiocyanate ($k_1 \sim 2k_2$)
- Nitration of durene with nitronium salts ($k_1 >> k_2$)
- Diazo coupling (1-napthol and diazotized sulphanilic acid are widely used in diazo coupling experiments, $k_1 >> k_2$)
- Precipitation of barium sulfate from a alkaline solution of sulfate ions and barium-EDTA complex by addition of acid ($k_1 >> k_2$)

Of the numerous choices available, only a handful of reaction schemes are actually used in studies on reactive mixing: the Bourne reactions, the iodine-tyrosine reaction developed by Paul and Treybal (1971) etc. These reactions are favoured primarily because of considerations of safety, ease of use, suitability of reaction kinetics for the range of mixing rates in the equipment under study, and the availability of accurate and reliable information on the reaction kinetics and measurement techniques. Detailed description of the kinetics, applicability and the safety issues that need to be considered for each reaction is given in Baldyga and Bourne (pages 637-673, 1999). Important characteristics are also summarized in Table 2.1.

Table 2.1 Details of reaction schemes commonly used in experiments on mixing limited reactions.

<table>
<tr><th>Practical Range of τ_R @ 25 to 30°C</th><th>Practical Range of ε, W/kg</th><th>Relative Ease of Use</th><th>Reagent Stability</th><th>Material Balance</th><th>Method of Analysis</th><th>LD_{50}, g/Kg rat</th><th>Reagents per m^3 solution</th><th>Waste stream constituent</th></tr>
<tr><td colspan="9"><i>First Bourne Reaction: 1-napthanol with diazotized sulfanilic acid (Bourne et al., 1990)</i>
$A1 + B \xrightarrow{k_{1p}} p-R$
$A1 + B \xrightarrow{k_{1o}} o-R$
$p-R + B \xrightarrow{k_{2p}} S$
$o-R + B \xrightarrow{k_{2o}} S$
where
A1 = 1 – napthol
B = Diazotized Sulphanilic acid
p – R = para – monoazo dye
o – R = ortho – monoazo dye
S = bisazo dye
and
$k_{1p} = 12238\ m^3/mol-s$
$k_{1o} = 921\ m^3/mol-s$
$k_{2p} = 22.25\ m^3/mol-s$
$k_{2o} = 1.835\ m^3/mol-s$</td></tr>
<tr><td>65-5000</td><td>Up to 4000</td><td>Difficult</td><td>Marginal</td><td>> 95%</td><td>Multicomponent UV</td><td>2</td><td>150</td><td>< 1 wt % dyes</td></tr>
<tr><td colspan="9"><i>Second Bourne Reaction: 1- and 2-napthanol with diazotized sulfanilic acid (Bourne et al., 1992)</i>
$A1 + B \xrightarrow{k_{1p}} p-R$
$A1 + B \xrightarrow{k_{1o}} o-R$
$p-R + B \xrightarrow{k_{2p}} S$
$o-R + B \xrightarrow{k_{2o}} S$
$A2 + B \xrightarrow{k_3} Q$
where
A2 = 2 – napthol
and rest same as above
and
$k_3 = 124.5\ m^3/mol-s$</td></tr>
<tr><td>30-5000</td><td>$< 10^5$</td><td>Good</td><td>Marginal</td><td>> 95%</td><td>Multiparameter UV</td><td>2</td><td>150</td><td>< 1 wt % dyes</td></tr>
</table>

Table (2.1) contd.

<table>
<tr><td colspan="9"><i>Third (a) Bourne Reaction: Hydrolysis of NaOH versus hydrolysis of ethylchloroacetate (Bourne and Yu, 1994)</i>
$A + B \xrightarrow{k_1} P + P_1$
$C + B \xrightarrow{k_2} Q + Q_1$
where
A = hydrochloric acid
B = sodium hydroxide
C = ethyl chloroacetate
P = sodium chloride
P_1 = water
Q = sodium chloroacetate
Q_1 = ethanol
and
$k_1 = 0.03\ m^3/mol-s$ @ 298K
$k_2 = 1.3x10^8\ m^3/mol-s$</td></tr>
<tr><td>350-9000</td><td>< 1</td><td>Good</td><td>Marginal</td><td>> 99%</td><td>Single Component GC</td><td>0.2</td><td>550</td><td><1% NaCl-acetate; < 1% alcohol; salts</td></tr>
<tr><td colspan="9"><i>Third (b) Bourne Reaction: Neutralization of NaOH vs hydrolysis of ethyl and methyl chloroacetate with HCl (Bourne and Yu, 1994)</i>
$A + B \xrightarrow{k_1} P + P_1$
$C + B \xrightarrow{k_2} Q + Q_1$
$D + B \xrightarrow{k_3} Q + R_1$
where
D = methyl chloroacetate
R = methanol
and rest same as above
and
$k_3 = \ m^3/mol-s$ @ 298K</td></tr>
<tr><td>200-5000</td><td>< 10</td><td>Good</td><td>Marginal</td><td>> 99%</td><td>Single Component GC</td><td>0.2</td><td>550</td><td><1% NaCl-acetate; < 1% alcohol; salts</td></tr>
<tr><td colspan="9">Fourth Bourne Reaction: Acid hydrolysis of 2,2-dimethhoxypropane versus neutralization of NaOH (Baldyga et al., 1998)</td></tr>
<tr><td>1-2000</td><td>$1\text{-}10^6$</td><td>Excellent</td><td>Excellent</td><td>> 99%</td><td>Single parameter GC</td><td>1</td><td>180</td><td>25% Ethanol; <5% Methanol-acetone; salts</td></tr>
</table>

The third Bourne reaction was used exclusively in the present study. The kinetics of this reaction are discussed in Yu (1993) and their observations are summarized in Section 2.2.2.1 below. The following sections are a review of previous studies on the influence of the modes of operation and operating parameters on byproduct yield. Many of these results have been described in detail on pages 671-803 of Baldyga and Bourne (1999); hence, only a summary is presented here.

2.2.2.1. Kinetics of the Third Bourne Reaction

The third Bourne reaction is a competitive reaction scheme (Table 2.1) consisting of an instantaneous acid-base neutralization reaction occurring simultaneously with a slower step involving neutralization of an ester (ethyl chloroacetate):

$$\begin{array}{lllll} NaOH(B) & + \; HCl(A) & \xrightarrow{k_1} & NaCl(P) & + \; H_2O(P_1) \\ NaOH(B) & + \; CH_2ClCOOC_2H_5\,(C) & \xrightarrow{k_2} & CH_2ClCOONa(Q) & + \; C_2H_5OH(Q_1) \end{array} \qquad (2.4a)$$

The rate expressions for the two steps are:

$$\begin{aligned} r_{\text{acid-base neutralization}} &= -k_1 C_A C_B \\ r_{\text{ester neutralization}} &= -k_2 C_C C_B \;\cong\; -k_2 C_B \end{aligned} \qquad (2.4b)$$

The approximation used in Equation (2.4b) is valid when B is the limiting reagent and A and C are present in excess. Yu (1993) provide a detailed survey of the rate constants k_1 and k_2. The ester can undergo hydrolysis under neutral, acidic and alkaline environments but the rate constants for these conditions are about $1.1\text{x}10^{-7}$ s^{-1}, $4\text{x}10^{-8}$ m^3/mol-s and 0.03 m^3/mol-s respectively. Neutral and acidic hydrolysis are therefore practically negligible as compared to the reaction with the alkali. Over a temperature range of 275-299K, Baldyga and Bourne (page 654, 1999) recommend the use of the following correlation for k_2:

$$k_2 = 2.0\text{x}10^5 \exp\left(-\frac{3.891\text{x}10^4}{RT}\right) \qquad (2.5)$$

At 298 K, Equation (2.5) gives a value of $k_2 = 0.03$ m^3/mol-s. Unlike the alkaline hydrolysis of ethyl chloroacetate, the acid-base neutralization reaction is virtually instantaneous ($k_1 \sim 108$ m^3/mol-s). The large difference in the rate constants between the two steps makes this reaction scheme very mixing sensitive. When mixing is slow, there is segregation of chemical species and the product distribution is very different from when mixing is very fast and there is complete mixing to the microscopic levels. These issues are revisited in greater detail in following sections.

In Equation (2.4a), P is the primary product and Q and Q_1 the byproducts. Reactor performance is often reported in terms of the byproduct yield for the reaction. This performance measure can be expressed either as the amount of ester (A) reacted per mole of alkali added or as the amount of ethanol (Q_1) formed per mole of alkali:

$$\begin{aligned} X_Q &= \frac{\text{amount of C reacted}}{\text{moles of A added}} = \frac{V_{Tank}C_{C0} - (V_{Tank} + V_f)C_C}{V_f C_A} \\ X_{Q1} &= \frac{\text{amount of } Q_1 \text{ formed}}{\text{moles of A added}} = \frac{(V_{Tank} + V_f)C_{Q_1}}{V_f C_A} \end{aligned} \tag{2.6}$$

In the present study, the concentration of ester and ethanol was measured in both the reactant and the product mixtures so the byproduct yield could be calculated using either expression.

An important limitation of the reaction scheme outlined in Equation (2.4a) is that ethyl chloroacetate is sparingly soluble in water. Stephenson and Stuart (1986) provide the solubility data of ethyl chloroacetate in water, which shows that at 30.8°C only 1.9 g of ethyl chloroacetate dissolves in 100 g of solution. The molecular weight and density of ethyl chloroacetate are about 122.55 g/mol and 1.145 g/cc respectively, which implies that the molar concentration of the saturated solution is only about 150 mol/m^3 at 30.8°C. Experiments with the Bourne third reaction therefore has to be carried out with relatively low concentration of reactants. The ethyl chloroacetate concentrations that have been commonly used in experiments range between 30 to 90 mol/m^3.

2.2.2.2. Effect of Reactant Concentrations

When the reactants are completely mixed, no molecular level concentration gradients exist and product quality is governed solely by chemical kinetics. Because $k_1 >> k_2$ for the third Bourne reaction, in this case molecules of B react first with A forming P and only when A is completely consumed does it start reacting with C to form Q. On the other hand, when segregation is complete, B reacts with both A and C producing P and Q in the amounts determined by the initial ratios of A and C. Product distribution in the mixing limited regime is therefore dependent on the relative amounts of reactants added. There are three parameters, which control the amounts of the chemical species undergoing reaction: the initial concentration of the species, the volumetric ratio ($a = V_{Tank}/V_f$) and the stoichiometric ratios (n_B/n_A etc.). Yu (1993), Bourne and Yu (1994) studied the effect of these parameters on the byproduct yield and their findings are summarized below.

A) Effect of initial concentration: When Da_{av} was increased by increasing reactant concentration, it was found that the byproduct yield increased i.e. an increase in reactant concentration caused greater segregation and more byproduct formation. Identical results for similar changes in parameters but based on numerical simulations were reported in other studies by Baldyga and Bourne (pages 675-678 and 686-688, 1999).

B) Effect of stoichiometric coefficient: The researchers also found that the widest window for experiments (with byproduct yields for completely mixed and segregated conditions separated by the widest margins) existed for equimolar amounts of reactants. If n_B/n_A is defined as the ratio of the number of moles of B added and reacted per mole of A (or C) initially present, the relation between X_Q and n_B/n_A is illustrated in Figure 2.2. For ideally mixed conditions only A reacts, while for completely segregated conditions both A and C react with B. Obviously, the greatest difference in the yields of P (or Q) between mixed and segregated conditions is at the point where $n_B/n_A = 1$. Hence, equimolar amounts of A, B and C is favored.

C) Effect of volume ratio: If the stoichiometric ratio is kept constant (equimolar), the scale of the tank is maintained (V_{Tank} = constant) and it is assumed that B is added to a premixed mixture of A and C then there are two scenarios under which the feed volume (V_f) can be increased:

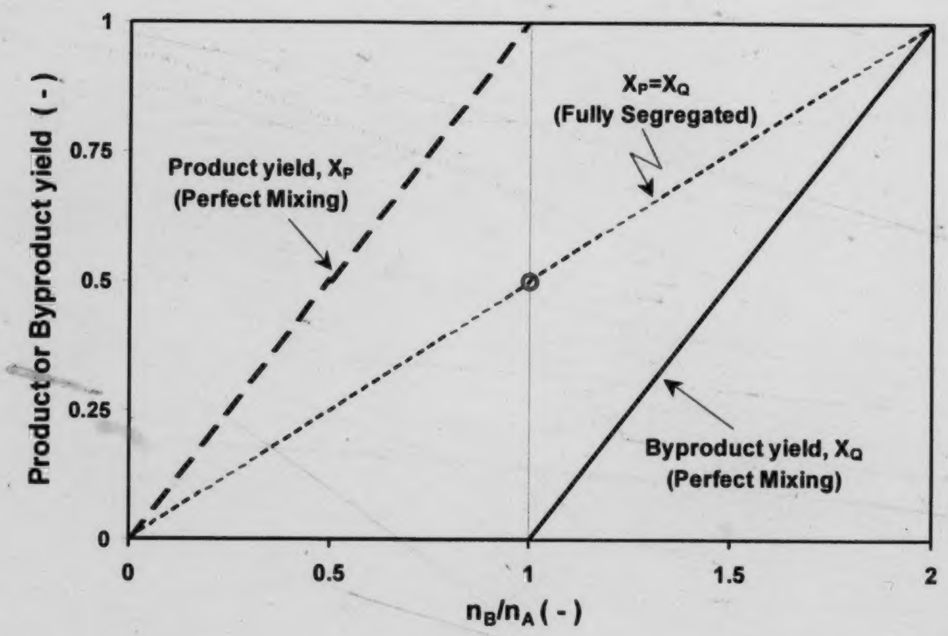

Figure 2.2 Optimum molar ratio for reactive mixing experiments (Reproduced from Figure 5.3, Yu, 1993)

- *Keep feed concentration (C_{B0}) constant but change reactor concentration (C_{A0} and C_{C0}).* Under this condition, an increase in V_f, ('a' is reduced) implies that more B is being added. Since V_{Tank} is constant, the concentration of A and C have to be consequently increased in order to maintain stoichiometric ratio, causing an all-round increase in the concentrations of all reactants. An increase in reactant concentration leads to an increase in segregation and more byproduct formation. Hence, increasing V_f while keeping stoichiometric ratio, V_{Tank} and C_{B0} constant will cause the formation of more byproduct.
- *Keep initial concentration of reactants in tank (C_{A0} and C_{C0}) constant but change C_{B0}.* In this case, if V_f is increased ('a' is reduced) then C_{B0} has to be reduced to maintain the stoichiometric ratio. Decreasing C_{B0} will cause a decrease in $\overline{Da}$ and lower byproduct. Increasing V_f while keeping stoichiometric ratio, V_{Tank}, C_{A0}, and C_{C0} constant therefore cause a drop in byproduct formation.

The two strategies result in opposite effects on byproduct formation for similar changes in volume ratio (a) and provide an added degree of freedom when deciding on reactor operating strategy.

A feed volume, one-fiftieth the tank volume (a = 50) has been widely used in the experiments of interest (Baldyga and Bourne, 1992; Baldyga et al., 1993 etc). Furthermore, experimental data for a majority of the experiments with the Bourne third reaction has been reported at a sodium hydroxide concentration of 4500 mol/m^3, and ester and acid concentrations of 90 mol/m^3 respectively for a = 50. These commonly used values have been adopted for the present study.

2.2.2.3. Effect of Feed Sequence

In the Bourne third reaction, B reacts with both A and C. Hence, for a semi-batch mode of operation, the reactants A (HCl), B (NaOH) and C (Ester) can be mixed only in the following four sequences:

- B added into premixed A and C
- A and B added separately into C
- A and C added separately into B

- B and C added separately into A.

Additionally, since C is only sparingly soluble in water the last two schemes would require very large feed volumes. The only feasible schemes are therefore the first two modes of addition. Bourne and Yu (1994), Yu (1993) studied the effect of these modes of addition of the reactants on byproduct yield. They found that larger amounts of byproduct was always formed when A and B were added separately into a solution of C as compared to the case when B was added into premixed A and C. In the former case, A and B were added far apart (180° apart in the experiments) and were unable to mix with each other in the beginning of the reaction. As more A was added into the tank, its concentration increased and only then could it start reacting with B. In the interim, the added A reacted with C forming large amounts of the byproduct. On the other hand, when B was added into a mixture of A and C, the former was already present in the tank and B could react with it as soon as reagent addition was started. Now the amount of byproduct formed depended only on the rate at which the feed stream was added into the tank (micromixing or mesomixing limited, Figure 2.3). Experiments in the present study have been carried out by adding B into a mixture of A and C since this is a more efficient scheme for feed addition.

2.2.2.4. Effect of Feed Time

Figure 2.3 shows the effect of the reagent feed time (t_f) on the byproduct yield (X_Q). The data is shown for an experiment using the Bourne third reaction (Bourne and Yu, 1994) where a known volume of B (V_f) was fed into a tank containing a mixture of A and C. Since the feed volume was fixed, the right hand side of the figure with the highest feed times represent the slowest feed flow rates while the left hand side with small t_f represent fast feeding. Figure 2.3 shows that at very slow feed rates, the byproduct yield is independent of feed time. X_Q increases sharply when the feed time (t_f) is decreased below a certain critical value, t_{crit}, or equivalently, the feed rate is increased beyond the critical value for a fixed volume of feed. This difference in behaviour across t_{crit} is due to a change from a micromixing limited to a mesomixing limited regime with an increase in the feed flow rate. When the feed is added very slowly, the fresh concentration eddies rapidly disintegrate into smaller scales ($\leq \eta$) and mixing at these micro-scales

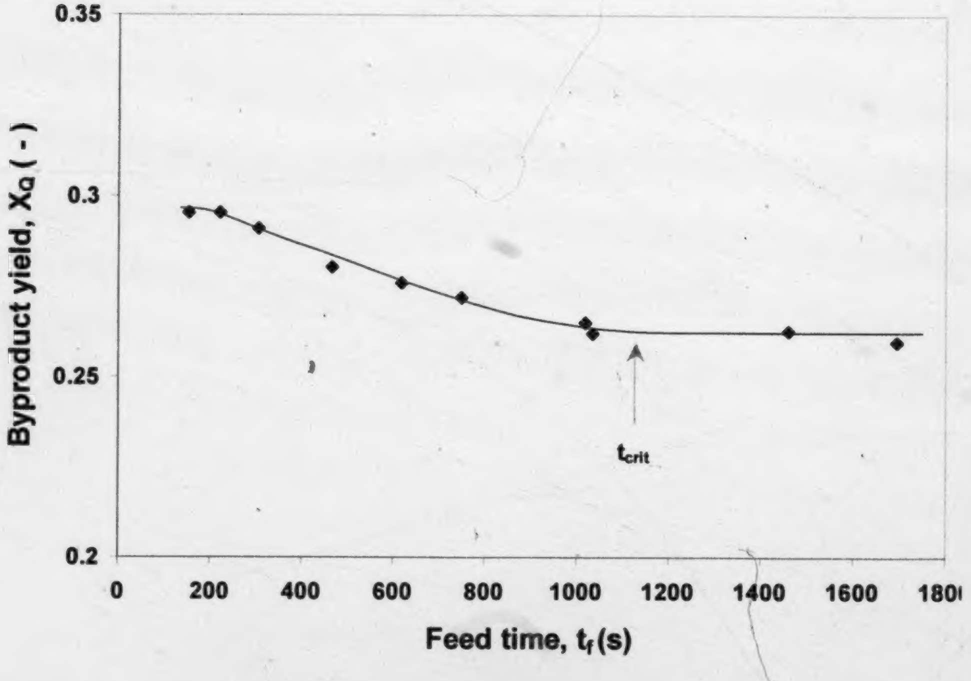

Figure 2.3 Representative data from literature on the effect of feed time on byproduct yield. The data was taken in a 19 L reactor with a Rushton turbine and surface feed. Bourne 2nd Reaction was used to test mixing limitations with sodium hydroxide being added into a tank containing a mixture of hydrochloric acid and ethyl chloroacetate. The experimental conditions were: H = T, D/T = 0.33, N = 100 RPM (Reproduced from Bourne and Yu, 1994).

(micromixing) homogenize the freshly added feed as reaction occurs. In this condition, product and byproduct formation is solely dependent on the rate of micromixing (described in section 2.4.3) and the characteristics mixing time is equal to the micromixing time scale seen later in Equation (2.39), $\tau_M = \tau_E$. On the other hand when feed velocity is very high, fresh feed is pumped into the reaction zone at such a high rate that the reduction in size of the large scale eddies is completely overwhelmed by the flood of fresh feed. Product formation is now governed by the rate at which these large eddies breakdown to the small scales. This is the process of mesomixing, occurring at intermediate scales (described later in section 2.4.4), and the regime $t_f < t_{crit}$ is the mesomixing limited regime. In this regime $\tau_M = \tau_{meso}$, where τ_{meso} is the mesomixing time scale described in section 2.4.5. Variation of X_Q with t_f similar to that in Figure 2.3 has been reported in numerous other studies and the processes by which this happens are now well established (Bourne and Hilber, 1990; Bourne and Thoma, 1991; Baldyga and Bourne, 1992; Baldyga et al., 1993, Bourne and Yu, 1994). The essence of these processes is captured by the characteristic mixing times for the two regimes (τ_E and τ_{meso}). Baldyga and Bourne (page 733, 1999) have shown that the change from micromixing to mesomixing controlled regimes can be predicted using these time scales and simple scaling argument. This is reviewed in section 2.4.5.

From an operational point of view, the critical feed time is an important parameter because it limits the maximum throughput that is allowable for a given reaction scheme and operational conditions. Studies have been carried out to identify the scaling behind the critical feed time. Bourne and Hilber (1990), Bourne and Thoma (1991) and Thoma et al. (1991) reported that $t_{crit} \sim D^{8/3}$ when the power dissipation was kept constant. This relation can also be obtained from dimensional arguments (see section 2.4.5). The strong dependence of t_{crit} on D shows that a rapid increase in t_{crit} is expected with an increase in scale. Hence, a feed time, which leads to operation in the micromixing regime in a small scale, can quickly become mesomixing controlled when the reactor is scaled up on the basis of power consumption.

2.2.2.5. Effect of Feed Pipe Diameter

Feed pipe diameter can have a significant influence on byproduct yield but the processes that cause this vary depending on the feed flow rate. When the feed pipe diameter, d_f, is increased while operation is in the slow, micromixing controlled regime (see Figure 2.3), the feed flow rates can reduce so much that there is an incursion of the surrounding fluid from the tank back into the fed pipe (backmixing) and reaction starts within it. Since this is a region with a very weak flow field, there is significant segregation of reagents and enhanced byproduct formation is likely. The situation is aggravated when the feed pipe is close to the impeller. A large increase in feed pipe diameter therefore cause backmixing and lead to increased byproduct formation in the micromixing regime. Researchers have however consistently reported that if backmixing is avoided then there is no effect of feed pipe diameter on byproduct yield in this regime (Bourne et al., 1993). Backmixing can be avoided by keeping the feed pipe velocity above a critical value. Bourne and Dell'Ava (1987) suggested a minimum velocity of about 0.1 m/s for feed locations close to a Rushton turbine. Jo et al. (1994) studied the effect of two different impellers and high impeller speeds on feed pipe backmixing and developed recommendations for the minimum feed pipe velocity needed to avoid backmixing, in terms of the ratio U_f/V_{Tip}. These are listed in Table 13.11, page 824 of Patterson et al. (2004).

In the mesomixing regime, an increase in feed pipe diameter has an inverse effect, causing an improvement in performance with increasing d_f, but this happens due to a different mechanism. When a feed stream is added into a turbulent flow field, it gets dispersed and the dispersed plume forms the environment within which inertial-convective reduction of scales occurs. This process brings down the size of the concentration eddies so that micromixing at the smallest scales can proceed. The initially dispersed plume therefore forms the environment, which interacts with the surrounding fluid in the tank and within which all the other mixing steps occur. Turbulent dispersion is very sensitive to the feed pipe diameter, with the concentration field generated by it being dependent on whether the source (the feed pipe) is a 'point source' or of finite dimensions. If the feed pipe diameter is sufficiently small, the dispersion occurs as if from a point source and conversely for sufficiently large feed pipes it follows the trends for finite sources. This is discussed in detail in section 2.4.4. The pipe diameter therefore has a bearing on the initial concentration gradients developed within the dispersing feed stream and thence effects byproduct yield when mesomixing is the limiting process. This was observed in the studies on the effect of feed pipe diameter by Baldyga and Bourne (1992), Bourne et al. (1993). Their conclusions are summarized in Baldyga and Bourne (page 743, 1999) who stated, "it has been shown theoretically and experimentally that as d_f increases, either segregation, as measured by X_Q and X_S [1], decreases when the feed flow rate, Q_f, and feed time, t_f, are held constant, or yield and product distribution are constant, whilst feed rate is increased and the feed time is decreased". This implies that within the mesomixing limited regime, product quality can be improved (for the same throughput) or throughput can be increased (for same product quality) by increasing the feed pipe diameter. The point to note here is that the feed velocity (U_f) remains very low and the kinetic energy in it does not have any major role to play in the change of reactor performance. The variation in product quality with a change in feed pipe diameter is soley due to a change in the concentration profile, because of different mechanisms of diffusion induced by a point or finite source.

2.2.2.6. Effect of Feed Location

The turbulent flow-field generated in a stirred tank is very inhomogeneous with the mean velocities and the level of turbulence changing drastically from point to point (section 2.3.1) within the tank. Since the characteristic mixing time is strongly dependent on ε, the rate of dissipation of turbulent kinetic energy (described in sections 2.3.2 and 2.4.1.2), the mixing rates in different positions within the tank also vary significantly and the location at which reagents is fed into the tank has an strong influence on product quality. In general, the region closest to the impeller are the most turbulent and give the best performance when feed is added in this location while further from the impeller the turbulence levels drop and reactor performance suffers when feed is added in those locations. This has been illustrated through numerous experiments (e.g. Paul and Treybal, 1971; Bourne et al., 1981; Bourne and Dell'Ava, 1987; Baldyga and Bourne, 1990; Bourne and Yu, 1994; Baldyga et al., 1997). Patterson et al. (2004) cite an example from Nienow and Inoue (1993), which is illustrative of the issues involved. The investigators used precipitation of barium sulfate to demonstrate the effect of feed location on product distribution by positioning the feed pipe at various locations in tanks with three different types of impellers. The feed addition and impeller speed was kept constant. The results are shown in Figure 2.4. The first tank is stirred by a radial impeller. In this type of impeller, the turbulence is highest near the impeller while it is low near the tank bottom and the liquid surface. The mixing rate is therefore highest near the impeller and low in the other two positions and byproduct is expected to be lowest near the impeller. This is indeed seen to be the case from the figure. The second tank is stirred with an axial impeller, which again has the highest turbulence near the impeller, followed by the tank bottom (due to the impacting discharge stream) and there is finally very little turbulence near the liquid surface. As expected, the byproduct yield is ordered in exactly the same sequence in Figure 2.4 due to the reducing mixing rates. For the unbaffled tank, byproduct yield is lowest near the highly turbulent impeller region but high everywhere else. The results therefore consistently show that the best performance is obtained when feed is added into the most turbulent region of the tank where ε is the highest, τ_M the lowest and the mixing limitations are the least. This has been shown universally in all experiments in reactive mixing.

---

[1] These are the byproduct yield defined in terms of the byproduct R and S for the second Bourne reaction in Table (2.1). Refer to page 650, Baldyga and Bourne (1999) or other references (e.g. Baldyga and Bourne, 1988; Bourne and Hilber, 1990; Baldya et al., 1997) for definition.

The increase in byproduct formation when reactant is fed at the surface is also seen in Figure 2.5, derived from the data of Bourne and Hilber (1990) for the first Bourne reaction. It is seen that the byproduct formation is about two times higher when the feed is added at the surface due to reduced turbulence and slower mixing rates. There is another interesting feature in this data on surface feed. At the surface feed location, the byproduct yield initially increases due to mesomixing limitation when t_f is decreased below t_{crit}. However, when the feed time is reduced further ($n_f t_f \sim 2700$s for $N = 7.9s^{-1}$ and $n_f t_f \sim 3500$s for $N = 4.2s^{-1}$), the behaviour changes and the byproduct yield

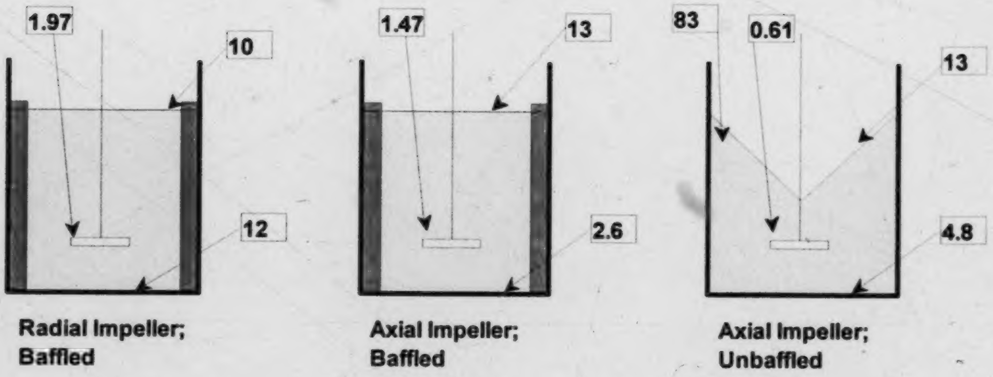
1.97
10
12
Radial Impeller; Baffled
1.47
13
2.6
Axial Impeller; Baffled
83
0.61
13
4.8
Axial Impeller; Unbaffled

Figure 2.4 Effect of feed position on product distribution. The numbers shown are the selectivity to the undesirable byproduct for the feed location indicated by the position of the arrow. The first two figures show the results for a baffled tank with a radial and an axial impeller respectively, while the last figure is for an unbaffled tank. Feed in regions of low levels of turbulence cause more byproduct formation (Adapted from Patterson et al., 2004. The results are from Nienow and Inoue, 1993).

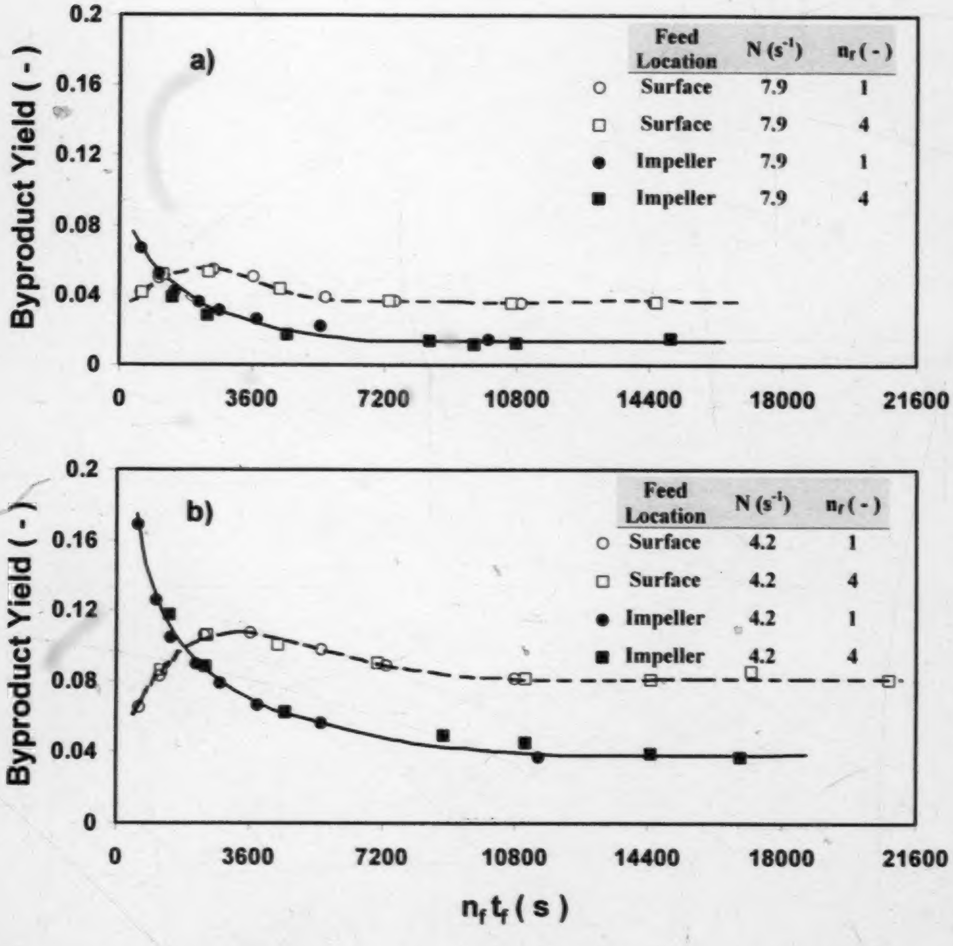

Figure 2.5 Effect of multiple feed pipes. Adapted from Figures 4 and 6 in Bourne and Hilber (1990)

reduces with decreasing t_f. This drop in X_S is noticed for the case of surface feed only. This abnormal behaviour was attributed to the additional kinetic energy of the feed (Bourne and Hilber, 1990), which plays a dominant role in the mixing process in this location where the ambient turbulence levels are very low. The turbulence levels near the impeller, already very high, dominate the mixing process and the kinetic energy in the feed is irrelevant. Assuming water like fluid properties, the Reynolds number of the feed stream is calculated to be about 700 at the t_f for which the byproduct yield reaches a local maxima. The question arises whether further reduction in feed time, or an increase in feed velocity, can cause better performance. This aspect of the problem is addressed in Chapter 3.

2.2.2.7. Effect of Multiple Nozzles

The main objective of the experiments by Bourne and Hilber (1990) was to study the effect of multiple nozzles on reactor performance in a tank stirred with Rushton turbines. They compared the performance of the reactor with one to four nozzles placed at different feed positions. Since reaction occurs in a localized zone close to the impeller, the byproduct yield is dependent on the flow rate through each nozzle and not on the overall flow rate. The flow rate per nozzle is given as

$$Q_{f,\text{nozzle}} = \frac{V_f}{n_f t_f} \tag{2.7}$$

It follows that byproduct yield should be a function of $n_f t_f$ and not of t_f. Experimental data from Bourne and Hilber (1990), shown in Figure 2.5 confirm this hypothesis. For a constant impeller speed, N, if t_{crit} is the critical feed time for the case where only one nozzle is used to feed V_f, the critical time per nozzle is reduced when multiple nozzles are employed to feed the same reactant volume:

$$t_{crit}\,(\text{multiple nozzle}) = \frac{t_{crit}}{n_f} \tag{2.8}$$

Bourne and Hilber (1990) concluded that by using multiple nozzles, the overall feed time (t_f) necessary to operate within the micromixed region could be reduced by a factor n_f thereby increasing the throughput. Similar observations were made by Thoma et al. (1991).

2.2.2.8. Effect of Tank Scale, Impeller Speed and Geometry

Bourne and Dell'Ava (1987) measured the product distribution from feed injections close to the impeller and far from it, in a stirred tank with feed velocities kept within the bounds discussed above (section 2.2.2.4 and 2.2.2.5). They observed higher rates of byproduct formation when the feed was injected into a region of lower turbulence as already discussed in section 2.2.2.6. However they also found that even for two different scales of reactor, which were otherwise geometrically similar, byproduct rates were higher in the larger reactor. This was attributed to the reaction zone convecting through various regions of the tank with different turbulence levels for the two scales. The reaction is completed in the larger reactor before the reaction zone can reach the highly turbulent impeller region, while in the smaller vessel the feed plume, being closer to the impeller, overlaps with the turbulent impeller region. Higher levels of turbulence enhance the rate of mixing and hence reduce byproduct formation. Thoma et al. (1991), Baldyga and Bourne (1992) have also shown similar results. This point needs to be considered while scaling up on the basis of average power consumption if the feed position is not in the impeller region.

An increase in impeller speed causes an increase in the average and local power dissipation at all positions in the tank. Hence, an increase in impeller speed leads to an increase in mixing rates and a reduction in byproduct yield. This is illustrated very clearly in Figure 2.5 for both feed location. Similar results have been reported in many other studies. An increase in impeller speed will however cause an increase in power consumption, which should be kept in mind while using this parameter for changing reactor performance.

Bourne and Yu (1994) reported an effect of even the shape of the tank bottom on reactor performance when feeding reactants at the surface. While using the third Bourne reaction and a Rushton turbine, they found that for the same impeller speed, byproduct yield for a tank with a dished bottom was always higher than a tank with a flat bottom. This reflects the effect of the tank bottom on the flow field and the sensitivity of byproduct formation to the flow characteristics in the tank. Using data from an earlier study, Bourne and Yu (1994) concluded that the ratio of the flow rates in the upper and lower sections of the tank was reduced when employing a tank with a dished bottom as a result of which dissipation near the surface is reduced further and the product distribution is affected.

2.3. Flow and Turbulence in a Stirred tank

To obtain good product quality it is essential that mixing limitations are minimized by keeping the rate of mixing in the reaction zone very fast. Since the mixing rate depends strongly on ε (see sections 2.4.2, 2.4.3, and 2.4.4 for a discussion on the characteristics mixing times τ_C, τ_E, τ_D and τ_S in various scales of mixing), the level of turbulence has a strong influence on reactor performance. Furthermore, the turbulence levels in various regions of the reactor depend on the characteristics of the flow field generated by the impeller. It is therefore important to have a good knowledge of the mean flow characteristics and the turbulence levels within a stirred tank before any analysis of reactor performance can be undertaken. This section, containing a review of the flow characteristics in a stirred tank, provide the necessary background on the terminology specific to mixing research and the flow field generated by impellers used in this investigation to enable proper analysis of the results.

2.3.1. Flow-Field in a Stirred Tank

A typical stirred tank reactor is shown in Figure 2.6a. It consists of a vertical cylindrical tank, containing rectangular baffles with a rotating impeller in the centre. The standard baffle configuration consists of four vertical, wall baffles although the actual number can be more or less depending on the process requirements. Normally, for liquid height between H = 0.3T and 1.2T, only one impeller is used. The conventional tank employs a flat or dished bottom though other types are also available. The distance from the bottom of the tank to the impeller is the clearance, C, of the impeller. This is an important parameter for a down-pumping impeller. The distance from the top of the impeller to the surface of the liquid, the submergence S, is of critical importance for up-pumping impellers. Standard dimensions for the various parts are given in Table 2.2, and further details can be obtained from the literature (e.g. Hemrajani and Tatterson,

Table 2.2 Geometric details of a stirred tank and impellers

Parameter	**Standard Dimension**	
Tank Details		
Shape	Usually round, can be square	
H	T (a single impeller can be used only in the range from 0.3T to 1.2T)	
Bottom type	Usually flat or dished but can be ellipsoidal, ASME dished, or hemispherical	
Impeller Details		
D	0.2T to 0.67T but most within T/2 to T/4	
C	~ T/2 for radial and ≤ D for down-pumping impellers	
S	-	
Baffle Details		
W	T/12 or T/10	
Number	Usually 4	
Shape	Rectangular but can be other types (see page 350, Hemrajani and Tattterson, 2004)	
Other details	For some applications, e.g. solid suspension, a gap (~1.5% of T) is left between baffle and wall	
Impeller Details		
	Rushton Turbine	Pitched Blade Turbine
Blade Length (D_L)	D/4	-
Blade Width (D_W)	D/5	D/5
Blade Thickness (D_t)	-	-
Others	Disk diameter: 0.66 to 0.75D	The blade angle can vary from 10 to 90°

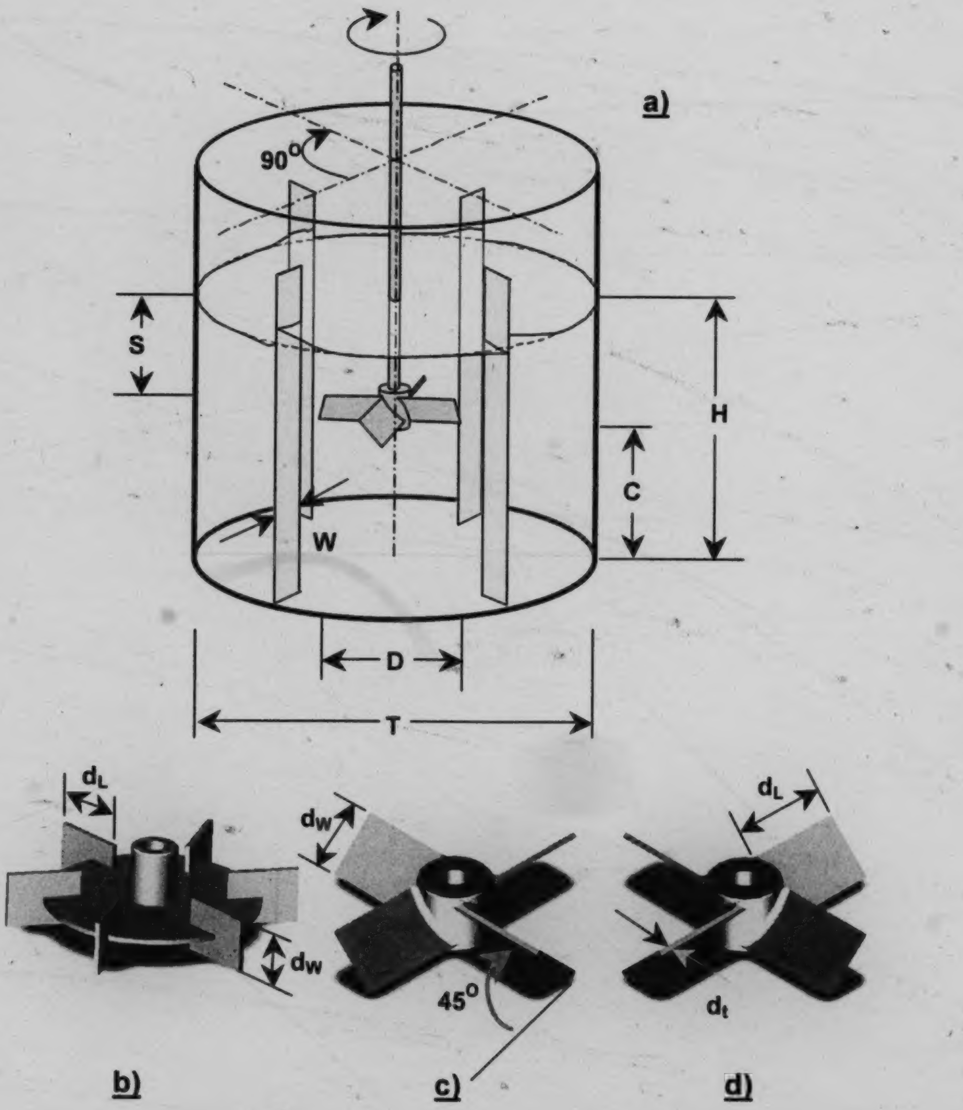
a)
90°
S
H
C
W
D
T
d_L
d_W
d_W
45°
d_L
d_t
b)
c)
d)

Figure 2.6 (a) Schematic diagram of a typical stirred tank (b) Rushton turbine (RT) (c) Down-pumping pitched blade turbine (PBTD) (d) Up-pumping pitched blade turbine (PBTU) (Drawings of the impellers are modified forms of sketches downloaded from www.postmixing.com)

2004). Also shown in the figure are the three types of impellers used in this study: the Rushton turbine (RT, Figure 2.6b), the down-pumping pitched blade turbine (PBTD, Figure 2.6c), and the up-pumping pitched blade turbine (PBTU, Figure 2.6d). Standard configurations for the Rushton turbine and the pitched blade turbines are also given in Table 2.2.

In a stirred tank, the impeller rotates (usually clockwise) within the liquid and imparts angular momentum to it. In the presence of the baffles, this circumferential motion of the fluid is transformed into axial flow. Nagata (Chapter 1, 1975) provides intricate calculations showing how the baffles impede tangential flow and cause additional power draw compared to an un-baffled tank. The power draw is an important design parameter for a stirred tank and like many other characteristics of the flow depends strongly on the regime of operation. The operating regimes, fully turbulent, laminar or transitional, are demarcated by the Reynolds number which can be obtained from the Navier-Stokes equation using correct characteristic length and velocity scales. In a stirred tank, the flow is driven by the impeller, the proper length and velocity scales are the impeller diameter (D) and the tip speed of the impeller (~ ND). The Reynolds number for agitation (or simply the impeller Reynolds number) is therefore obtained as:

$$Re_I = \frac{\rho N D^2}{\mu} \tag{2.9}$$

When Re_I is less than 10, the flow within the impeller region is considered completely laminar while it is fully turbulent for $Re_I \geq 2\times10^4$. The later criterion is supported by numerous observations such as the flattening of the power number curve (Rushton et al., 1950) or the scaling of the blend time with N (Grenville, 1992) beyond this Reynolds number. Apart from the Reynolds number, there are two other dimensionless numbers commonly used to characterize the hydrodynamic condition of an impeller, one related to its power consumption and the other to the flow generated by it.

The power consumption by an impeller can be related to N and D from purely dimensional considerations (Rushton et al., 1950) as reviewed on pages 358-360 in Hemrajani and Tatterson (2004). The analysis gives the following expression for power:

$$P = P_O \rho N^3 D^5 \qquad (2.10)$$

Equation (2.10) can also be obtained from an angular momentum balance across the impeller if the three-dimensional flow field is accurately known in the suction and the discharge sides of the impeller as illustrated by Chapple et al. (2002). P_O, called the power number, is a proportionality constant dependent on the impeller type and in general also on Re_I. For fully turbulent conditions, P_O becomes independent of the impeller Reynolds number while continuing to be dependent on the impeller type: P_O = 1.27 for four bladed, 45° PBT, while it is about 5.5 for RT. Further, Bujalski et al. (1987), Rutherford et al. (1996) and Chapple et al. (2002) found that P_O for the RT is sensitive to its size (D/T) as also to its blade width and thickness while the PBT has a P_O dependent only on its size (D/T) but not on the details of the impeller shape. For the RT power consumption is dominated by form drag, so details of the blade geometry and flow separation have a significant impact on P_O. On the other hand, in the PBT, the discharge from the impeller interacts strongly with the tank wall while the form drag is not so important; hence, power draw is unaffected by the details of impeller shape (Chapple et al., 2002).

The amount of material/fluid discharged from an impeller is termed its pumping capacity, Q. Using dimensional analysis, Q can be related simply to the volume of the impeller (~D^3) and the rate at which this volume is swept out (~N) from it:

$$Q = N_Q N D^3 \qquad (2.11)$$

N_Q is the pumping number and is dependent on the Reynolds number of the impeller. For a PBT it is also dependent on the size of the impeller (Hemrajani and Tatterson, 2004) because of the strong interaction between the impeller and the tank wall. N_Q for the PBT is about 0.79 while it is about 0.72 for the Ruston turbine (Table 6.3, Hemrajani and Tatterson, 2004). This shows that for the same impeller diameter and impeller speed, both impellers pump similar amounts of fluid.

Based on the first law of thermodynamics, the energy input (shaft work) into an adiabatic, batch, stirred tank can be dissipated only as internal energy in the liquid since there is no energy stream flowing out of the tank. Hence, if P is the total power input into the system and $m_{Tank} = \rho V_{Tank}$ is the total mass of fluid in the tank then the total dissipation in the tank is obtained as:

$$\varepsilon_{Total} = \frac{P}{m_{Tank}} = \frac{P}{\rho V_{Tank}} \qquad (2.12)$$

On further assumption that the turbulence in the tank is homogeneous, Equations (2.12) and (2.10) combine to give Equation (2.2). In reality, this assumption of homogeneity in turbulence levels is incorrect since the rate of dissipation of turbulent kinetic energy within the discharge stream of the impeller is quite different from the dissipation in the bulk of the tank. Kresta and Brodkey (2004) have however pointed out that if geometric similarity is maintained, ε_{Total} becomes simply a scaling parameter and the local dissipation or other dissipation dependent parameters can be safely compared based on ε_{Total}. Equation (2.2) is therefore often used, with good results, to compare stirred tanks that are geometrically similar.

2.3.2. Rushton Turbine (RT)

The Rushton turbine (RT) is one of the most widely studied impellers. It is a radial flow impeller and produces the well-known figure of eight flow pattern shown in Figure 2.7a. As the impeller rotates it generates a radial discharge, which entrains liquid from the surrounding and broadens as it moves towards the wall (Figure 2.7b). The radial velocity profile within this discharge stream has been successfully modeled as a swirling radial jet (Kolar, 1984; Kolar, 1985 and Kresta and Wood, 1991). The jet splits in two on reaching the wall and the two streams are diverted upwards and downwards. The upwards-moving stream bends back, moves towards the center and then axially downwards as it is finally pulled back into the impeller suction. A similar toroidal, circulation loop, but with a clockwise rotation, is formed in the lower section of the tank. For an impeller with standard clearance, qualitative agreement to this mean flow field is found in numerous studies covering a gamut of flow visualization and velocity measurement techniques (Sachs and Rushton, 1954; Cutter, 1966; Cooper and Wolf, 1968; Costes and Couderc, 1988; Ranade and Joshi, 1990; Scähffer et al., 1997). The flow along the tank wall is primarily axial (up or down) and has been successfully

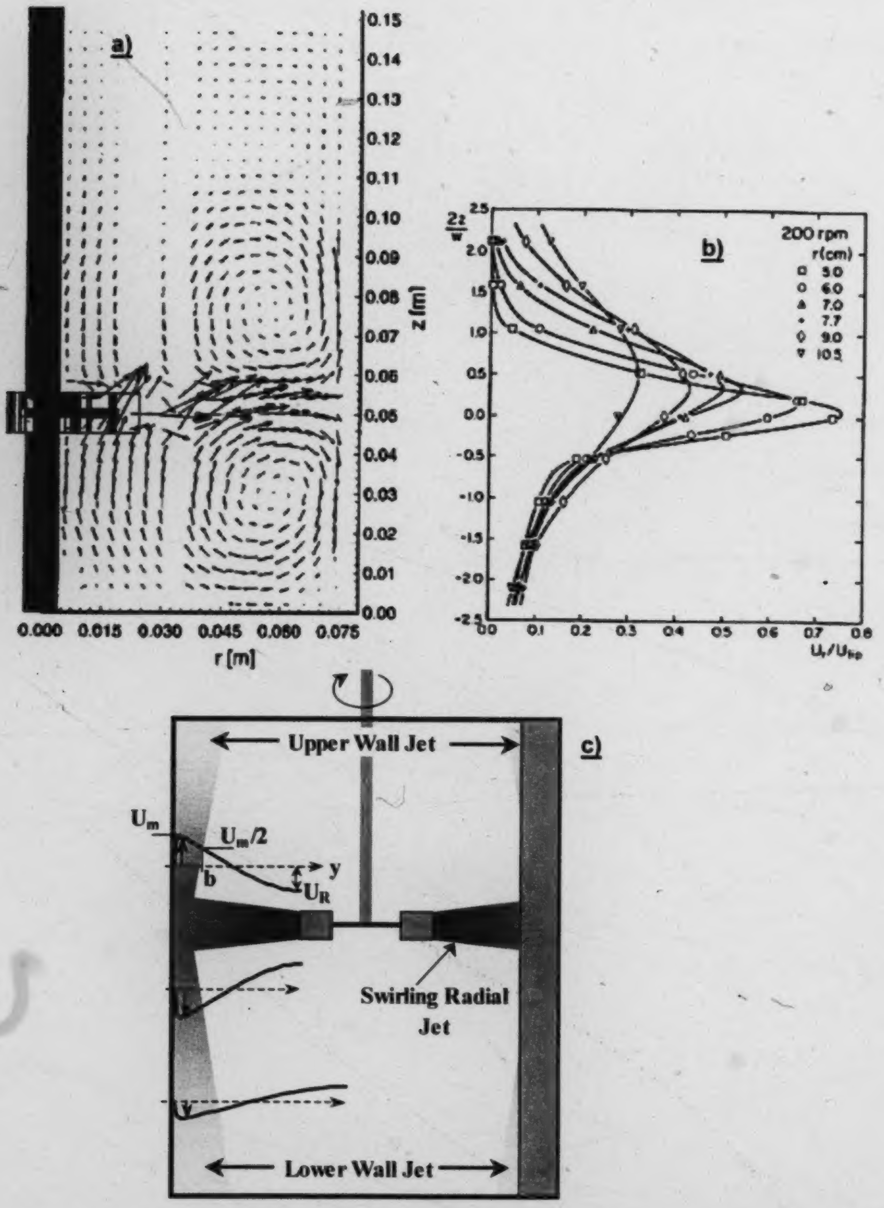

Figure 2.7 **(a) Mean flow field of a Rushton Turbine (Schäffer et al., 1997). (b) Axial profile of mean radial velocity at different radial positions (Wu and Patterson, 1989). (c) Schematic diagram of a SRJ and the internal annular wall jet in a stirred tank with a Rushton turbine (Kresta et al., 2001)**

modeled as annular wall jets as shown in Figure (2.7c; Kresta et al., 2001). More details on the models for this region and the impeller discharge are provided in Appendix A.

The turbulence levels in a stirred tank is very inhomogeneous with ε varying from a maximum close to the tip of the impeller to very low values at locations far from it, e.g. the liquid surface. The average energy dissipation based on the total mass of the fluid in the tank (Equation 2.2) therefore does not give a complete picture of the turbulence characteristics and local measurements are preferred. While point-to-point measurement of the local ε and even the implementation of such measurements into numerical models for mixing are difficult, zonal models are sometimes used to represent the variation in turbulence levels over larger sections of the tank. Yu (1993) extensively reviewed available literature on the flow-field generated by a Rushton turbine and proposed a simplified Eulerian, zonal model (see also Baldyga and Bourne, 1988) to represent the distribution of ε. Bourne and Yu (1994) used this model to investigate the role of micromixing on byproduct formation in mixing sensitive reactions. Kresta et al. (2004) used a similar model of the mixing field in a stirred tank with RT to simulate the complicated processes leading to the formation and precipitation of silver halide crystals. An illustration of their representation of the turbulence field is given in Figure 2.8. Dissipation is the highest within the impeller discharge stream and significantly smaller in the bulk of the tank.

Accurate measurement and estimation of ε is a very difficult task. The rate of dissipation of turbulent kinetic energy at any point can be obtained accurately only if all three components of the instantaneous velocity are measured simultaneously and a rigorous definition (see Equation 2.17) based on the spatial gradients of all velocity components are used to calculate ε. Earlier, accurate measurements of the spatial gradients were not possible and other indirect means of quantifying turbulence was used. These indirect methods, which are still employed, involve numerous assumptions and as a result the estimation of ε is itself very approximate with the values calculated by different researchers sometimes varying by as much as 400% (see e.g. Table 2.3 adapted from Table 1 in Ng and Yianneskis, 2000). Many of these methods have been reviewed

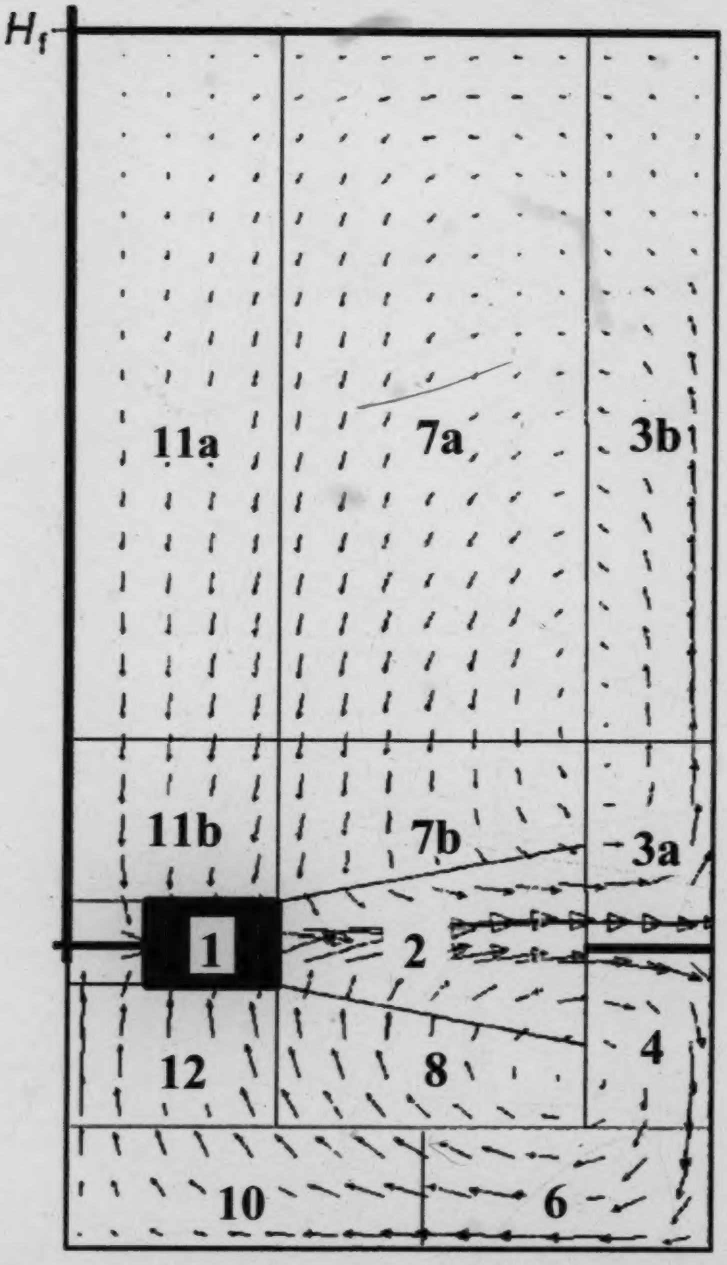

Turbulence levels: $\varepsilon_1 > \varepsilon_2 > \varepsilon_{3a} \sim \varepsilon_4 > \varepsilon_6, \varepsilon_{7a}, \varepsilon_{7b}, \varepsilon_8, \varepsilon_{10}, \varepsilon_{11a}, \varepsilon_{11b}, \varepsilon_{12}$

Figure 2.8 **Zonal Model for flow and dissipation in a stirred tank. The numerical values represent zones. The characteristic features of each zone are described in Table 1, Kresta et al. (2004).**

Table 2.3 **Distribution of the rate of dissipation of turbulent kinetic energy per unit mass in various regions of a tank stirred with a Rushton turbine (Adapted from Ng and Yianneskis, 2000)**

Reference	**Percentage of ε in**		
	Impeller Swept region	**Impeller Stream**	**Rest of Tank**
Cutter (1966)	20	50	20-40
Gunkel and Weber (1975)	-	38	-
Fort et al. (1792)	60	-	-
Laufhutte and Mersmann (1985)	30	30	40
Wu et al. (1989)	30	30	40
Ranade and Joshi (1989)	30	34	36
Zhou and Kresta (1996)	15.3	28.2	-
Kresta and Wood (1991)	54	35	11
Ng and Yianneskis (2000)	12	31	57

in Kresta and Wood (1993), Kresta (1998). It has generally been found that the methods based on dimensional analysis (see also Equation 2.20) are the most successful:

$$\varepsilon = A\frac{u^3}{L} \tag{2.13a}$$

A is a constant of order one, while u and L are the characteristic velocity and length scales. Kresta (1998) analyzed eighteen possible combinations of u and L, compared them to selected experimental data and concluded that the most reliable form of Equation (2.13a) is

$$\varepsilon_{max} = \frac{u_l^3}{(D/10)} \tag{2.13}$$

Here ε_{max} is the local maximum dissipation, u_l is the *streamwise* component of the fluctuating velocity and the length scale is taken to be equal to one-tenth the impeller diameter. While originally meant for the impeller discharge stream, Equation (2.13) is sometimes used to estimate local values of ε in other regions of the tank. Extreme care should be used while estimating ε in the bulk of the tank using Equation (2.13). Some of the difficulties that may be encountered while using this method include:

- It is difficult to obtain the correct length scale for use in the bulk of the tank. Attempts to use Equation (2.13) to estimate dissipation in all parts of the tank employing a single, fixed length scale has been found to cause serious inaccuracies in the estimation of ε (Schäffer et al., 1997).
- Zhou and Kresta (1996) reported that even the geometry of the impeller has a significant effect on the distribution of ε. The form of Equation (2.13) does not consider geometry effects and makes the estimation of ε all the more difficult.
- Equation (2.13) implicitly assumes local isotropy in the region under consideration. While this may be true for specific regions in the tank, it is generally not applicable to the whole tank. Kresta (1998) analyzed energy spectrums, values of root mean square (RMS) velocities in three dimensions and the typical values of local Reynolds number from various experiments reported in the literature and concluded that:

- Close to the impeller, local isotropy could indeed be invoked over a restricted region of the energy spectrum starting with the blade passage frequency.
- There is however not much support for making similar arguments in the bulk of the tank even for restricted parts of the spectrum.

Equation (2.13) should therefore be used with caution while estimating ε in the bulk. More often, the later quantity is estimated indirectly by calculating the power dissipation in the impeller region, subtracting it from the total power input to obtain the net power dissipated in the bulk which is then averaged over the fluid mass outside the impeller region to obtain ε in the bulk.

Methods based on two and three-dimensional Particle Image Velocimetry (PIV; Baldi and Yianneskis, 2003; Baldi and Yianneskis, 2004; Micheletti et al., 2004) have more recently made it possible to obtain spatial gradients of fluctuating velocity directly from experiments; however, doubts remain about spatial resolutions achievable by these methods. The latest measurements using PIV and three-dimensional LDV suggest that dimensional methods may be underestimating ε by as much as 50% in the vicinity of the impeller and overestimating it at locations in the bulk (Micheletti et al., 2004). The investigation by Micheletti et al. (2004) further proposed the use of the integral length scale in the estimation of ε while employing dimensional methods. The subject is however not resolved and further research is continuing on it. In any case, with the present level of knowledge it is possible to identify regions with the highest and lowest ε and use zonal models with reasonably good approximation of the turbulence field in a stirred tank with RT.

2.3.3. Down-pumping Pitched Blade Turbine (PBTD)

A schematic diagram of the flow-field generated by a four-bladed, 45°, PBTD is shown in Figure 2.9a. Such flow fields have been observed by numerous researchers (Ranade and Joshi, 1989; Jaworski et al., 1991; Kresta and Wood, 1993; Bakker et al., 1996; Scähffer et al., 1998; Bittorf and Kresta, 2000; Jaworski et al., 2001; Aubin et al., 2001 etc). At low clearances, the discharge stream from the impeller impinges on the

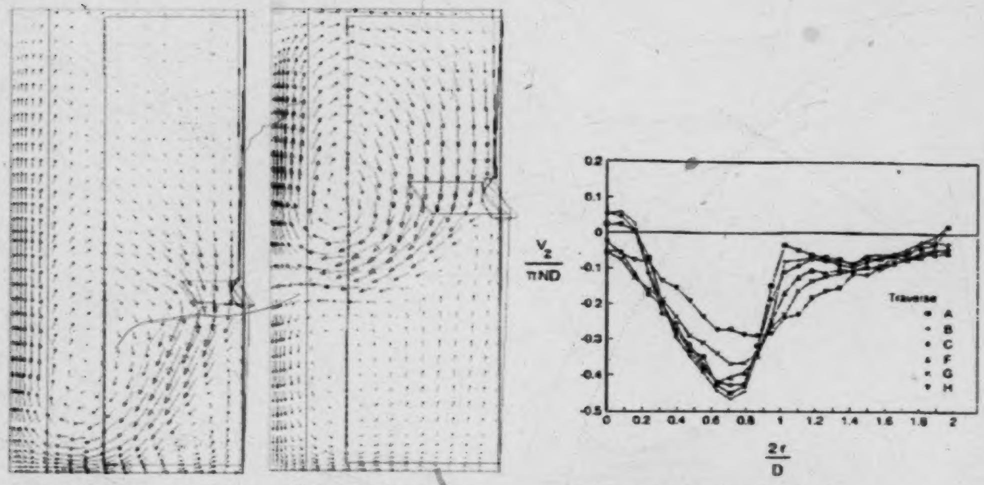

a) C/D = 1.1 (D=T/3)

b) C/D = 1.0 (D=T/2)

c) Dimensionless Mean Velocity Profile Below PBTD.

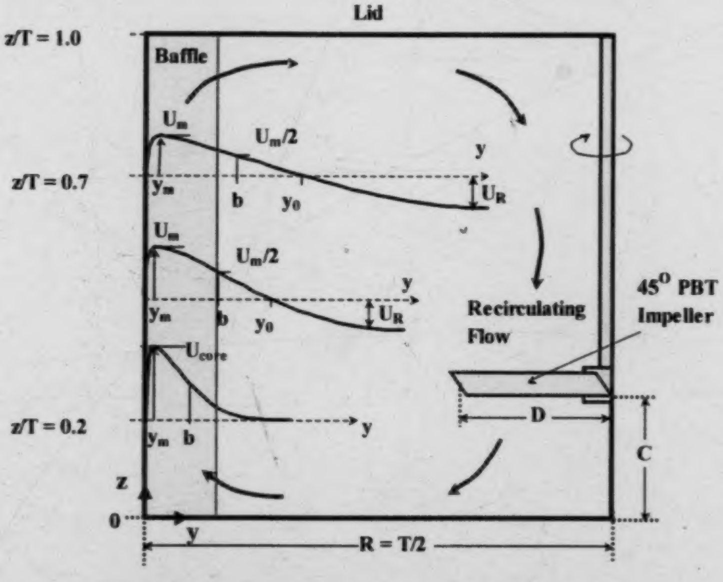
Lid
z/T = 1.0
Baffle
U_m
$U_m/2$
y
z/T = 0.7
y_m
b
y_0
U_R
U_m
$U_m/2$
y
y_m
b
y_0
U_R
Recirculating Flow
45° PBT Impeller
U_{core}
z/T = 0.2
y_m
b
y
D
C
z
0
y
R = T/2

d) Radial velocity profiles in the wall jet at different axial locations in a stirred tank

Figure 2.9 Mean flow field from a PBT (a) at low clearance (b) at high clearance (Bhattacharya and Kresta, 2002) (c) Radial profile of mean velocity below impeller (Kresta and Wood, 1993) (d) Radial velocity profiles in a three dimensional wall jet (Bhattacharya and Kresta, 2000).

bottom of the tank, moves outwards and on reaching the tank wall is turned upwards at the baffles. The liquid stream continues to climb upward along the tank wall, then turns around in the upper regions of the tank, and is finally pulled back into the suction of the impeller to complete the circulation loop. The radial profile of the axial velocity leaving the impeller is shown in Figure 2.9c. For relatively low clearances, the discharge from the impeller leaves at an angle of about 45° to the horizontal and moves downwards. The discharge velocity increases from very low values near the hub, to reach a peak of about $0.45V_{Tip}$ at a radial position of about $2r/D = 0.8$ and then reduces sharply (Figure 2.9c). This was observed in numerous studies including those by Jaworski et al. (1991) and Kresta and Wood (1993). The angle of the discharge stream can however be affected by its interaction with the vessel wall. Kresta and Wood (1993) noted that if the impeller clearance was raised above a certain value ($C/D \sim 0.67$ for $D = T/2$) then its discharge stream started impinging on the tank wall and a secondary loop formed in the bottom of the tank as shown in Figure 2.9b. Similar reversal of flow near the bottom of the tank for high clearances was also noted by Jaworski et al. (1991). In the case of a small impeller, e.g. $D = T/3$, this loop is relatively weak, but for larger impeller sizes ($D = T/2$) the loop can be sufficiently strong to deflect the impeller discharge stream away (towards the wall) from its normal path. The interaction between the impeller discharge stream and the tank wall makes the flow field generated by a PBT very dependent on geometry and difficult to predict accurately (see also Fokema et al., 1994; Bhattacharya and Kresta, 2002). Apart from the difficulties of a geometry dependent flow field, another complicating feature in the flow generated by a PBT is the presence of macro-instabilities (Roussinova et al., 2003). Numerous studies have detected the existence of these low frequency coherent structures in the flow. The structures are elusive, occurring in only some geometries (e.g. a 45° PBT with diameter $D = T/2$ and off-bottom clearance $C/D = 0.5$). When they occur they have been found to scale with the impeller speed. Macroinstabilities can cause large vibrations and cause significant damage to tank internals, impeller shaft or the impeller itself. Rousinnova et al. (2003) present a detailed discussion of the possible mechanisms for macroinstabilities and the group of Yianneskis has also reported experimental data on this phenomena. Because of the problems associated with sensitivity of the flow field to impeller/tank geometry and instability in the flow, many researchers prefer RT while conduct mixing experiments. PBT are however, also very important impellers, being used extensively in applications such as solids suspension etc. They have been used extensively in the present study.

The top one-third of the stirred tank has a weak velocity field with very low levels of turbulence (Kresta and Wood, 1991). The CFD simulations by Bhattacharya and Kresta (2002) showed that this inactive zone in the top of the tank remained even when the impeller was placed at extraordinarily high clearances (C/D ~ 1.4 for T/3 impeller). Bittorf and Kresta (2001) explained this in terms of the formation of three-dimensional wall jets. The upward moving fluid trapped between the four baffles and the wall form four, three-dimensional wall jets. One of these jets is shown in Figure 2.9d. The jet engulfs fluid, expanding laterally and slowing down as it rises. The expansion of the jet and decay of axial velocity in a vertical plane close to the baffle is shown in Figure 2.9d for different axial positions in the tank. Near the top of the tank (z/T ~ 0.7 for D = T/3 and C/D ~ 1.0) the jet velocity becomes too small and it collapses. The section of the tank beyond the reach of the wall jet therefore remains relatively quiescent. Few details of the model for the three-dimensional wall jet proposed by Bittorf and Kresta (2001) are provided in Appendix A. The quiescent region in the top one-third of the tank causes very low mixing rates in this region of the tank and lead to high levels of byproduct formation when surface feed is used as seen in section 2.2.2.6.

Detailed studies with PBT started only in the late 80s, so the amount of information available on the turbulence characteristics of a PBT is much less than what is available for a RT. Like the RT, investigators have generally found that the level of turbulence is the highest in the impeller region. Zhou and Kresta (1996) reported that the maximum axial, radial and tangential components of the fluctuating velocity existed just below the impeller blade for axial impellers including a PBT. Jaworski et al. (1991) measured a maximum fluctuating velocity of about $0.13V_{Tip}$. Aubin et al. (2004) measured the radial and axial components of the fluctuating velocities in the impeller discharge and found that the maximum in the axial component was about $0.12V_{Tip}$ and

$0.15V_{Tip}$ for the radial. This study also reported that the global maximum turbulent kinetic energy in the impeller discharge had a value of about $0.028V_{Tip}^2$.

While estimating ε, researchers have mostly resorted to dimensional forms of Equation (2.13). Zhou and Kresta (1996) used this method to calculate ε for a PBT and found the maximum dissipation to be located in the impeller discharge very close to the blade. For constant power input into the tank, almost 50% of the power is dissipated in the impeller discharge stream in the case of a PBT. This is almost three times higher than that for a RT (see Table 2 in Kresta, 1998). Consequently, there is less ε in the bulk of the tank for a PBT as compared to a RT. Table 13.3 in Patterson et al. (page 781, 2004), gives a comparison of ε_{max} for different types of impeller in the form of a ratio of ε_{max} to the power input per unit mass of material in the tank (Equation 2.12).

It is generally reported that the flow close to the discharge of a PBT is locally isotropic over a range of the energy spectrum. While, some studies have found that the three components of the fluctuating velocity in the impeller discharge are significantly different from each other (Ranade and Joshi, 1989; Jaworski et al., 1991) others reported that they were quite similar suggesting local isotropy (Kresta and Wood, 1991; Zhou, 1997 and Zhou and Kresta, 1996). Kresta (1998) concluded that although the large scales of motion in the impeller discharge are anisotropic, the assumption of local isotropy may be applied over a restricted range of eddies if the blade passage frequency is removed from the data[2]. As one moves to the bulk of the tank the existence of local isotropy becomes questionable. Moreover, the local Reynolds number (based on λ) in the bulk is expected to be at least 2.5 times less than at the impeller and the condition required for the existence of an equilibrium range is itself in doubt. It is much more difficult to present the turbulence field of a PBT than a RT because of the greater sensitivity of the flow-field to the impeller/tank geometry and the greater complexity in the flow and zonal models are not readily available.

---

[2] The range of wave numbers were local isotropy is expected to exist starts from that corresponding to the blade passage frequency.

2.3.4. Up-pumping Pitched Blade Turbine (PBTU)

The up-pumping axial impellers were first employed in the early 1980's when it was discovered that the upward pumping configuration could be beneficial for efficient dispersion of gases in gas-liquid mixtures (Nienow et al., 1983; Chapman et al., 1983). More recently, these impellers have found their use in much wider areas of operation covering numerous other applications (see review by Nienow and Bujalski, 2004). Because of its relatively recent beginnings, there is not much information available on the details of the flow field generated by up-pumping impellers in general and the up-pumping pitched blade turbine in particular. The findings reported here are from relatively new studies involving LDV and CFD simulations by Aubin et al. (2001), Jaworski et al. (2001), Aubin et al. (2004) and the very recent review by Nienow and Bujalski (2004).

Figure 2.10a shows the mean flow field generated by an up-pumping pitched blade turbine and the flow field generated by a similar PBTD is also presented alongside (Figure 2.10b) for comparison. The discharge stream from the PBTU travels upwards, on reaching the higher regions of the tank turns around, and thence moves down along the tank wall. The down flowing liquid is pulled back into the impeller suction completing the circulation loop. Much like the PBTD placed at a high clearance, a second circulation loop rotating in a reverse direction is generated when the PBTU is placed far from the liquid surface (large submergence) as seen in the figure. Such secondary circulation loops were also observed by Aubin et al. (2001) for a PBTU with D = T/2 and S/D ~ 1.13 (corresponding to a C/D ~ 0.33). In the measurements by Aubin et al (2001; Figure 2c), the discharge stream leaves the impeller almost at an angle of 45° very similar to the discharge produced by a PBTD. Jaworski et al. (2001) also report good similarity between the discharge flow generated by an up-pumping and a down-pumping impeller. This is however not an universal observation since the data of Aubin et al. (2004) obtained by Particle Image Velocimetry (PIV) show a discharge that is a slightly more axial for the PBTU when compared to a PBTD. This point has also been highlighted in the review by Nienow and Bujalski (2004). Thus, while generally similarity exists, impeller discharge for the two cases could also have slightly different progressions. There

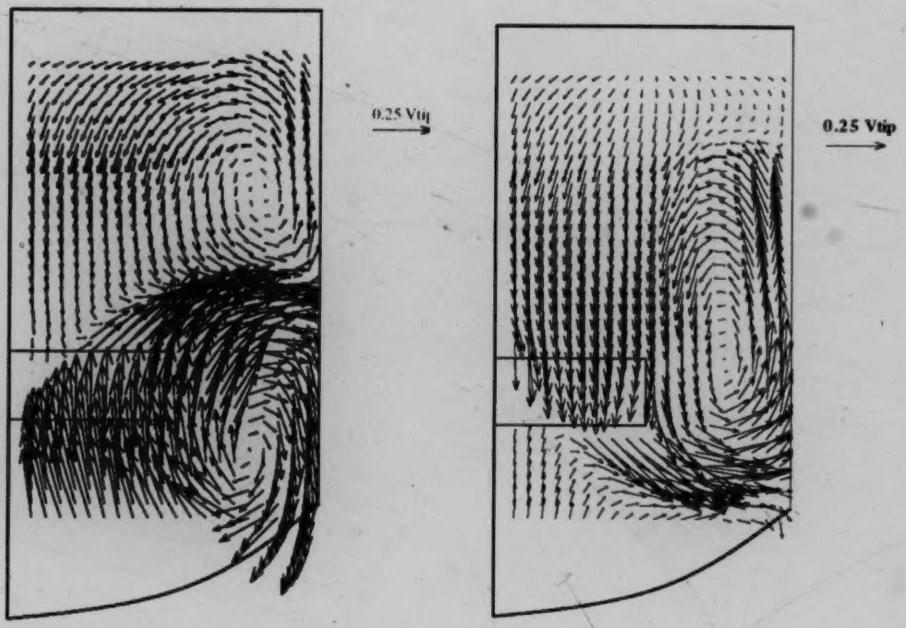

Figure 2.10 (a) Mean flow field generated from a PBTU (b) Mean flow field produced from a PBTD

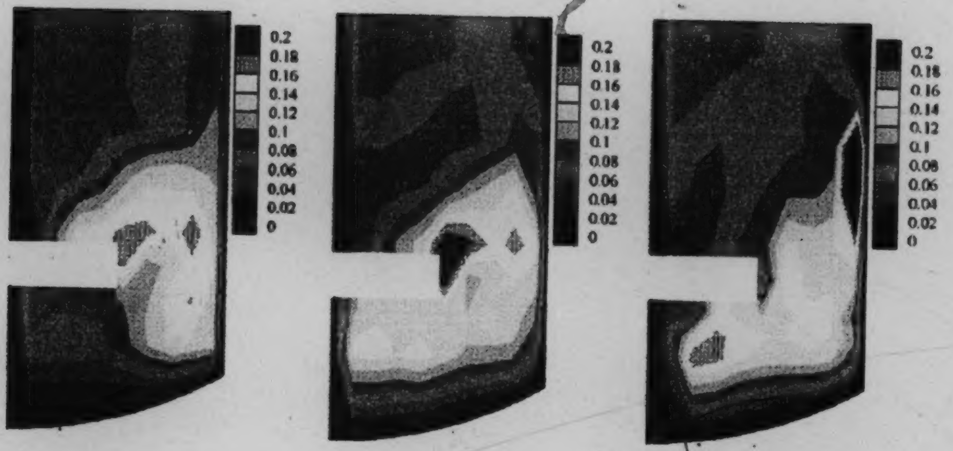

Figure 2.10 (c) Axial RMS velocity, u/V_{Tip} for a PBTU (d) Radial RMS velocity v/V_{Tip} for a PBTU and (e) Tangential RMS velocity, w/V_{Tip} for a PBTU

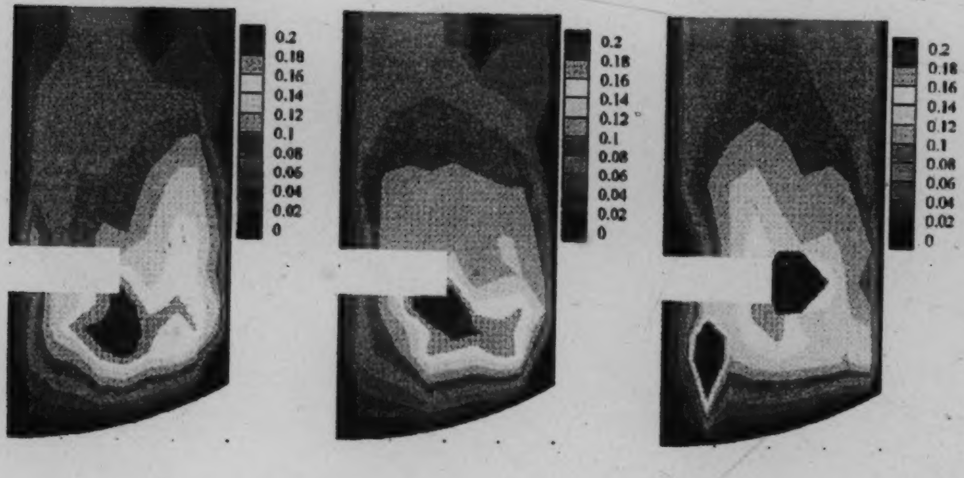

Figure 2.10 (f) Axial RMS velocity, u/V_{Tip} for a PBTD (g) Radial RMS velocity v/V_{Tip} for a PBTD and (h) Tangential RMS velocity, w/V_{Tip} for a PBTD

can also be an effect of the impeller size on the discharge with many studies reporting a more axially oriented discharge stream for smaller impellers (D = T/3 as against D = T/2) for both flow fields: up and down pumping.

Although relatively scarce, some details on the magnitudes of the various components of the velocity vectors in different regions of the tank are nonetheless available. Aubin et al. (2001) measured the maximum values of the axial, radial and tangential velocities in the tank stirred with a PBTU and a similar PBTD. They found that the maximum axial velocity for a PBTU was in the discharge and was about $0.41V_{Tip}$, which was very similar to the value of $0.44V_{Tip}$ observed in the discharge of a PBTD. The vector plot of the velocities in Figures 3 and 4 of Jaworski et al. (2001) indicate peak axial velocity values of about $0.3V_{Tip}$ for a PBTU and $0.48V_{Tip}$ for a PBTD. Aubin et al. (2001) also reported higher radial (turning of the upward moving stream for the PBTU and similar turning of the downward moving stream for a PBTD) but smaller tangential velocities for the up-pumping impeller. The study (Aubin et al., 2001) revealed that

- The PBTU was able to generate a secondary loop more easily and caused a more effective circulation of the liquid covering a greater volume of the tank than a PBTD
- Power consumption was higher for the former (P_O for a PBTU was about 2.58 as against 1.93 to 2.21 for the PBTD, both impellers being 6-bladed) and
- The discharge flow from the impeller was inferior for the PBTU as compared to the PBTD (N_Q for the PBTU was about 0.68 as against 0.75 to 0.8 for the PBTD).

Aubin et al. (2001) also measured the RMS velocities (see section 2.4.1.1 for definition) and estimated the turbulent kinetic energy in various regions of the tank containing a PBTU. Contour maps from their experiments are reproduced in Figures 2.10c, 2.10d and 2.10e and similar maps for a PBTD are also shown in Figures 2.10f, 2.10g and 2.10h. While the peak values for the RMS velocities are slightly lower for the PBTU as compared to the PBTD, the high turbulence region spreads out over a larger area for the former. A seen in many previous investigations, the maximum turbulence is found in the impeller discharge. The investigators found that the axial component of the

RMS velocity was about $0.18V_{Tip}$ for a PBTU while it was $0.2V_{Tip}$ for a PBTD, the radial component had values of $0.21V_{Tip}$ (PBTU) and $0.24V_{Tip}$ (PBTD) and the tangential component were $0.28V_{Tip}$ for the PBTU and $0.5V_{Tip}$ for the PBTD. The peak turbulent kinetic energy, which also is in the discharge stream, was found to be about 9% lower in the case of the PBTU as compared to the PBTD. As compared to a PBTD, lower values of the RMS velocity for a PBTU were also reported by Aubin et al. (2004; 0.12 and 0.17 times V_{Tip} for the PBTD and 0.11 and 0.13 times V_{Tip} for the axial and radial components of the RMS velocity for the PBTU). From these observations, it appears that the PBTU spreads out the dissipation of turbulent kinetic energy over larger regions of the tank and this could account for both the higher power draw and lower values of the RMS velocity in the discharge stream of this impeller configuration. Aubin et al. (2004) also reported that the turbulence field around the impeller for the PBTU was more isotropic as compared to the PBTD. The maximum value of the turbulent kinetic energy was found to exist in the impeller discharge stream and was measured it to be $0.02V_{Tip}^2$.

The part of the flow field that has been of the most interest to previous investigators has been the impeller region. For the present study where more attention is directed towards surface feed of reagents, the turbulence characteristics near the liquid surface is of greater interest. New measurements were therefore made for this region and the results will be reported later in Chapters 4 and 5. Like the PBTD, information is not readily available for the distribution of ε in various regions of the tank for this impeller configuration. The flow field for the PBTU is expected to be as much geometry dependent as the PBTD and zonal models are also not available, presumably due to similar reasons.

2.4. *Turbulent Mixing*

The coupling between reactions and mixing is complicated tremendously by the fact that turbulent mixing occurs at multiple scales. Not only does the length scales range from the size of the tank to the smallest microscopic scales, but the times scales also vary. An overview of the characteristic turbulent mixing scales is presented in the next three sections, starting with a brief review of the basic concepts of turbulence theory.

2.4.1. Turbulence

Turbulent flows are common but it is very difficult to formulate a precise definition for turbulence. Several researchers have attempted to describe its key features (Batchelor, 1953;Bradshaw, 1975; Hinze, 1975; Tennekes and Lumley, 1989; Leisure, 1990) and a synthesis of their idea leads to the following list of characteristics:

- They develop at high Reynolds number.
- They are chaotic with very irregular temporal and spatial dynamics. The flow is marked by energetic vortices and velocity fluctuations.
- They have enhanced ability to mix and transport scalars, momentum, or energy. The fluxes of these quantities are many times that observed in the laminar flow regime.
- Turbulent flows are characterized by a wide range of spatial wavelengths ranging from the largest, constrained only by the boundaries of the flow to the smallest determined only by viscous forces.

Because of its temporal and spatial dynamics, all variables that characterize turbulent flows have time or space averaged properties. Time averaging is used for stationary, random turbulent flows while space averaging is required for homogeneous flow-fields. Most studies on turbulence in stirred tanks make an assumption of quasi-stationarity. Kresta (1998) discusses some of the difficulties and the implications of these assumptions.

2.4.1.1. Definitions

The 'ith' component of the instantaneous velocity ($\widetilde{U}_i$) at any spatial location in the flow can be deconstructed into its constituent mean and fluctuating parts:

$$\widetilde{U}_i = \overline{U}_i + u'_i \tag{2.14}$$

where, i takes the values 1, 2 and 3 representing the three axes of symmetry. u'_i are the turbulent fluctuations and the overbar represents a mean quantity (see also Appendix B. Note that in this dissertation, the mean velocity is often shown as a capital letter without the overbar). The fluctuating velocity is defined as the root of the mean of the square (root-mean-square or RMS) of the turbulent fluctuations:

$$u_i = \sqrt{\overline{u_i'^2}} \tag{2.15}$$

The amount of turbulent kinetic energy contained per unit mass of fluid in the turbulent flow (k) can be obtained from the fluctuating velocities along the three axes of symmetry:

$$k = \frac{\overline{q^2}}{2} = \frac{u_i^2}{2} = \frac{u^2 + v^2 + w^2}{2} \tag{2.16}$$

Turbulent kinetic energy is generated at the largest scales of the flow while it is dissipated at the smallest. The transfer of energy between the scales is often explained using the concepts of an energy cascade developed by Kolmogoroff. The multiscalar nature of turbulent mixing is best explained using the energy and concentration cascades; hence, a brief description of the concept is presented.

2.4.1.2. The Rate of Dissipation of Turbulent Kinetic Energy (ε)

A schematic representation of the energy cascade is shown in Figure 2.11. In the model the turbulent flow field is visualized as containing eddies of all sizes, the largest comparable to the dimensions of the turbulent flow boundary (e.g. δ, the boundary layer thickness in the flow over a plate) and the smallest of microscopic size determined by viscous forces. The mechanical energy supplied into the mean flow (e.g. by stirring) is absorbed into the largest eddies as turbulent kinetic energy by means of velocity gradients in the flow-field. This energy cascades down progressively smaller eddies by the mechanism of vortex stretching until an eddy size is reached where viscous forces become predominant. The turbulent kinetic energy is dissipated from the smallest eddies by viscous work and converted into the internal energy of the fluid. The rate of dissipation of the turbulent kinetic energy per unit mass of the fluid (ε, encountered earlier in this chapter) is a very important quantity often used in engineering to quantify the levels of turbulence in the flow-field. The first moment of the Navier-Stokes equation gives the equation for the transport of turbulent kinetic energy, which contains a rigorous definition for ε:

$$\varepsilon = -2\nu\left[\overline{\frac{1}{2}\left(\frac{\partial u_i'}{\partial x_j} + \frac{\partial u_j'}{\partial x_i}\right)\frac{\partial u_j'}{\partial x_i}}\right] \tag{2.17}$$

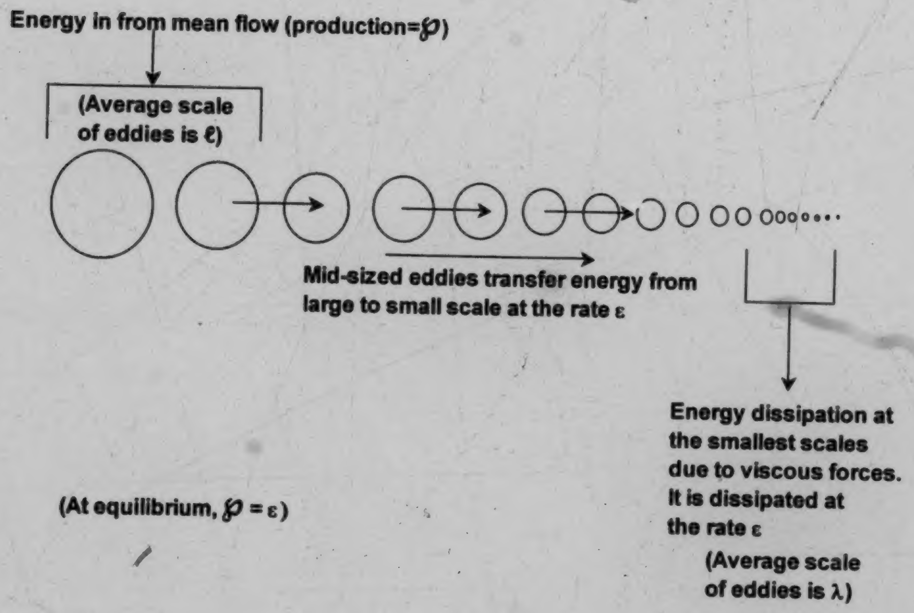
Energy in from mean flow (production=$\wp$)
(Average scale of eddies is ℓ)
Mid-sized eddies transfer energy from large to small scale at the rate ε
Energy dissipation at the smallest scales due to viscous forces. It is dissipated at the rate ε
(Average scale of eddies is λ)
(At equilibrium, $\wp = \varepsilon$)

Figure 2.11 An idealized scheme showing the production (at the rate, $\wp$), the transfer and the final dissipation (at the rate, ε) of turbulent kinetic energy. In this simplified scheme, approximate length scales are defined for the largest and the smallest eddies. ℓ represents the volume averaged size of the large eddies containing most of the energy, while λ represents the volume averaged size of the small eddies involved in the dissipation of the turbulent kinetic energy. In a more rigorous framework, Λ_g (Taylor's integral scale, 1935) and λ_g (Taylor's microscale, 1935) should be used. For the special case of isotropic turbulence ℓ can be defined in terms of Λ_g and λ in terms of λ_g.

Taylor (1935) showed that the complicated form of Equation (2.17) is reduced to the relation:

$$\varepsilon = 15\nu\overline{\left(\frac{\partial u_1}{\partial x_1}\right)^2} \qquad \text{or} \qquad \varepsilon = 7.5\nu\overline{\left(\frac{\partial u_2}{\partial x_2}\right)^2} \tag{2.18}$$

(where 1 and 2 represent the x and y directions) using the continuity equation and a simplification involving the assumption of isotropy at the smallest scales where dissipation occurs. Another useful expression for ε is obtained from scaling arguments, a form of which has already been seen in section 2.3.2. If a turbulent velocity scale, u_S, is defined such that

$$u_S = \frac{\overline{q^2}}{3} \tag{2.19}$$

and an average scale of the energy containing eddies is defined as ℓ (see Figure 2.11), then it follows that

$$\varepsilon = \frac{\text{kinetic energy per unit mass}}{\text{decay time}} \sim \frac{3u_S^2/2}{\ell/u_S} \,\alpha\, \frac{u_S^3}{\ell} \tag{2.20}$$

where the time required for the representative eddy of size ℓ to decay (the turn-over time, τ_U) is ℓ/u_S. Equation (2.20) is also used in conjunction with the characteristic velocity and length scales defined in other ways; a few of these definitions for ε are described in the Appendix B. The selection of the length and velocity scales for stirred tanks has already been seen in Equation (2.13).

2.4.1.3. The Energy and Concentration Spectrums

The multitude of scales in turbulent flows is best illustrated by the three-dimensional energy spectrum, E(k). The spectrum is defined such that (see Appendix B for details):

$$\int_0^\infty E(k)dk = \frac{u_i^2}{2} \tag{2.21}$$

k is the modulus of the corresponding wave number vector, k_i ($|k_i| = k$). The three dimensional spectrum therefore gives the distribution of kinetic energy among wave numbers of different magnitude, or more simply it shows how the turbulent kinetic energy is distributed among eddies of different sizes, r (page161, Baldyga and Bourne, 1999):

$$r = \frac{2\pi}{k} \sim \frac{1}{k} \tag{2.22}$$

An example for the three-dimensional energy spectrum for a fully turbulent flow with very high local Reynolds number is shown in Figure 2.12. Three regions with differing energy transfer characteristics can be identified:

1. Energy Containing Eddies: The biggest eddies with the smallest wave number contain the largest amounts of energy. This 'range of energy containing eddies' is characterized by the wave number $k_o \sim 1/\ell$, also shown in the figure. ℓ is dependent on the flow elements generating turbulent kinetic energy from the mean flow and the size of the large eddies depend on the scale of the system. As the wave number increases, the eddy size decreases and the energy content of the eddies reduces, i.e. $\int_{k_1}^{k_2} E(k)dk$ decreases as [k1, k2] moves down the spectrum.
2. Viscosity Dominated, Dissipative Eddies: On the other end of the spectrum, the energy content in the eddies with wave numbers comparable to $k_K \sim 1/\eta$ is the least but on the other hand viscous dissipation of the turbulent kinetic energy is the highest for these tiny eddies. In fact, the dissipation spectrum, related to the energy spectrum through the relation:

   $$D(k) = 2\nu k^2 E(k) \tag{2.23}$$

   shows a maximum at a wave number comparable to k_K. The rate of dissipation of turbulent kinetic energy, ε, is related to the dissipation and energy spectrums through the relation

   $$\varepsilon = \int_0^\infty D(k)dk = 2\nu\int_0^\infty E(k)k^2 dk \tag{2.24}$$

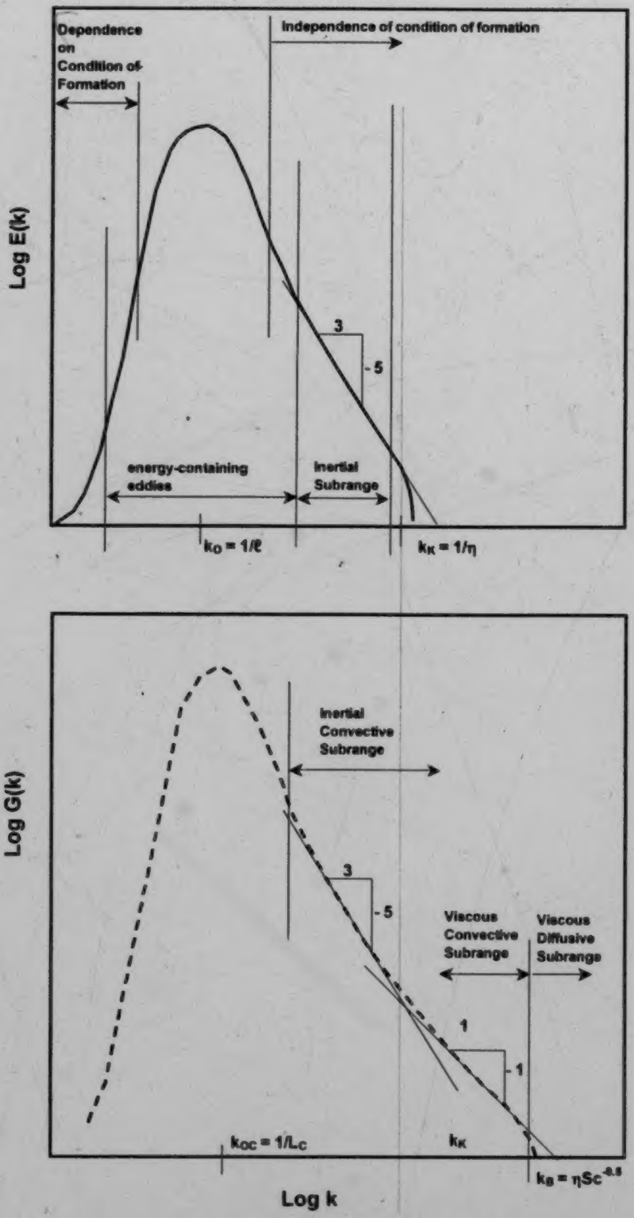

- Three-dimensional Energy Spectrum showing the large energy containing eddies, the small dissipating eddies and the inertial subrange. The area under the curve between two wave numbers gives the total tke in all eddies between the two sizes:

$$\int_{k_1}^{k_2} E(k)dk = \frac{u_i^2}{2}$$

- Three-dimensional Concentration Spectrum for Sc >> 1. The area under the curve between two wave numbers gives total mean of concentration variance:

$$\int_{k_1}^{k_2} G(k)dk = \frac{\overline{c_\alpha'^2}}{2}$$

Figure 2.12 **Three-dimensional Energy Spectrum and Concentration Spectrum in turbulent flows with very high local Reynolds number (inertial subrange exists).**

3. Inertial Subrange: The eddies in between these two extremities ($k_o << k << k_K$) are involved in a transfer of energy from the large energy containing eddies to the small dissipative ones. When the local Reynolds number (defined in terms of ℓ) is large, and the Kolmogoroff scale, η, is sufficiently small there exist a range of wave numbers where the eddy size is sufficiently large so that viscosity effects are negligible and the amounts of energy dissipated is small compared to the energy transported by inertial effects. Kolmogoroff hypothesized that the energy spectrum in this range of wave numbers is independent of ν and solely dependent on ε. The region is called the 'inertial subrange' and a dimensional analysis shows that for this region:

   $$E(k) = \alpha \varepsilon^{2/3} k^{-5/3} \qquad \text{for } k_O << k << k_K \tag{2.25}$$

   Within the inertial subrange energy coming into the cascade from the larger eddies are simply transferred to the smaller eddies without dissipation and is shown in Figure 2.12 with the slope of –5/3.

Figure 2.12 also shows the spectrum of concentration fluctuations G(k), which is defined such that:

$$\int_0^\infty G(k)dk = \overline{c'^2_\infty} \tag{2.26}$$

Differences in the shapes of the concentration and the energy spectrum arise due to the differences in the momentum (ν) and scalar ($\mathcal{D}$) diffusivities. These will be discussed in more details in the next section.

2.4.1.4. **Commonly Used Simplifications**

Two simplifications are often used when dealing with turbulent flows: the concept of frozen turbulence, which leads to the one-dimensional energy spectrum and the concept of local isotropy. In order to obtain the two-point correlation tensor (Q_{ij}, defined in Appendix B) it is necessary to measure all three-components of velocity at two spatial locations separated by the vector, r_m. The three-dimensional energy spectrum in Figure 2.12 can only be obtained if such three-dimensional measurements are available. Often velocity data are available from only one probe fixed in space in the turbulent flow field that is moving by, say, at an average velocity, $\overline{U}_C$. Now the probe can measure only a one-dimensional record of the fluctuations caused by a random group of eddy orientations as they are swept by at the velocity $\overline{U}_C$ and hence only a one-dimensional slice of the complete three-dimensional spectrum can be obtained. If the one-dimensional velocity record is mean centered, and transformed from the time to frequency domain using Fourier transform we obtain the one-dimensional energy spectrum, $E_1(f)$, defined such that:

$$\overline{u_1^2} = \int_0^\infty E_1(f)df \tag{2.27}$$

The problem that arises when spectra are expressed in terms of frequency (f) is that as the mean velocity $\overline{U}_C$ increases, a *frozen* eddy of *fixed wavelength* will be swept by the probe at higher speeds and cause frequency to increase. Because it is the eddy size (or wave length) and not the frequency that remains constant in a flow, it is more convenient to express frequency in terms of wave number, k_1 (with units of 2π/wavelength, where the wavelength is $\overline{U}_C/f$)

$$k_1 = \frac{2\pi f}{\overline{U_C}} \tag{2.28}$$

The requirement of constant wavelength implies that Equation (2.27) implicitly assumes *frozen turbulence*, often called the Taylor's hypothesis. The one-dimensional wave number leads to the one-dimensional spectral density or power spectrum:

$$\overline{u_1^2} = \int_0^\infty E_1(k_1)dk_1 \tag{2.29}$$

A typical one-dimensional spectrum for a stirred tank is shown in Figure 2.13a. The main difference between the three and the one-dimensional spectrum is that

$$\begin{array}{ll} E(k) \rightarrow 0 & \text{for} \quad k \rightarrow 0 \\ E_1(k_1) \rightarrow \text{maximum} & \text{for} \quad k_1 \rightarrow 0 \end{array} \tag{2.30}$$

This is due to the effect of aliasing, a concept illustrated in Figure 5.15 of Baldyga and Bourne (1999) and Figure 6.8, page 209 in Pope (2000). A one to one comparison of the three-dimensional and one-dimensional spectra is also provided in Figure 6.11, page 229 of Pope (2000). Note the large *blip* at the top of the energy spectrum in Figure 2.13a. This is the effect of blade passage close to the point of measurement. As the impeller rotates, a trailing vortex remains attached to the tip of each blade as shown in Figure 2.13b for a Rushton turbine. These trailing vortices first discussed in details by van't Riet and Smith (1975) and now well established (see Kresta, 1998 for a list of references), cause strong oscillations in the mean flow that are picked up by the probe and reported in the energy spectrum. The trailing vortices are strongly anisotropic, are found in both radial and axial impellers and have to be suitably treated when determining the characteristics of the turbulent flow field. The usual method is to filter out the lower frequencies from the spectrum (see e.g. Kresta, 1998).

The concept of local isotropy is often needed to quantify dissipation (ε) when direct measurements of spatial gradients are not available. True isotropy is a very rigorous condition and requires that there be no directional preference in the three-dimensional flow. Though true isotropy allows simplification of the equations in turbulence, because now only one velocity component can describe the whole spectrum, it is not a condition possible in real three-dimensional flow fields, especially a stirred tank. The concept of local isotropy however comes to the rescue by allowing one to use the equations developed for truly isotropic flow-fields over a *restricted range* of eddy sizes. Local isotropy states that "if the local Reynolds number (based on the turbulence length scale, λ and the fluctuating velocity, not on the equipment length scale, D and mean velocity) is high enough, there may be a range of eddy sizes over which the turbulent energy cascade is in equilibrium. Under these conditions energy enters at the top of the isotropic scale of eddy sizes and is dissipated at the smallest locally isotropic

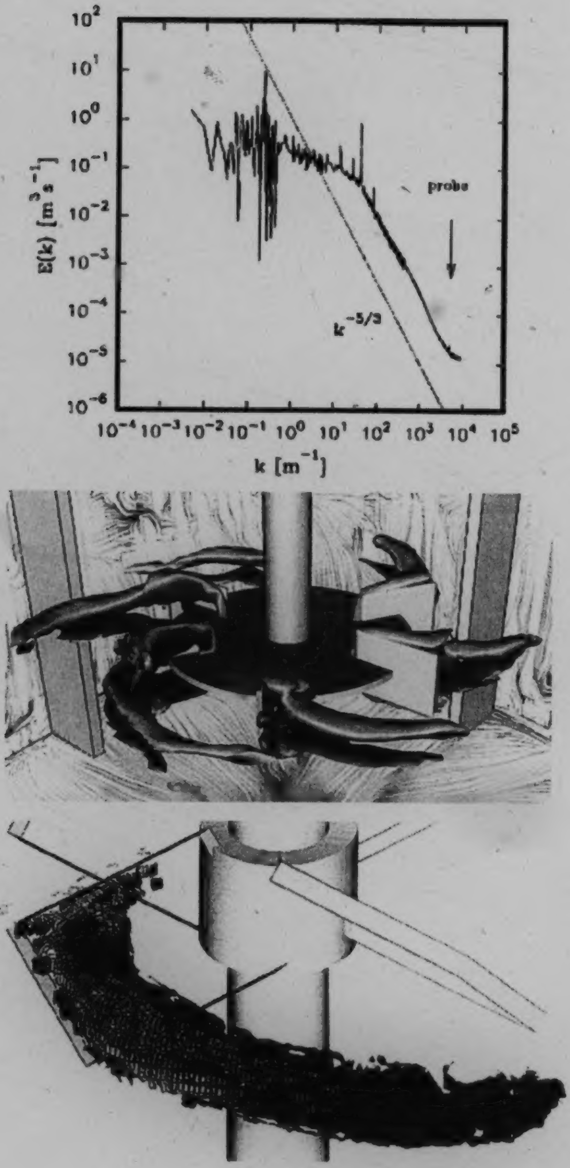

a) 1-D Energy Spectrum

b) Trailing Vortices Attached to a RT

c) Trailing Vortices Attached to a PBT

Figure 2.13 a) One-dimensional energy spectrum for a tank stirred with a Rushton turbine. (Reproduced from Wernersson, 1997). b) Trailing vortices attached to the blades of a Rushton turbine visualized through LES (Reproduced from Bakker and Oshinowo, 2004) c) Trailing vortex attached to the blade of a PBT. PIV measurements (Reproduced from Schäffer et al., 1998).

scales of motion with no loss of energy at the intermediate scales. Over this range of eddy sizes, no memory of the oriented large-scale motions (i.e. trailing vortices) remains and there is no directional preference in flow. The condition extends up the cascade to some large eddy size ℓ. Below this length scale the flow can be treated as locally isotropic (Kresta, 1998)". In these smaller length scales, the equations developed for true isotropy (e.g. the Kolmogoroff scale) can be used. Several indicators (Kresta et al., 1998) are used to test the assumption of local isotropy:

- A high local Reynolds number.
- The existence of –5/3 slope in the frequency spectrum of the velocity signal and
- Equality of the three RMS components of velocity.

The concept of local isotropy is essential in all indirect methods for calculating ε.

2.4.2. Scales of Mixing

The characteristic length and time scales in turbulent mixing are shown in Tables (2.4) and (2.5). Turbulent kinetic energy is dissipated at the smallest length scales by viscous deformation of the fluid elements and the mechanism is completely laminar in nature. Although the small eddies are characterized by the Kolmogoroff length scale, η, it is not necessarily the scale at which dissipation is maximum (e.g. pages 270 and 271 in Tennekes and Lumley, 1989). The length scale at which dissipation actually reaches its peak, λ_d, is about five times η. However, since the two quantities η and λ_d are of the same order of magnitude the wave number for dissipation is often approximated by

$$k_d \sim \frac{1}{\eta} \tag{2.31}$$

The Kolmogoroff scale marks the end of the inertial subrange where $E(k) \propto k^{-5/3}$.

$$k_O \le k \le \frac{1}{\eta} \quad \text{(inertial subrange)} \tag{2.32}$$

k_O denotes the wave number at the characteristic length scale (ℓ). This scale along with the integral scale (Λ_g), represent the eddy size at the other end of the spectrum. Similar to the integral length scale derived for velocity fluctuations, the integral length scale for concentration fluctuations (Λ_C) can also be defined to describe the size of the

Table 2.4 Characteristic Length Scales in Turbulent Mixing

Length Scale	Expression
Integral length scale (cross-stream, Λ_g)	$\Lambda_g = \int_0^\infty g(\xi)d\xi$ where, $g(\xi) = \frac{\overline{u'(x,y+\xi)\cdot u'(x,y)}}{\overline{u'^2}}$ (Taylor, 1935)
Characteristic length scale (ℓ)	Hypothetical characteristic length scale obtained by volume averaging the size of the large eddies in the turbulent flow. For isotropic turbulence $\ell = 2.66\Lambda_g$ (Hinze, 1975)
Kolmogoroff length scale (η)	$\eta = \left(\frac{\nu^3}{\varepsilon}\right)^{1/2}$
Length scale at which dissipation is maximum (λ_d)	5η (see also pages 270 and 271 in Tennekes and Lumley, 1989)
Corrisin scale of turbulence (η_C)	$\eta_C = \left(\frac{D^3}{\varepsilon}\right)^{1/4}$
Batchelor scale (η_B)	$\eta_B = \left(\frac{D^2\nu}{\varepsilon}\right)^{1/4} = \eta \cdot Sc^{-1/2}$
Integral length scale for concentration fluctuations (Λ_C)	$\Lambda_C = \int_0^\infty R_{CC}(r,t)dr$ where $R_{CC}(r_i) = \frac{\overline{c'_\alpha(x_i)\cdot c'_\alpha(x_i+r_i)}}{\overline{c'^2_\alpha}}$ where $c'_\alpha(x_i)$ and $c'_\alpha(x_i+r_i)$ are the concentration fluctuations of species 'α' at two locations separated by the vector r_i.

Table 2.5 Characteristic Time Scales in Turbulent Mixing

Time Scale	Expression
Blend time (θ_B)	$N\theta_B = \frac{5.4}{P_O^{1/3}}\left(\frac{T}{D}\right)^2$ (turbulent) $N\theta_B = \frac{1}{Re_I}\frac{184.2}{P_O^{2/3}}\left(\frac{T}{D}\right)^2$ (transitional) (Grenville, 1992). Laminar blending is based on completely different mechanism (cutting and folding) hence blend time for that regime is not presented here.
Kolmogoroff time scale for viscous dissipation (τ_K)	$\tau_K = \frac{1}{s_K} = \left(\frac{\nu}{\varepsilon}\right)^{1/2}$ where the rate of strain is $s_K = \left(\frac{\varepsilon}{\nu}\right)^{1/2}$
Batchelor time scale (τ_B)	τ_B is equal to τ_K by definition (see Appendix B also)
Corrsin mixing time scale (τ_C)	$\tau_C = 2\left(\frac{L_S^2}{\varepsilon}\right)^{1/3} + \frac{1}{2}\left(\frac{\nu}{\varepsilon}\right)^{1/2}\ln(Sc)$ for Sc >> 1 $\tau_C = 1.36\left(\frac{L_S^2}{\varepsilon}\right)^{1/3}$ for Sc ~ 1
Mean lifetime of an energy-dissipating vortex (τ_ω)	$\tau_\omega = 17.3\left(\frac{\nu}{\varepsilon}\right)^{1/2}$
Characteristic time for micromixing from the Engulfment model (Equation 2.39, Baldyga and Pohorecki, 1995)	$\tau_E \approx 12\left(\frac{\nu}{\varepsilon}\right)^{1/2}$
Characteristic time for turbulent dispersion (see Equation 2.41)	$\tau_D = \frac{Q_f}{UD_T}$
Characteristic time for inertial convection disintegration of large eddies (see Equation 2.45)	$\tau_S \approx A\left(\frac{\Lambda_C^2}{\varepsilon}\right)^{1/3}$

concentration eddies (Table 2.4). Λ_C is a measure of the largest concentration eddies, or spots of tracer, present in the turbulent mixture. The notation L_C is often used to denote the characteristic length scale (comparable to Λ_C) associated with the large concentration eddies.

It is seen from Figure (2.12) that the concentration spectrum, G(k), although similar in shape to the energy spectrum, E(k), is spread out over a different range of wave numbers. The spread of the concentration spectrum depends on the Schmidt number (Sc) of the fluid, defined as:

$$Sc = \frac{\nu}{\mathcal{D}} \tag{2.33}$$

Figures (2.14a and b) shows the concentration spectrum at high Reynolds number for a gas with $Sc \sim 1$ and a liquid with $Sc >> 1$. When $Sc \sim 1$ (typical for gases) diffusivity starts affecting the concentration spectrum in the inertial subrange even *before* viscous effects have started. The wave number at which this happens is smaller than the Kolmogoroff wave number ($k_K = 2\pi/\eta$) and is characterized by the Corrisin scale of turbulence, η_C. The corresponding wave number, $k_C = 1/\eta_C$ is shown in Figure (2.14a) where it demarcates the *inertial-diffusive subrange*:

$$k_C = \frac{1}{\eta_C} \leq k \leq \frac{1}{\eta} = k_K \quad (\text{inertial} - \text{diffusive subrange}) \tag{2.34}$$

In this subrange, the spectral flux of concentration variance (see section 2.4.2) is no longer equal to ε_C but decreases due to molecular diffusion. The mechanism of mixing in liquids is very different from that in gases due to the absence of this subrange. For $Sc \sim 1$ (typical in most liquids) molecular diffusivity does not yet affect the concentration spectrum even when the wave number has reached k_K. The scales of concentration fluctuations therefore have to be reduced further (wave number increases) by viscous deformations. This region extending beyond k_K is the *viscous-convective subrange*, which ends when the scale of the concentration fluctuations becomes so small that diffusion can compete with deformation. This happens at a wave number comparable to the Batchelor scale, η_B, defined in Table (2.4). The wave number for the Batchelor scale

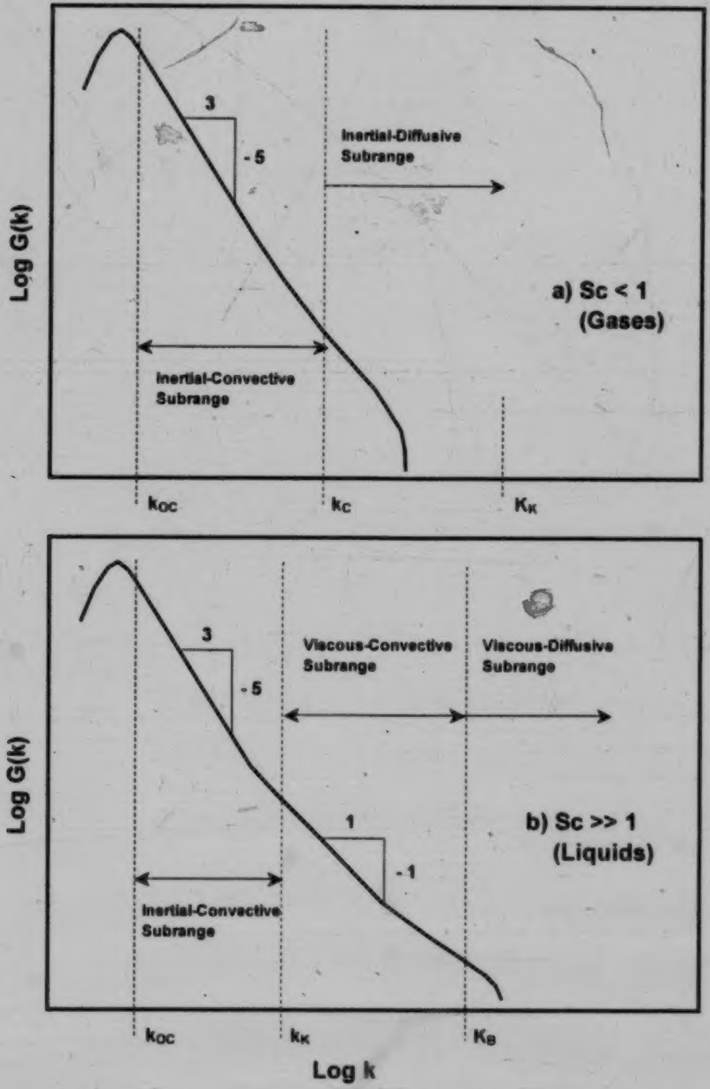
Log G(k)
3
- 5
Inertial-Diffusive Subrange
a) Sc < 1 (Gases)
Inertial-Convective Subrange
k_{OC}
k_C
K_K
Log G(k)
3
- 5
Viscous-Convective Subrange
Viscous-Diffusive Subrange
1
- 1
b) Sc >> 1 (Liquids)
Inertial-Convective Subrange
k_{OC}
k_K
K_B
Log k

Figure 2.14 Schematic spectrums of concentration variance for fluids at very high Reynolds number. (a) The spectrum for a liquid with high Schmidt number and (b) the spectrum for a gas with low Schmidt number. Not to scale.

is used to demarcate the viscous-convective and the viscous-diffusive subranges, as seen in Figure (2.14b):

$$\begin{aligned} &\frac{1}{\eta} \leq k \leq \frac{1}{\eta_B} \quad &&(\text{viscous}-\text{convective subrange}) \\ &k \geq \frac{1}{\eta_B} \quad &&(\text{viscous}-\text{diffusive subrange}) \end{aligned} \qquad (2.35)$$

The concentration spectrums for the inertial-diffusive and the viscous-convective subranges were developed by Corrisin (1964) and Batchelor (1959). Note that the energy spectrum remains unaffected by the diffusivities of the scalar. As progressively smaller eddies are encountered in the energy spectrum, the energy transfer characteristics of the eddies and the characteristic time scales change. The time scales of particular importance to turbulent mixing are shown in Table (2.5). More detailed descriptions of these scales are provided in Appendix B. Complex models for turbulent mixing have been developed using the concentration and energy spectrums and these characteristic scales of turbulence.

From a general perspective, three stages can be identified amongst the complicated processes of turbulent mixing based simply on the scale at which they occur: macromixing, mesomixing and micromixing (Baldyga and Pohorecki, 1995). Each of these stages contains one or more of the subranges shown in Figure (2.14b). The mechanism in the individual stages can be observed by tracing the history of a blob added into the turbulent environment:

a) As the blob is added into the turbulent flow it disperses and the concentration scale of the dispersed material become smaller until it reaches a size comparable to η. This is equivalent to a movement from left to right along the inertial subrange of the concentration spectrum in Figure (2.14b). For highly turbulent environments, this initial decrease in scale occurs by turbulent dispersion and inertial-convective disintegration of the large, concentration eddies.

b) As the scale of the concentration eddies reaches the Kolmogoroff scale, viscous-convective deformations further reduce their size. Finally, the Bachelor scale is reached and the process moves into the viscous-diffusive subrange where diffusive processes become important and the striations of the chemical species are smeared out completely by diffusion (and reaction when reactive species are present).

c) Simultaneous with the dispersion and diffusion processes, fresh material is also brought into the mixing zone from other regions of the turbulent environment by large-scale circulations.

The initial dispersion of the blob in stage (a) occurs at scales which are smaller than the largest dimensions of the flow (e.g. the diameter of a stirred tank) but larger than the microscopic scale (η and η_B) at which diffusion is important. Mixing at this scale is called *mesomixing* to highlight its intermediate size. In the final, diffusion dominated stage (b), the scale of mixing is very small and this constitutes *micromixing*. *Macromixing* occurs in a scale comparable to the size of the vessel and causes large-scale distribution of material described in stage (c). Experimental methods such as determination of the residence time distribution (RTD) of a dye injected into the reactor or the spatial distribution of the mean concentration are used to determine the macromixing characteristics of a reactor. Since meso and microscales are contained within this larger scale, macromixing indirectly affects the later by (i) setting up the concentration environment within which the former operate and (ii) conveying fluid undergoing micro and mesomixing through regions of varying turbulence properties which changes the mixing rates. When dealing with fast reactions any one of these three steps, especially micro and mesomixing steps, can become rate limiting and adversely affect product formation. Hence, it is vitally important to understand the mechanisms of these processes. This is continued in the next section.

2.4.3. Micromixing – Mechanisms and Models

Micromixing starts within the viscous-convective subrange of the concentration spectrum (see the demarcation by Baldyga and Pohorecki, 1995) and one of its characteristic features is the acceleration of molecular diffusion by viscous-convective processes. The concentration eddies (blobs of reactants) are subjected to laminar strain leading to a reduction in size. As the eddy size becomes smaller, and ultimately less than η_B, the viscous-diffusive subrange is reached and the effects of diffusion becomes important. Numerous mechanistic models have been developed to provide simple, idealized mechanisms of micromixing that are not necessarily realistic but which are amenable to fitting of model parameters using theories of turbulence to obtain reasonable results. A detailed description along with the time-line of development of these models is available in Yu (1993). Two of the newer models widely used for micromixing calculations are presented below. Note that these models can show the progression of reaction with the formation of the products and by-products only when the mixing field is known properly. For a more detailed simulation of reactive mixing when the mixing field is also unknown, it is required to solve the complete set of balance equations: the Reynolds averaged Navier-Stokes equation, along with the component mass balance equations for each species and the appropriate models for velocity (e.g. Reynolds stresses) and concentration cross-correlations. A discussion on these computational models is provided on pages 833-846 of Patterson et al (2004).

2.4.3.1. Engulfment, deformation, and diffusion (EDD) model

This mechanistic interpretation of micromixing visualizes the process to be a series of steps initiated by the effects of laminar strain on vortex tubes. First fluid from the local environment is drawn into the vortices (engulfment – E), the fluid elements are distorted to form thin striated concentration fields (deformation – D), simultaneously diffusion and reaction continue in these reduced length scales (diffusion – D). The main processes occurring are the follows:

- Straining of the concentration eddies in the turbulent flow field gives rise to the long thin vortex tubes shown in Figure (2.15a). Vortices of initial size, $\delta_{\omega} = 11.5\eta$ form an important part of the fine dissipating structure[3]. These vortex tubes stretch longitudinally due to the straining motion, resulting in elongation of contamination

---

[3] Because of the opposing effects of strain and viscosity on vorticity, the vortices of the size $\delta_{\omega} = 11.5\eta$ been found to have the largest amount of vorticity and the highest frequency. A rate of strain acting in the direction of the vortex increases its vorticity, while viscosity reduces it. Hence, the vorticity in the eddies increase with decreasing eddy size in the inertial subrange. Near the Kolmogoroff scale, however, viscosity effects take over and vorticity starts to decrease with decreasing size giving rise to maximum vorticity at an eddy size of about 11..5η (pages 561-53, Baldyga and Bourne, 1999).

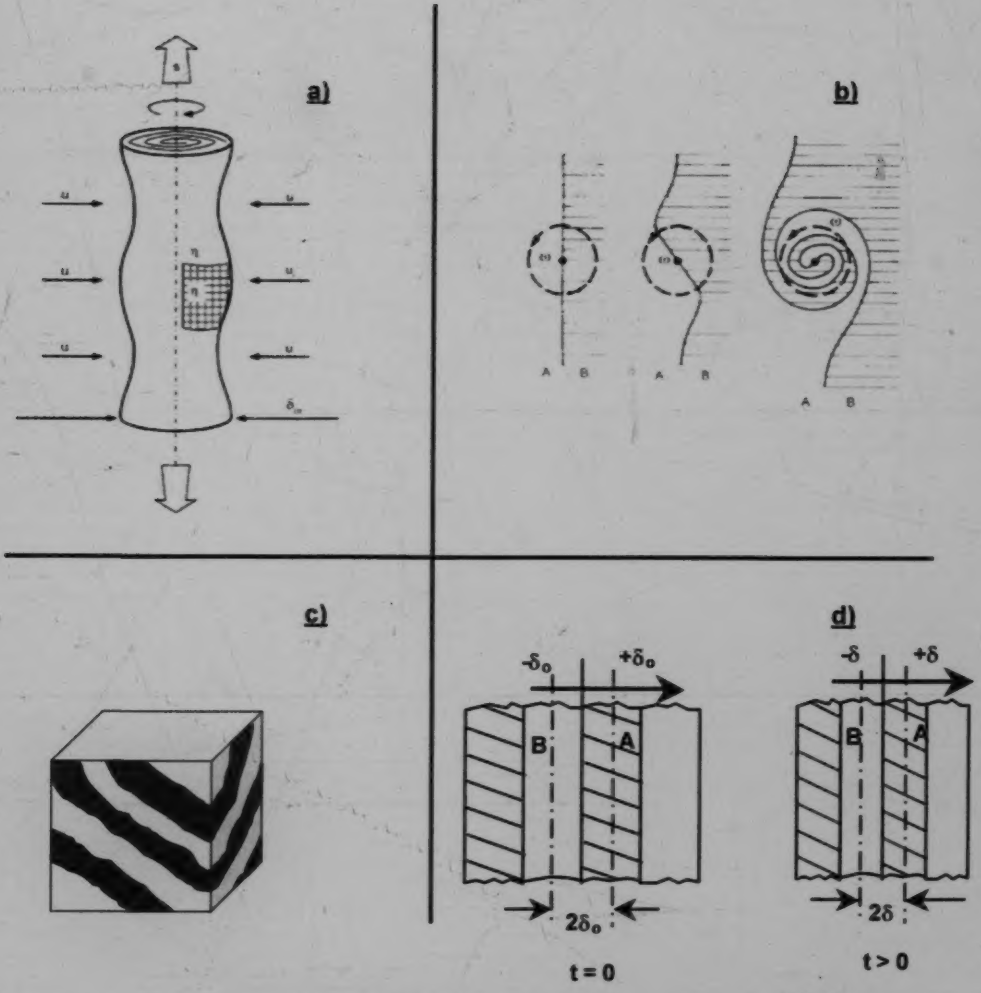

Figure 2.15 Schematic representation of (a) a Vortex tube (b) Formation of laminated structure by the action of vorticity (c) Engulfment of fluid from by the local environment due to the action of strain on the vortex tubes (d) Lamellar structure of the fluid in the vortex (A) and the fluid from the local environment (B) inside a vortex tube. Figures adapted from Figures 8.14, 8.13, 8.16 and 8.17 in Baldyga and Bourne (1999).

spots and the inflow of fluid towards the vortex (Figure 2.15b); the later being termed engulfment.

- Engulfment of fluid by the vortex results in the formation of the partially segregated lamellar structure within the vortex tubes as shown in Figure (2.15c). Although the vortices are themselves intermittent, since $\mathcal{D} << \nu$ the fine concentration structures within the lamellae persist and the deformation, diffusion and reaction can continue within the striations even after the vortex has died out. Species mass balances give the rate of diffusion and reaction within the lamellar structure. The resulting mass balance equations are a set of parabolic partial equations (Appendix B).
- The mean lifetime of an energy-dissipating vortex is defined as the time required for the vortex fluid to return to a hydrodynamically isotropic state under the action of viscosity, in the absence of strain and is given by

  $$\tau_\omega = 17.3\left(\frac{\nu}{\varepsilon}\right)^{1/2} \qquad (2.36)$$

  Within the period, τ_ω, vortices are deformed by laminar strains, engulf fluid which then undergo diffusion and reaction. After the time, τ_ω, the old vortex disappears and a second generation of vortices is formed by engulfing fresh layer of fluid from the local environment. Deformation, diffusion and reaction again follow. This process continues with a frequency, τ_ω^{-1}, until the fluid is completely homogenized. Several generations of vortices are therefore needed to completely homogenize the added 'blob' of fluid.

The species mass balances result in a set of parabolic, partial equations (See Appendix B) that need to be solved multiple times until the end of the process, with homogeneous concentration, is reached. Because these equations are stiff, computations are very costly. Baldyga and Bourne (1989) proposed a simplification of the EDD model for Sc < 4000.

2.4.3.2. **Engulfment model**

When Sc < 4000 the role of molecular diffusion is very small compared to fluid engulfment even at scales equivalent to or smaller than η (Baldyga and Bourne, 1989). For this Schmidt number, molecular diffusion is completed inside the eddies even before the next generation of vortices is formed; hence it is the rate of engulfment that is the limiting process. The main considerations then are the rate of increase of the mixing or reaction volume (V_m, where the reactants are undergoing micromixing) and the convective mass transfer within this volume and its environment. Consider a reaction between reactants A and B and the mechanism of growth of the mixing volume shown in Figure (2.16). If the volume of B is very small compared to the volume of A, so that self-engulfment of B by the reaction volume is negligible, the growth of V_m is given by:

$$\frac{dV_m}{dt} = EV_m \qquad (2.37)$$

E is the engulfment parameter, defined by Baldyga and Pohorecki (1995) as:

$$E \approx 0.058\left[\frac{\langle \varepsilon \rangle}{\nu}\right]^{1/2} \qquad (2.38)$$

The characteristic time describing micromixing (τ_E) is proportional to E^{-1}, the exact definition being (Baldyga and Pohorecki, 1995):

$$\tau_E \approx 12\left(\frac{\nu}{\varepsilon}\right)^{1/2} \qquad (2.39)$$

V_m is the reaction or mixing volume under consideration and is initially equal to the volume of B added, V_{B0}. The species mass balances do not contain diffusion terms and coupled with the equation for growth of the mixing volume by engulfment (Equation 2.37) give the equation for the evolution of the concentration of species α:

$$\frac{dC_\alpha}{dt} = E\left[\langle C_\alpha \rangle - C_\alpha\right] + r_\alpha \qquad (2.40)$$

r_α is the reaction rate for species 'α' and $\langle C_\alpha \rangle$ denote the concentration of species α in the local environment of the growing eddy or reaction volume. The set of equations represented by Equation (2.40) can be solved much more easily than the partial differential equations resulting from the EDD model. Details are given in Appendix B.

2.4.4. Mesomixing – Mechanisms and Models

As outlined above, concentration gradients in the microscale (micromixing) have a direct influence on the chemical reaction. Inhomogeneity on a coarser scale, involving

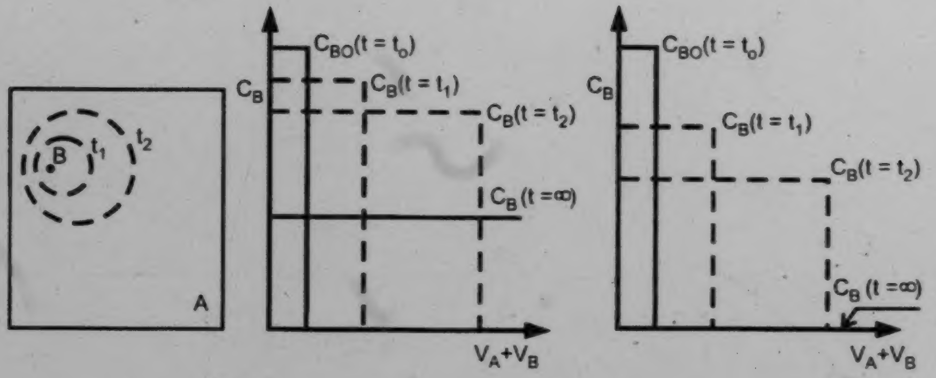
B
t1
t2
A
CB
CBO(t = to)
CB(t = t1)
CB(t = t2)
CB(t =∞)
VA+VB
CB
CBO(t = to)
CB(t = t1)
CB(t = t2)
CB (t =∞)
VA+VB

Figure 2.16 Schematic representation of the engulfment model. (a) shows the growth of the mixing volume (V_m) by engulfment from the surrounding (b) concentration profile of B for mixing without reaction (c) concentration profile of B with instantaneous reaction ($t_2 < t_1 < t_0$). Figure reproduced from Figure 8.22 in Baldyga and Bourne (1999).

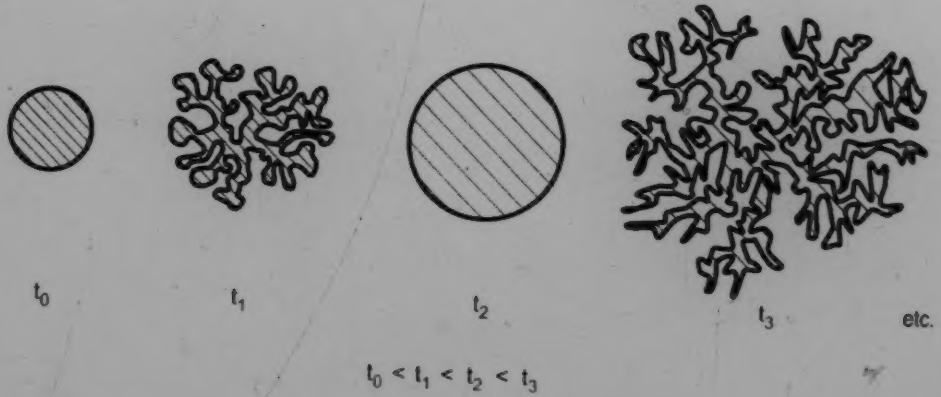
t_0
t_1
t_2
t_3
etc.
$t_0 < t_1 < t_2 < t_3$

Figure 2.17 Schematic representation of the mesomixing process by inertial-convective disintegration accompanied by micromic. A blob of fluid undergoes inertial-convective disintegration and distortion between times [t_o and t_1] and [t_2 and t_3]. Micromixing homogenizes the concentration between times [t_1 and t_2]. Note that inertial-convective disintegration and micromixing occur simultaneously and not in series. Reproduced from Figure 8.31, page 596, Baldyga and Bourne (1999)

macro and mesomixing while not affecting the course of a reaction directly can nonetheless have a significant influence on the overall yield and selectivity. Macromixing is linked to the overall flow-field/circulation in the mixing equipment and is quantified by the blend time. Mesomixing on the other hand occurs at a relatively smaller scale of the feed-pipe, and involves turbulent exchange between fresh feed and its surroundings. Two mechanisms have been identified for this process (Baldyga et al., 1997):

2.4.4.1. Turbulent dispersion

The first process that the feed stream undergoes as it leaves the feed pipe is dispersion by the ambient turbulence which causes it to spread transverse to the direction of discharge. The characteristic time, τ_D, for this process for a 'point' feed source is:

$$\tau_D = \frac{Q_f}{\overline{U}\mathcal{D}_T} \tag{2.41}$$

where Q_f is the volumetric flow rate of feed, $\overline{U}$ is the average velocity of the surrounding fluid and $\mathcal{D}_T$ is the turbulent diffusivity. Turbulent dispersion results in a feed plume containing the feed as well as the surrounding reactant, hence it sets up the environment within which micromixing proceeds. In processes undergoing turbulent dispersion, it is necessary to determine whether the feed is a point source or not because the concentration profile within the feed plume (Baldyga et al., 1997) and hence the progression of the reaction are significantly different for the two cases. The concentration profiles for both cases are given in Appendix B. The identification of a point, or its converse, a finite source, is through the characteristic length scale, L_D, defined in terms of Q_f and $\overline{U}$:

$$L_D = \sqrt{\frac{Q_f}{\overline{U}}} \tag{2.42}$$

A feed is a point source if $d_f/2 << L_D << L_x$, where d_f is the diameter of the feed pipe and L_x is the scale of the system/reactor. When $L_D << L_x$ but $L_D \sim d/2$, the feed can no longer be considered to be a point source and another parameter is needed to characterize completely the system. The parameters commonly used are:

$$R_u = \frac{U_f}{\overline{U}} \tag{2.43}$$

or, $$\tau_{Dl} = \frac{r^2}{\mathcal{D}_T} \tag{2.44}$$

Apart from the diffusion based approach used by the groups of Bourne and Baldyga, other methods of representing the traverse growth of the feed stream due to ambient turbulent have also been proposed. E.g., Villermaux and David (1987) proposed a method wherein that the rate of growth of the reaction volume is assumed proportional to the volume of feed and the turbulent diffusivity. Expressions for the growth of reaction volume for pulse input of reactant and continuous addition are provided in the appendix.

2.4.4.2. Inertial-convective disintegration

Within the feed plume, the concentration eddies are progressively disintegrated from the large scales of concentration fluctuations (comparable to the integral scale, Λ_C) down to the Kolmogoroff scale, η. For this process, the characteristic time, τ_S, is given by

$$\tau_S \approx A\left(\frac{\Lambda_C^2}{\varepsilon}\right)^{1/3} \tag{2.45}$$

where, A is a constant whose value is approximately between 1 - 2. Comparison between τ_D (and τ_{Df}) and τ_S allows identification of a controlling mechanism for mesomixing. However, τ_S is not easily calculated. The difficulty in estimating τ_S from Equation (2.45) lies in the accurate determination of the integral length scale for concentration fluctuations. As the blob of fluid leaves the feed pipe, the initial concentration integral scale (Λ_{co}) undergoes relaxation in the ambient flow field containing the full spectrum of velocity eddies. Baldyga et al. (1997) have discussed some of the theories and the methods for estimating Λ_c.

The disintegration of large spots of contaminant (e.g. a blob of reactant B in reactant A) by inertial convective processes, down the concentration spectrum, is shown schematically in Figure (2.17). Baldyga and Bourne (page 596, 1999) describe this process as "a cascade in concentration spectrum where decreasing concentration scale conveys material towards scales of molecular diffusion". Molecular diffusion causes local homogenization of concentration forming a new spot on which the disintegration-micromixing process is repeated. This process of reduction in concentration fluctuations has been interpreted either as (i) breakup of blobs of pure, unmixed solution resulting in *erosive mixing* or as (ii) formation of small micromixing eddies within larger eddies, giving the *eddies in eddies* interpretation. Baldyga et al. (1997), Baldyga, and Bourne (page 597, 1999) give a list of references for these interpretations. Both interpretations of the inertial-convective mesomixing process give the same time constant for the process, τ_S, described earlier.

If the eddies in eddies interpretation is chosen as the representative mechanism of inertial-convective mesomixing, a mathematical model can be developed on the basis of the mechanism shown in Figure (2.18), reproduced from Baldyga et al. (1997). The figure shows segregated regions of reactant B in reactant A in a macroscopically well-mixed system, so that the average concentration of B in the system, X_{Bm}, is present uniformly throughout the reactor. The segregated regions or "islands" of B each have a composition X_B^e and the total volume fraction of the islands in the reactor is X_U, such that

$$X_{Bm} = X_U X_B^e \tag{2.46}$$

When the reactant B is added into the reactor, the islands are purely B, so the initial volume fraction of the islands, X_U, is equal to the volume fraction of reactant B, X_{B0}. As mixing proceeds, A is mixed into the islands because of which the island volume increases, even as X_B^e reduces. The key feature in the model for inertial-convective disintegration is the prediction of the rate of growth of these islands (see details in Appendix B):

$$\frac{dX_u}{dt} = \frac{X_u(1 - X_u)}{\tau_S} \tag{2.47}$$

If τ_S is constant then Equation (2.47) can be integrated to give $X_U = f(t)$, using the initial volume fraction of the islands, X_{B0}, which is equal to the volume fraction of pure B in the reactor. Equation (2.47) gives the rate of increase in the total volume of islands of B but the reaction takes place only in a small region within each island, where the A and B

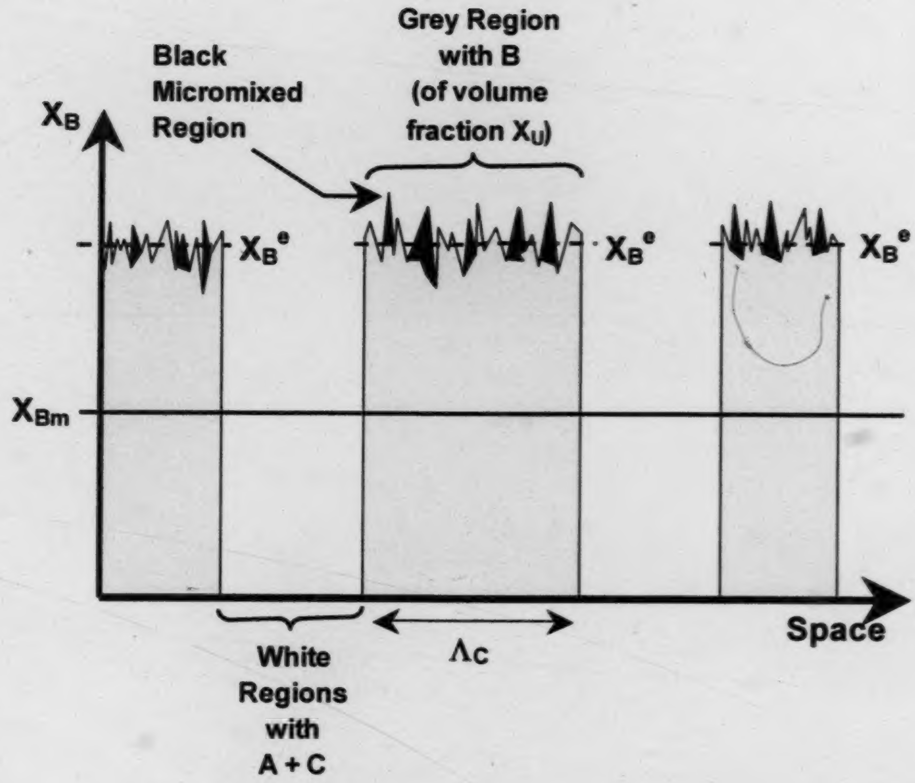
Grey Region with B (of volume fraction X_U)
Black Micromixed Region
X_B
X_B^e
X_B^e
X_B^e
X_{Bm}
Space
White Regions with A + C
Λ_C

Figure 2.18 A view of mesomixing: structure of partially segregated islands. The islands contain two regions: grey regions with only B and black micromixed regions where A, B and C are chemically homogeneous. The islands are immersed within the surrounding mixture (white) containing only A and C.

molecules are micromixed. The remaining issues in the model for inertial-convective disintegration is the development of expressions to account for the change in the micromixed volume (within the growing islands) and the mass transfer within this region to calculate the final product composition. Details of the model are given in Appendix B.

2.4.5. Hierarchy of Time Scales in Reactive Mixing

From the previous discussion in sections (2.2.1), (2.4.2). (2.4.3) and (2.4.4) on the relation between the rates of mixing and reaction and the rates of mixing at various scales, it can be concluded that the following conditions can exist for reactive mixing:

- $\tau_R > \tau_M$: Mixing is very fast. Product distribution is *controlled by the kinetics* of the reaction, which is the slowest process and the limiting step.
- $\tau_M > \tau_R$: Reaction is fast or instantaneous i.e. the rate of *mixing controls product distribution.* When this happens the following conditions can occur:
    a. $\underline{\tau_M \sim \tau_E > \tau_{meso}}$ ($\tau_{meso} = \tau_D$ for $\tau_D > \tau_S$ and $\tau_{meso} = \tau_S$ for $\tau_S > \tau_D$). In this regime product quality is *controlled by the rate of micromixing*, which is the slowest mixing step. The characteristic mixing time (τ_M) is given by Equation (2.39). Use the micromixing model to find the amount of byproduct formed.
    b. $\underline{\tau_M \sim \tau_{meso} > \tau_E}$. In this regime product quality is controlled by the rate at which concentration eddies are reduced to the size η or smaller by the process of mesomixing. Here, *mesomixing* is slower than micromixing and is therefore the *limiting step.* Two more regimes can be identified within the mesomixing limited regime:
        - $\underline{\tau_{meso} \sim \tau_D > \tau_S}$. The dispersion of the feed by the process of *turbulent dispersion* is the slowest step and is rate controlling. The characteristic mixing time (τ_M) is given by Equation (2.41). The byproduct yield can be estimated by using the turbulent dispersion model described in section (2.4.4)
        - $\underline{\tau_{meso} \sim \tau_S > \tau_D}$. The slowest step is the *inertial-convective* process of reduction of scale of the concentration eddies, down the concentration spectrum, to the size η and smaller where diffusion and reaction can

occur. The characteristic mixing time (τ_M) is given by Equation (2.45). Model the process using the inertial-convective model of mesomixing.

2.4.6. Sample Calculations Using Characteristic Mixing Time Scales

2.4.6.1. Estimation of the Controlling Mechanism as a Function of t_f

In the experiments corresponding to the data shown in Figure (2.3), as in most previous experiments on reactive mixing, the flow rate of the feed, Q_f, is so low that the feed momentum is negligible compared to the flow around the feed pipe where the average velocity is, say $\overline{U}$. When the feed stream leaves the feed pipe, it soon attains the velocity of the surrounding. The size of the fluid eddy is approximately Λ_C. Hence the volumetric flow rate of the feed stream can be related to its cross sectional area as follows:

$$Q_f = \frac{V_f}{t_f} \sim \pi \overline{U} \Lambda_C^2 \tag{2.48}$$

From Equations (2.45) and (2.48):

$$\tau_S \sim A\left(\frac{V_f}{\pi \overline{U} t_f} \cdot \frac{1}{\varepsilon}\right)^{1/3} \tag{2.49}$$

From Equations (2.39) and (2.49):

$$\frac{\tau_S}{\tau_E} \sim \left[A\left(\frac{V_f}{\pi \overline{U} t_f} \cdot \frac{1}{\varepsilon}\right)^{1/3}\right] \left[\frac{1}{17.3}\left(\frac{\varepsilon}{\nu}\right)^{1/2}\right] \propto \left(\frac{\varepsilon^{1/2}}{\overline{U}\, t_f}\right)^{1/3} \tag{2.50}$$

For a given power input in to the tank, as t_f decreases below a particular value (t_{crit}), τ_S starts to overtake τ_E and mesomixing becomes the relevant mechanism for mixing of reagents.

2.4.6.2. Estimation of the Functional Relationship Between t_{crit} and D

Baldyga and Bourne (page 738, 1999) continued the dimensional arguments of Equation (2.50) to show that the relationship between the critical feed time, t_{crit} and the impeller speed, D can be obtained from dimensional considerations also. When exact geometric similarity is maintained, D/T remains constant hence

$$D^3 \propto V_{Tank}$$

Also

$$V_f = \frac{V_{Tank}}{a}$$

Hence,

$$V_f \propto D^3 \tag{2.51}$$

The power input into the tank is related to the impeller speed and diameter,

$$\varepsilon \propto N^3 D^2$$

and since,

$$\overline{U} \propto V_{Tip} \sim ND$$

it follows that

$$\overline{U} \propto \varepsilon^{1/3} D^{1/3} \tag{2.52}$$

Using Equations (2.51) and (2.52), the mesomixing time scale in Equation (2.49) can be rewritten simply in terms of simply ε and D:

$$\tau_S \sim A\left(\frac{V_f}{\pi \overline{U} t_f} \cdot \frac{1}{\varepsilon}\right)^{1/3} \sim \left(\frac{D^3}{\varepsilon^{4/3} D^{1/3} t_f}\right)^{1/3} = \left(\frac{D^{8/3}}{\varepsilon^{4/3} t_f}\right)^{1/3} \tag{2.53}$$

And,

$$\frac{\tau_S}{\tau_E} \propto \left[\left(\frac{D^{8/3}}{\varepsilon^{4/3} t_f}\right)^{1/3}\right] \cdot \left[\left(\frac{\varepsilon}{\nu}\right)^{1/2}\right] \propto \left(\frac{D^{8/3}}{\varepsilon^{5/2} t_f}\right)^{1/3} \tag{2.54}$$

At the critical feed time, $\tau_S \sim \tau_E$, hence from Equation (2.54), $t_{crit} \sim D^{8/3}$ as reported in the experiments.

2.5. Concluding Remarks

This chapter has extensively reviewed the effects of mixing on the product distribution in the case of complex reaction. The main point are summarized below:

- The relative rates of mixing and reaction determine the mechanism (reaction kinetics or mixing dynamics) that governs product formation. This can be quantified with the Damköhler number.
- Turbulent mixing is a process involving numerous time and length scales. The scale at which the mixing occurs determine the predominant mechanism driving the process: inertial-convective disintegration of concentration eddies for scales > η and viscous-diffusive processes for scales < η. The time scale of the process of mixing at any one of these scales (micro or mesomixing) depends strongly on the rate of dissipation of the turbulent kinetic energy, ε. When product distribution is mixing limited, the step with the slowest rate of mixing governs the formation of products and byproducts.
- The flow field in a stirred tank is very inhomogeneous. The level of turbulence at any position varies widely from location to locations. Moreover, the level of turbulence at any position also depends on factors such as the impeller type, size, speed and the scale of the tank. Hence, byproduct yield is sensitive to any of these factors.

The observation and conclusions from the various sections of this chapter will be used extensively throughout the dissertation to explain results and gain insights from the observations.

Chapter 3

Surface Feed at High Velocity with PBTD

3.1. Introduction

It was seen in section (2.2.2.6) of Chapter 2 that introducing feed near the surface of a stirred tank reactor causes a significant drop in product quality owing to a mismatch between the requirement of intense mixing at the feed point and the turbulent flow characteristics close to the surface of the tank. The turbulence level is at its maximum close to the impeller but decays quickly in the impeller discharge, dropping to a low bulk value by the time the discharge stream meets the walls of the tank. For a standard down-pumping axial impeller, clearly defined mean circulation patterns develop only in the lower two-thirds of the tank while the top one-third (the surface region) remains largely inactive (Jaworski et al., 1991; Kresta and Wood, 1993; Fokema et al., 1994; Bittorf and Kresta, 2000 and Bhattacharya and Kresta, 2002). In this configuration reactants fed at the surface are exposed to very little turbulence, there is insufficient mixing and product quality suffers. In spite of this well documented drop in reactor performance, surface feed is often preferred over submerged feed pipes due to many operational difficulties associated with the later, some of which have been outlined in Chapter 1. Surface feed of reactants therefore continues to be a desirable configuration and the problem of high byproduct formation needs to be addressed effectively.

In the present chapter, one solution to the problem is evaluated: the reactant stream is fed with a high velocity at the liquid surface. This feed 'jet' has two promising attributes: it entrains reactants into the feed stream thus inducing additional mixing near the surface, and it also transports the reactants rapidly to the highly turbulent impeller region. The combined effect of higher turbulence levels in the jet and fast transport down to the impeller is expected to offset the lack of ambient turbulence near the surface and improve performance. Another approach to the problem is to employ an up-pumping axial impeller to enhance turbulence near the liquid surface. Experiments were conducted for the later configuration also but the results are deferred to Chapter 4, this chapter being devoted solely to experiments with high velocity feed at the surface.

For the high velocity feed configuration results are presented for two nozzle sizes operated over a wide range of flow rates, encompassing (i) high feed velocities as well as the (ii) slower operation in the traditional mesomixing, and micromixing regimes in the laminar limit. Some results are also reported for plunging feed jets. The results provide new information about the challenges faced in maintaining product quality when using surface feed and a detailed analysis of the results leads to a method for evaluating the operational limitations of this approach.

3.2. Theory and Analysis

The effects of very short feed times or very high feed flow rates on mixing limitations and thence on byproduct formation and the fluid dynamic behaviour of the high velocity feed stream as it progresses through the tank are the two aspects which need to be assessed when analyzing reactor performance. These points are reviewed below.

3.2.1. Effect of Feed Time

As discussed in Chapter 2, studies (Bourne and Thoma, 1991; Baldyga and Bourne, 1992; Baldyga et al., 1993; Baldyga et al., 1997) have shown that there is a sharp increase in byproduct yield when the reactant feed time is reduced below a critical value due to mesomixing limitations. In the mesomixing-limited regime, byproduct yield is strongly affected by the feed flow rate with a significant increase in byproduct formation with an increase in feed flow rate or a decrease in feed time. The maximum extent to which byproduct yield increases and the behaviour of the feed stream as the feed time is continuously decreased is however largely unanswered. The present study explores the effect of very high feed velocity with much higher feed flow rates on byproduct formation. The feed times used in this study drop down to values as small as 20s, much lower than the minimum feed time used in most previous studies. The regime of operation is therefore shifted out of the laminar flow regime. When the feed velocity is increased sufficiently, it is expected that entrainment and mixing will be enhanced in the feed zone irrespective of the ambient levels of turbulence. Moreover, higher feed stream velocity and momentum ensures that the reactants are conveyed faster to the impeller region before too much reaction has occurred. Bourne and Hilber (1990) reported a reduction in X_Q when the feed velocity was sufficiently high (Figure 2.5, Re_f between 1000 and 2000). In other experiments involving jet reactors Baldyga et al. (1994) have also shown the benefits of high feed stream velocities.

3.2.2. Turbulent Axisymmetric Jets

The high velocity feed stream is expected to have features similar to an axisymmetric jet, with close similarities near the liquid surface and deviations near the impeller. There is essentially no active circulation and very little turbulence near the liquid surface in the tank. Any turbulence and flow in the tank will tend to augment the energy in the feed jet, not decrease it, so the jet analysis is the worst case scenario for the top third of the tank. As the jet closes in on the impeller there would be differences in behaviour from the classical description of a fully turbulent jet because of the strong, non-homogeneous ambient flow field existing in this region. Close to the impeller, the turbulent jet analysis therefore becomes a limiting case and can be expected to deviate from reality. However, the well-established characteristics of a classical turbulent jet can still be used as a starting point for an approximate, operational description of the high velocity feed jet.

The axisymmetric turbulent jet has been widely used, firstly as a benchmark for validating numerical codes and secondly as a prototype of free turbulent flow to gain insights into the physics of turbulence. A huge volume of publications is available covering experimental research, theoretical analysis and mathematical modelling. Literature data include the older studies by Wygnanski and Fiedler (1969) and newer data of Panchapakesan and Lumley (1993a) and (1993b), point velocity measurements by Hussein et al. (1994) and particle image velocimetry and planar laser induced fluorescence data by Fukushima et al. (2002). Details on modeling are available in the reviews and discussions of Tennekes and Lumley (1972), Hinze (1975), Rajaratnam

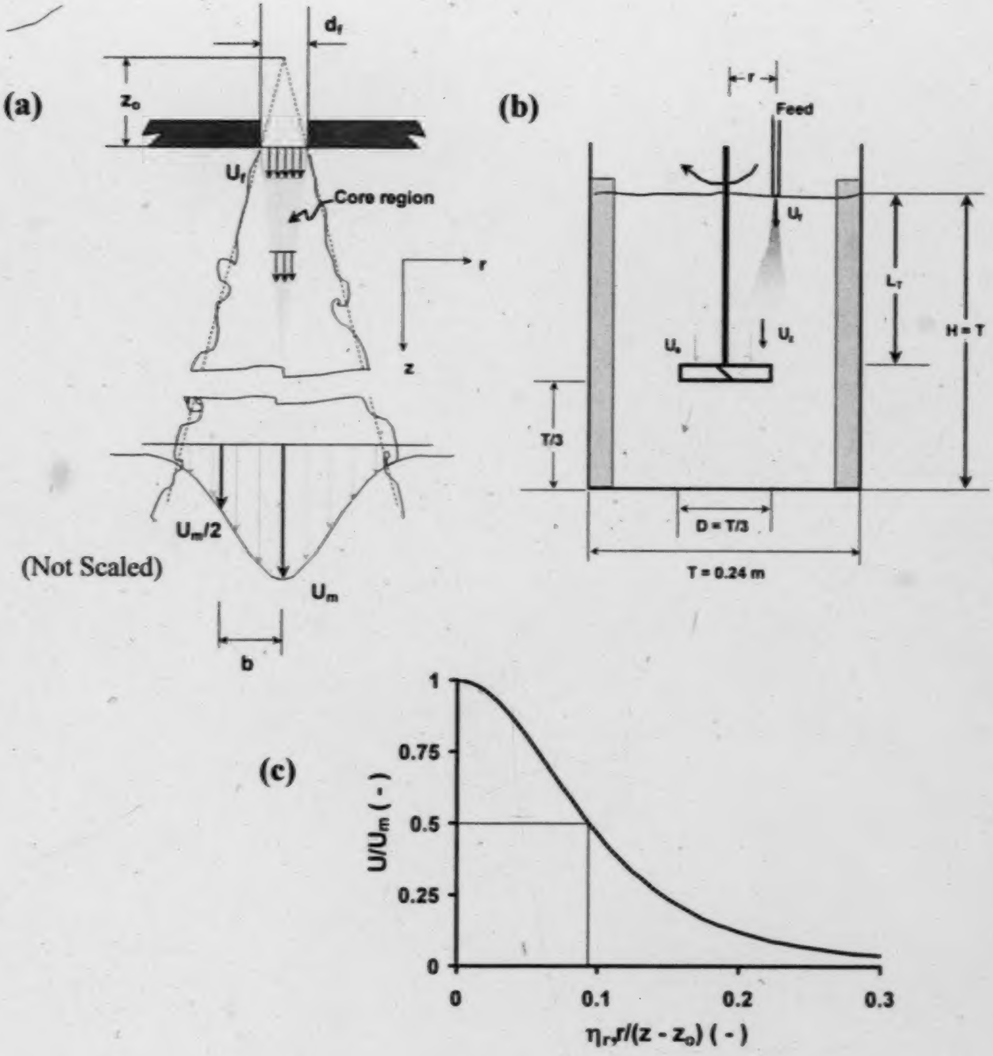
(a)
d_f
z_o
U_f
Core region
r
z
U_m/2
(Not Scaled)
U_m
b
(b)
r
Feed
U_f
L_T
H = T
U_s
U_z
T/3
D = T/3
T = 0.24 m
(c)
1
0.75
0.5
0.25
0
0.1
0.2
0.3
U/U_m (-)
η_r,r/(z - z_o) (-)

Figure 3.1 (a) Schematic of free, axisymmetric jet (b) Schematic of feed jet in stirred tank ($U_z = U_m$) (c) Self-similar profile of axial velocity in a fully turbulent axisymmetric jet (Equation 3.55)

(1976), George (1989), Boersma et al. (1998) and Pope (2000). From this large body of information a few salient features, central to the description of a turbulent jet and more importantly to the analysis of the high velocity feed jet, are selected and summarized below:

- A schematic of an axisymmetric turbulent jet is shown in Figure 3.1a. The jet is introduced from a small round opening and propagates in the z direction. Very close to the nozzle the axial velocity in the jet remains constant and equal to the nozzle velocity, U_f. This is the 'core region' of the jet and extends to about $5d_f$. Further down, the jet slows down as it travels away from the nozzle while it spreads out laterally by entraining fluid from the surroundings. At any downstream location the streamwise velocity, U, is maximum at the center (U_m) and gradually reduces in the radial direction to asymptotically reach the velocity of the external/ambient stream. The radial position at which $U = U_m/2$ is called the jet half-width, b.
- A review of the literature on turbulent jets shows that the Reynolds number at which the jet becomes fully turbulent is not explicitly defined. This could partly be related to the fact that instabilities can cause a jet with even relatively small Reynolds number at the nozzle to ultimately become unstable. Most experiments that produced reliable, consistent data have however reported a nozzle Reynolds number, $Re_f > 1\times10^4$ (Table 3.1) and this has been chosen as the limit for a fully turbulent jet in the present study. The laminar limit of the jet has been defined at $Re_f < 300$ (Boersma et al., 1998).
- For a fully turbulent jet, the radial profile of the axial velocity is found to be self-similar, that is, if properly scaled the radial velocity profiles collapse into a single curve irrespective of the axial location at which this profile is taken. An example of this self-similar profile with the proper scaling for U and r is shown in Figure 3.1c. The similarity profile can be derived from the Reynolds averaged Navier-Stokes equations once boundary layer and other simplifying assumptions are made (Hinze, 1975; see also Appendix D). The general form of the solution is:

$$\frac{U}{U_m} = f(\eta) = \frac{1}{\left(1+\phi\eta_r^2\right)^2} \qquad (3.55)$$

Table 3.1 **Summary of axisymmetric jet experiments reported in the literature.**

Reference	Reynolds Number		Self-similar region	Emphasis of research
	Laminar	Turbulent		
Jayanti (2001)		> 2x10^4		CFD simulation to characterize jet mixing in a tank
Pope (2000)		1x10^4	x/d > 30	Define self-similar profile of different quantities
Fukushima et al. (2000)		2x10^3	Experiments were conducted at x/d ~ 20 to 140	Scalar and velocity measurements using PIV and LIF
Boersma et al. (1998)	300	2.4x10^3	U: x/d > 10 u: x/d > 35	Test universality of symmetry solution through DNS simulation
Grenville and Tilton (1996)		> 1x10^4		Determine blend time correlation for a jet mixer
Hussein et al. (1994)		9.55x10^4	Experiments were conducted at x/d ~ 30 to 100	Measurement of mean and turbulent quantities
Baldyga et al. (1994)		1.6x10^4 to 12.8x10^{4**}		Determine byproduct formation and liquid dispersion in a jet reactor
Panchapakesan and Lumley (1993) - b		Same as above (?)	Experiments were conducted at x/d ~ 50 to 120	Measurement of mean velocity and turbulence quantities in a He jet
Panchapakesan and Lumley (1993) - a		1.1x10^4	Experiments were conducted at x/d ~ 30 to 150	Measurement of mean velocity and turbulence quantities in an air jet
Tennekes and Lumley (1989)			Self-preserving when U_zx/v > 4x10^5	Define self-similar profile of different quantities
Wygnanski and Fiedler (1969)		Experiments conducted at Re_f ~ 10^5	Self-preserving flow may be realized for x/d > 70	Measuremnt and analysis (mean and turbulence quantities) of self-preserving jets
Fox and Gex (1956)	100	2x10^3		Determination of jet and properller mixing times for single phase liquid blending
Fossett (1951)		> 4.5x10^{3*}		Seminal paper on jet mixing

* Does not present this as a turbulent jet, but shows that mixing time is independent of Re_f in this range

** The limit of fully turbulent jet has been given in the text as 1x10^3

A value of $\phi = \frac{\sqrt{2}-1}{S^2} = 46.8$ can be used in Equation (3.55, Pope, 2000). Many new studies (George, 1989; Hussein et al., 1994; Boersma et al., 1998) have argued against the implicit assumption in Equation (3.55) that the self-preserving state is independent of the initial conditions (see also Appendix D). It has been shown that this is not strictly true and instead of the universal similarity assumed in the original theory, there is actually a dependence of the jet growth on the initial conditions of the nozzle. In the present investigation, the original similarity theory is assumed to be valid as a first approximation.

- The mass of the jet increases in proportion to the reduction in its velocity to conserve momentum of the jet (J) as it travels outwards. External forces in the form of gravity and the static head in the tank can cause some changes in J, however at high velocities the magnitude of these forces is expected to be relatively small.
- According to the theory of self-similarity, far from the nozzle ($z/d_f > 30$) U_m decays linearly with the distance from the nozzle (z in Figure 3.1a) and spreads linearly with distance traveled. Expressions for U_m and b are as follows:

$$\frac{U_m}{U_f} = \frac{Bd_f}{(z - z_o)} \qquad (3.56)$$

$$b = S(z - z_o) \qquad (3.57)$$

In Equations (3.56) and (3.57) the proposed values for the parameters are B = 5.8, S = 0.094 and $z_o = 4d_f$ (Pope, 2000).

- The flowrate of the jet at any axial position z can be found by integrating U over the jet cross-section, πR_{jet}^2. If the radial extent of the jet is defined as $R_{jet} = \beta b$, then the jet flow rate is obtained as:

$$Q(z) = \int_0^{\beta b} (2\pi r dr) U \qquad (3.58)$$

The similarity profile in Equation (3.55) shows that the axial velocity changes sharply in the inner region of the jet, reducing to just 14% of its peak value by the time it has extended to r = 2b. When integrated with β = 2, Equation (3.58) gives:

$$Q(z)=\frac{4\pi U_m b^2}{1+4\left(\frac{\phi}{(z-z_o)^2}\right)b^2} \qquad (3.59)$$

or, $$Q(z)=\frac{4\pi BS^2}{\left(1+4\phi S^2\right)}U_f d_f\left(z-z_o\right)=0.24U_f d_f\left(z-z_o\right) \qquad (3.60)$$

Equation (3.60) can be rearranged to express the volumetric flow of the jet at distance z from the nozzle in terms of the volumetric flow at the nozzle, Q_f:

$$Q(z)=0.31\frac{Q_f}{d_f}\left(z-z_o\right) \qquad (3.61)$$

Baldyga et al (1994) reported:

$$Q(z)=0.23\frac{Q_f}{d_f}z \qquad (3.62)$$

Although Equation (3.62) is obtained from experiments, its form and value are approximately equal to Equation (3.61) that is obtained solely from theoretical reasoning. Equation (3.62) can be reproduced from Equation (3.58) by assuming $\beta = 1.5$ and $(z - z_o) \sim z$.

As stated earlier, some characteristics of the feed jet in the stirred tank are expected to be quite different from that of a classical turbulent jet. Assumptions are therefore made when the later is used in an analysis of the operational limits of high velocity feed. These assumptions are:

- A jet in a confined space behaves similarly to a classical free jet in an infinitely large environment
- U profiles in the jet are undisturbed by the very heterogeneous velocity field surrounding it. This is clearly a worst case assumption which will not be valid close to the impeller.
- The analytical solution resulting in Equation (3.55) is only possible when the velocity of the jet is much larger than the velocity of the external stream. This condition implicit in Equation (3.55) will not hold near the suction of the impeller where the surrounding velocities are quite high while the jet velocity is itself relatively low. This is clearly a conservative assumption.

3.2.3. Operational Limits for High Velocity Surface Feed

A relationship between the design variables feed time (t_f), feed pipe diameter (d_f) and the impeller speed (N) can be developed using the symmetry solution for an axisymmetric jet, mixing requirements and the knowledge of the flow field near the impeller suction. Keeping in view the main factors that can improve reactor performance (highest possible levels of turbulence and quick transport to the impeller) the primary objective here is to introduce the feed stream into the tank at a high speed so that it forms a fast moving, turbulent jet. Seven design constraints can be identified based on operational limitations and the requirements of a turbulent jet:

Constraint 1. $Re_f \geq 1x10^4$, the Reynolds number at which the feed jet is fully turbulent:

$$Re_f = \frac{U_f d_f}{\nu_f} \geq 1x10^4 \tag{3.63}$$

In semi-batch operation, the volume of feed (V_f) is fixed a-priori, being dependent only on the tank volume (V_T) and the reaction kinetics (stoichiometry and concentration of the reagents). U_f can therefore be related simply to d_f and t_f:

$$U_f = \frac{Q_f}{A_f} = \frac{V_f/t_f}{\pi d_f^2/4} \tag{3.64}$$

Combining Equations (3.63) and (3.64):

$$d_f t_f \leq 1.27x10^{-4} \frac{V_f}{\nu_f} \tag{3.65}$$

Equation (3.65) gives the relationship between d_f and t_f needed to satisfy Constraint 1.

Constraint 2. $\Delta P_f < \Delta P_{pump}$. The pressure drop across the feed nozzle is:

$$\Delta P_f \approx K_L \frac{\rho_f U_f^2}{2} \tag{3.66}$$

where $K_L = 1.5$ for contraction into and expansion out of the nozzle (Young et al., 2001). This head has to be supplied by the feed pump ($\Delta P_f = \Delta P_{pump}$). Equations (3.64) and (3.66) together give the minimum feed pipe diameter, d_{min} that will allow pressure drop across the nozzle to be within the required limits (ΔP_{pump}):

$$d_{min} = \left[\frac{V_f}{t_f} \sqrt{1.22 \frac{\rho_f}{\Delta P_{pump}}} \right]^{0.5} \qquad (3.67)$$

Once the reactor scale has been decided and the pump has been selected d_{min} is therefore only a function of t_f.

Constraint 3. $U_z \sim U_s$. The feed jet can overshoot the impeller if the maximum feed jet velocity in the vicinity of the impeller (U_m) is larger than the velocity at the suction of the impeller (U_s). This is detrimental to product formation because the most turbulent region of the tank is bypassed. While U_s can be obtained from measurements or CFD simulations it is more difficult to estimate U_z. As a first approximation, U_z can be calculated from the similarity solution of a fully turbulent jet, Equation (3.56). As stated earlier, this approach will give only a first approximation since the ambient and the jet velocities are similar in magnitude and the similarity solutions are no longer truly valid in this region.

Constraint 4. $\dot{n}_A \geq \dot{n}_B$. $\dot{n}_A$ and $\dot{n}_B$ are the molar flow rates at which A (HCl) and B (NaOH) are brought to the reaction zone. In this constraint the moles of A brought to the reaction zone by the ambient circulation are equated to the moles of B brought into this region by the feed jet. This ensures that there are no stoichiometric limitations due to insufficient A reaching the reaction plume and corresponds to the Convective Stoichiometric Limit (CSL) proposed by Anthieren (section 4.5.2, page 267, 2004). This constraint, along with Constraint 3 determines the relation between the feed conditions (pipe diameter, feed time) and the impeller speed.

Constraint 5. $Re_I \geq 2x10^4$. This constraint ensures that the impeller is fully turbulent. It is always met when $N \geq 188$ rpm for the fluid (water) and geometry ($T = 0.24m$; $D = T/3$) used for this study. The constraint is used to calculate the lowest speed at which the impeller can be operated (N_{min}).

Constraint 6. $N < N_{max}$. The maximum impeller speed (N_{max}) is determined from operational and mechanical considerations. These include

(i) The speed at which air starts being entrained into the tank from the open liquid surface (N_E, = 763 rpm for the present tank and impeller geometries) and

(ii) The maximum allowable torque for the stirrer motor.

Constraint 7. $d < d_{max}$. The maximum feed pipe diameter is determined by the spatial constraints of the tank and also by the fact that the feed time will become unreasonably small for very large pipe diameters in semi-batch operation with fixed feed and tank volumes.

Constraints 1 to 7 can be used to develop a relation between the design variables t_f, d_f and N for a given tank geometry (T and D) and feed volume (V_f). In most cases, the ratio d_f/T will be reasonably small and Constraint 7 is not limiting. The remaining constraints provide a quantitative relationship between the feed velocity, feed time and the feed pipe diameter as follows:

1. ΔP_{pump} and V_f are set based on the pump selection/material limitation, stoichiometry, reactor volume and desired concentration.
2. For a given feed pipe diameter, d_f, the upper and lower limits for t_f are obtained from Equations (3.65) and (3.67). Equation (3.65) gives the upper limit for t_f (t_{max}) above which the feed stream velocity is too low and Constraint 1 is no longer satisfied:

$$t_{max} = 1.27\text{x}10^{-4}\,\frac{V_f}{v_f d_f} \tag{3.68}$$

while Equation (3.67) gives the lower limit for t_f (t_{min}) below which the nozzle pressure drop is too large and Constraint 2 is not met:

$$t_{min} = \frac{V_f}{d_f^2}\sqrt{\frac{1.22\rho_f}{\Delta P_{pump}}} \tag{3.69}$$

Since t_{min} and t_{max} vary differently with d_f, a change in d_f causes a change in the operating range (t_{min} to t_{max}) of t_f. This is shown in Figure 3.2a for the operating conditions given in Table 3.2. When d_f is too small, operation is not possible since t_{min} is too large and it is impossible to meet Constraint 2 for the given

ΔP_{pump}. For larger d_f both constraints are met when t_f is within the shaded region but now the feed time is reduced significantly increasing the risk of stoichometric limitations. Equations (3.68) and (3.69) can be equated to obtain the minimum operable feed pipe diameter:

$$d_f = 8.9x10^3 v_f \sqrt{\frac{\rho_f}{\Delta P_{pump}}} \qquad (3.70)$$

The feed time for this d_f can then be found using d_f and either Equations (3.68) or (3.69). Two comments need to be made about the utility of Equation (3.70). Firstly, the available operating zone for d_f and t_f can be changed by changing the available pump head. Hence, if there are additional constraints that need to be satisfied then these will also be used in the selection of ΔP_{pump} along with the other issues of pump characteristics, cost analysis and the material of construction. Secondly, according to Equation (3.70) there is no effect of the scale of the reactor on the minimum feed pipe diameter, since it is determined solely by the conditions at the feed nozzle. A change in scale (V_f) will however affect t_f and the width of the operating band ($t_{max} - t_{min}$, see Equations 3.68 and 3.69). If the batch time is fixed a-priori due to other considerations then a change of scale can indirectly affect d_f.

3. Once t_f and d_f have been determined, U_f is obtained from Equation (3.64). Next the feed jet velocity near the impeller suction (U_s) is calculated using Equation (3.56) and the geometry in Figure 3.1b:

$$U_z = \frac{BU_f d_f}{(L_t - 4d_f)} \qquad (3.71)$$

4. Next, the impeller speed ($N_{Constraint\,3}$) required to satisfy Constraint 3 is obtained by equating U_z and U_s. The suction velocity at the impeller is (CFD simulations from Bhattacharya and Kresta, 2002):

$$U_S = 0.25U_{tip} = 0.25\pi ND \qquad (3.72)$$

Equating Equations (3.71) and (3.72) (i.e. $U_S = U_z$):

$$N_{Constraint\,3} = 1.27\frac{BU_f d_f}{(L_t - 4d_f)D} \qquad (3.73)$$

5. The impeller speed required to satisfy Constraint 4, $N_{Constraint\,4}$, is then obtained. In order to arrive at the relationship between $N_{Constraint\,4}$ and t_f it is needed to develop expressions for (1) the molar flow rate of A pumped into the reaction zone by the impeller and (2) the molar flow rate of B exiting the feed nozzle. This can be achieved as follows. The pumping rate for an impeller in a stirred tank is given by Equation (2.11):

   $$Q = N_Q N D^3$$

   Hence, the molar flow rate of A passing through the impeller is:

   $$\dot{n}_{A,Imp} = C_A Q = C_A N_Q N D^3 \qquad (3.74)$$

   Of this, only a fraction is in active circulation at the top of the tank close to the the reaction zone:

   $$\dot{n}_A = \alpha\, \dot{n}_{A,Imp} \qquad (3.75)$$

   The quantity 'α' is a fraction less than one and has to be determined experimentally. In terms of the impeller pumping rate, Constraint 4 is therefore:

   $$\alpha\, \dot{n}_{A,Imp} \geq \dot{n}_B \qquad (3.76)$$

   Note that the concentration of A is time dependent, changing from an initial value of C_{AO} to a much lower value by the time the experiment is completed. For the equimolar quantities of reagents used in this investigation, this implies that A will be depleted and the reaction will be stoichiometrically limited in the last few seconds of the feed time, t_f. $C_A = C_{AO}$ represents the converse, best case limit where B is the limiting reagent and A is present in large excess. In the following calculations $C_A = C_{AO}$ has been used and α is to be determined experimentally.

   The molar flow rate of B into the reaction zone is equal to the molar flow rate of B introduced through the feed:

   $$\dot{n}_B = C_B Q_f = \frac{C_B V_f}{t_f} \qquad (3.77)$$

   Thus from Constraint 4 and Equations (3.75) and (3.77), the limiting expression for $N_{Constraint4}$ is:

$$N_{\mathrm{Constraint\,4}} = \left(\frac{C_{BO}}{C_{AO}}\right) \cdot \frac{1}{N_Q D^3} \cdot \frac{V_f}{\alpha t_f} \qquad (3.78)$$

In the present investigation $C_{BO} = 50C_{AO}$, and the experimentally determined value of α was about 1/6, so

$$N_{\mathrm{Constraint\,4}} = \frac{300}{N_Q D^3} \cdot \frac{V_f}{t_f} \qquad (3.79)$$

The larger of the two speeds ($N_{\mathrm{Constraint\,3}}$ or $N_{\mathrm{Constraint\,4}}$) determines the impeller speed (N) that is required.

6. Then Constraint 5 is verified:

$$Re_I = \frac{N^2 D}{\nu_T} \geq 2x10^4 \qquad (3.80)$$

7. And finally Constraint 6 is verified

$$N < N_{max} \qquad (3.81)$$

Equation (3.68) to (3.81) can be used to design the feed pipe, estimate the impeller conditions, and clarify that all constraints are met once the tank geometry, the reaction kinetics and the reagent concentrations are known. In the present study, the third Bourne reaction was chosen since it is a suitable reaction scheme for the turbulence levels in the tank. The concentration of the reagents, volume of feed, the tank and impeller geometries and the fluid properties are tabulated in sections (a), (b) (c) and (e) of Table 3.2. A gear pump, able to produce 75psig maximum pressure was available. With these experimental conditions a feed pipe was designed and N calculated using Equations (3.68) to (3.81). Sample calculations are shown in Table 3.3. The calculations show that the impeller speed required to satisfy Constraint 3 and Constraint 4 is very large and consequently Constraint 6 is not met. A closer look reveals that Constraint 6 will often be the critical factor determining operability. This is illustrated graphically in Figure 3.2b where N obtained from Equation (3.73, i.e. the case where $N = N_{\mathrm{Constraint\,3}}$) and calculated at t_{min} and t_{max} (Equations 3.68 and 3.69, corresponding to the limits of the shaded region in Figure 3.2a) are shown for various feed pipe diameters. The operable region is the clear zone in the lower right of the figure bounded by $N < N_{max}$ at the top, $N > N_{min}$ at the

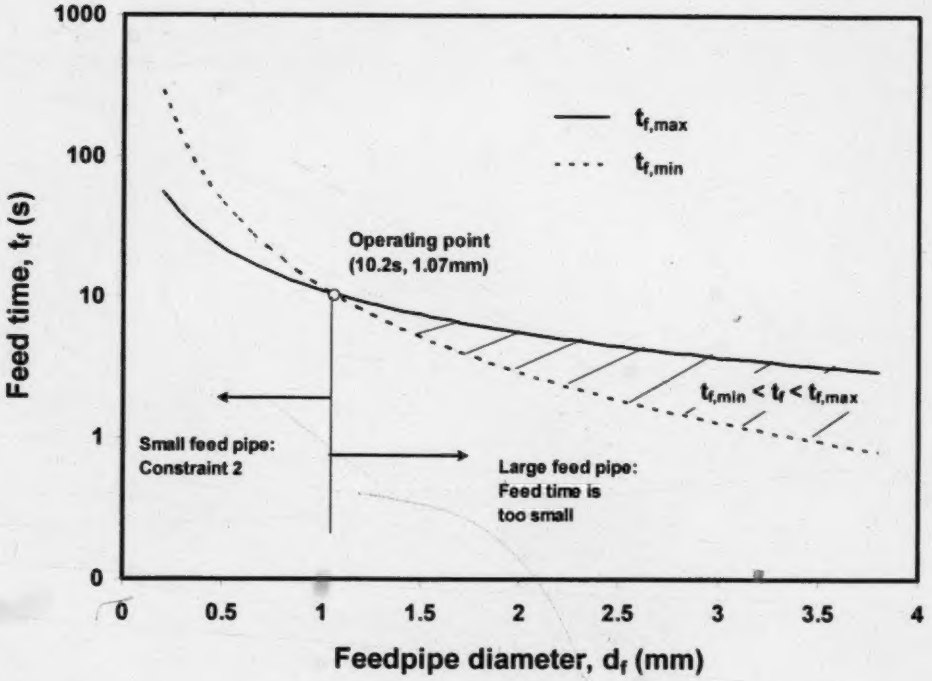

Figure 3.2a Operating range for a fully turbulent feed jet

Table 3.2 Experimental conditions

a)	Tank:			
	Geometry:	Flat bottomed, $H = T = 0.24$m		
	Baffles:	Square, $W = T/10$		
	L_t:	0.14 m		
b)	Concentration of reagents:			
	Sodium hydroxide:	4500 moles/m^3 ($V_f = 1/50V_{tank}$)		
	Hydrochloric acid:	90 moles/m^3		
	Ethyl chloroacetate:	90 moles/m^3		
c)	Impeller:			
	Type:	Pitched blade turbine		
	Diameter:	$D = T/3$		
	Clearance:	$C = T/3$		
	N_Q	0.79 (fully turbulent)		
	P_O	1.27 (fully turbulent)		
	Speed:	252rpm (separate set of experiments at 375 and 500rpm)		
	Da_{av}	0.24 at 252rpm (0.14 at 375rpm and 0.09 at 500rpm)		
	θ	10.2s at 252 rpm (6.9s at 375rpm and 5.2s at 500rpm)		
c)	Feed pipe:			
	Diameter:	0.762 and 3mm		
	Feed time	19.8 to 537s (0.762mm) and 19.8 to 3006s (3mm)		
	Re_f:	273 to 7606 (0.762mm) and 12 to 1866 (3mm)		
	ΔP_{pump}	75psig		
c)	Fluid properties (at 20 to 22°C):			
		Density (kg/m^3)	Kinematic viscosity (m/s^2)	Suraface tension (N/m)
	Feed:	~1160	$2.5\text{x}10^{-6}$	~ 81.6
	Tank:	~1000	$1\text{x}10^{-6}$	

Table 3.3 **Sample calculation for high velocity feed. In these calculations d_f, t_f and N are estimated so that Constraints 1 to 4 are all satisfied. Conditions as in Table 3.2.**

1.	Given: $V_T = 10.97\text{x}10^{-3}$ m^3 and $V_f = V_T/50$. So, $V_f = 2.19\text{x}10^{-4}$ m^3.		
	$\Delta P_{pump} = 75$psi or 517 Kpa		
2.	Find t_f and d_f, so that Constraints 1 and 2 are satisfied		
	$d_f = 1.07$ mm	(Equation 3.70)	
	$t_f = 10.21$s	(Equation 3.68)	
	$U_f = 23.89$ m/s	(Equation 3.64)	
	$Re_f = 1.02\text{x}10^4$	(Equation 3.63)	- Constraint 1 satisfied)
	$\Delta P_f \sim 73$ psi	($\Delta P_f < \Delta P_{pump}$,	- Constraint 2 satisfied)
3.	Estimate velocity of feed jet close to the impeller suction		
	$U_z = 1.09$ m/s	(Equation 3.71)	
4.	Calculate impeller speed required to satisfy Constraint 3		
	$N_{Constraint\ 3} = 1043$ rpm	(Equation 3.73)	
5.	Calculate impeller speed required to satisfy Constraint 4		
	$N_{Constraint\ 4} = 954.5$ rpm	(Equation 3.79)	
6.	Select impeller speed and verify Constraint 5		
	$N = N_{Constraint\ 3}$ ($N_{Constraint\ 3} > N_{Constraint\ 4}$		- Constraint 3 satisfied; - Constraint 4 satisfied)
	$U_{tip} = 4.37$ m/s, $U_s = 1.09$ m/s	(Equation 3.72)	
	$Re_I = 1.11\text{x}10^5$	(Equation 3.80	- Constraint 5 satisfied)
5.	$N_{max} = N_E = 763$ rpm. Hence, $N > N_{max}$ and Constraint 6 is *not* satisfied.		

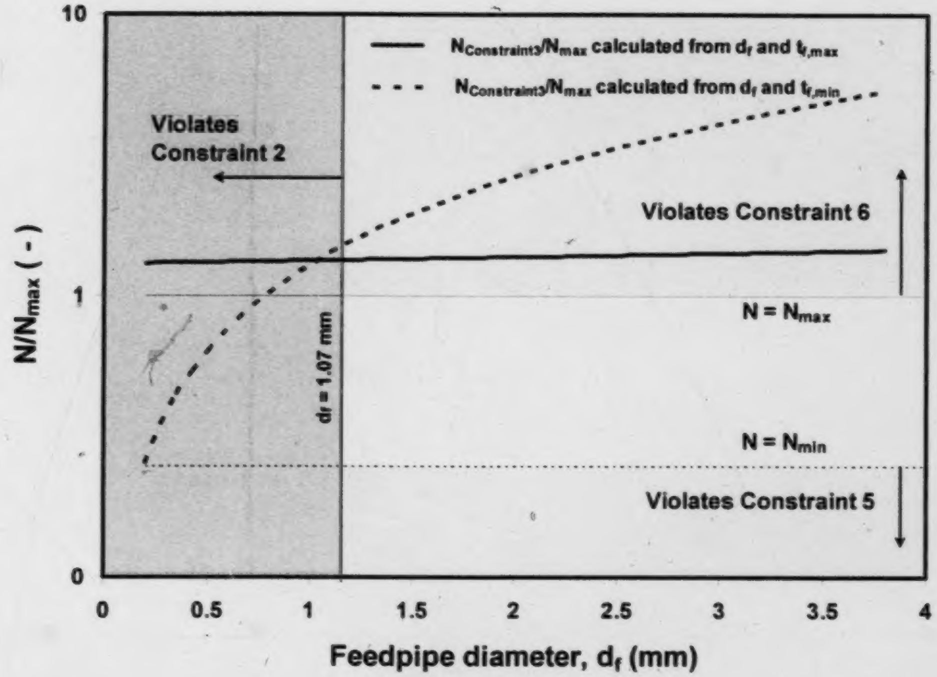

Figure 3.2b **In the small scale it is difficult to operate the impeller while satisfying all constraints (T = 0.24m, D/T = 1/3).**

bottom and $d_f > d_{min}$ in the left. It is evident that it is impossible to keep $N < N_{max}$ with $N_{max} = N_E$. Similar results are obtained (not shown) even when Constraint 4 is controlling. Constraint 6 could therefore seriously restrict the operability of the system if there is a restriction on the maximum impeller speed. Operation at these high speeds would in any case lead to the consumption of large amounts of power. This could severely affect performance at high feed velocities for semi-batch operation. Note however, that the above analysis is ultimately based on the stoichometric limit and the requirement that $Re_f > 1 \times 10^4$ for the feed stream to be fully turbulent. As noted earlier, this limit on Re_f is not very well defined in the literature. Since analysis in the transitional flow regime is not possible, the best method to check the limit and also study reactor performance in the high velocity feed mode is to conduct experiments. Moreover, while it may be difficult to achieve fully turbulent conditions in the feed it is nevertheless possible to convect reactants rapidly to the turbulent impeller region and cause an improvement in performance. It is necessary to know if such an improvement is indeed possible and whether it can effectively limit the maximum amount of byproduct formed.

3.3. *Experimental*

The third Bourne reaction (Table 2.1) was used to test the effect of high velocity surface feed on the mixing rate and byproduct formation:

$$\begin{aligned} &NaOH(B) + HCl(A) \xrightarrow{k_1} NaCl(P) + H_2O(P_1) \\ &NaOH(B) + CH_2ClCOOC_2H_5(C) \xrightarrow{k_2} CH_2ClCOONa(Q) + C_2H_5OH(Q_1) \end{aligned} \tag{3.82}$$

This scheme can be used to determine the severity of mixing limitations from the amount of byproduct (Q or Q_1) formed when reactant B (sodium hydroxide) is added in limiting quantities to a mixture of A (hydrochloric acid) and C (ethyl chloroacetate). Details of the reaction scheme and its kinetics are available in Chapter 2.

3.3.1. Determination of Byproduct Yield

The byproduct yield is defined either in terms of the amount of ester reacted ($X_{Q,Ester}$) or the amount of ethanol formed ($X_{Q,Ethanol}$; Equation 2.6). Since the stoichiometric coefficients in the Bourne third reaction are all unity, $X_{Q,Ethanol}$ is theoretically equal to $X_{Q,Ester}$. Mass balances can therefore be checked by comparing the byproduct yields obtained by the two methods. Yu (1993) used the deviation between the two quantities:

$$\Delta\% = \frac{\mathrm{abs}\left(X_{Q,Ethanol} - X_{Q,Ester}\right)}{\left(X_{Q,Ethanol} + X_{Q,Ester}\right)} \times 100 \tag{3.83}$$

as a check of mass balance and reported an average deviation of 3.2% from 406 experiments. In the present study, the average deviation from 198 experiments was 4%. While either form of X_Q can be used to report results, it was found that measurements were more accurate and there was less variation in the data (Table 3.4) when the byproduct yield was reported in terms of the amount of ethanol formed. Results are presented here using the later definition:

$$X_Q = \frac{\text{amount of } Q_1 \text{ formed}}{\text{moles of A added}} = \frac{(V_T + V_f)C_{Q_1}}{V_f C_A} \tag{3.84}$$

3.3.2. Determination of Chemical Concentration

Gas chromatography was used to measure the concentration of ester and ethanol in the samples of the liquid mixture collected from the reactor. Measurements were made in a HP-5890 gas chromatograph with a fused silica, capillary column from Supelco and the raw data was analyzed by a HP-3393A integrator. The settings used for the column and integrator are tabulated in Table 3.5.

The gas chromatograph was first calibrated with an internal standard which is necessary to minimize measurement errors. 2-butanone was used as the internal standard. Calibration consisted of the following steps:

1) An aqueous solution of ester (or ethanol) with a known concentration was prepared by mixing predetermined amounts of water and the chemical. Initial experiments showed that the preparation of aqueous solution of ester in glass bottles caused errors in measurement, with the measured values being consistently lower than the actual amounts even when no reaction product was indicated in the resulting

Table 3.4 Variability in the results when byproduct yield is calculated in terms of the amount of ethanol formed or the amount of ester reacted for the case of PBTD with feed at the surface with a 3mm nozzle and N = 252 rpm.

Feed Time (s)	Number of Repeats	Std. Deviation/Mean (%)	
		$X_{Q,Ethanol}$	$X_{Q,Ester}$
50	3	2.5	26.7
70	3	1.4	28.2
80	2	5.6	6.7
90	2	1.8	3.6
100	2	2.7	26.6
150	2	1.5	5.8

Table 3.5 Parameter settings and conditions used for the gas chromatograph.

Gas Chromatograph	
Model	- Hewlett Packard – 5890
Column Type	- Supelco SPB-1000 (Column # 16171-01B) - Capillary column, 300m x 0.53mm with a film thickness of 0.5 µm
Detector type	- Flame Ion Detector (FID)
Gas Flow Rates	- Carrier gas (helium): 25.2 ml/min - FID gas (hydrogen): 33.8 ml/min - FID gas (air): 418.8 ml/min
Chromatograph Program settings	- Initial temperature: 30°C - Rate of heating: 5°C/min - Final temperature: 150°C - Injector temp: 150°C - Detector temp: 200°C - Oven maximum temperature: 200°C
Integrator	
Model	- Hewlett Packard – 3393A
Settings	- Zero (baseline): 0, 0.076 - Attenuation (^2): 6 - Chart Speed: 1.0 cm/min - Area Reject: 0 - Threshold: 0 - Peak Width: 0.04

Table 3.6 Chemical used for calibration and in the reactive experiments.

Chemical Name	Manufacturer	Unit amount	Purity and/or Assay
Ethyl choloacetate			
Calibration:	Sigma-Aldrich	100g	99+% v/v
Reaction Experiments:	Fisher-Scientific (Acros Chemicals)	2.5 lit	99+% v/v
2-Butanone	Sigma-Aldrich		99+% v/v
Ethanol	Inter-Departmental Purchase	4 lit	Anhydrous
Sodium hydroxide	Fisher-Scientific	4 lit	50.5% wt.
Hydrochloric acid			
Titration:	Fisher Scientific	1 lit	1.005-0.995 N
Reaction Experiments:	Fisher Scientific	2.5 lit	36.5-38% v/v

chromatogram. This is probably due to a combined effect of the moderate solubility of the ester and its tendency to stick to glass, which results in a part of the ester remaining out of solution. Polypropylene sample bottles, which are not wetted by the ester, were found to give better results and have been used for calibration and sampling in the rest of the study.

2) 3.35 ml of the solution was taken in a vial and mixed with 0.03 ml of 2-butanone
3) 0.6 μl of the mixture from step 2 was then injected into the gas chromatograph under the conditions outlined in Table 3.5.
4) 2-butanone has the lowest boiling point and is eluted first, followed by ethanol or ethyl chloroacetate. A sample chromatogram, when all three components are present is shown in Figure 3.3.
5) The ratio of the retention area of the chemical to that of the internal standard is recorded. A new sample with a different concentration is prepared and steps 2 to 5 repeated to obtain the relation between area ratio and concentration.

The calibration curves for ethanol and ester obtained by this method are shown in Figures 3.4a and 3.4b. These curves can be used to convert the ratio of the retention area of the chemical to the internal standard from the chromatogram of an unknown sample to its concentration in the solution.

3.3.3. Experimental Procedure

A schematic diagram of the experimental set-up used in this study is shown in Figure 3.5. Sodium hydroxide (reactant B) was fed into a fully baffled, cylindrical glass tank of diameter, T = 0.24 m, containing a mixture of A and C. A cavity style gear pump was used to transfer A from the reservoir to the tank. The amount of the reactant added into the tank was obtained by weight difference of the reservoir before and after addition and was accurate to ±0.1 g. The pump was digitally controlled and is guaranteed to be virtually pulseless (Micropumps Inc.). Visual observation of the rotameter float qualitatively confirmed that there were no large-scale fluctuations in the flow. The feed time of the reactant B could be set to within 0.1s. The reaction was carried out at 23°C±0.5°C.

a) Aqueous Solution of Ester Prepared Initially

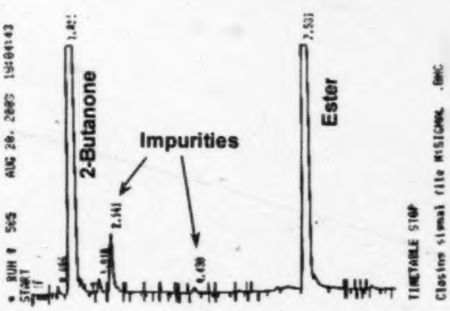

```
RUN#  585          AUG 20, 2003  18:04:43

SIGNAL FILE: N:SIGNAL.BNC
AREA%
     RT        AREA TYPE  WIDTH      AREA%
   .606         886   VH   .062     .01466
  1.021     4418896  SHB   .056   73.12746
  1.810        2142   BB   .055     .03545
  2.141       12017   PB   .106     .19887
  4.430         850   PP   .101     .01407
  7.531     1607941   VV   .092   26.60950

TOTAL AREA=6042733
MUL FACTOR=1.0000E+00
```

Area of Ester/Area of 2-Butanone = 0.364

b) Aqueous Solution of Ester and HCl Before Addition of NaOH

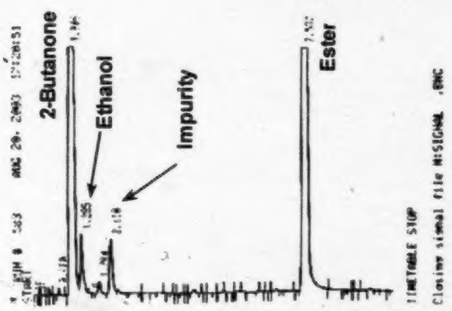

```
RUN#  583          AUG 20, 2003  17:20:51

SIGNAL FILE: N:SIGNAL.BNC
AREA%
     RT        AREA TYPE  WIDTH      AREA%
   .680         652   PB   .043     .01313
  1.006     3641126  SBB   .040   73.33754
  1.285        7230  TBB   .071     .14562
  1.704        1756   PP   .079     .03537
  2.110        9329   PV   .090     .18790
  7.533     1304796   PB   .091   26.28047

TOTAL AREA=4964890
MUL FACTOR=1.0000E+00
```

Area of Ester/Area of 2-Butanone = 0.365

Area of Ethanol/Area of 2-Butanone = 0.002

c) Aqueous Solution of Ester and HCl After Addition of NaOH

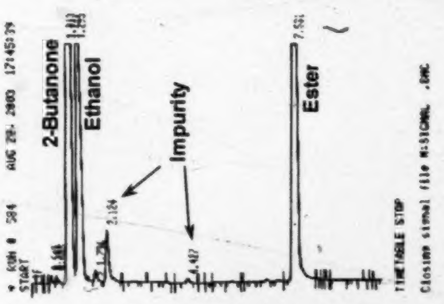

```
RUN#  584          AUG 20, 2003  17:45:39

SIGNAL FILE: N:SIGNAL.BNC
AREA%
     RT        AREA TYPE  WIDTH      AREA%
   .545         718   PV   .045     .01364
   .683         653   VV   .040     .01241
  1.013     3961320  SVB   .032   75.25821
  1.295      120069  TBB   .082    2.28110
  1.796        1953   BP   .087     .03710
  2.124       10891   VV   .105     .20691
  4.427         868   PV   .111     .01649
  7.531     1167169   PB   .091   22.17414

TOTAL AREA=5263640
MUL FACTOR=1.0000E+00
```

Area of Ester/Area of 2-Butanone = 0.295

Area of Ethanol/Area of 2-Butanone = 0.037

Figure 3.3 Chromatograms of samples collected at various stages of an experiment (PBTU, $d_f = 3mm$, $t_f = 2848s$). Note the formation of a small amount of ethanol after addition of HCl and the larger amounts of ethanol in the final product. The peaks are truncated only in the recorded graphs. Calculation of area is not affected in the integrator.

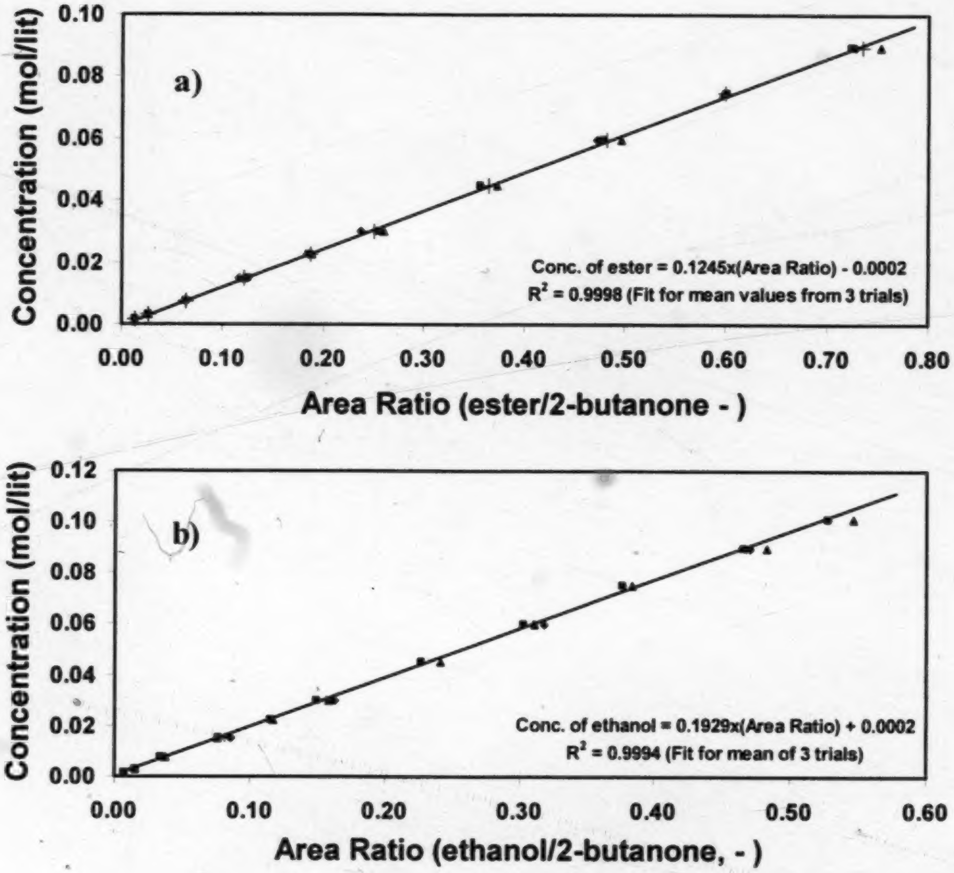

Figure 3.4 Calibration curve for ethyl chloroacetate. The abscissa is the ratio of the retention area of the peak for ethyl chloroacetate to that for 2-butanone. The ordinate is the known concentration of the ester in the injected sample.

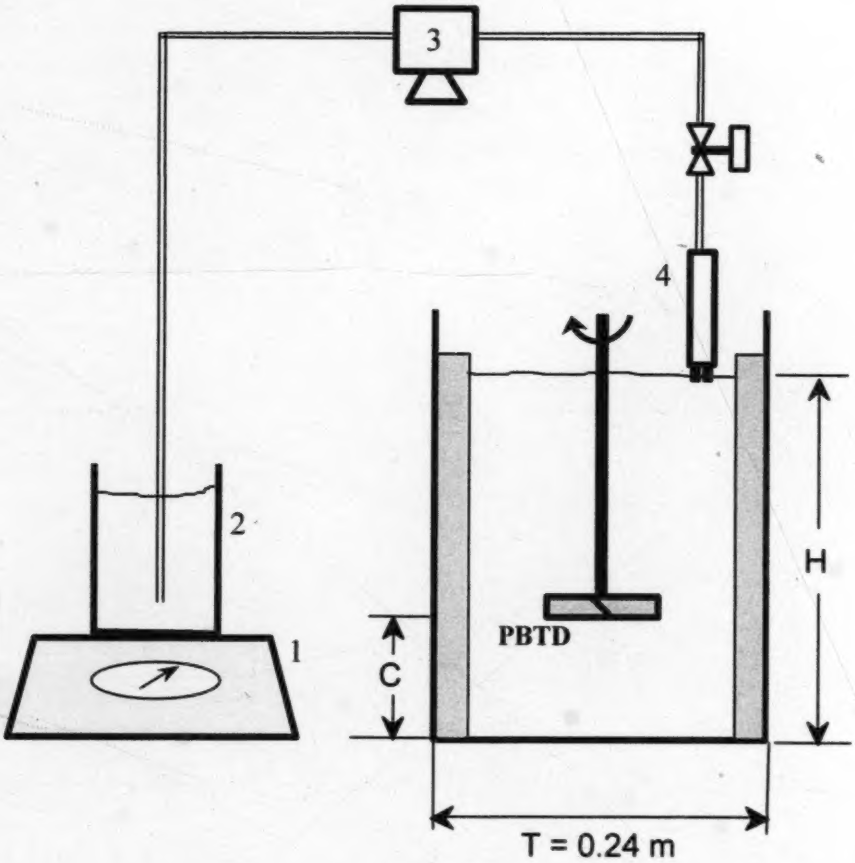

Figure 3.5 **Schematic of feed assembly and tank. Sodium hydroxide (2) is fed through the nozzle (4) by a cavity style gear pump (3). The amount of feed added is measured by difference using a Mettler balance (1).**

Byproduct yield[4] is affected by the initial concentrations of reactants. Using the results from section (2.2.2.2), concentrations of A, B and C were selected based on the following considerations:

(i) Equimolar amounts of A, B and C give the largest possible range of X_Q.

(ii) The maximum concentration of the ester is limited by the low solubility of ethyl chloroacetate in water. At 30.8°C, the maximum concentration of ester is 150 mol/m^3 (Stephenson and Stuart, 1986).

An ester concentration of 90 mol/m^3 (60% of the saturation value for the tank volume) was selected, which fixes the initial concentrations of A and C at 90 mol/m^3. This concentration has been used in several previous studies (Baldyga and Bourne, 1992; Baldyga et al., 1993; Bourne and Yu, 1994 etc). The concentration of B in the feed stream was 4500 mol/m^3, which gave a feed volume 1/50th the volume of the tank.

Experiments were carried out in the semi-batch mode where B was added into an aqueous mixture of A and C. The mixture of A and C was prepared ensuring that

1. The moderately soluble species of C, was completely dissolved in water.
2. There was minimal reaction between A and C.

This was achieved with the following dissolution sequence:

(i) 122 g of pure C (99.9% v/v) was first dissolved into 0.0108 m^3 of filtered water that had been doubly purified with reverse-osmosis. The amount of ester added was recorded to within 0.1g. A dissolution time of least 30 minutes was allowed to ensure complete dissolution of the ester.

(ii) 97.4g of A was then added into the aqueous solution of C. Concentrated hydrochloric acid (37.5±1% wt) was used to reduce inventory of the acid but it was added dropwise to minimize acidic hydrolysis between C with A.

Ten millilitres of the mixture were withdrawn from the tank after each of the steps (i) and (ii) and added into a 50 ml polypropylene sample bottle already containing 10 ml of water. Dilution of the sample slowed down any further reaction and reduced adsorption of the ester onto the walls of the bottle. 178 μl of 2-butanone was added into the sample bottle and then 0.6 μl of the resulting mixture was injected into the GC. The concentrations of ester and ethanol in each sample were determined using the calibration charts.

---

[4] This section is a modified version of the experimental section in Bhattacharya and Kresta (2004)

After the dissolution sequence, 252 g of B was added into the freshly prepared mixture of A and C over a period t_f, the feed time for that run. The tank contents were then agitated for additional 2 minutes to homogenize contents and finally a sample was withdrawn from the tank and analyzed. The difference in the concentrations of ethanol between the initial and final samples gives the byproduct yield using Equation (3.84). Note that the height of liquid in the tank changes continuously during the addition of sodium hydroxide but because of the large volume ratio, the total change is only 2% of the liquid height.

3.3.4. Experimental Conditions Studied

The experimental conditions for the study are summarized in Table 3.2. The configurations investigated in this study are as follows:

(i) Nozzle size: nozzle diameter was changed almost four folds from 3 to 0.762 mm.

(ii) Feed time: t_f was varied over a wide range for both nozzle sizes to encompass three regimes: high velocity feed, mesomixing limited and micromixing limited regimes. Both nozzles were operated in the high velocity feed and the mesomixing regimes but only the 3 mm nozzle was tested in the fully micromixed regime. Earlier studies (Baldya et al., 1993) show that there is no effect of feed diameter on byproduct formation in this regime.

(iii) Impeller speed: The base case was 252 rpm where Da_{av} was matched with values from similar studies in the literature (Baldyga et al., 1993; Bourne and Yu, 1994). The impeller speed was increased to 375 and 500 rpm in a separate set of experiments.

(iv) Plunging jet: Preliminary investigation were also carried out with a plunging jet to investigate its effect on the turbulence levels in the reaction zone and hence performance of the reactor.

3.4. Results and Discussions

Turbulence in the reaction zone can originate from two different sources, ambient turbulence in the tank driven by the impeller and the turbulence within the feed jet due to high Re_f. In the case where the feed stream was added at a very slow rate (long feed times) the byproduct yield is governed completely by the ambient turbulence. On the other hand, when the feed stream is turbulent, both the ambient turbulence and the feed stream turbulence can affect byproduct quality, their relative magnitudes determining the degree of influence on the mixing rates. Furthermore, when the high velocity feed is introduced near the liquid surface, a region with very low levels of turbulence, the turbulence in the feed stream itself is expected to have a tangible effect on the byproduct yield. This study investigates the high velocity feed stream. Experimental results for the various cases are presented in this section starting with (i) the effect of changes in feed condition (feed pipe diameter and feed time) on byproduct yield and then continuing on to (ii) the effect of the changes in ambient flow conditions (impeller speed) on the reactor performance. Finally, a plunging jet is used in an attempt to improve the local turbulence characteristics near the surface and hence increase the mixing rate.

3.4.1. Effect of nozzle size and feed time on byproduct yield

Figure 3.6 delineates the operating regime of the feed stream into laminar and transitional flow regimes, and shows the effect of Reynolds number on byproduct yield. Results are shown for two nozzle diameters ($d_f = 0.762$ mm and 3 mm) with a majority of the data in the laminar flow regime belonging to the larger nozzle. The data at higher velocities are available for both nozzle sizes. For the large nozzle it is seen that in the laminar flow regime, where X_Q is governed by the ambient turbulence in the tank and $Re_f \leq 300$, byproduct yield initially decreases with decreasing Re_f and finally becomes independent at very small Re_f. For a constant d_f, reducing Re_f corresponds to decreasing U_f or increasing t_f. The results in Figure 3.6 support previous literature for operation with drop wise feed:

- At very large t_f, X_Q is independent of feed time and dependent only on the rate of micromixing, which is driven solely by turbulence in the reaction zone

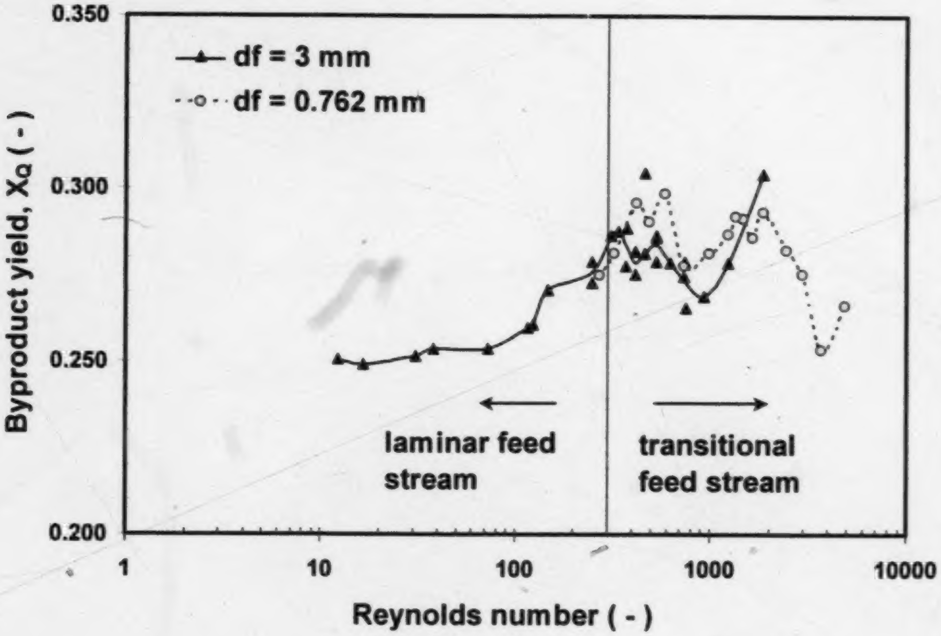

Figure 3.6 Effect of Re_f on byproduct yield. For the larger nozzle size, replicates are shown for various different feed times (see also Table 3.4). The solid line connects the averages of these replicates.

- As the feed time is reduced, or the feed stream velocity and Reynolds number is increased, X_Q starts showing the influence of t_f due to mesomixing limitations.

In the fully micromixed regime the byproduct yield was, $X_Q \sim 0.25$ for the present experiments. This value is similar to that reported in literature for surface feed and a Ruston turbine operated at similar average Damkoehler number (Bourne and Yu, 1994, $Da_{av} \sim 0.24$, $X_Q \sim 0.25$).

For larger Reynolds number (Re_f in the thousands) the following observations can be made about the byproduct yield:

- There is significant fluctuation and variation in the measured byproduct yield
- A local maxima in X_Q, is observed for both nozzle sizes and is similar for both cases
- The maximum byproduct yield ($X_Q \sim 0.3$) is about 50% higher than in the fully micromixed regime

The variations in the byproduct yield can be attributed to two sources. Firstly, if $Re_f > 1\text{x}10^4$ is the right limit for fully turbulent flow then the feed stream is in the transitional flow regime. In this flow regime turbulence levels are very erratic and this can cause similar unexpected variations in the byproduct yield. Secondly, in the mesomixing limited region a large 'reaction zone' forms near the feed pipe. This reactant plume flaps in the impeller generated ambient turbulent flow field (Verschuren et al., 2002) exposing the reactants to varying levels of ambient turbulence. This large-scale intermittency in the turbulence levels could also cause variations in the byproduct yield. The similarity in the trends of the X_Q curves with respect to the feed Reynolds number for both nozzle sizes tend to support the contention that the phenomenon is driven more by the feed stream rather than by the ambient turbulence. The experimental results show that within the range of Re_f studied, results are unstable, the flow regime is transitional and the limit for fully turbulent flow, $Re_f > 1\text{x}10^4$, used earlier is a practical and useful one.

The byproduct yield in the transitional flow regime also does not show the gradual monotonic increase seen in the laminar, mesomixing limited region. The peak in the byproduct yield is the resultant of two opposing influences. As the feed jet velocity is increased mixing limitations owing to the lagging rates of turbulent dispersion of the feed stream and inertial-convective disintegration of reactant eddies tend to increase byproduct yield. On the other hand, turbulence within the feed stream (albeit in transitional flow) and the fast convection of the reactants to the highly turbulent impeller region tend to suppress byproduct formation. The interaction between these two opposing influences leads to the maxima in X_Q.

The byproduct yields for both nozzle sizes are shown in Figure 3.7 as a function of the feed time. Presenting the byproduct yield as a function of the feed time is useful in showing the influence of macromixing limitations which can come into effect when the feed times are very small. The local maxima in X_Q are seen clearly for t_f between 80 to 120s. The point at which the feed stream becomes laminar is shown for both sizes in order to relate this figure to the Reynolds number domain of Figure 3.6. The traditional mesomixing and micromixing-limited regions are seen clearly in the laminar region. Further, in the mesomixing-limited region, byproduct yield is larger for the smaller nozzle, which is similar to the observations in literature (Baldyga et al., 1993). As the feed time is reduced, or feed velocity increased, the byproduct yield varies with the feed time as also seen in the transitional flow regime in Figure 3.6. The two curves seem to collapse onto each other at $t_f < 200$s. This is an effect of the multiple peaks in the transitional flow regime and similarity of the two curves in Figure 3.6. Below a feed time of about 40s, the byproduct yield for both nozzles increases sharply. This sudden increase in X_Q is due to either the convective stoichiometric limitation (Constraint 4) or the feed jet overshooting the impeller (Constraint 3) rather than the Reynolds number. At the short feed time when $t_f < 40$s, the total feed volume (V_f) is added at very high flow rates. At these short feed times Constraint 4 is reached and it becomes more and more difficult for the impeller to pump sufficient amount of reagent A into the reaction zone to keep up with the increasing flow rate at which reagent B is added into the tank. Increasing the impeller speed would enhance the flow rate of A into the reaction zone and could be used as a check to determine whether the rise in byproduct yield is indeed due to stoichiometric limitations. An increase in impeller speed will cause larger $\dot{n}_{A,Imp}$ and hence the sudden increase in byproduct yield should occur at smaller

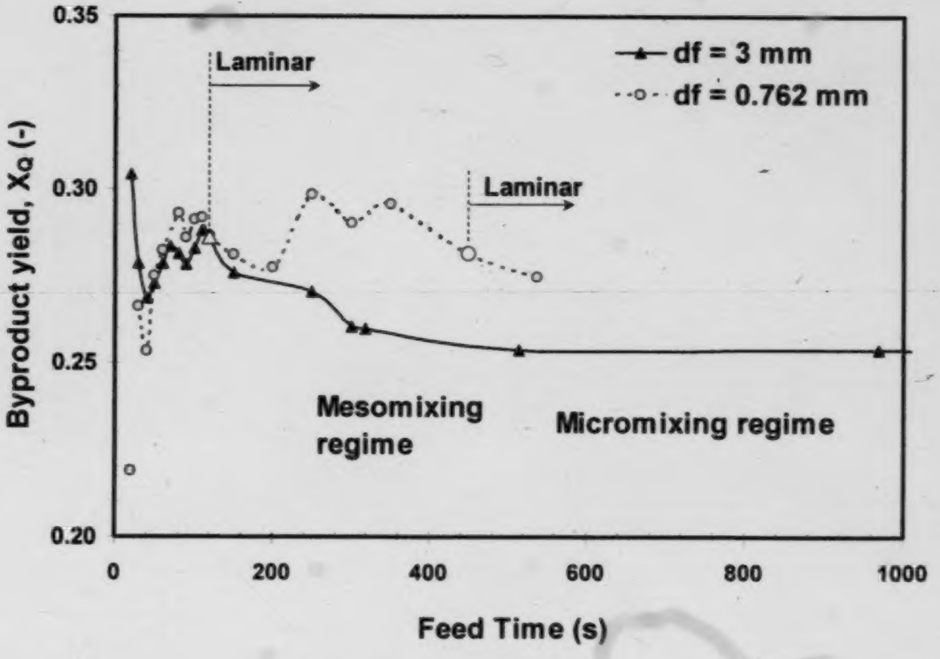

Figure 3.7 Effect of feed time on byproduct yield

feed times. Another factor, which could cause an increase in the byproduct yield, is the overshooting of the feed stream through the impeller, especially for the smaller nozzle. The impeller speed in Figure 3.7 is 252 rpm which gives $U_s = 0.264$ m/s (Equation 3.72). Using Constraint 3, the feed time at which the feed jet will overshoot the impeller works out to be 58.8s for $d_f = 0.762$mm and 16s for $d_f = 3$ mm. Constraint 3 could play a role in increased byproduct formation for the small nozzle but not the large one. The stoichiometric limitation is the main constraint in the present conditions.

The byproduct yield is sharply reduced for the small nozzle when the feed is added into the tank with a feed time of about 20s. This individual data point is shown separately in Figure 3.7 because unlike any of the other cases, a large amount of air entrainment was observed for this particular case. The feed velocity was about 25 m/s and $Re_f = 7606$. At this high velocity, the feed jet broke the liquid surface entraining large amounts of bubbles. The increased turbulence may have helped in additional entrainment of surrounding reagent into the feed stream and better mixing. Because of the marked improvement of reactor performance in this particular case, additional experiments were carried out with plunging jets. The results of these experiments will be presented in a later section.

3.4.2. Effect of impeller speed (N) on byproduct yield

Figure 3.8a shows the effect of an increase in impeller speed on byproduct yield. It is seen that the byproduct yield decreases with an increase in impeller speed. As the impeller speed is increased, the power input into the tank increases as a whole and the turbulence levels in all parts of the tank increase. Although turbulence in the feed jet has a prominent role in determining the mixing rate (which is the case when $t_f < 120$s and the jet is in transitional flow regime) the overall levels of turbulence will also increase due to the increase in ambient turbulence. The increased levels of turbulence in the reaction zone cause a decrease in the formation of byproduct. It is seen from Figure 3.8a that the points at which an increase in X_Q occurs at very high flow rates are approximately at 40s, between 20 and 30s and 20s for the three impeller speeds. It is believed that this increase in byproduct yield at high flow rates is due to convective stoichiometric limitation and

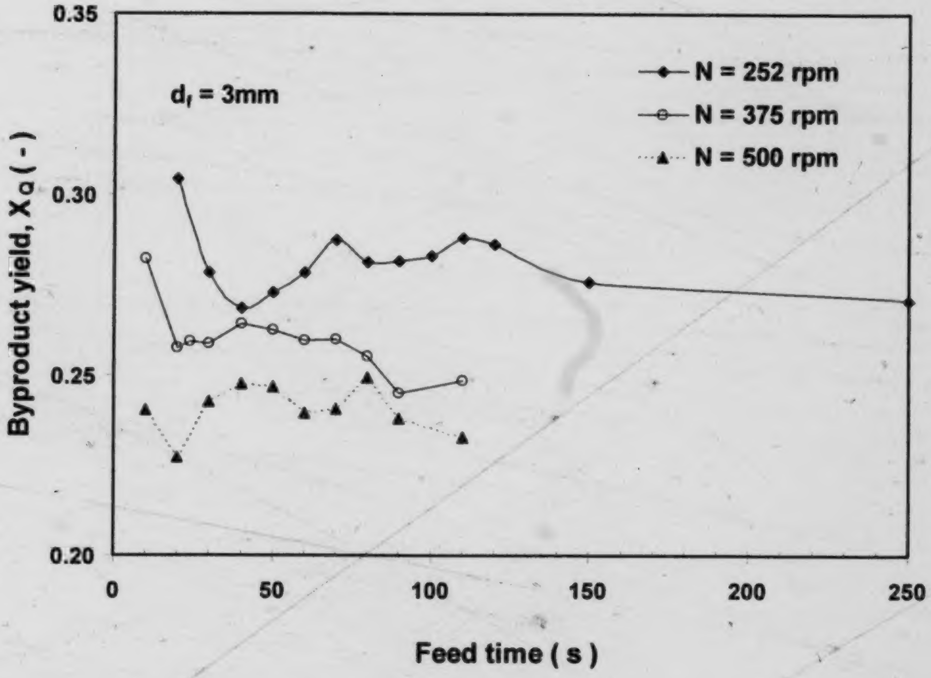

Figure 3.8a Effect of impeller speed on byproduct yield

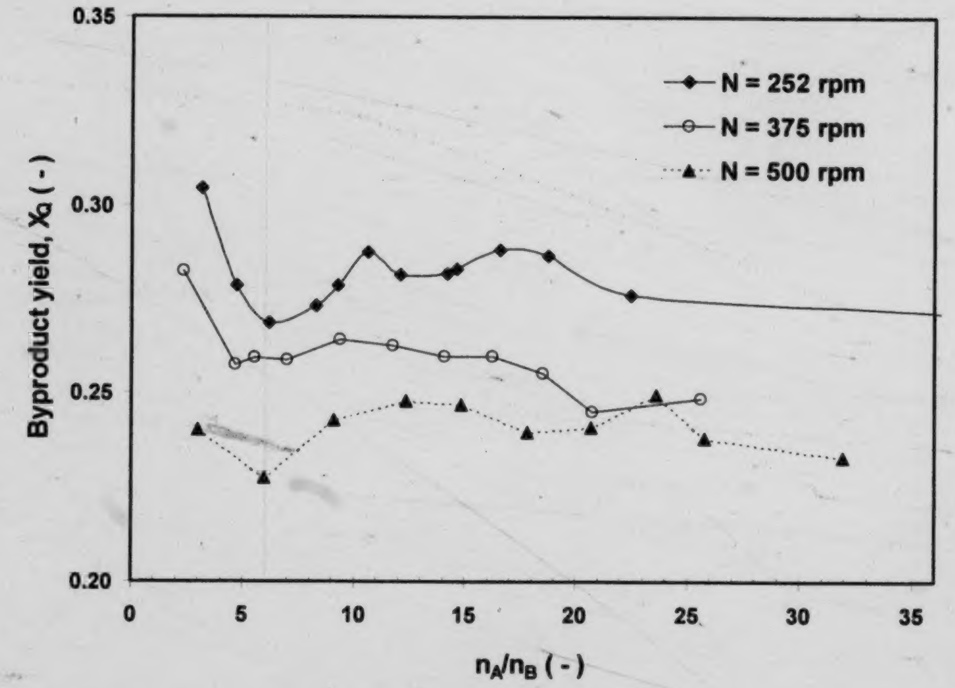

Figure 3.8b Effect of impeller speed and molar flow rates of A and B on the byproduct yield

this is clarified in Figure 3.8b. In this figure the byproduct yield for the three impeller speeds are shown as a function of the ratio of the molar pumping rate of A at the impeller to the molar feed rate of B into the tank via the surface nozzle. It is seen that for all impeller speeds the local minima in X_Q occurs at $\dot{n}_A/\dot{n}_B \sim 6$, i.e. the molar pumping rate of A at the impeller needs to be at least 6 times the molar feed rate of B to avoid CSL.

3.4.3. Plunging Jet

In Figure 3.7 at $t_f \sim 20$s, the byproduct yield was 0.22, less than the amount formed even in the micromixed region. At this feed time ($U_f = 25$ m/s and $Re_f = 7606$) there was entrainment of large amounts of air bubbles into the tank, which increased the turbulence levels near the surface and reduced byproduct yield. It was decided to conduct exploratory experiments with the feed nozzle above the liquid surface so that a plunging jet was formed which could actively entrain air bubbles. Experiments were carried out with the 0.762 mm nozzle, where the nozzle velocities were higher, and results are shown in Figure 3.9.

The main quantities characterizing a plunging jet are (i) the threshold nozzle velocity above which air is entrained into the receiving pool of fluid (ii) the volume of air entrained and (iii) the size and shape of the bubbles entrained. In context of the present investigation, the first quantity delimits the feed time which needs to be employed while the other two influence the amount of turbulence generated. A review of the literature dealing with circular plunging jets show that the threshold for air entrainment depends on the feed pipe Reynolds number and the Weber number (We_f, Hammoumi et al., 2002). The limits are:

- $Re_f < 200$ there is no air entrainment,
- $200 < Re_f < 1200$ there is air entrainment when $We_f > 170$
- $1200 < Re_f < 2300$ air entrainments occurs when $We_f > 270$
- $2300 < Re_f < 2600$ is unexplored
- $Re_f > 2600$ air entrainment occurs at all We_f

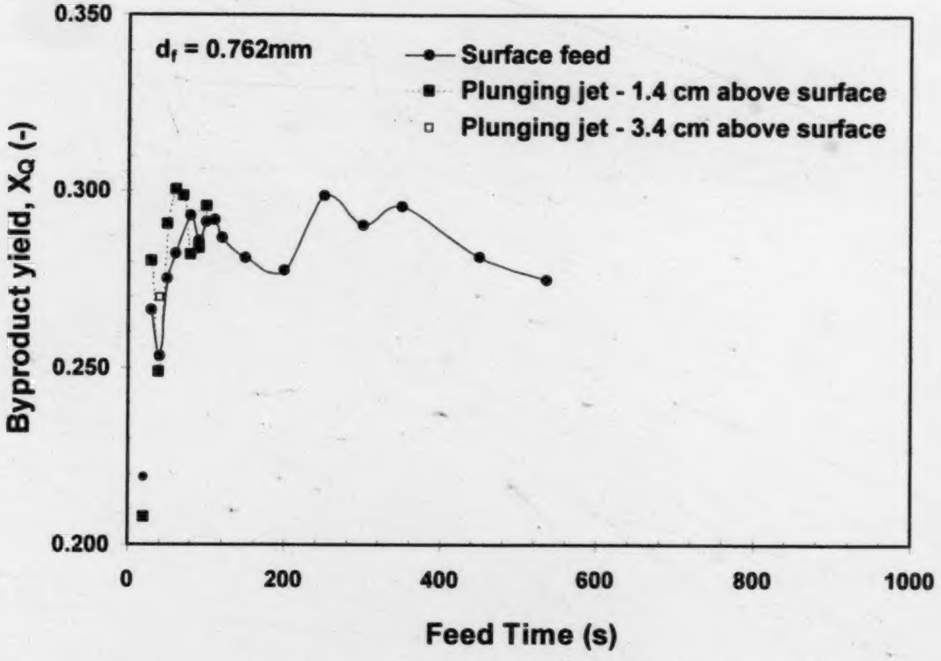

Figure 3.9 Plunging Jet

Table 3.7 Dimensionless numbers for plunging jet

Z_1 (cm)	t_f (s)	U_f (m/s)	Re_f (-)	Fr_f (-)	We_f (-)
3.4	40	12.01	3651	139	1558.35
1.4	20	24.34	7399	282	6400.29
	30	15.72	4779	182	2670.50
	39	12.06	3666	140	1571.28
	50	9.66	2938	112	1009.22
	60	8.02	2438	93	694.79
	70	6.88	2090	80	510.86
	80	6.02	1829	70	391.13
	90	5.37	1634	62	311.98
	100	4.82	1466	56	251.11

7

Table 3.7 shows that except at $t_f = 100s$, the condition for air entrainment is always obeyed. Air bubbles were also observed visually during the experiments. The amounts of air entrained were however not enough to cause a significant change in turbulence levels and hence affect the reaction results. This is seen in Figure 3.9 where the effect of the plunging jet on byproduct yield is minimal, except for marginal improvement at very short feed time. It is concluded that changing to a plunging jet does not change the reactor performance substantially.

3.5. Conclusions

Reagents have traditionally been fed into the most turbulent, impeller region of the stirred tank reactor to utilize the highest levels of turbulence, improve mixing rates and hence reduce mixing limitations. There are however numerous problems associated with this configuration due to which surface feed is preferred over submerged feed. The ability of high speed feed stream to reduce mixing limitations has been investigated in this study. The observations and the findings from the investigation are summarized below:

- The Reynolds number at which a jet becomes fully turbulent is not very clearly defined in the literature. A limit reported by many investigators is $Re_f > 1x10^4$ although lower values have also been used. The higher limit was verified from the behaviour of the jet and the performance of the reactor at high feed Reynolds numbers. Results showed that when the feed was slow and the operation was laminar ($Re_f < 300$), byproduct yield was stable and replicated observations in the literature. However, at higher velocities (Re_f from 300 to thousands) the relation between byproduct yield and feed time became erratic with numerous peaks and troughs in X_Q. This behaviour is attributed to operation in the transitional flow regime. $Re_f > 1x10^4$ is a practical limit for turbulent operation.
- For semi-batch operation the volume of feed added is fixed a priori; hence the feed pipe size and the feed time have to be carefully chosen to satisfy the requirement for fully turbulent feed flow. At the same time the feed pump has to be properly chosen with enough available head to overcome the pressure drop through the nozzle. Analysis shows that while a reasonably sized pump can be used with a

reasonable feed pipe diameter, the feed time then becomes too small, bringing in undesirable macroscale convective stoichiometric limitations. To increase the feed time, the feed pipe diameter has to be reduced significantly, which leads to a drastic increase in the pump head.

- When a fully turbulent jet is obtained by either reducing t_f or d_f, the velocity of the jet can be such that it shoots through the impeller completely bypassing the most turbulent region of the tank. Very small feed times can also lead to stoichiometric limitations in the reaction plume. To avoid this situation the impeller speed has to be increased significantly. Approximate calculations using concepts of ideal, axisymmetric jets show that in the scale of the tank used for the experiments the required impeller speed surpasses N_E at which air entrainment starts into the tank and which forms a probable upper limit for N. The combined requirements of very small feed time and very high impeller speed therefore make the deployment of a fully turbulent jet, very difficult. Experimental results showed that stable results could not be obtained even at small feed times (using even $d_f = 0.762$ mm) illustrating the difficulty in obtaining and maintaining a fully turbulent jet.
- In the absence of a fully turbulent jet, a fast feed stream could transport the added reagents quickly to the impeller so that a major part of the reaction completes in the impeller region and then reduces byproduct yield. This hypothesis was tested by using feed stream velocities higher than hitherto reported in the literature. Results do not show substantial improvement in reactor performance even at the higher velocities. Indeed control of the reactor would be more difficult in this regime unless fully turbulent conditions are reached, due to the substantial variations in X_Q and its dependence on t_f.
- At very small feed times, convective stoichiometric limitation ($\alpha\, \dot{n}_{A,Imp} \geq \dot{n}_B$) was observed. The value of α was found to be about one-sixth. This was verified by changing the impeller speed to change the flow characteristics in the tank.
- When the feed velocity at the surface was very high, air bubbles where entrained into the tank and the reactor performance was also improved significantly. This lead to experiments where the feed pipe was placed above the liquid surface to

form plunging jets. The plunging jet experiments did not show any improvement in performance.

It is concluded that feed jets at high velocities are operationally difficult to achieve and do not show substantial improvement in performance.

Chapter 4

Surface Feed at Normal Velocity with PBTU[5]

4.1. Introduction

Studies on mixing limited reactions consistently show that the level of turbulence is an important factor determining reactor performance. Mixing limitations are minimized and product yield is best when the reaction zone is in the most turbulent region of the stirred tank. Reagents are therefore fed near the impeller by means of dip tubes and surface feed which leads to bad product quality is traditionally avoided. As discussed in Chapter 1, submerged feed of reagents however causes many additional problems. The surface feed configuration therefore continues to be favoured from an operational point of view even when the requirements of reactive mixing, fluid mechanics and best mixing practice clearly point to a sub-surface feed.

In Chapter 3, it was attempted to improve reactor performance with surface feed by modifying feed conditions while keeping the impeller unchanged. Reagent was fed at the surface of the stirred tank at a high velocity to provide additional turbulence in the feed stream itself and thence improve performance. The investigation outlined in the present chapter uses another approach. The feed conditions are left unchanged but the ambient turbulence near the surface is increased by modifying the impeller type. Several feed geometries and impeller configurations are tried out to determine if surface feed with low by-product formation is possible and operationally feasible. The key requirement is to produce a high local rate of dissipation near the surface.

4.2. Experimental

4.2.1. Measurement of Mixing Characteristics

The third Bourne reaction employed in the experiments described in Chapter 3 was again used to probe mixing effects. The kinetics of the reaction and the methodologies used for the experiments and the measurement of the chemical concentrations has already been discussed in detail in Chapter 3, hence only additional issues relevant to the present investigation are described here. The impeller and feed geometry were varied to investigate several mixing strategies, as outlined in Figure 4.1 and Table 4.1. The experimental design is based on the following considerations:

---

[5] This chapter is an enhanced form of the work published by Bhattacharya and Kresta (2004)

Case 1. A Rushton turbine (RT) with submerged feed through a dip-tube located in the impeller discharge stream allows comparison with literature values, and definition of the best possible result.

Case 2. A down-pumping pitched blade turbine with submerged feed at the impeller suction gives the best case for the conventional down-pumping geometry (PBTD, Figure 4.1a).

Case 3. A down pumping pitched blade turbine with surface feed defines the worst case.

Case 4. A combination of one down-pumping pitched blade impeller at C = T/3 with an up-pumping pitched blade impeller at submergence, S = 0.31T (PBTU, Figure 4.1b) is the first alternate impeller configuration. In this configuration, several feed locations and nozzle diameters are tested. The feed locations are at the peak impeller discharge velocity (2r/D = 0.8) and the point where the impeller discharge stream meets the surface.

Case 5. A single up-pumping pitched blade impeller at varying S, varying N, and varying D (PBTU, Figure 4.1b) is the second alternate impeller configuration. This clarifies the effect of the lower impeller and the impeller submergence on the reaction.

The first three geometries provide the baseline data. Recent studies with Laser Doppler Velocimetry (LDV), Particle Image Velocimetry (PIV) and computational fluid dynamic (CFD) simulations (Jaworksi et al, 2001; Aubin et al., 2001 and Aubin et al., 2004) show that the upper regions of the tank have better turbulence characteristics when agitated with a PBTU. Configurations 4 and 5 represent a shift in approach based on this observation: instead of moving the feed from the surface to the highly turbulent impeller region, the highly turbulent impeller stream is moved to the surface. The impeller speed for the PBT was kept at (N = 252 rpm) to match the average Damkhoeler number (Da_{av} =

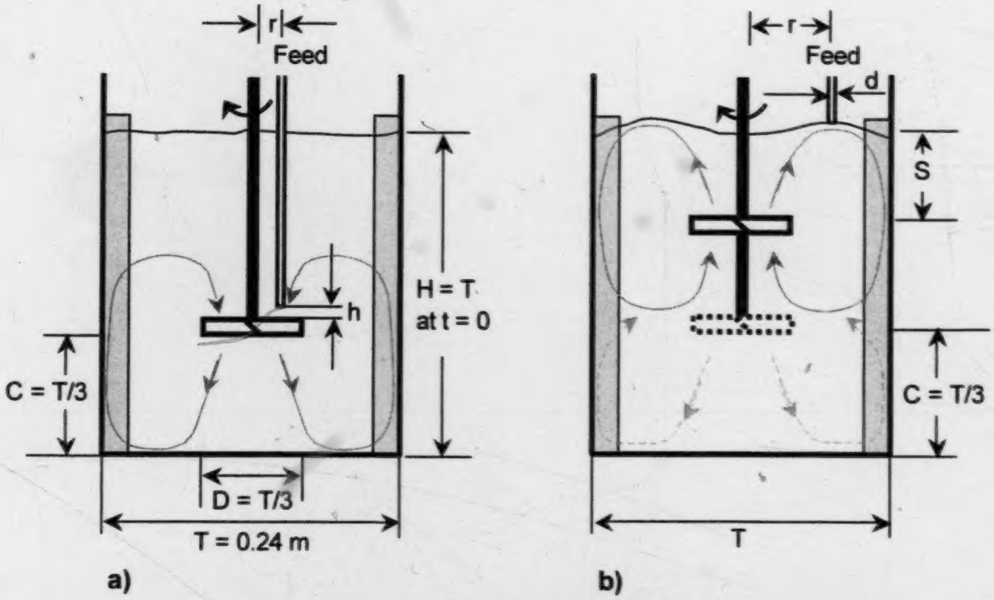
r
Feed
h
H = T
at t = 0
C = T/3
D = T/3
T = 0.24 m
a)
r
Feed
d
S
C = T/3
T
b)

Figure 4.1 **Schematic of feed and impeller configurations: a) conventional submerged feed b) surface feed with up-pumping PBT. Table 4.1 gives full details of the feed and impeller geometry for all five cases considered.**

Table 4.1 Details of Feed and Impeller configurations. The nozzle diameter was d = 3 mm for all cases. A smaller nozzle diameter of d = 0.762 mm was also tested for Case 4.

Case	Da_{av}	Impeller				Feed Location	
		Type	D/T	N (rpm)	Clearance (C/T)	Radial Position (2r/D)	Vertical Position (h/D)
1	0.19	Rushton turbine	1/3	189	1/3	1.125	-0.0625
2	0.24	PBTD	1/3	252	1/3	0.8	0.0625, 0.2625
3	0.24	PBTD	1/3	252	1/3	1.75	Surface
4	0.24	PBTD + PBTU	1/3 1/3	252 252	1/3 S/T=0.31	0.8, 1.75	Surface
5	0.32-0.16	PBTU	1/3 1/2	210-328	S/T= 0.04-0.31	0.8	Surface

0.24) used in the experiments reported in Chapter 3 and in the reference literature (Bourne and Yu, 1994; Baldyga et al., 1993). The one exception to this is the Rushton turbine, where Da_{av} was 0.19. In this case, the impeller speed was limited by the requirement that $Re_I \geq 2x10^4$, so Da_{av} could not be increased further. This difference will not lead to a significant difference in X_Q (Yu, 1993; Bourne and Yu, 1994).

4.2.2. Measurement of Flow Characteristics

Previous studies with a PBTU (Jaworksi et al, 2001; Aubin et al., 2001 and Aubin et al., 2004) measured the flow and turbulence characteristics in the bulk of the tank while it is mainly the turbulence characteristics at the liquid surface, which determine reactor performance when surface feed is employed. New LDV measurements were therefore made close to the open liquid surface in a tank identical to that employed for the reaction experiments. This section provides details of the LDV setup and the procedure adopted for velocity measurements.

Laser Doppler Velocimetry is an accurate, non-intrusive method for measuring instantaneous velocity in fluid flows. The measurement volumes are so small that the technique practically gives point measurements of velocity. Fluid velocity measurements using this technique depend on the changes in intensity (modulated intensity) of the scattered light from a particle flowing with the fluid as it crosses alternate dark and light fringes created by interference between two linearly polarized laser beams crossed at the measuring volume. The light intensities in the laser beams are Gaussian in distribution so that the measuring volume is ellipsoidal in shape. Another interpretation of the phenomenon is that the frequency of the scattered light is a resultant of different Doppler shifts of the two light beams scattered by the particle from the two incident beams. Different angles of the incident beams give rise to the difference in Doppler shifts of the two scattered beams. Both interpretations lead to the same expression for the frequency of variation in intensity (the Doppler shift frequency), f_D, of the scattered light which is given as:

$$f_D = \frac{2U_P}{\lambda}\sin\left(\frac{\theta_{LDV}}{2}\right) \tag{4.1}$$

If the scattered light is focused on to a photodetector to measure f_D, the velocity of the particle, U_P, can be calculated since the wavelength of the light (λ) and the angle between the two beams (θ_{LDV}) are already known. However, while the magnitude of U_P can be estimated from Equation (4.1) the direction of movement of the particles cannot be discerned. In order to detect the direction of velocity also, light-beating (moving) fringes are created by shifting the frequency of one beam relative to the other with a Bragg cell. Particles moving in the same direction as the fringe reduce the frequency of the scattered light while movement in the opposite direction increases it. Hence, the up or down displacement of the particle along the direction of fringe movement can now be detected. The component of velocity that is measured is the one that lies in the plane of the two intersecting beams and is exactly parallel to the bisector of the outer angle between them as illustrated in Figure 29, page 57 in Kresta (1991). By changing the plane of the two intersecting beams, velocities along all three co-ordinate axes can be measured.

An experimental setup for LDV consists of a laser and optical train, a photodetector, a signal analyzer and a traverse/positioning system. The relative location of each of these components with respect to each other and the stirred tank is shown in Figure 4.2a. The cylindrical glass tank was kept inside a square vessel (made of plexiglass) and both tanks were filled with the same fluid to minimize distortion due to the curvature of the stirred tank wall (Figure 4.2b). The laser and optical train used for the present one-component system from Aerometrics Inc. consisted of a 300 mW air-cooled Argon-ion laser ($\lambda \sim 457$ to 514.5 nm), polarization filter, beam splitter, a Bragg cell capable of producing a frequency shift of 40 MHz and a focusing lens with a focal length of 500 mm. The two beams coming from the optical train are focused on to the measurement volume in the stirred tank. The scattered light from the particles passing through this zone is collected via a focusing lens and optical aperture into a receiver containing the photodetector (three photo multipliers in the present case) and a signal amplifier. Depending on the position of the photodetector there are two types of LDV, one operating in the forward scattering mode when the laser and receiver are placed on opposite sides of the measuring volume and the other operating in the back scattering

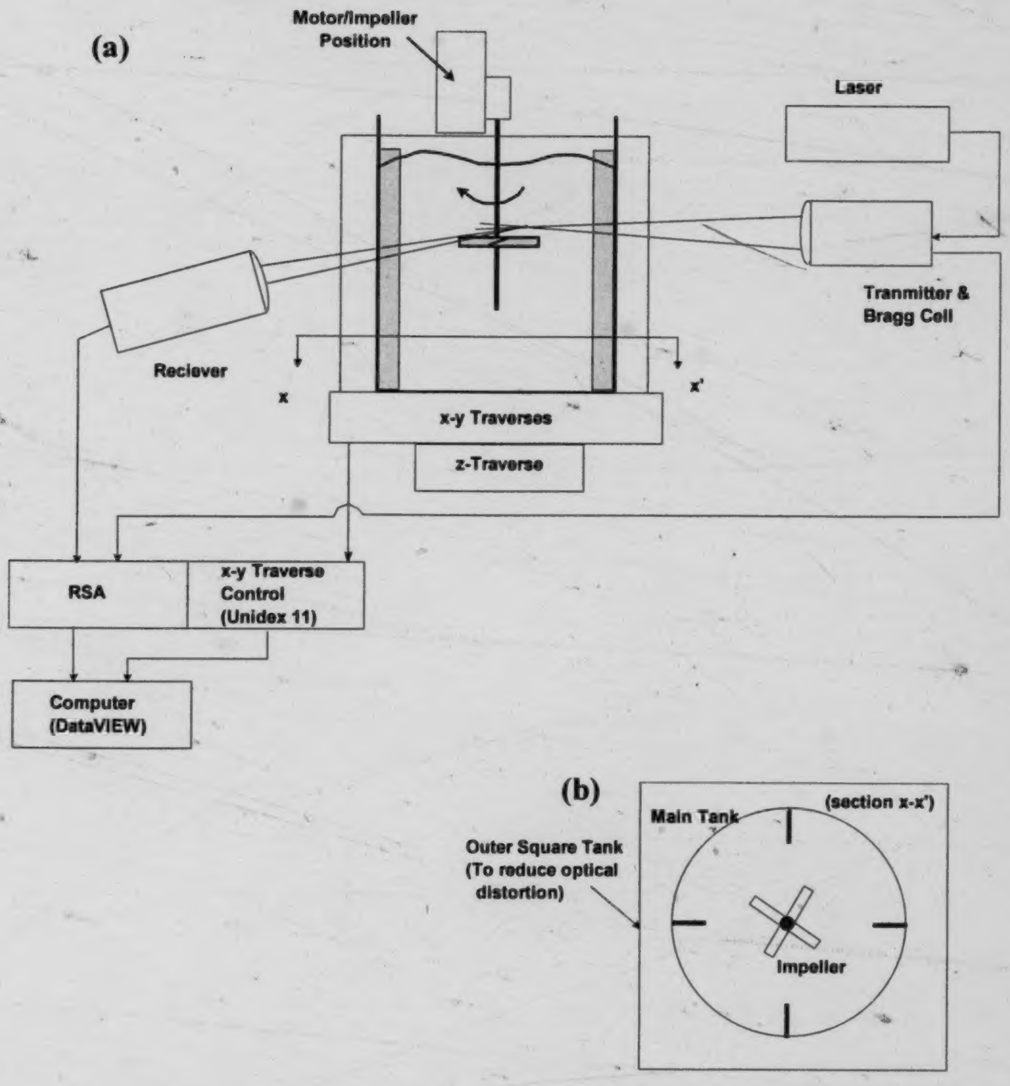
(a)
Motor/Impeller Position
Laser
Tranmitter & Bragg Cell
Reciever
x
x'
x-y Traverses
z-Traverse
RSA
x-y Traverse Control (Unidex 11)
Computer (DataVIEW)
(b)
Main Tank
(section x-x')
Outer Square Tank (To reduce optical distortion)
Impeller

Figure 4.2 (a) Aerometrics LDV setup used to measure instantaneous velocity.
(b) Tank cross section

mode when the laser and receiver are on the same side of the measuring volume. In the present study, the photodetector was placed in the forward scattering mode. The burst signal generated by the particles passing through the measurement volume are captured by the photodetector, amplified and then passed on to the Aerometrics real-time signal analyzer (RSA). The primary tasks of the signal analyzer are to filter off very low and very high frequencies, center record time to the middle of the burst, extract frequency information from the signal and produce an output proportional to the frequency of the signal. The data from the RSA is acquired into the computer through a data acquisition board (DAB). DataVIEW©, version 1.1, Build 0008 (June 1998) from Aerometrics Inc., a data acquisition and analysis software allows control over the acquisition and analysis of the data from the RSA and the DAB. Details of the various parameters in the LDV setup are outlined in Table 4.2.

The DataVIEW software was also used to program and control the x-y traverse of the stirred tank. An automatic traverse system was used to position the tank accurately in two directions, x and y. Positioning in the z-direction and the adjustment of the off-bottom clearance or the submergence of the impeller was done manually. The accuracy of the x-y positioning was ± 0.5mm and that in the z-direction was ± 1 mm. The zero position for the x-y traverse was found by using a 1mm zeroing spike machined on to the end of the impeller shaft. The x and y traverse positions were adjusted (with the Bragg cell shut off) till the laser was focused exactly on to the tip of the spike. For the z-traverse, first, the impeller position was set manually and then the z position of the laser beam was located relative to the impeller.

As the laser beams pass through the inner and outer walls of the flat and cylindrical tanks they are bent due refraction and can affect the positioning of the control volume. The positions of the laser beams and thence the measuring volume were corrected for refraction using a beam-tracing routine from Kresta (1991). Data rate depends on proper focusing of the various optical parts (mainly the receiver optics), the magnitude of the velocity and the number of particles in the liquid. The liquid used in the tank was seeded with titanium dioxide (size less than 5μm) to increase the data rate. The

Table 4.2 Parameters of Aerometrics LDV system used in this work

Laser Characteristics	
Model	Spectra-Physics Model 177-G
Wavelength	458 – 514.5 nm
Output Power	300 mW
Beam Diameter	0.82 ± 5% mm
Beam Divergence	0.78 mrad (nominal)
Optics (Aerometrics Inc.)	
Focal length of lens (transmitter)	500 mm
Beam separation before expander	16.9 mm
Expansion ratio	2 (knob combination A and C)
Expanded beam separation	33.8 mm
Fringe spacing	7.6 μm (calculated)
Number of fringes	18
Beam waist	140 μm (calculated)
Beam intersection angle	0.067 or 3.87°
Focal length of lens (receiver)	Two lenses with focal lengths: 500 and 240 mm
Automatic Traverse (Aerotech)	
Model	Unidex 11
Control direction	x and y
Accuracy	± 0.5 mm
Receiver/Signal processor Settings	
High voltage to photomultipliers	148 Volts
Sampling rate	2.5 MHz
Burst threshold	0.9 mV
Filter	1.25 MHz
Others	
Vertical (z) traverse	Manual, accuracy of ± 1.0mm
Impeller positioning	Manual, accuracy of ± 1.0 mm
Signal Processor	Aerometrics Real Time Signal Analyzer (RSA)
Acquisition and Analysis Software	DataVIEW 1.1, Build 0008 (June 11, 1998)

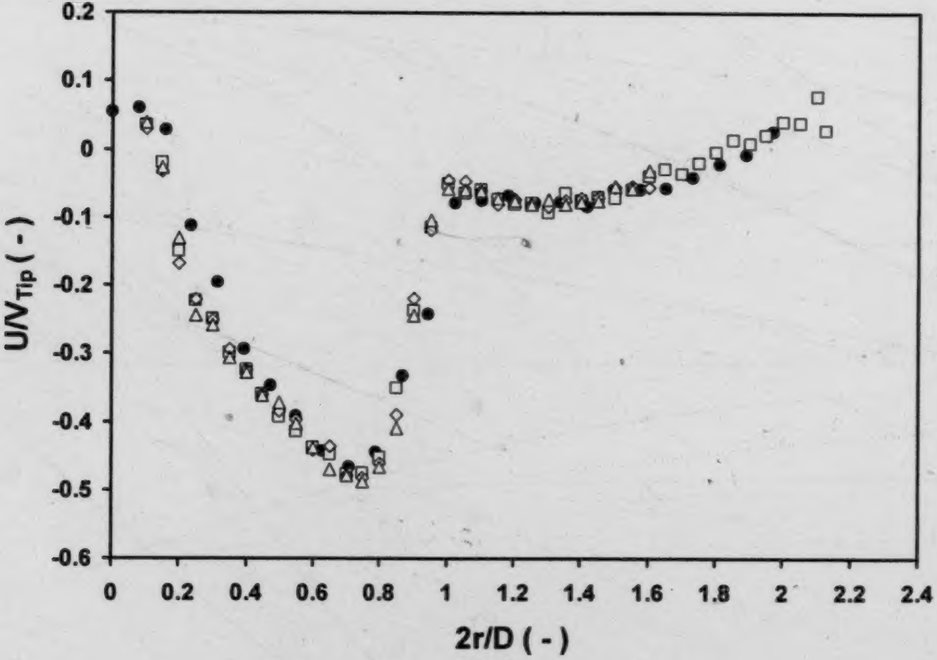

Figure 4.3a Comparison of mean velocity data from present study with data from Kresta (1991). The data from Kresta (1991) are shown filled while the replicates from this investigation are shown hollow. Measurements are shown for a PBTD with D = T/3, located at an off-bottom clearance, C/D = 1. The measurement traverse is at a distance of 4 mm below the lower edge of the impeller. The impeller speed in Kresta (1991) was 450 rpm while the present data were collected at 400 rpm for similar tank sizes.

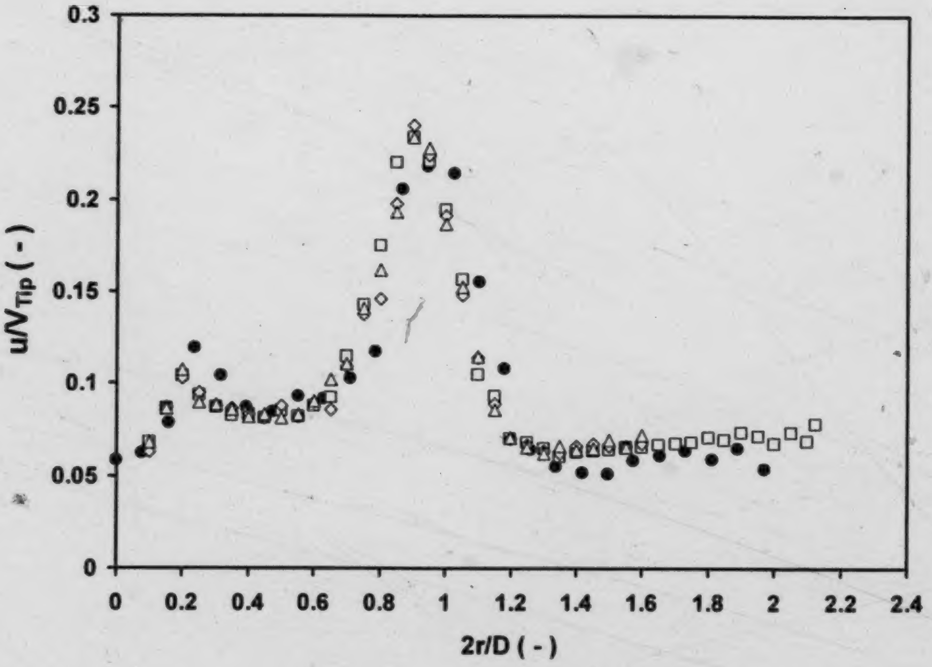

Figure 4.3b Comparison of RMS velocity data from present study with data from Kresta (1991). The data from Kresta (1991) are shown filled while all replicates from the present investigation are shown hollow. Measurement conditions are the same as in Figure 4.3a.

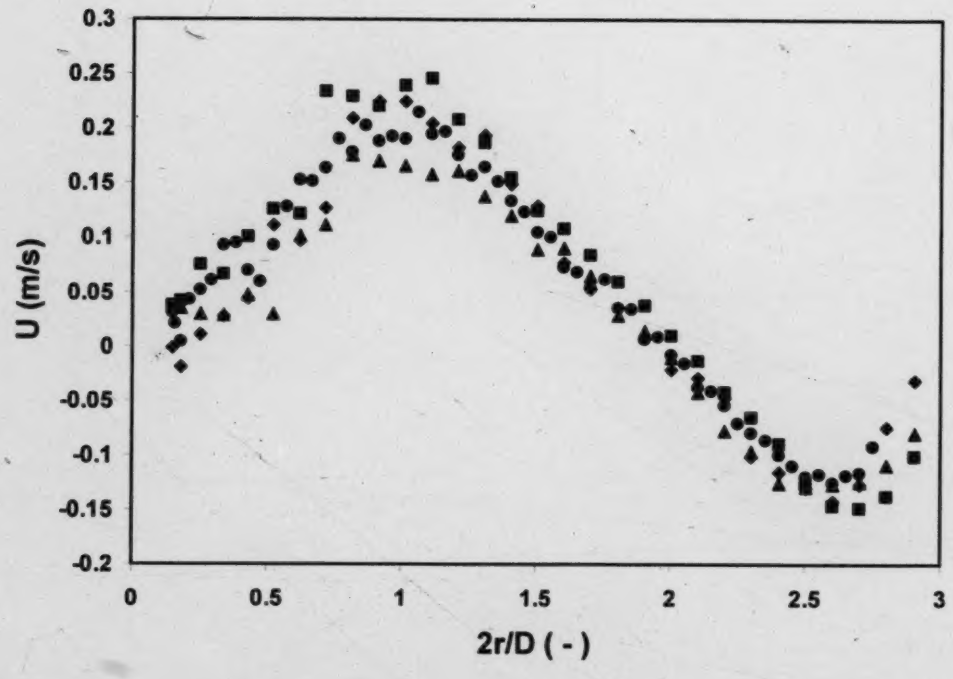

Figure 4.4a Reproducibility of velocity measurements. Axial mean velocity data is shown for the up-pumping pitched blade turbine (D = T/3) with the impeller operated at S/D = 1 and a speed equal to 98% of the speed at which air bubbles are entrained into the tank ($0.98N_E$). The first and the last set of data shown in this figure were collected over a period separated by more than 12 months.

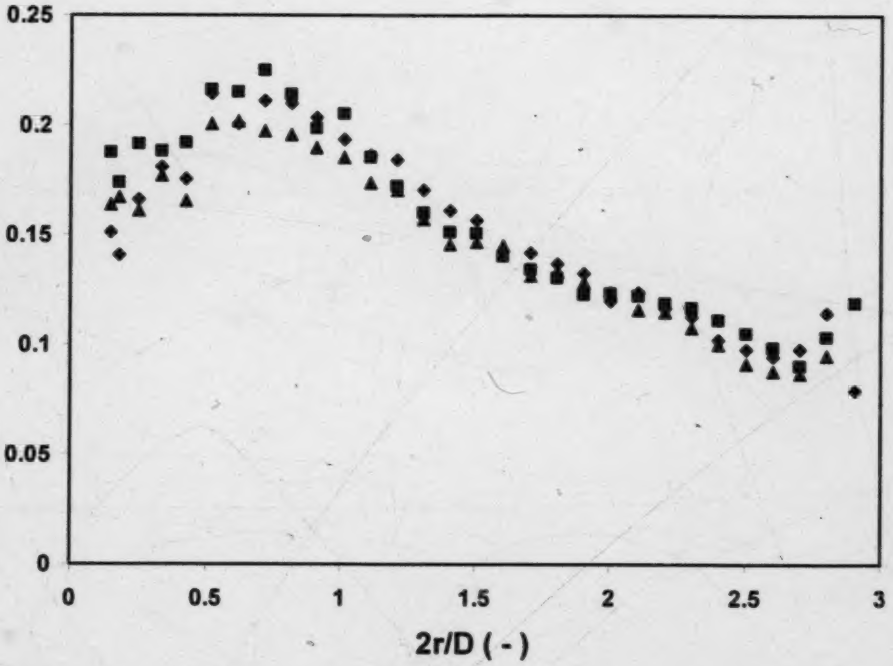

Figure 4.4b Reproducibility of RMS velocity measurements. Data is shown conditions similar to that in Figure 4.4a.

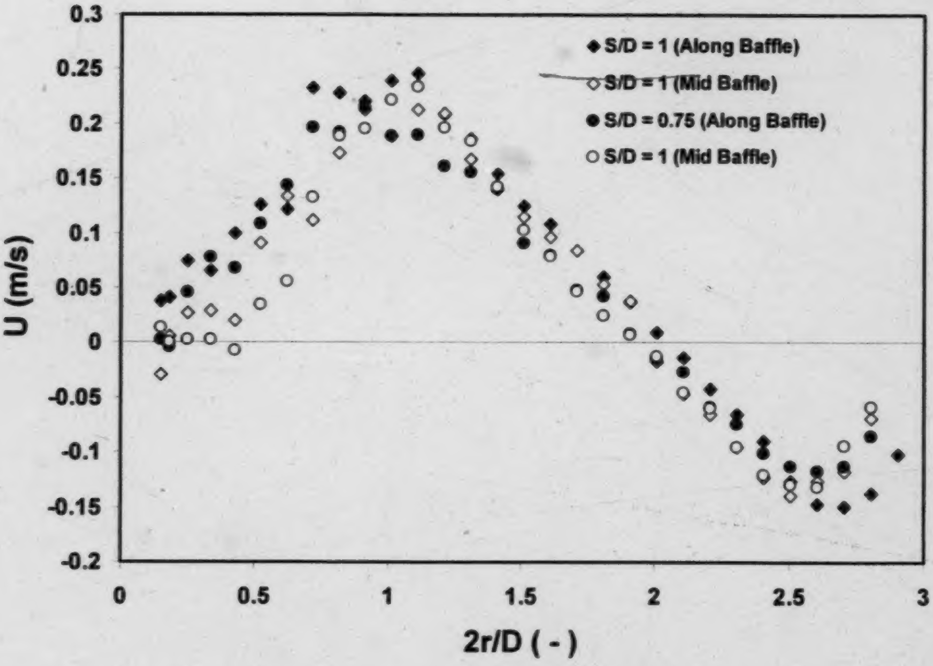

Figure 4.5 Radial profiles of the axial velocity, at a location 1.5cm below the quiescent surface is shown for two planes: mid-baffle and at a plane located with an offset of 6mm from the baffle.

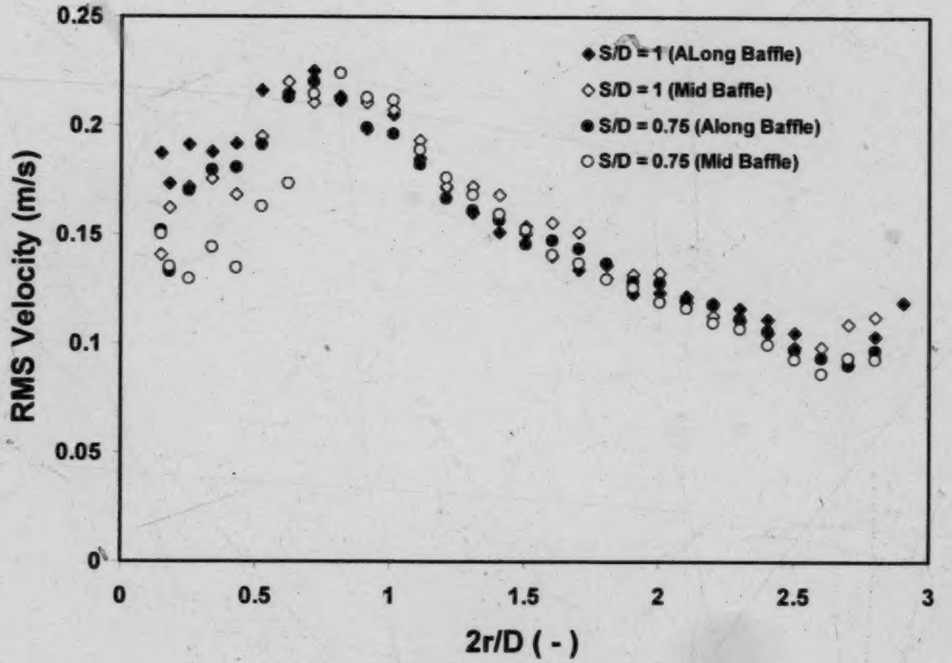

Figure 4.6 Radial profiles of the axial velocity, at a location 1.5cm below the quiescent surface is shown for two planes: mid-baffle and at a plane located with an offset of 6mm from the baffle.

axial component of velocity was measured 1.5 cm below the surface of the quiescent liquid (N = 0 rpm, z = 0.9375 H) every 4 mm along a radial traverse. 60,000 points were collected for each measurement location. The number of samples and the sampling time were selected based on the criteria developed in previous studies (Zhou, 1997; Grgic, 1998 and Bittorf, 2000). Details of these parameters used in the present investigation are provided in Table 4.2.

The experimental procedure and the LDV setup were verified by first comparing the velocity data collected in this study with data from previous experiments. Figures 4.3a and 4.3b shown comparisons of the axial mean and RMS velocities obtained for a PBTD in the present study with corresponding values from Kresta (1991). It is seen that not only does the present data show excellent agreement with the data of Kresta (1991) but the repeatability is also very good. When a PBTU is used with an open tank, the liquid surface undergoes significant movement because of which measurements close to the liquid surface can be difficult. A depth of 1.5 cm from the stagnant surface was specifically chosen as the location closest to the surface, which was still free from any obstruction to the laser beams due to distortions of the liquid surface. Figures 4.4a and 4.4b show that even at this location the repeatability for both the mean and RMS velocities are quite good. Finally the effect of the position of the plane of measurement (mid-baffle or close, 6mm, from one of the baffles) on velocity measurement near the surface is shown in Figures 4.5 and 4.6.

4.3. Results and Discussions

The base cases, 1, 2 and 3, provide the upper and lower limits of reactor performance and a reference point for comparison with literature. Cases 4 and 5 examine an up-pumping impeller which has the potential to improve performance because it places a highly turbulent impeller discharge zone close to the surface. Initial experiments were designed to achieve the following objectives:

- Test the viability of the up-pumping configuration
- Determine the sensitivity of this configuration to changes in the feed pipe location, nozzle size, impeller submergence, and impeller diameter

- Determine whether a second impeller in the lower half of the tank affects the reaction selectivity
- Find the maximum rotational speed, or best possible performance, of the up-pumping configuration

The critical or maximum value of a modified form of the impeller Froude number, $Fr' = N^2S/g$, was used to define the maximum rotational speed (N_E). Above Fr'_{crit} ($Fr'_{crit} = N_E^2 S/g$) air is entrained into the tank. While air entrainment may be acceptable for some reactions, it is generally not recommended. Furthermore, the effect of bubble formation on local turbulence is poorly understood. The results are discussed, starting with the base cases and ending with the performance at Fr'_{crit}.

4.3.1. Submerged feed

Figure 4.7 shows the effect of feed time (t_f) on X_Q for Cases 1 and 2. Experiments were conducted with the RT in the micromixed region for comparison with literature data. Values of X_Q for Case 1 are reported by Baldyga et al. (1993, $X_Q \sim 0.069$ at $t_f \sim 1320s$, $Da_{av} = 0.24$) and Bourne and Yu (1994, $X_Q \sim 0.09$ at $t_f = 1140s$, $Da_{av} \sim 0.24$). These values bracket the value of X_Q measured in this work ($X_Q = 0.087$ at $t_f = 1122s$, $Da_{av} = 0.19$). For the PBTD, experiments were conducted over a wider range of t_f at two feed locations. X_Q for both feed positions exhibits trends similar to those reported in literature: a flat micromixing region at long feed times, followed by a mesomixing-limited region where X_Q increases with decreasing t_f. The byproduct formation, X_Q, deviates from the classical trend at intermediate feed times ($300s < t_f < 1200s$) when the feed is at h/D = 0.2625. Here, X_Q first drops with decreasing t_f before increasing with t_f. This effect is not seen for h/D = 0.0625, but is easily explained.

When the feed is moved away from the impeller (in this case by 16 mm), it is moved into a region of lower turbulence. The level of turbulence on the suction side of the impeller decreases rapidly with increasing h/D (Khan et al, 2003; Aubin et al., 2004). At large feed times ($t_f > 1200s$) and large h/D the reaction completes in a region of low turbulence and X_Q is higher at a larger h/D. When the feed time is reduced, the feed

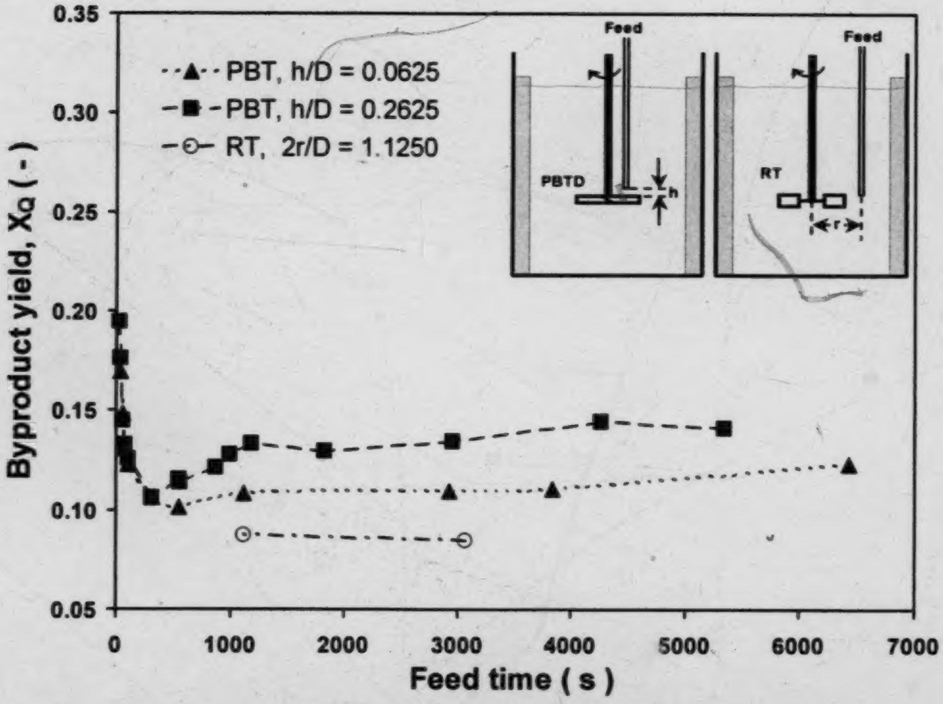

Figure 4.7 Effect of feed time on byproduct yield for submerged feed. Results are shown here for the base case configurations (Cases 1 and 2). For Case 2, the PBTD, the feed pipe is located at two heights above the impeller to illustrate the sensitivity of byproduct yield to feed location.

enters with some momentum and convects progressively larger amounts of unreacted feed directly into the turbulent impeller region before the reactions are completed. With further increases in feed velocity; however, X_Q becomes dominated by mesomixing and reverts back to the general trend. When the feed nozzle is placed very close to the impeller (h/D = 0.0625) the local level of turbulence is already close to the maximum. As t_f decreases X_Q is dominated by mesomixing and no deviation from the general trend is observed. These results underscore the sensitivity of product distribution to local levels of turbulence, and hence to the precise location of the feed relative to the impeller.

4.3.2. Surface feed

Very little turbulence reaches the surface of the tank with a single PBTD and hence byproduct formation is large when the reactant is fed at the liquid surface. When a second PBTU is added in the upper third of the tank, the highly turbulent impeller discharge stream is directed upwards thus increasing the level of turbulence near the surface. Byproduct formation is expected to drop in this configuration.

4.3.2.1. Single PBTD

When feed is introduced at the liquid surface in Case 3, the byproduct yield with a single PBTD goes up to 0.26, as shown in Figure 4.8. Experiments conducted over the full range of feed times show that X_Q is high over the whole range. Even in the micromixed region, X_Q is more than double that obtained with a submerged feed for the same impeller. Similar results have been reported for surface feed configurations in numerous earlier studies and are attributed to the very low levels of turbulence near the liquid surface (Bourne and Yu, 1994; Baldyga and Bourne, 1999, Nienow and Inoue, 1993). This configuration is the worst possible mode of feed injection and gives the highest possible yield of byproduct.

4.3.2.2. PBTU and PBTD combination

Using a PBTU improves performance because the up-pumping impeller augments turbulence at the surface. Unlike the submerged feed, this impeller configuration is

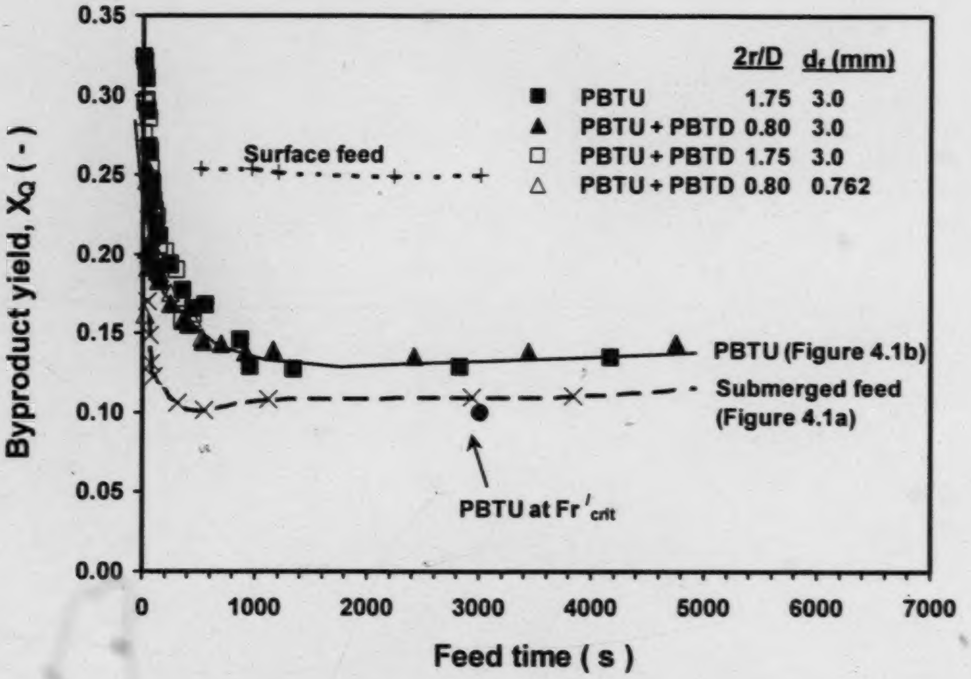

Figure 4.8 Effect of feed time on byproduct yield for surface feed configurations: Cases 3, 4 and 5. A PBTU dramatically improves performance relative to a conventional PBTD (dotted line), but does not quite attain the performance of the submerged feed at small h/D unless the impeller is operated at Fr'_{crit}. The up-pumping configuration shows little effect of geometry on byproduct yield. See an expanded scale of the mesomixing range in Figure 4.9.

shown to be relatively insensitive to a number of geometric variables, as shown in Figures 4.8 and 4.9. In particular, we note from Figure 4.8 that the removal of the lower impeller has no effect on the byproduct formation, so the results from Cases 4 and 5 can be compared directly.

4.3.2.2.1 Effect of radial location of feed – low feed velocity

The effect of feed location on byproduct yield was studied by placing the feed stream at two radial positions, 2r/D = 0.8 and 1.75. The results for the full range of t_f are shown in Figure 4.8. In the micromixed regime ($t_f > 1100$s), the radial location of the feed pipe has no effect on X_Q. Since only the local dissipation governs the rate of mixing and hence the amount of byproduct formed, the insensitivity of X_Q to radial position suggests that similar levels of turbulence exist at both radial locations.

From an operational point of view, the lack of effect of radial position on X_Q at low feed rates is beneficial because it indicates stable reactor operation. The byproduct yield is still higher than that obtained with the submerged feed in the micromixed regime ($X_Q \sim 0.11$), showing that the feed is not yet exposed to the maximum available ε in the impeller discharge. This suggests the possibility of further optimization for this configuration. Particle image velocimetry for a PBTU (Aubin et al., 2004) shows that the highly turbulent region extends to only a short distance above the impeller. Thus, at a deeper submergence of the PBTU, the turbulence at the surface is lower and X_Q will be higher. The impeller submergence is an ideal candidate for further optimization.

4.3.2.2.2 Effect of radial location of feed – high feed velocity

Numerous previous studies (Baldyga and Pohorecki, 1995; Baldyga and Bourne, 1999 and others) have shown that at high feed velocities byproduct yields are much higher than those observed in the micromixed region. This has been attributed to the necessity of a slower mesomixing step. Although operation in this region is not recommended, mesomixing data provides some valuable insights into the mixing field. Some results from this regime are presented before moving on to the optimization of reactor performance.

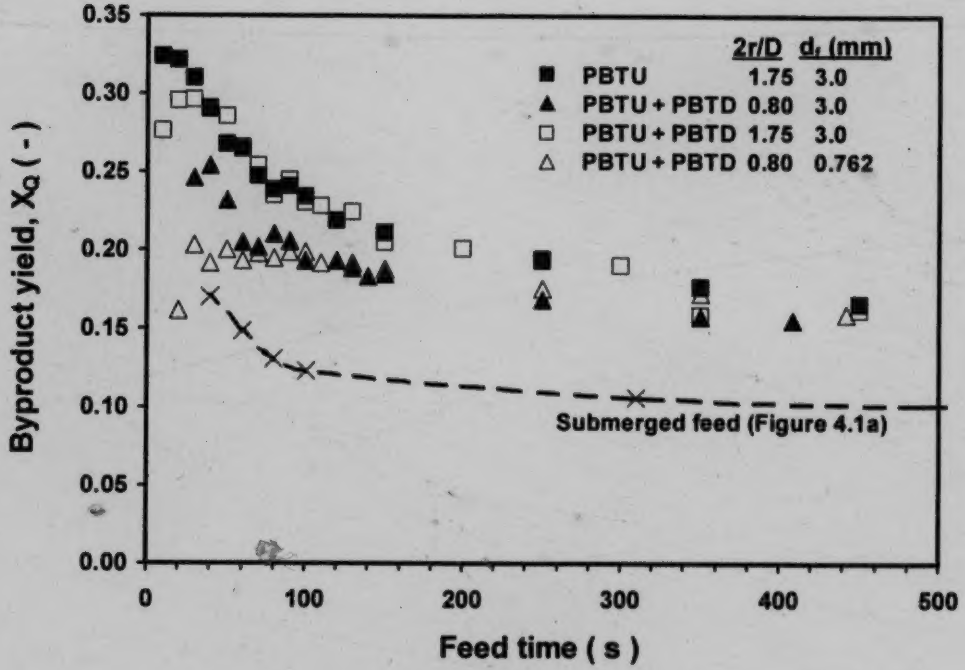

Figure 4.9 Expanded Figure 4.8 showing the effect of feed time on byproduct yield in the mesomixing regime. A small, but significant effect of feed location (2%) and nozzle diameter (up to 10%) is evident for very short feed times.

Figure 4.9 shows the mesomixing data from Figure 4.8 on an expanded scale to highlight operation at high feed velocities. The PBTU with the feed pipe at 2r/D = 1.75 and the PBTU, PBTD combination with feed at 2r/D = 0.8 are again compared. A distinct influence of radial position on X_Q is observed for mesomixing conditions. For moderate values of t_f (in hundreds of seconds) X_Q increases steadily with decreasing t_f due to the increasing effect of mesomixing. The value of X_Q is smaller at 2r/D = 0.8 than at 2r/D = 1.75. When the feed stream is placed closer to the center it penetrates into the discharge stream closer to the impeller and is exposed to higher levels of turbulence. The increase in byproduct formation with reducing t_f continues until very high feed velocities are reached. At very high feed velocities X_Q decreases with decreasing t_f for both cases. This 'tipping over' of the curves and reduction in X_Q at very high feed stream velocities ($t_f \leq$ 20s for 2r/D = 1.75, $Re_F = 1847$ and $t_f \leq 40$s for 2r/D = 0.8, $Re_F = 940$) is due to (i) faster convection into the region of high ambient turbulence and (ii) added turbulence created by the feed streams themselves which are now in the transitional flow regime.

4.3.2.2.3 Effect of nozzle size

In the previous cases reduced feed time was used to increase the feed velocity. Another way of creating a high velocity feed is to decrease the nozzle size. The diameter of the feed nozzle was reduced from 3 mm to 0.762 mm to increase the feed velocity 16 fold at a constant feed time. The Reynolds number of the feed stream was thus also increased 16 times, with Re_F reaching values above 2000 for $t_f < 70$s. Figure 4.9 shows that the byproduct yield for this high velocity feed is substantially reduced for $t_f < 100$s compared to the other surface feed cases where a 3 mm diameter nozzle was used. This is due to the substantially higher turbulence within the jet. The byproduct yield in this high velocity region ($X_Q = 0.20$) is still much higher than the best-case performance with Case 2 ($X_Q = 0.10$).

4.3.2.3. Single PBTU

Figures 4.8 and 4.9 show that in the micromixed region, byproduct yield is unchanged whether the PBTU is used alone or in combination with a PBTD. This result is expected since X_Q in the micromixed regime depends entirely on the turbulence and the feed point and the rate of dissipation of turbulent kinetic energy (ε) near the surface is driven mainly by the up-pumping impeller. The second PBTD improves the overall circulation in the tank but has no direct bearing on local levels of ε near the surface. A second impeller may still be necessary due to other process considerations which require high velocities near the bottom of the tank (e.g. suspension of solid catalysts) or more uniform distribution of turbulence levels.

Summarizing the results from this section, we can clearly conclude that the byproduct yield for surface feed is dramatically reduced by an up-pumping PBT. The large values seen for surface feed with a PBTD ($X_Q = 0.25$) drop to ($X_Q = 0.135$) with a PBTU. This value is close to that obtained with a submerged dip-tube ($X_Q = 0.11$). An up-pumping impeller is recommended when surface feed is necessary. The possibility of further improvements by optimizing impeller submergence and speed remains to be evaluated. This requires definition of the operational limits for the uppumping configuration.

4.3.3. Air entrainment and critical Froude number

Maximizing ε at the liquid surface will minimize X_Q. The rate of dissipation of turbulent kinetic energy at the liquid surface can in turn be maximized by keeping the PBTU as close to the surface as possible for any given impeller speed. However, at any submergence the impeller can be operated only up to a critical Froude number, beyond which air bubbles are entrained into the stirred tank. Experiments were carried out to find the impeller speed at which air bubbles start to be entrained for a range of impeller diameters. In these experiments, the PBTU was positioned at a fixed submergence and the impeller speed was gradually increased until bubbles formed and remained trapped in the tank. This topic will be revisited in greater details in Chapter 5 which also contains additional information about the experimental techniques used for measurement of the impeller speed for air entrainment.

Figure 4.10 shows the critical Froude number as a function of submergence. As expected, increasing submergence gives a higher critical Froude number. Similar trends were observed for two impeller diameters, $D = T/3$ and $D = T/2$. The curves for the two cases do not collapse, indicating that Fr does not capture all of the physical effects. This is discussed further in Chapter 5. Note that for both impellers the Reynolds number was always greater than 2×10^4, even at the lowest critical Froude numbers.

4.3.4. Optimized operation

Given the maximum impeller speed for the PBTU at various submergences (Figure 4.10), performance of the reactor at the maximum N was studied with varying submergence using the smaller impeller ($D = T/3$). Sodium hydroxide was added at a radial position of $2r/D = 0.8$ with $t_f \sim 3000$s for all cases so that operation was in the micromixed regime where byproduct yield is the lowest. Figure 4.11 shows that at any submergence, operating the PBTU at its critical speed reduces X_Q to the minimum value obtained for a submerged feed. Moreover, the amount of byproduct formed for all S is similar to that obtained for the best case submerged feed value ($X_Q = 0.11$). The remarkably constant byproduct yield when feed is added at very low feed rates, but for different submergences, indicates similar levels of turbulence at the surface at Fr'_{crit} for all submergences.

Turbulence levels at the surface were studied further by measuring the velocity near the surface with LDV. Figure 4.12 shows the axial component of the root-mean-square (RMS) velocity, u, for both the uppumping and the down-pumping impellers. For the PBTU, the impeller submergence was varied while the impeller was operated at 98% of its maximum speed, $0.98\ N_E$; results are shown for three submergences. It is seen that u is almost exactly equal for all submergences. This result combined with the data from Figure 4.11 confirms that air entrainment starts at a critical level of turbulence at the surface. Further work is required to determine the full relationship between turbulence at the surface and entrainment and entrapment of air bubbles at the critical Froude number.

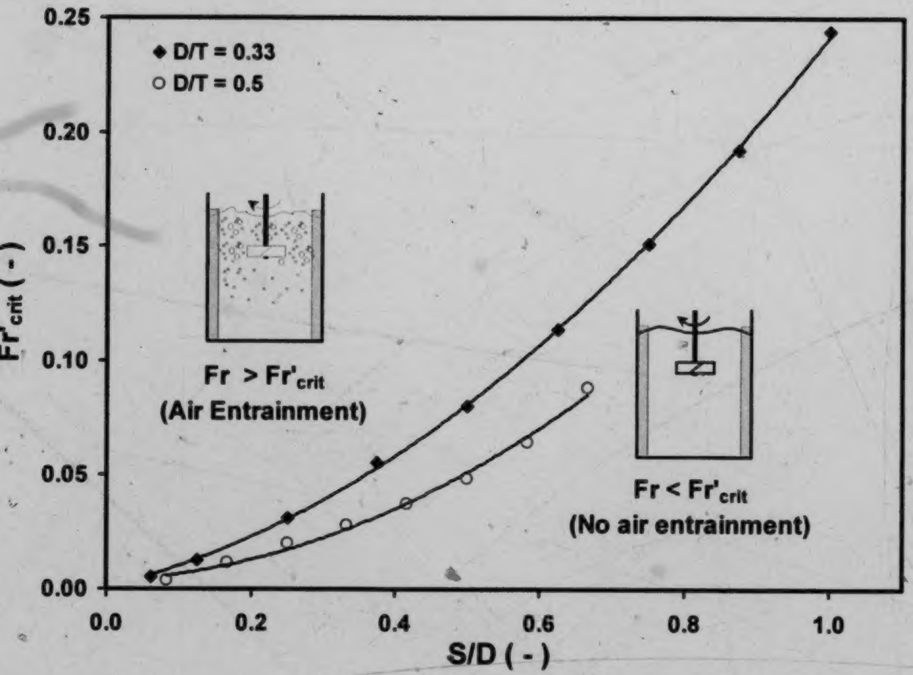

Figure 4.10 Critical Froude number (N_E^2S/g) for the up-pumping impeller as a function of impeller submergence, S. When the impeller is operated above the critical Froude number, air bubbles are entrained into the tank. Since the curves for the two impeller sizes do not collapse, the Froude number does not completely capture the physics of air entrainment at the surface.

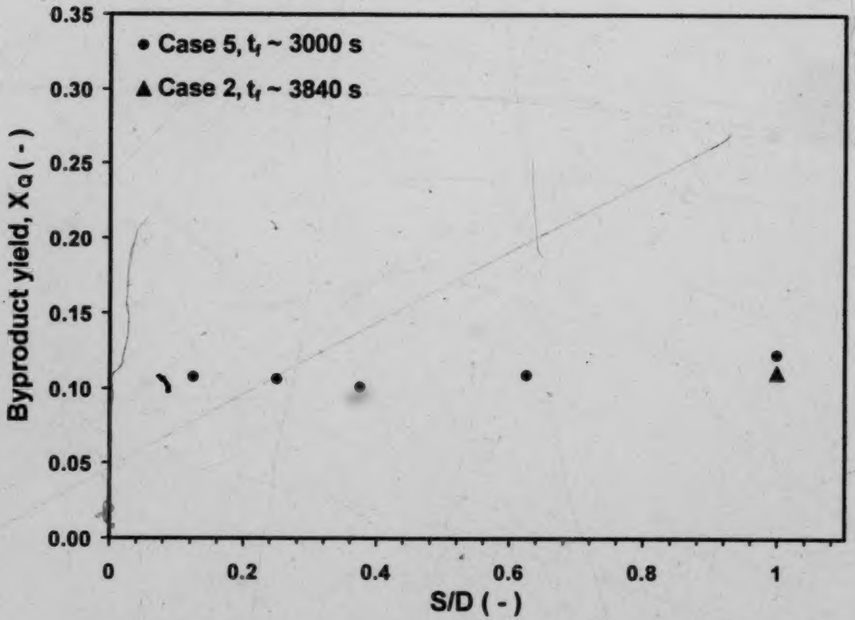

Figure 4.11 Best performance near ($0.96Fr_{crit}$) the critical Froude number. When the up-pumping impeller is operated close to the critical Froude number, the byproduct yield is minimized and is comparable to the best possible performance obtained with a submerged feed pipe, shown as a triangle. Near the critical Froude number, the byproduct yield is independent of submergence, suggesting that air entrainment is a function of surface turbulence rather than of Froude number.

A critical Froude number was also obtained with the PBTD though the value of N_E was much larger (about 763 rpm at C/D = 1 as against 328 rpm at S/D = 1) as expected. Figure 4.12 shows that the turbulence levels at the surface for the outer half of the tank match the values for the PBTU operated at Fr_{crit}. Finally it is seen that the turbulence level at the surface is very small when the PBTD is placed at C/D = 1. This observation is expected and agrees with the data in Figure 4.8 showing large X_Q for surface feed. The peak value of the RMS velocity in the PBTD discharge matches the u for the successful uppumping cases, in agreement with the observation that X_Q for PBTU operated at Fr'_{crit} is close to the value obtained with submerged feed. An important observation from Figure 4.12 is that the radial profile of turbulence is much flatter for the PBTU than the PBTD. This implies a more robust performance with the PBTU with more flexibility in the feed position compared to a submerged feed.

To obtain the best possible performance ($X_Q = 0.11$) at any impeller speed N, the PBTU should be located at a submergence such that $N = N_E$.

4.4. Conclusions

When dealing with certain classes of competitive reactions the current best practice is to feed close to the impeller with a submerged feed pipe. Numerous mechanical, metallurgical and/or operational problems however, arise with the use of dip tubes. An up-pumping impeller is shown to be a stable and robust alternate configuration for minimizing byproduct yield where surface feed is required.

An up-pumping pitched blade turbine located in the upper third of the tank shows very little effect of feed location on byproduct yield in the micromixed regime. A second down-pumping impeller can be added to agitate the lower section without affecting the reaction results. This provides more operational flexibility for difficult or multi-objective processes.

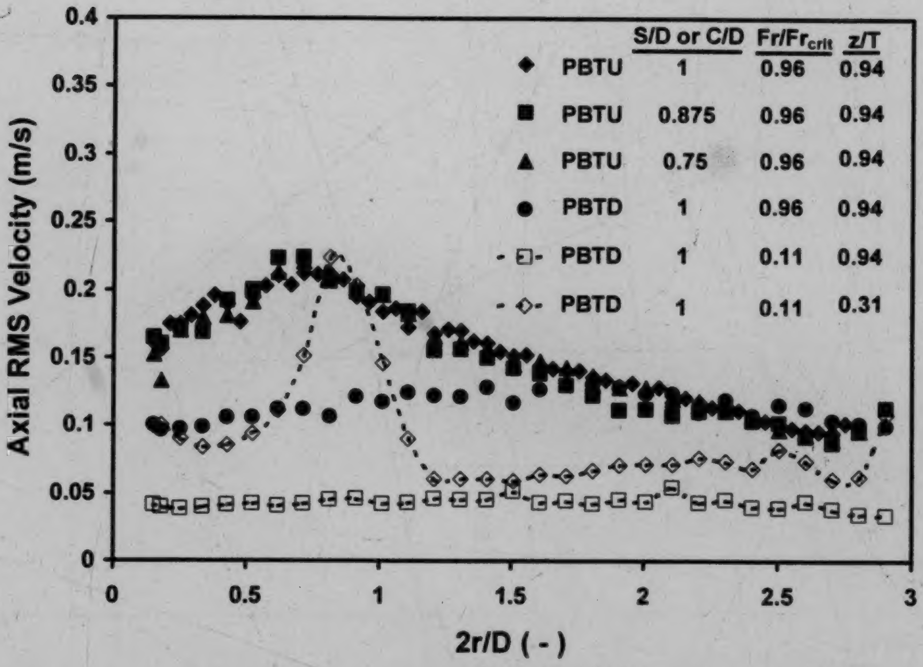

Figure 4.12 RMS velocity measured close to the surface for PBTD and PBTU. At Fr'_{crit} the turbulence levels at the surface are similar irrespective of the submergence or impeller type. These results indicate that the onset of air entrainment occurs when surface turbulence levels reach a critical value.

The lowest byproduct yield was obtained when the PBTU was operated at the critical Froude number. When the impeller is operated at speeds higher than those corresponding to the critical Froude number, air bubbles are entrained into the tank. At $\mathrm{Fr}'_{\mathrm{crit}}$, the byproduct formation matches that obtained for a submerged feed located very close to the impeller. The same result was obtained for a range of impeller submergences. Velocity measurements near the surface show that when the impeller is operated at $\mathrm{Fr}'_{\mathrm{crit}}$, the RMS velocity near the surface is similar irrespective of the submergence: thus air entrainment occurs when the turbulence at the surface reaches a critical value. The ability to obtain the same byproduct formation and levels of surface turbulence for various submergences bodes well for scale-up of this feed configuration.

Chapter 5

Air Entrainment in Baffled Stirred Tanks

5.1. Introduction

Since its advent in the early 1980s the up-pumping axial impeller has been employed in numerous applications ranging from gas dispersion, ingestion of floating solids to the rapid mixing of feed at the surface of stirred tank reactors (Nienow and Bujalski, 2004). The present work looks further into the operation of these versatile impellers. In a stirred tank reactor, feed is traditionally introduced into a submerged impeller region via dip tubes. While this mode of feed addition produces the best results for rapid mixing with competitive reactions, its implementation is often problematic. Bhattacharya and Kresta (2004) showed that product quality could be maintained with surface feed of reactants if

- An up-pumping pitched blade turbine (PBTU) was used and
- The impeller was operated at the point of air entrainment

At high impeller speeds the PBTU starts ingesting air bubbles from the open surface of the vessel. While entrainment of gases from the headspace and the additional mass transfer it provides can be beneficial for some processes it can lead to serious problems in the case of others. Entrainment of gases from the headspace and additional mass transfer is beneficial in processes such as wastewater treatment, reactions with significant heat effects and those requiring large amounts of recycle. On the other hand, in processes such as suspension polymerization, entrained bubbles can adhere to droplets and give rise to poor polymer beads (Tanaka et al., 1986; Tanaka and Izumi, 1987). The impeller speed N_E at which the entrainment of air bubbles commences is therefore an important operational limit. Many previous studies have been conducted in agitated tanks with $N > N_E$, most directed towards the development of parametric models from experimental data. While empirical correlations provide simple and practical design guidelines, they are not applicable universally and often fail in conditions outside those under which they were developed. Given the importance of the impeller speed at the onset of air entrainment it is desirable to obtain better understanding and models of the processes occurring at the liquid surface. That is the primary objective of this study.

Gas entrainment from open liquid surfaces can occur under a variety of conditions, which can be broadly classified into three groups:

- Dispersion and entrainment of gases from surface vortices in *un-baffled stirred tanks*,
- Entrainment of gases from open liquid surfaces of *baffled mixing vessels* and
- Surface aeration of *fast moving bodies of liquid* e.g. in flow down spillways, chutes or in turbulent flows with breaking waves.

Gas entrainment into un-baffled vessels occurs by a mechanism significantly different from that for baffled vessels and breaking waves. In un-baffled tanks, a large central vortex forms due to the centrifugal forces acting on the rotating liquid. Studies (experiments by Rieger et al., 1979; review by Markopoulos and Kontogeorgaki, 1995; and numerical analysis by Ciofalo et al., 1996) show that when the impeller speed is increased beyond a critical value, dependent on the liquid properties, the vortex reaches the impeller and is broken up by the blades into bubbles that are entrained into the tank. On the other hand, air entrainment in the case of baffled vessels and breaking waves is a result of more subtle interactions between the liquid surface and the turbulent flow field below it.

While the mechanisms of air entrainment into baffled vessels and through moving liquid surfaces are somewhat similar, the focus of investigations in these two cases has been traditionally very different. Studies on air entrainment into baffled vessels (reviewed recently by Patwardhan and Joshi, 1998) have dealt mainly with characterization of the liquid circulation that is sufficient for dispersal of gas bubbles formed at the surface. Less attention has been directed towards the turbulent surface itself. Investigations on aeration in fast moving bodies of water, on the other hand, have been devoted more to identifying the conditions for bubble formation and the behaviour of the turbulent surface. While conclusive understanding of the phenomenon is hampered by the inability to accurately measure the flow at the surface, progress has nonetheless been significant (Banerjee, 1994; Eggers, 2001; Brocchini and Peregrine, 2001; Hazuku et al., 2003). Summaries of results from both categories are presented below.

5.1.1. Studies on Gas Entrainment in Baffled Vessels

One of the first published reports on air entrainment from the surface of a stirred tank (often called surface aeration) was by Calderbank (1958). While conducting experiments to measure interfacial area of bubbles in sparged stirred tanks, Calderbank observed an increase in the total interfacial area of the dispersed bubbles at high impeller speeds and attributed it to aeration from the surface of the tank. Similar increase in gas hold up and/or mass transfer coefficient due to surface aeration was reported in later studies with Rushton turbines (Nienow et al., 1979, Chapman et al., 1980) and six-bladed pitched blade turbines (Albal et al., 1983; Veljković et al., 1991). General conclusions from these studies are that an increase of impeller speed or a decrease in impeller submergence causes an increase in aeration. Gas sparging affects liquid circulation and has also been found to decrease the rate of surface aeration (Nienow et al., 1979; Chapman et al., 1980; Albal et al., 1983; Veljković et al., 1991).

While sparged vessels have been the focus of a majority of the investigations, some were also conducted in unsparged tanks. Sverak and Hrubý (1981) measured the impeller speed at which gas entrainment from the surface was enough to cause a change in the power consumption. They proposed that small vortices appeared at the surface of the liquid at high impeller speeds, which were throttled by the action of surface tension and turbulent fluctuations to form bubbles. Greaves and Kobbacy (1981) conducted experiments in a 6L flat-bottomed tank agitated with Rushton turbines and studied the effects of fluid properties on the onset of surface aeration. They too measured surface aeration by the drop in power consumption and found that the impeller speed and clearance had a significant affect on aeration, as did the fluid properties. Heywood et al. (1985) carried out experiments with radial and down-pumping axial impellers and correlated their data with geometric parameters (C, D, T) and fluid properties. They reported that surface aeration could be observed at different levels of intensity depending on impeller speed and graded speeds starting with that at which bubbles first form (n_{SA1}), the speed at which they are drawn down to the impeller (n_{SA2}) and finally the speed at which air entrainment is sufficiently large to cause a noticeable drop in power consumption (n_{SA3}). In general $n_{SA1} < n_{SA2} < n_{SA3}$. From their experiments the authors reported that n_{SA1} increases with

- A reduction in D (depending on impeller design) and C
- An increase in H, the later being more prominent in axial than in radial impellers and
- Surface tension (in the range 0.073 and 0.022 N/m) had only a small effect on n_{SA1}. Other studies (Sverak and Hrubý (1981); Tanaka et al., 1986; Tanaka and Izumi, 1987; the present work) have found a greater influence of the fluid properties on the onset of aeration.

The earlier studies based on a drop in power consumption could measure only the highest speed, n_{SA3}. The later studies have been directed towards measurement of the onset of aeration and dispersion of bubbles but the distinction between n_{SA1} and n_{SA2} is not always very clear.

Tanaka et al. (1986) studied the formation of bubbles at the surface of a tank containing polymer solutions and agitated with a Rushton turbine, containing polymer solutions. They studied the effect of parameters such as D/T, S, H and of the fluid viscosity and surface tension. Working on a similar system, Tanaka and Izumi (1987) carried out a similar experimental study but expanded their variables to include the type of impeller, number and length of baffles and presence of a draft tube. They conducted experiments not only with Rushton turbines, propellers and down-pumping pitched blade turbines but also with up-pumping pitched blade turbines. Their results show that N_E was the lowest for a Rushton turbine and highest for the up-pumping axial impellers with the down-pumping configuration in between. They also found that very short baffles made aeration easier, N_E increased with an increase in number of baffles and an increase in surface tension, varying by a power of 1.8. Veljkovič et al. (1991) studied the effect of sparging on air entrainment from the surface of a fully baffled tank agitated by six-bladed 45° PBT. When the tank was unsparged, they observed that the onset of air entrainment occurred at a constant impeller tip speed, $N_SD = 0.732$. Correlations from these investigations, developed for the types of impellers used in this study, are reproduced in Table 5.1. These correlations are also compared with each other by evaluating them for the conditions of the present experiment and shown as a parity plot in Figure 5.1. There is a wide scatter in the data highlighting the problems of using parametric models across a range of experimental conditions.

Due to the strong dependence of the flow field on geometry, it is difficult to obtain an empirical correlation that is universally applicable. There is a requirement for more rigorous modelling of surface aeration but only a few such studies are available. Greaves and Kobbacy (1981) proposed a model of surface aeration where the process was visualized as consisting of two steps (i) formation of surface vortices which give rise to the bubbles and (ii) drawing down of the bubbles by liquid circulation. They assumed that there was an excess of bubbles near the surface so that only the second step involving bubble draw down needed to be considered in the model since it was rate controlling. The liquid circulation had to be strong enough to drag bubbles into the tank, hence the impeller speed for onset of surface aeration was modeled simply by equating the circulation velocity to the bubble rise velocity. Joshi et al. (1982) used the same approach and assumptions but relied on more sophisticated methods for estimating the circulation velocity and the bubble rise velocity. Sverak and Hrubý (1981) modeled bubble formation at the surface by comparing it to the formation of a non-rotational vortex when fluid is sucked into a thin, vertical tube placed a short distance below the surface and pointing towards it. When the flow rate of the fluid into the tube is increased sufficiently, the vortex from the surface reaches the tube and gas starts entraining into the opening of the tube. They further assumed that this type of vortex formation was governed only by the Froude number ($Fr = N^2D/g$) and a modified Strouhal number ($Sl = ND/v^*$, where v^* is the suction velocity into the pipe at onset of gas entrainment) such that: $Fr^p.Sl^q$ = constant, where p and q are constant indices. Using this argument they developed a semi-empirical relation for N_E. Patwardhan and Joshi (1998) also proposed a two-step model for surface aeration using scaling arguments. An empirical relation was derived for the rate of bubble entrapment by assuming it to be proportional to the square of the impeller

Table 5.1 Minimum impeller speeds for the onset of surface aeration. The nomenclature for impeller speed is adopted from the parent reference. They are all roughly equivalent to the minimum impeller speed for air entrainment, N_E, used in the present study.

Reference	Experimental Conditions	Impeller Type	Correlation
Sverak and Hrubý (1981)	▪ $D/T = 0.33$ ▪ C/T - ▪ $H/T = 1$ ▪ Fluids used: Distilled water, glycerine solution, carbon tetrachloride, ethyliodide, aq. solution of tenside ▪ Agitator with two flat blades also used ▪ $V_{Tank} = 0.16$ to 140L	Rushton Turbine	$n_{crit} = 4.8D^{-0.614}\left(V^{*}\right)^{0.228}\left(\frac{1000}{\rho}\right)^{0.317}\left(\frac{1}{V_{Tank}}\right)^{0.094}$
Joshi et al. (1982)	Data from literature	Rushton Turbine	$\frac{N_S D^{1.98}}{T^{1.1}} = \frac{1.65}{P_O^{0.125}}\left(\frac{\sigma g}{\rho}\right)^{0.19}\left(\frac{\mu}{\mu_g}\right)^{0.031}\left(\frac{d_W}{D}\right)^{0.625}$
Heywood et al. (1985)	▪ $D/T = 0.22$ to 0.938 ▪ $C/T = 0.25$ to 0.50 ▪ $H/T = 0.56$ to 1.29 ▪ Fluids used: Distilled water, potassium sulphate solution and Isopropanol analar ▪ $D = 0.128$ to 0.54 m ▪ Propeller, Torrance disperser also used	Rushton Turbine	$n_{SA1} = 1.04\,T^{0.616}\,D^{-0.97}\,C^{-0.23}\,H^{0.59}$ (for water)
		6-Bladed 45 Pitched Blade Turbine	$n_{SA1} = 0.139\,T^{-0.545}\,D^{-2.05}\,C^{-0.25}\,H^{1.64}$ (for water)

Table 5.1 Contd.

Tanaka et al. (1986)	- D/T = 0.25 to 1 - C/T = 0 to 0.9 - H/T = 0.66 to 1.33 - Fluids used: Aqueous Polyvinyl alcohol solutions - T = 0.1, 0.15 and 0.2m - D = 0.05, 0.075 and 0.1m	Rushton Turbine	$N_r = 126\left(\frac{\mu}{\sigma}\right)^{0.94}\left(\frac{D}{T}\right)^{-2.3}\left(\frac{H}{T}\right)^{0.44}\left(1-\frac{C}{H}\right)^{0.3}$
Tanaka and Izumi (1987)	- D/T = 0.32 to 0.50 - S/T = 0.2 to 0.75 - H/T = 0.67 to 1.42 - Fluids used: Aqueous Dodecyl-ether solution - T = 0.12, 0.15, 0.2m and D = 0.05m - 0-4 full baffles and 2 half baffles	Rushton Turbine	$\left[Fr = \frac{N_E^2 D}{g}\right] = 0.023\left(\frac{\sigma}{\sigma_o}\right)^{3.6}\left(\frac{D}{T}\right)^{-3.6}\left(\frac{H}{T}\right)^{0.88}\left(1-\frac{C}{H}\right)^{0.6}$
		Downpumping Pitched Blade Turbine	$\left[Fr = \frac{N_E^2 D}{g}\right] = 0.084\left(\frac{\sigma}{\sigma_o}\right)^{3.6}\left(\frac{D}{T}\right)^{-3.6}\left(\frac{H}{T}\right)^{1.44}\left(1-\frac{C}{H}\right)^{1.06}$
		Up-pumping Pitched Blade Turbine	$\left[Fr = \frac{N_E^2 D}{g}\right] = 0.080\left(\frac{\sigma}{\sigma_o}\right)^{3.6}\left(\frac{D}{T}\right)^{-3.6}\left(\frac{H}{T}\right)^{1.72}\left(1-\frac{C}{H}\right)^{1.24}$
Veljković et al. (1991)	- D/T =1/3 - C/T ~ 1/3 - H/T = 1 - Fluid used: Distilled water - T = 0.2 to 0.675m	Rushton Turbine	$N_S D = 0.732$

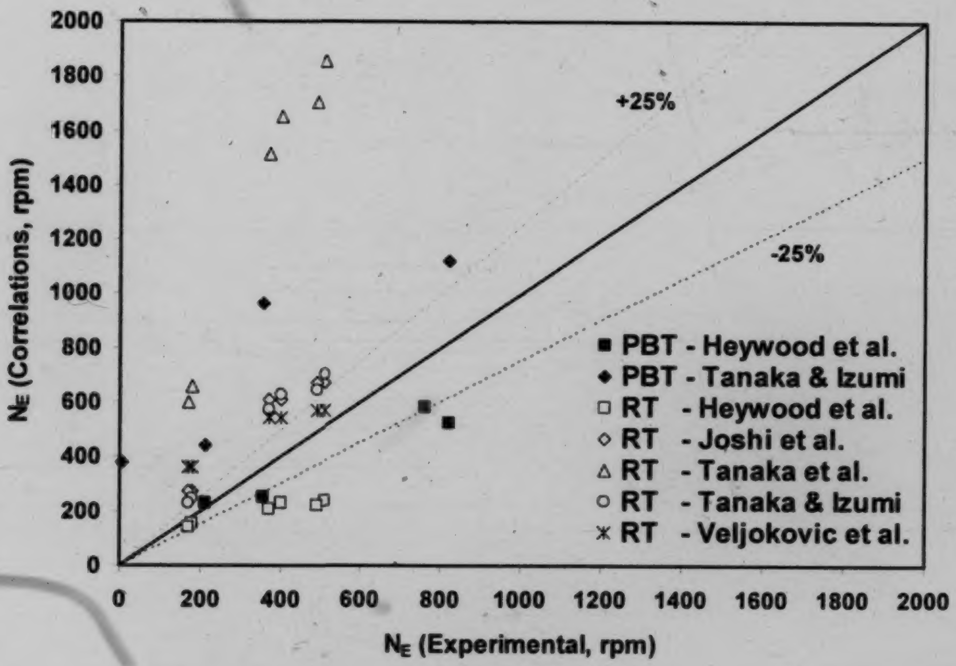

Figure 5.1 Comparison of experimental results from the present study with parametric models from previous studies. Empirical correlations are not applicable outside the conditions for which they are developed.

tip speed (~ ND) and inversely proportional to the distance of the surface from the impeller (~ 1 – S/H). In the second step, the newly formed bubbles are carried from the surface to the interior of the tank. The rate of bubble carriage was assumed to be proportional to the liquid flow generated by the impeller (~ N_QND^3) and inversely proportional to the distance from the surface (~ 1 – S/H). The two steps together gave the total rate of air entrainment and hence an expression for the gas holdup due to surface aeration. Although these models correctly envision separate bubble formation and bubble draw down steps, they are mainly geared towards development of relation between liquid circulation and draw down of bubbles which is used to develop conditions for the onset of aeration. The present study shows that consideration of only this step is insufficient. Another perspective of surface aeration is presented here, where the conditions necessary for bubble formations are studied more closely.

5.1.2. Studies on Gas Entrainment in Fast Moving Bodies of Liquid

Civil and environmental engineers and oceanographers have all studied self-aeration in fast flowing bodies of water in steep, open channels like spillways, chutes etc. (Volkart, 1980; Chanson, 1993; Rein, 1998), and ocean-atmosphere interactions in breaking waves (Deane and Stokes, 2002). In all these flows gases are entrained into a liquid thorough the gas-liquid interface due to complex interactions between the interface and the flow-field underneath it. Studies have broadly identified three mechanisms as being responsible for entrainment of air bubbles into fully turbulent liquid flows:

- Breaking waves
- Drop impact on the liquid surface (Lane, 1939; Volkart, 1980, Rein, 1998).
- Entrapment of air by vortices near the liquid surface (Chanson, 1993; Ervine and Falvey, 1987)

The first mechanism of breaking waves falls into the category where very strong turbulence interacts with the surface causing a rupture of the interface with subsequent air entrainment. This mechanism can be eliminated as an explanation for the initial stages of air entrainment in an open stirred tank.

The second mechanism, air entrainment by drop impact, has been observed in self-aerating flows in steep channels with open tops. Lane (1939) was among the first researchers to report that air bubbles formed in spillways due to plunging drops of water. Clumps of liquid are periodically ejected from the turbulent gas-liquid interface. These drops eventually fall back, impinge on the liquid surface and entrain air bubbles. It has been proposed that it is the transverse turbulent velocity fluctuations at the surface that cause the initial ejection of the drops. The equations describing the conditions necessary for ejection of liquid and subsequent bubble entrainment were developed in early studies using energy and force balances (Gangadharaiah et al., 1970). These balances were further modified and improved by later workers (Volkart, 1980; Rein, 1993 and 1998) who found the Weber number of the drops to be one of the key parameters defining the critical conditions. Volkart (1980) reported that the diameter of the drops formed in their experiment averaged about 6 mm (ranging from 1 to 10 mm) and that these drops were ejected to a height of 7.4 cm from the liquid surface for a liquid velocity near the surface of about 5 m/s. The mean flow velocities reported in other experiments on self-aerating open channel flows and that obtained from the model of Rein (1998) are even higher. Compared to these values, the maximum measured mean velocity near the liquid surface of the stirred tank was only 0.25 m/s even when the impeller was being operated at $0.97N_E$. Large amounts of liquid drops were never observed above the liquid surface for $N \sim N_E$. It therefore appears that bubble formation by ejection of a drop and its subsequent impact on the liquid surface is not a realistic representation of the onset of air entrainment at the open surface of a stirred tank.

In the third mechanism of air entrainment, air is entrapped by turbulent velocity fluctuations on the free surface (Hino, 1961; Chanson, 1993). When the turbulent kinetic energy is strong enough to overcome surface tension and gravity effects, there is a localized deformation of the surface and air is entrained. In order to determine incipient air entrainment workers used force or energy balances with the condition that the turbulent energy normal to the surface had to be large enough to overcome the surface tension of the entrained bubble (Rao and Rajaratnam, 1961 and Ervine and Falvey, 1987). In this mode of air entrainment, turbulence plays an active role in deforming the surface to form a bubble. This balance of hydrostatic pressure, surface tension and turbulent kinetic energy at the surface is the most widely accepted mechanism for air entrainment through turbulent liquid surfaces.

5.1.3. Interactions Between Turbulence and the Open Surface

The nature and magnitude of the free surface deformations is determined by the relative strength and the interactions between gravity, surface tension and the turbulent kinetic energy reaching the surface. Gravity and surface tension stabilize the free surface while turbulence tries to disrupt it. The relative magnitude of these influences can be estimated from the Froude (Fr) and Weber (We) numbers at the surface:

$$Fr = \frac{q}{\sqrt{gL}} \tag{5.1}$$

$$We = \frac{\rho q^2 L}{\sigma} \tag{5.2}$$

where q is a suitable characteristic turbulent velocity scale and L a characteristic length scale near the surface. When Fr is small, turbulence has insufficient energy to cause changes in the surface and gravity effectively stabilizes it. On the other hand when Fr is large, turbulence is the dominating influence and can cause large surface deformations or excursions. Similarly, surface tension stabilizes the interface at low Weber numbers while at higher We turbulence takes over and causes breakage of the surface with eventual formation of drops and sprays. Brocchini and Peregrine (2001) presented a comprehensive description of the interactions between gravity, surface tension and turbulent kinetic energy in their discussions on free surface deformations in water flows. Their ideas are used here to identify the dominating influences that may be present at the free surface of an open tank. Figure 5.2 is reproduced from their work. The two dotted lines with positive and negative slopes represent the critical Froude (Fr_{crit}) and Weber (We_{crit}) numbers and delineate the L-q plane into four regions. Fr_{crit} and We_{crit} are the values of the Froude and Weber numbers above which the effects due to turbulence dominate over those due to gravity and surface tension, respectively. While the dotted lines imply unique values for the critical Froude and Weber numbers, the interactions between turbulence and the liquid surface are not sharply demarcated into completely

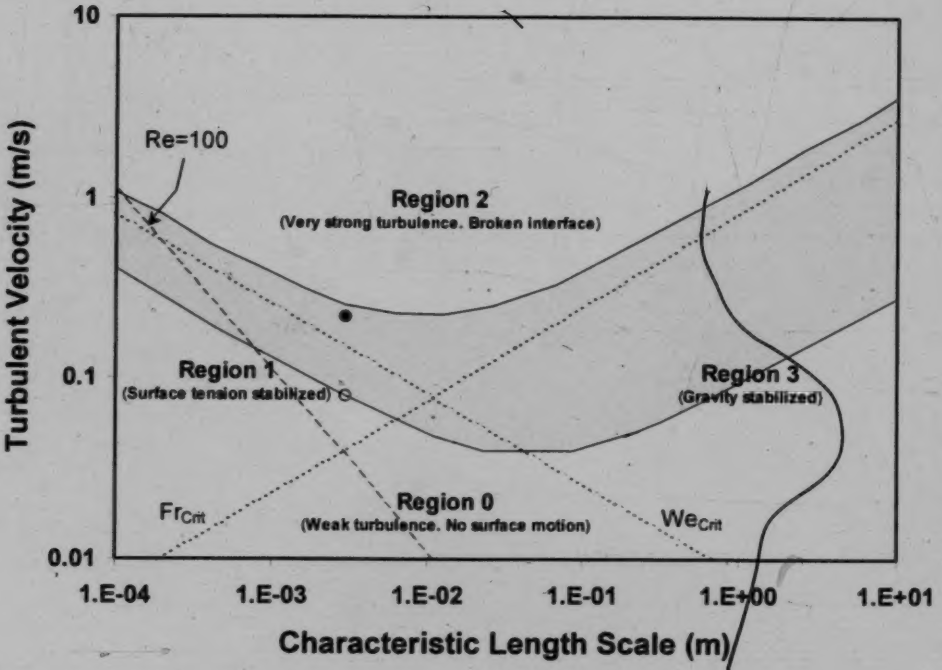

Figure 5.2 Regions characterizing the effect of turbulence on a free surface (Brochinni and Peregrine, 2001). In the shaded region interaction between turbulence and the surface increases from gentle surface undulations at the lower limit to surface breakage at the upper. Four limiting regions are shown by the dotted lines at the We and Fr limits. The dashed line is for Re = 100. The filled and hollow symbols represent the maximum and the minimum RMS velocities measured at the surface of the tank. The characteristic length scale for these symbols is the diameter of the entrained bubbles.

turbulence dominated or only gravity and surface tension affected regions. Rather, there is a gradual shift from a surface that is slightly deformed due to the incipient effects of turbulence, to a surface that is strongly affected by turbulence and breaks up. The shaded band in Figure 5.2 represents this gradual change in surface characteristics. Brocchini and Peregrine (2001) used simplified energy balances to estimate the upper and lower bounds of this region.

While the shaded region is closer to the actual state of the surface, the two dotted straight lines delineate the L-q plane into regions where the relative importance of gravity, surface tension and turbulence change according to the characteristic length and velocity scales. The characteristics of the four regions in Figure 5.2 are as follows:

- Fr and We numbers are both very small in *Region 0*. The turbulent kinetic energy in this region is so low that the surface remains unaffected with little or no disturbance.
- In *Region 1*, the Froude number is large ($Fr > Fr_{crit}$) while the We number is small ($We < We_{crit}$). Gravity is unable to resist deformation of the surface due to turbulence but the influence of surface tension is strong and this prevents the surface from being substantially ruptured.
- In *Region 3*, the Weber number is large ($We > We_{crit}$) but the Froude number is small ($Fr < Fr_{crit}$). Gravity stabilizes the surface, giving rise to an interface which is essentially flat, but turbulence can disturb the surface locally to form small waves, dimples and scars. These can give rise to localized surface breaking and entrainment of gas.
- In *Region 2*, both Fr and We are above the critical value, neither surface tension nor gravity can maintain surface cohesion and the interface breaks up violently into small drops and bubbles.

It is possible to identify the dominant factor affecting the liquid surface if its location on the L-q plane can be estimated using suitable values of L and q. Approximate operating points for the free liquid surface in an open stirred tank are shown in Figure 5.2. The velocity scale, q is equated to the vertical component of the root mean square velocity (RMS, u), measured close to the surface. The highest and lowest measured values of u are

0.22 and 0.08 m/s. The characteristic length scale is related to the local integral length scale of turbulence. Taking this to be close to the scale of the entrained bubbles (3 mm from visual observations) puts surface entrainment on the surface tension stabilized side of the figure, below the level of a violently broken surface.

5.2. *Model of turbulence-surface interactions*

The operating points for the stirred tank in Figure 5.2 show that bubbles form due to the interaction between turbulence and the air-liquid interface. The mechanism of bubble formation and its subsequent distribution throughout the tank is shown in Figure 5.3. Two steps have to occur simultaneously to produce noticeable air holdup. The turbulent kinetic energy at the surface has to overcome surface tension, deform the surface and produce bubbles. The mean flow near the surface then has to be strong enough to drag down the newly formed bubbles. Once the bubbles join the main liquid circulation loop they remain trapped within the tank for a period of time. Force and energy balances provide a framework for analysis.

5.2.1. Bubble Formation

Bubbles will form when air is entrapped by the vortices near the surface. The turbulent kinetic energy deforms the surface and pulls in a bubble at the air-liquid interface. The specific turbulent kinetic energy available at the surface is

$$E_T = C_1 u^2 \qquad (5.3)$$

The surface energy needed to deform the surface with a radius of curvature 'r_b' is:

$$E_S = \frac{2\sigma}{\rho r_b} \qquad (5.4)$$

As the bubble forms, hydrostatic pressure resists bubble submergence in the liquid. The specific potential energy associated with this gravitational influence is:

$$E_P = g \cdot y \qquad (5.5)$$

where y is the depth of the deformation at the surface. Combining Equations (5.3), (5.4) and (5.5) gives:

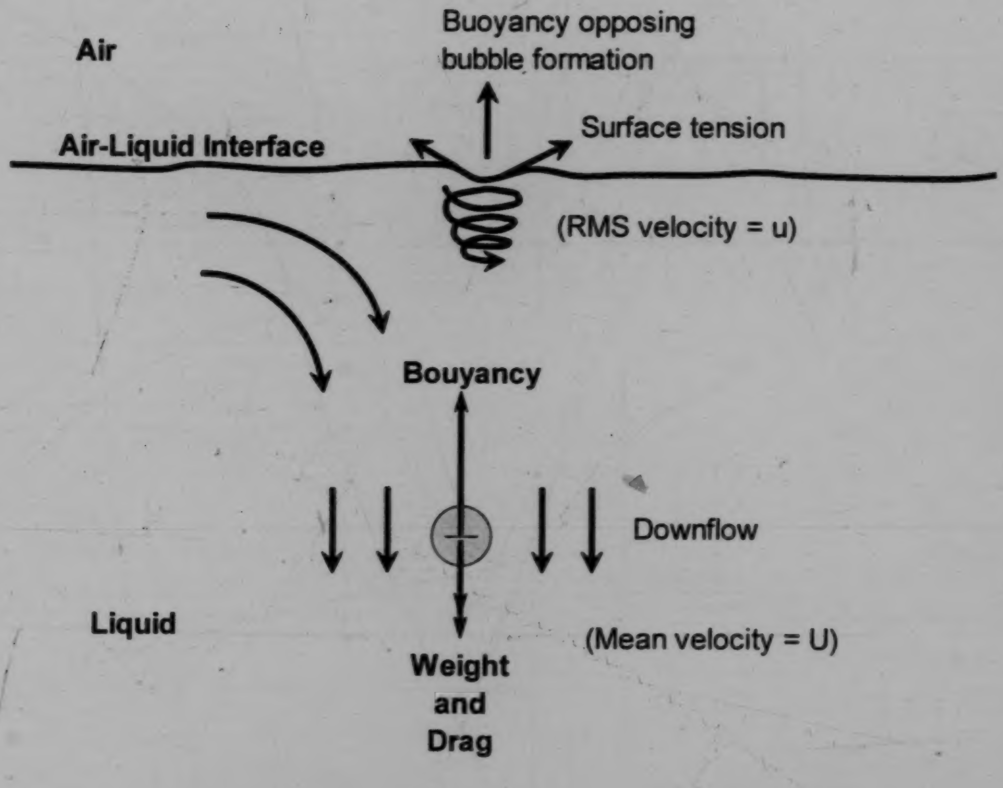
Buoyancy opposing
bubble formation
Air
Surface tension
Air-Liquid Interface
(RMS velocity = u)
Bouyancy
Downflow
Liquid
(Mean velocity = U)
Weight
and
Drag

Figure 5.3 Proposed mechanism for air entrainment. Bubbles are formed at the interface when the turbulent kinetic energy is strong enough to break the stabilizing effects of surface tension and gravity. The newly formed bubbles are pulled into the tank by the mean down-flow.

$$C_1 u^2 = \frac{2\sigma}{\rho r_b} + gy \qquad (5.6)$$

It is difficult to measure the depth of deformation, y, directly but its magnitude can be estimated by relating it to the inverse mechanism of eddy impingement on liquid surfaces. Davies (1972) developed an expression for the maximum height of the bulge, y_m, by assuming it to be a normal error curve and relating its apex (y_m) to the length scale of the impinging eddy, ℓ. He noted that the relative importance of hydrostatic pressure to surface tension depends mainly on the fluid properties and used a simple force balance at the surface to obtain the eddy length (ℓ_{crit}) where the two influences were equal:

$$\ell_{crit}^2 = \frac{16\sigma}{\rho g} \qquad (5.7)$$

In the case of water $\ell_{crit} = 11$ mm, therefore the effect of hydrostatic pressure can be neglected when $\ell < 11$mm. With reference to Figure 5.2 this is equivalent to restricting operation to the surface tension dominated Region 1 on the left. Since the maximum bubble size observed in the tank was of the order of a few millimeters, the length of the bubble forming eddy, $\ell < 11$ mm and the hydrostatic term can be neglected in the energy balance at the surface. Equation (5.6) is then simplified to the condition for bubble entrainment:

$$u^2 \geq C_1' \frac{\sigma}{\rho d_b} \qquad (5.8)$$

where it is assumed that the radius of curvature is equivalent to the bubble radius. The inequality in Equation (5.8) emphasizes the fact that E_T in Equation (5.3) is the minimum turbulent kinetic energy needed to form a bubble.

5.2.2. Bubble Retention

Bubbles with $d_b \leq 2$ mm can be approximated as spheres. If it is also assumed that there is no slip at the surface of the sphere and that the bubble interface is absolutely uncontaminated then the drag force on the bubble can be calculated after Stokes (1851). The equilibrium between the weight of the bubble, the drag force, and the buoyancy force gives the rise velocity U_∞ of this simplified bubble:

$$U_\infty = \frac{1}{18}\frac{(\rho-\rho_g)}{\mu} g d_b^2 \qquad (5.9)$$

In order to retain the bubble in the tank, the downward component of the mean velocity near the surface (U) has to be equal to the bubble rise velocity. Hence, a mean flow with a downward axial velocity component equal to or greater than U will drag down bubbles of size up to d_b. where:

$$d_b = \sqrt{\frac{18\mu U}{g(\rho-\rho_g)}} \qquad (5.10)$$

Since $\rho_g << \rho$, Equations (5.8) and (5.10) simplify to give:

$$u^4 \; \alpha \left[\sigma^2 \frac{1}{\mu\rho^2}\frac{g}{U}(\rho-\rho_g)\right] \approx \left[\frac{\phi}{U}\right] \qquad (5.11)$$

where ϕ depends only on the fluid properties:

$$\phi = \frac{\sigma^2 g}{\mu\rho} \qquad (5.12)$$

Equation (5.11) shows that a higher level of turbulence is needed to deform the surface and form bubbles when there is an increase in surface energy due to an increase in surface tension, while an increase in the other fluid properties (μ or ρ) makes it easier to entrain air. Equation (5.11) encapsulates the key feature of the proposed mechanism of initial air entrainment: a critical relation exists between the fluctuating velocity that forms the bubble and the mean velocity that traps the bubble inside the tank.

The Reynolds, Weber and Froude numbers associated with the mean flow near the liquid surface are defined using the mean axial velocity (U) as the characteristic velocity scale:

$$Re_{surf} = \frac{\rho U L}{\mu} \qquad (5.13)$$

$$We_{surf} = \frac{\rho U^2 L}{\sigma^2} \qquad (5.14)$$

$$Fr_{surf} = \frac{U^2}{gL} \qquad (5.15)$$

Equation (5.11) combined with the definitions in Equations (5.13) to (5.15) gives the relation between u/U and the dimensionless numbers associated with the mean flow at the point of incipient air entrainment:

$$\frac{u}{U} \sim C''\left[\frac{Re_{surf}}{We_{surf}^{2}\,Fr_{surf}}\right]^{0.25} \qquad (5.16)$$

The characteristic length scale, L, falls out of Equation (5.16) so its choice is really arbitrary and Equation (5.16), like Equation (5.11), simply presents the critical relation between fluid properties, the mean flow and the ratio u/U at the point of incipient air entrainment. When the left hand side of Equation (5.16) is larger than the right hand side air bubbles are expected to form at the surface and get dragged into the tank. Velocity measurements made close to the surface at the onset of air entrainment will be are used to test the proposed mechanism.

5.3. Experimental procedure for measurement of N_E

In each run, a 10L cylindrical glass tank was first filled with the experimental fluid and the impeller was positioned at the desired location. The impeller location is defined by its clearance (C) from the tank bottom for a PBTD or RT (Figure 5.4a) and by its submergence (S) from the liquid surface for a PBTU (Figure 5.4b). After fixing the impeller location the impeller speed was set and the tank allowed to equilibrate for a period of 2-3 minutes. The impeller speed at the onset of air entrainment was determined by observing the number of bubbles entrained into and remaining within the tank. Once N_E was found approximately, the impeller speed was reduced by 10 rpm, the step-size was reduced and N was again increased stepwise to obtain a better estimate of N_E. The bubble density in the tank varied with the impeller speed as follows:

- At very low impeller speeds there were hardly any bubbles in the tank. This is seen in Figure 5.5 for $N < N_E$. The liquid surface was almost undisturbed with very little perturbation at the surface.
- As the impeller speed was increased the liquid surface became more active, a few bubbles were entrained temporarily into the tank before escaping out of it. At these

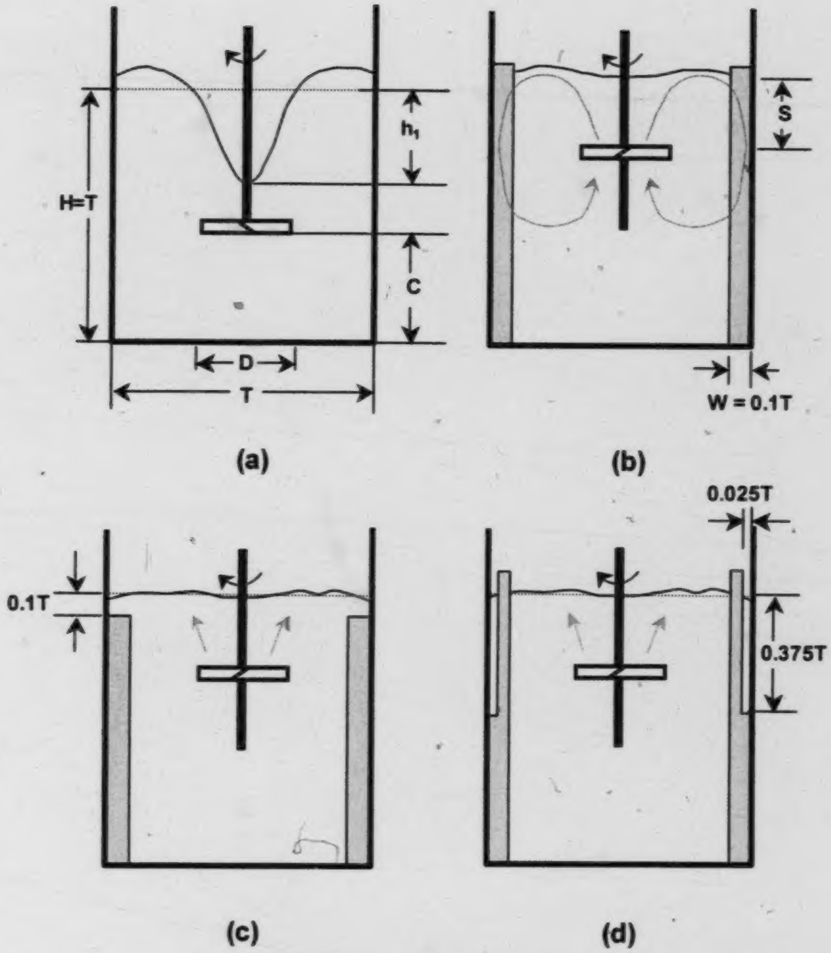
h1
H=T
C
D
T
(a)
S
W = 0.1T
(b)
0.025T
0.1T
(c)
0.375T
(d)

Figure 5.4 **Experimental configurations: (a) Vortex formation in un-baffled tank (b) Standard baffles and PBTU (c) Short baffles and PBTU (c) Notched baffles and PBTU.**

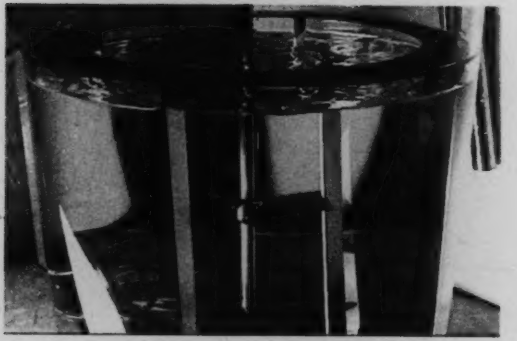

N < N_E

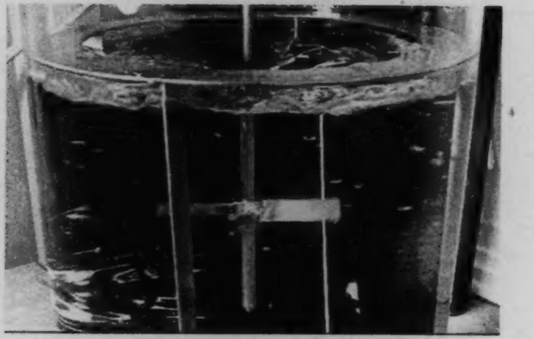

N ~ N_E

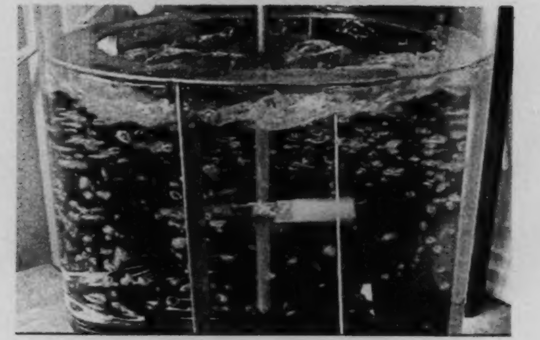

N > N_E

Figure 5.5 **Qualitative description of the surface of the tank when the impeller speed is below, at and above N_E.**

low impeller speeds the number of bubbles remaining permanently in the tank was negligible.

- As the impeller speed approached N_E the number of entrained bubbles increased until finally around N_E there was a marked increase in the bubble population which stayed permanently within the tank. This is shown in Figure 5.5 for $N \sim N_E$. The liquid surface at N_E was turbulent but there was no splashing or formation of sprays.
- When $N > N_E$ the gas holdup in the tank was substantial. The most distinctive feature was the large convolutions of the liquid surface accompanied by loud noise, splashing and ejection of liquid droplets from the surface. The violent movement of the liquid surface and the large gas holdup in the tank is evident in Figure 5.5 when $N > N_E$.

The change in state of the liquid surface with increasing N is traced by the locus of the operating point that moves vertically in Figure 5.2. The operating point starts in Region 0 at very low speeds ($N < N_E$), moves through the shaded region with increasing N and finally reaches Region 2 when $N > N_E$.

Because of the subjectivity involved in visual measurements of bubbles a bubble-density-scale was developed for more accurate definition of the number of bubbles in the tank and description of the changes in Figure 5.5:

None:	No permanent bubbles in the tank or no bubble formation whatsoever.
Negligible:	Less than five bubbles in the entire tank at all times.
Very Low:	Several bubbles form but remain in clusters in specific regions of the tank.
Low:	The bubbles break away from the clusters but the overall density of bubbles is still extremely low (about a dozen bubbles).
Onset:	Increased density of bubbles is observed throughout the tank (refer Figure 5.5 for $N \sim N_E$). N_E was chosen as the impeller speed at which this level of bubbles was first reached.
High:	Very high bubble density in the entire tank, accompanied by violent movement of the liquid surface, splashing and loud noise.

This scale was then used to estimate N_E. Two different observers measured N_E using the bubble density scale and the procedure outlined above and obtained measurements with an average standard deviation of 2.5% of the mean value of N_E.

Velocity measurements were also made with an LDV about 1.5 cm below the open liquid surface. Since air bubbles interfere with LDV measurements, experiments were conducted at impeller speeds slightly slower than the critical value ($N = 0.98N_E$). An Argon ion laser with total output power of 300 mW was used. The axial and radial components of velocity were measured every 4 mm along a radial traverse which was in a plane parallel to the baffle, at a baffle-offset of about 6 mm. 60,000 points were collected for each velocity measurement. Details of the experimental setup, laser and optical parameters, and description of the traverse system are given in Chapter 4.

5.4. Experimental Details

Experiments were conducted to study the effect of impeller type, size and fluid properties on the onset of air entrainment (N_E). All experiments were carried out in an open cylindrical glass tank with a diameter, $T = 0.24$m. The tank was filled with the experimental liquid to a height of $H = T$. The ambient temperature in the laboratory was maintained at 23°C with variations in temperature within ±1°C. The impeller speed was accurate to within ± 1 RPM of the set value.

Four different fluids were used in the study: deionized ultra-filtered (DIUF) water, triethylene glycol (TEG), Bayol-35 and a saturated solution of sodium chloride in DIUF water. The fluid properties were measured in the laboratory under conditions similar to those used in the experiments and the measured values are tabulated in Table 5.2. Three types of impeller were used: PBTU, PBTD and RT. While two sizes were used for the axial impellers, three impellers with differing geometries were used in the case of the RT. The impeller geometries are given in Table 5.3.

Table 5.2 Physical Properties of fluids measured @ 23°C

Chemical Name	S.G. (-)	Viscosity (cP)	Surface Tension (dynes/cm)
DIUF Water	0.997	1.11	70.4
Triethylene glycol (TEG)	1.122	44.38	42.9
Bayol – 35	0.780	3.07	24.7
Saturated NaCl Solution	1.194	1.98	75.5

Table 5.3 Overview of Experiments

Experiment Type	Impeller Type	Impeller Size, D (m)	S or C (m)	Fluid	Impeller Speed, N (RPM)
Vortex formation in un-baffled tank	PBTU	0.08 and 0.12	C: 0.08	RO Water	100-480
	PBTD	0.08 and 0.12	C: 0.08	RO Water	100-480
	Rushton Turbine	0.077, 0.081 and 0.121	C: 0.08	RO Water	100-400
Different Baffles	PBTU	0.08 and 0.12	S: 0.01-0.10	RO Water, Bayol-35, TEG	75-525
Air Entrainment in fully baffled tank	PBTU	0.08 and 0.12	S: 0.005 - 0.12	DIUF Water, Bayol-35, TEG, NaCl Solution (Saturated)	70-700
	PBTD	0.08 and 0.12	C: 0.08 and 0.12	RO Water	200-900
	Rushton Turbine	0.077, 0.081 and 0.121	C: 0.08 and 0.12	RO Water	100-550

The experiments conducted in this study are summarized in Table 5.3 and can be grouped into three sets: Air entrainment into un-baffled vessels, into vessels with non-standard baffles and into vessels with standard baffles. These configurations are described next.

5.4.1. Air Entrainment Into Un-baffled Vessel

The first set of experiments was conducted in the un-baffled tank shown in Figure 5.4a. Results were compared with values available in the literature. Two sizes of PBTD were tested along with three sizes of Rushton turbines (RT) and two PBTUs'. The vortex depth was measured at varying impeller speeds and at a clearance of C = T/3. Water purified by reverse osmosis was used for all trials in this set of experiments. The main measured quantity was the distance of the tip of the surface vortex from the initial liquid level (h_l in Figure 5.4a). During experiments the impeller speed was set to the desired value and the tank was allowed to equilibrate for a few minutes. h_l was then measured relative to the stationary liquid height. This was continued for a range of N. The onset of air entrainment occurs when h_l approaches the suction surface of the impeller.

5.4.2. Air Entrainment with non-Standard Baffles

In the second set of experiments, two non-standard baffles were tested with the PBTU as shown in Figures 5.4c and 5.4d. Experiments were conducted with all three fluids. The non-standard baffles had the following configurations: first the baffle height was reduced so that the baffles were submerged T/10 below the stationary surface of the fluid (Figure 5.4c), and secondly the baffles were notched adjacent to the wall to allow fluid flow along the wall near the liquid surface (Figure 5.4d).

5.4.3. Air Entrainment with Standard Baffles

The third set of experiments form the major part of the study. In these runs he tank was fully baffled with four equally spaced rectangular baffles of width W=T/10. Seven different impellers were employed in this set: two four-bladed 45° PBTU; four-bladed 45° PBTD and three RT. Dimensions of the impellers are given in Table 5.3. Four different fluids were tested with surface tension varying between 25 to 76 N/m, viscosity between 1 to 44 cP and density between 780 to 1194 kg/m^3.

5.5. Results and Discussion

Air entrainment into baffled stirred tanks occurs due to complex interactions between the free liquid surface and the turbulent flow field below it. Since the flow field generated in the tank is strongly affected by the impeller and tank geometries, it follows that the onset of air entrainment also depends on them. Hence, semi-empirical correlations that are used to predict the onset of air entrainment (Table 5.1) fail when used in conditions that are significantly different from those in which the correlations were developed, as seen in Figure 5.1. It is therefore necessary to shift focus from curve fitting of experimental data to the development of more detailed description of the process. In the present investigation, experiments were conducted in the various configurations described in section 5.4 and the results from these experiments are presented here to show the influence of the impeller and baffle geometries and fluid properties on N_E. The results are presented starting with the un-baffled tank which represents the simplest case, to the baffled vessels where the process of air entrainment is more complex. LDV measurements were made close to the free liquid surface. The RMS and mean velocities obtained from these measurements are used in the model developed in section 5.2 to verify the mechanism of air entrainment proposed in that section.

5.5.1. Air Entrainment in Un-baffled Tank

In an un-baffled vessel, the rotation of the impeller sets up a strong circumferential flow within the tank. The centrifugal forces generated by the rotating liquid causes the liquid to move outwards to the tank wall forming a large central vortex. Numerous models have been proposed to describe the shape of the vortex, mostly based on a momentum balance at the liquid surface. Nagata (1975) divided the tank into regions unaffected by the shear from the tank wall (forced vortex) and strongly affected by the shear from the tank wall (free vortex) and then used a momentum balance to find the geometry of the deformed liquid surface. Reiger et al. (1979) used a momentum balance

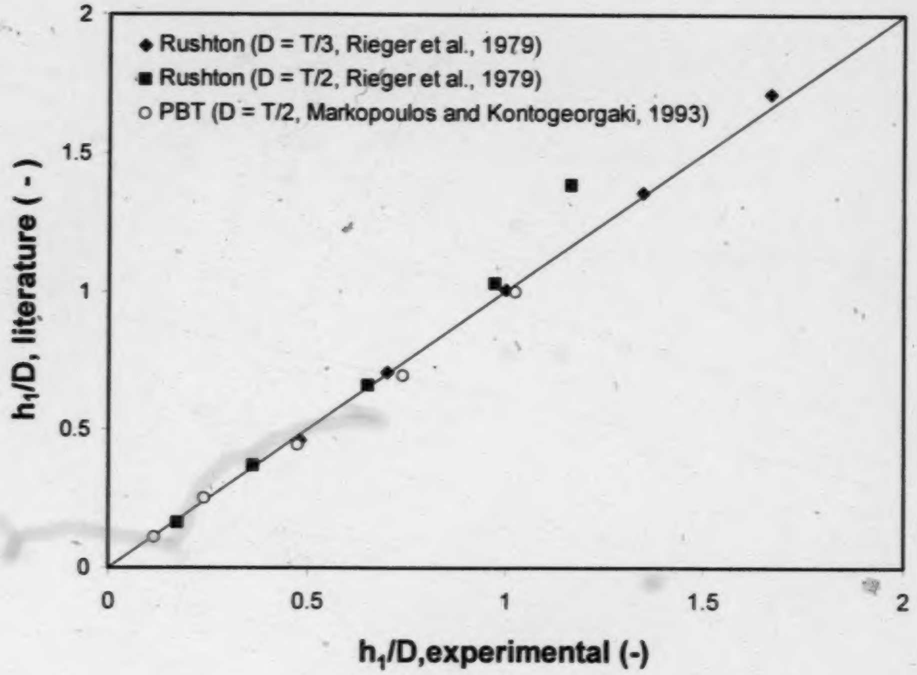

Figure 5.6 Parity plot of h_1/D from experiments in an un-baffled tank in this study and previously reported parametric models. Good agreement is obtained in the data from three different laboratories.

Table 5.4 **Results with un-baffled vessel. The reported values are from the literature, the experiments (Expts) column is from this study.**

	Reiger et al (1979) (B_1 from Equation 15)			Markopolous and Kontogeorgaki (1995) (K_1 from Equation 16)		
Impeller Type	**Reported**	**Expts**	**r^2**	**Reported**	**Expts**	**r^2**
Small Rushton Turbine #1	1.51	1.49	0.999	-	1.75	0.996
Small Rushton Turbine #2	1.51	1.43	0.997	-	1.65	0.995
Large Rushton Turbine	-	1.07	0.971	1.6	1.44	0.982
PBTD 80 mm	-	1.00	0.989	-	1.17	0.995
PBTD 120 mm	-	0.82	0.997	1.09	1.14	0.998
PBTU 80 mm	-	0.98	0.999	-	-	
PBTU 120 mm	-	0.82	0.999	-	-	

Note:

Small Rushton #1: Thin Blades

Small Rushton #2: Thick Blades

at the surface along with dimensional analysis to obtain the free surface geometry while Markopoulos and Kontogeorgaki (1995) used the Nagata model of vortex formation combined with momentum balance and dimensional analysis to obtain the surface geometry. A common feature in all these models is that the resulting equation contains two unknowns: the height of the vortex tip (h_1) and the height of the liquid at the wall (h_2). h_1 and h_2 can be related to each other through a mass balance between the liquid in the valley and in the peak regions of the vortex. The remaining unknown (either h_1 or h_2) is however very strongly dependant on the fluid properties and the tank and impeller geometries. Researchers have invariably had to resort to curve fitting of experimental data to develop correlations for this quantity. Two commonly used and relatively robust results are:

$$\frac{h_1}{D} = B_1 Ga_1^{0.069} \left(\frac{D}{T}\right)^{0.38} Fr_1^{1.14 Ga^{-0.008} \left(\frac{D}{T}\right)^{-0.008}} \tag{5.17}$$

$$\frac{h_1}{D} = K_1 Ga_1^{0.05} Fr_1 \left(\frac{D}{T}\right)^{0.1} \tag{5.18}$$

where Equation (5.17) was developed by Reiger et al (1979) and Equation (5.18) by Markopoulos and Kontogeorgaki (1995).

In the present study h_1 was measured for different impeller types and compared with either Equation (5.17) or (5.18) depending on the impeller geometry. The results are reported in Figure 5.6 and Table 5.4. It is seen that the present data match the previous correlations quite well. Table 5.4 also contains data on the formation of a vortex with a PBTU which has not been reported before. In the absence of baffles, the strong rotational flow that develops in the tank completely overpowers the radial and axial components of velocity, even though the impeller discharge stream for this impeller is directed upwards towards the liquid surface. The surface profiles for a PBTU are very similar to those obtained for a PBTD of a similar size.

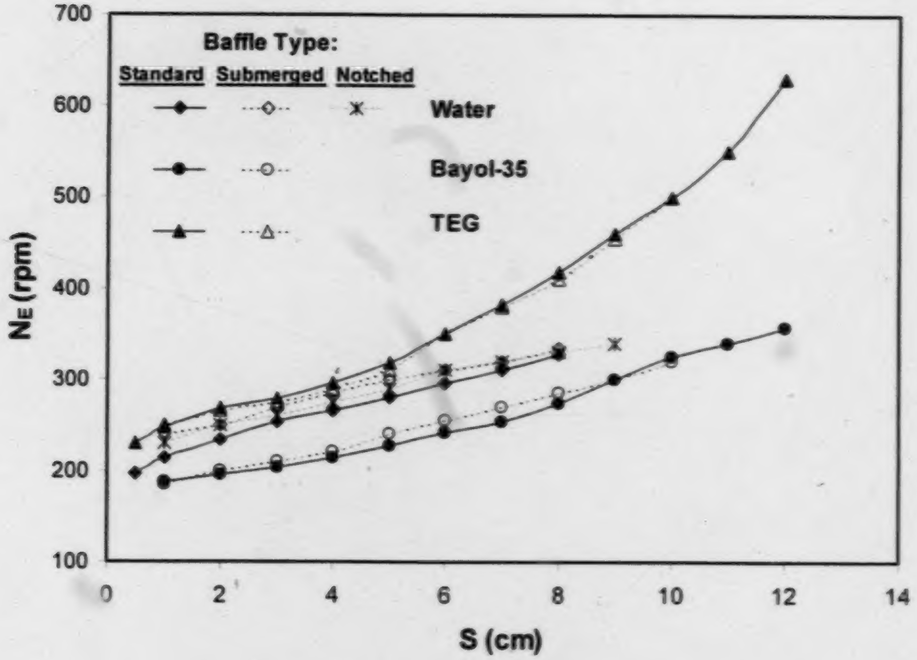

Figure 5.7 Critical impeller speed for air entrainment (N_E) for a PBTU (D = T/3) with different fluids and baffle geometries. While fluid properties affect N_E, baffle geometry does not. Note also the increasing N_E with deeper submergence for all fluids.

5.5.2. Air Entrainment in a Baffled Tank

5.5.2.1. Effect of Baffle Geometry on Air Entrainment

Experiments were conducted with non-standard baffles with geometries designed to cause less restriction to flow to determine if the localized vortices that sometimes form on the downstream of baffles or any other large-scale structure associated with the mean flow could lead to earlier onset of air entrainment. The results for the two non-standard baffle geometries (shown in Figures 5.4c and d) are presented in Figure 5.7 along with the results for the standard baffles (shown in Figure 5.4b, W = T/10). The results show that while fluid properties have a significant influence on N_E, changes in the baffle geometry do not cause an appreciable change in the impeller speed for air entrainment. Unlike the present case, Tanaka and Izumi (1987) reported a significant effect of the baffle length on N_E with a drop in the impeller speed for the onset of entrainment with shorter baffles. The baffle length in their experiment was however half the liquid height and it is possible that a large central vortex formed, similar to that observed in un-baffled tanks, which would have lead to an earlier air entrainment. This contention is supported by the observations of Hsu et al. (1998) who experimented with very short baffles and reported the formation of a large vortex in the center of the tank, which supplied the bubbles for entrainment.

5.5.2.2. Air Entrainment with Standard Baffles

The influence of the impeller submergence on N_E for standard baffles is shown in Figure 5.8a for two impeller sizes and four liquids. It is seen that an increase in submergence causes an increase in N_E irrespective of the impeller diameter or the type of the fluid used. As S is increased the turbulent energy reaching the surface drops. Figure 5.8a also shows that an increase in impeller diameter causes a decrease in N_E. This is consistent with previous studies. The data do not collapse with Fr, We, power consumption ($P = \rho P_O N^3 D^5$), or $\bar{\varepsilon}$. This result is consistent with the proposed mechanism. The propagation of the turbulence from the impeller to the liquid surface is strongly dependent on geometry and cannot be directly predicted from the average power consumption. Air entrainment is affected not only by turbulence (more specifically the

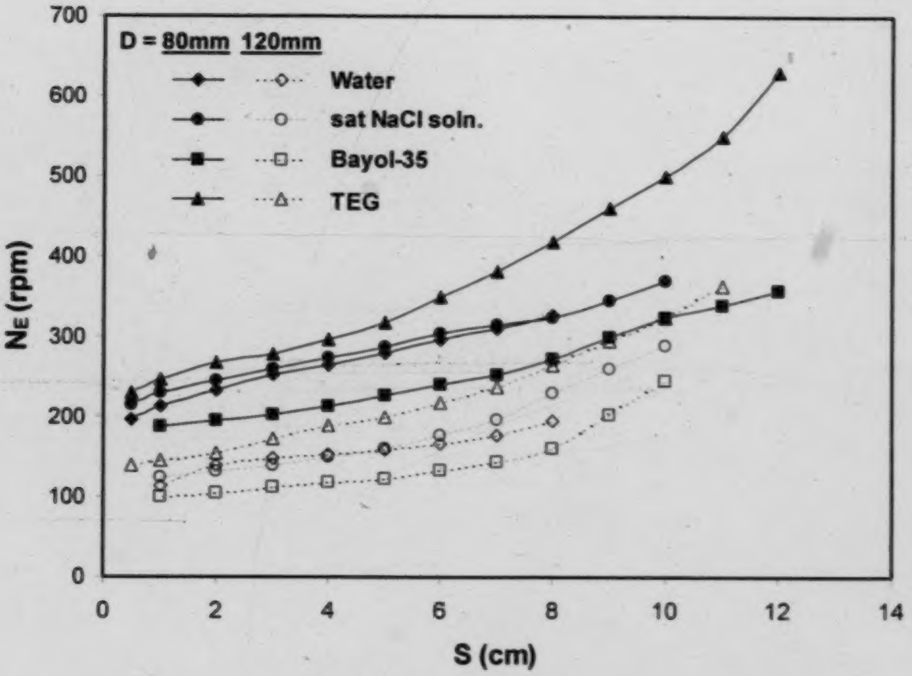

Figure 5.8a Raw data showing the critical impeller speed required for air entrainment (N_E) at different submergences for a PBTU at two impeller sizes (D = T/3 and D = T/2) with standard baffles. N_E increases with increasing impeller submergence. Fluid properties (ρ, σ and ν, see Table 5.2) also affect N_E.

Table 5.5 Impeller speed for air entrainment with impeller types other than PBTU

Impeller Type	Impeller Diameter (cm)	C/D (-)	N_E (rpm)	F_{rcrit} (N^2D/g) (-)
PBTD	8	1.000	762.5	1.317
PBTD	8	1.500	820	1.523
PBTD	12	0.667	355	0.428
PBTD	12	1.000	212.5	0.153
Rushton Large	12.1	0.661	180	0.111
Rushton Large	12.1	0.992	170	0.099
Rushton #2	7.7	1.039	510	0.567
Rushton #2	7.7	1.558	490	0.523
Rushton #1	8.1	0.988	400	0.367
Rushton #1	8.1	1.481	370	0.314

Note:

Sm. Rushton #1: Thin Blades

Sm. Rushton #2: Thick Blades

RMS velocity) but also by the mean flow near the surface (Equation 5.11), which is more dependent on the impeller tip speed than on $P/\rho V_{Tank}$. As expected, Figure 5.8a also shows that N_E is affected by the fluid properties. Experiments were also conducted for a PBTD and an RT in water and the results are presented in Table 5.5. N_E is substantially higher for the down-pumping impeller compared to the PBTU and less so for the RT. For all impellers, an increase in impeller size causes a reduction in N_E. These trends are similar to those reported in previous experiments (section 5.1.1). While the trends are as expected, the values of N_E obtained for these configurations using the various correlations given in Table 5.1 did not match the experimental data, as previously shown in Figure 5.1.

The raw data (as in Figure 5.8a) gives the general trends for the individual effects of the variables (S, D, impeller type and fluid properties) on N_E. To develop a more general understanding of the interrelation between the dominant influences (gravity, surface tension, viscosity and inertial forces), dimensionless numbers like Froude, Weber or Reynolds number are often used. In a stirred tank these numbers are defined in terms of the balance of forces at the impeller. In Figures 5.8b and 5.8c the results for air entrainment in a tank with standard baffles are reported in terms of the impeller Froude number (Fr_I):

$$Fr_I = \frac{ND^2}{g} \qquad (5.19)$$

and the dimensionless submergence, S/D. Figure 5.8b is for D = T/3 and Figure 5.8c is for a larger impeller diameter (D = T/2). It is seen from Figures 5.8b and 5.8c that the general nature of the curves for the two impeller sizes is similar, with similar effects of the fluid and impeller submergence, but the impeller Froude numbers for the two cases differ roughly by a factor of two. The curves for the two cases do not collapse, indicating that Fr_I does not capture all of the physical effects. Similar results were obtained for other dimensionless numbers calculated at the impeller, including the impeller Weber number (We_I). Finally, in Figure 5.8d the impeller speed measured at the onset of surface aeration is compared to the values obtained from the only published parametric model for a PBTU (Tanaka and Izumi, 1987). N_E for the two cases, obtained under somewhat different

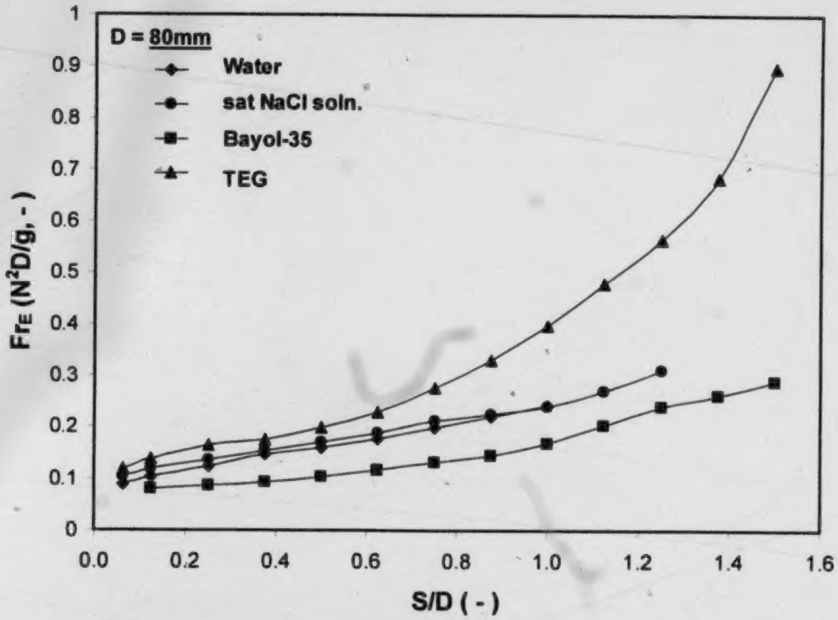

Figure 5.8b The impeller Froude number required for air entrainment for a small diameter PBTU (D = T/3).

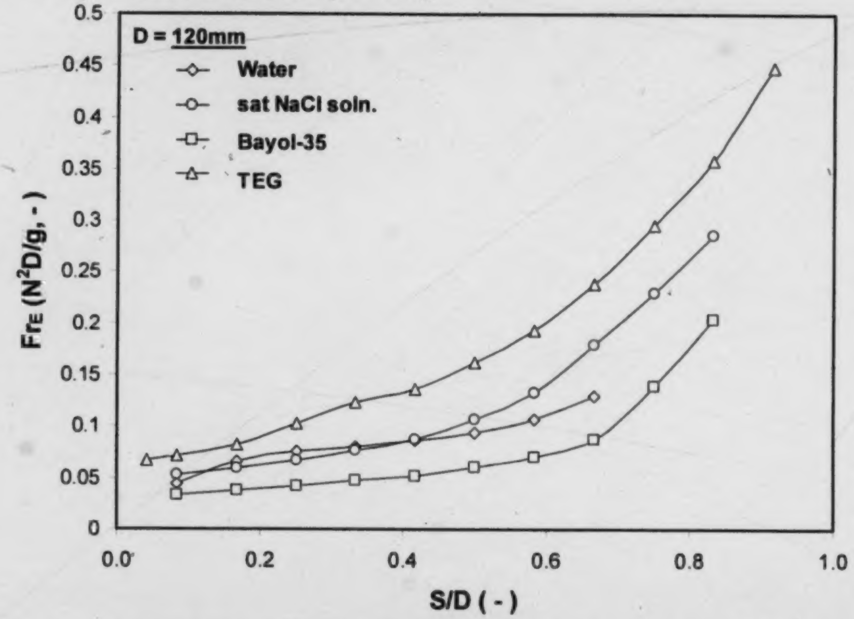

Figure 5.8c The Froude number required for air entrainment for a large diameter PBTU (D = T/2). Note that air entrainment starts at much smaller impeller speeds for the larger impeller and the change in axes scales.

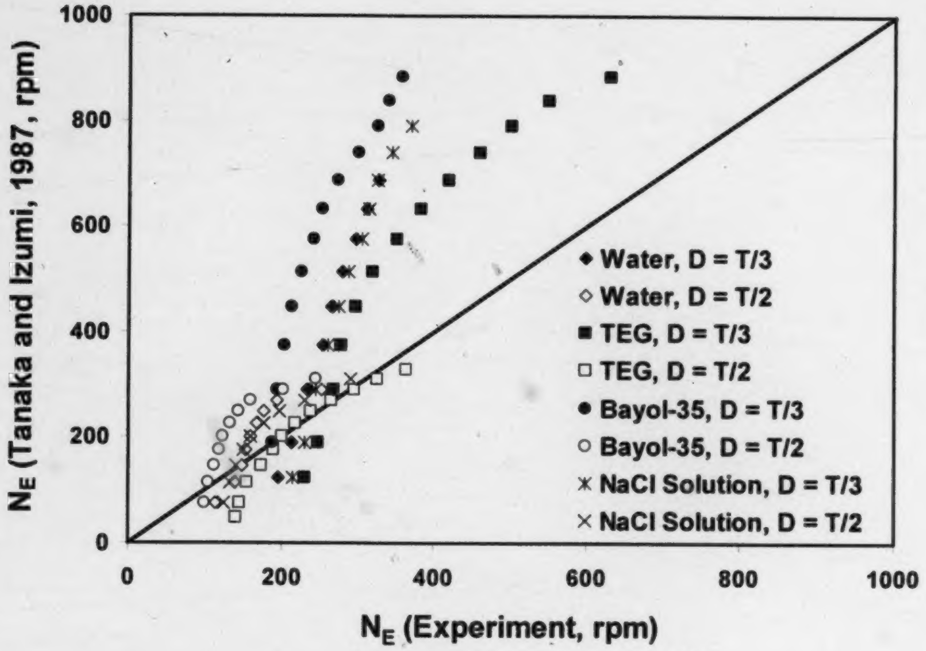

Figure 5.8d Parity plot of the impeller speed at the onset of air entrainment for a PBTU. Experimental data from the present study are compared with the only available parametric model for a PBTU (Tanaka and Izumi, 1987).

experimental conditions, cannot be represented universally by means of parametric correlations. The propagation of the flow from the impeller to the surface is severely complicated by its dependence on tank and impeller geometry: in this case the impeller diameter and varying submergence. While correlation of air entrainment at the surface to impeller variables is desirable this problem is quite possibly ill posed. If geometric similarity is released as a constraint, interaction terms between the impeller and the tank walls make attempts at general correlation both cumbersome and specific to a single data set. This problem is well illustrated by Figure 5.8d and also by the general lack of universality among the numerous correlations developed from various studies on surface aeration (Table 5.1, Figure 5.1).

In the next step of the analysis the objective of a general result is retained, but the focus on impeller variables is released and conditions at the surface are measured directly. The RMS and mean velocities are measured close to the liquid surface. At N_E,the impeller flow was fully turbulent ($Re_I > 2x10^4$) in all configurations for water while it was at the upper end of the transitional regime for the other fluids. The measurements are reported here are for water and Bayol-35.

5.5.3. Velocity field in a Baffled Tank with PBTU

In order to develop an understanding of the mechanism of air entrainment the raw flow field near the surface needs to be studied in detail. To this end, the velocity field near the surface was measured with an LDV. Due to the turbulent nature of the surface the levels of measurement errors increased very close to the surface. Consistent results were obtained if the measurement control volume was held 1.5 cm below the air-liquid interface.

5.5.3.1. Mean Flow

Figures 5.9a and 5.9b show the mean velocity near the tank surface with the PBTU for two impeller diameters and four impeller submergences both for water and Bayol-35. The upward pointing impeller discharge stream causes an upflow near the center of the tank. This upward moving fluid eventually turns around and flows down

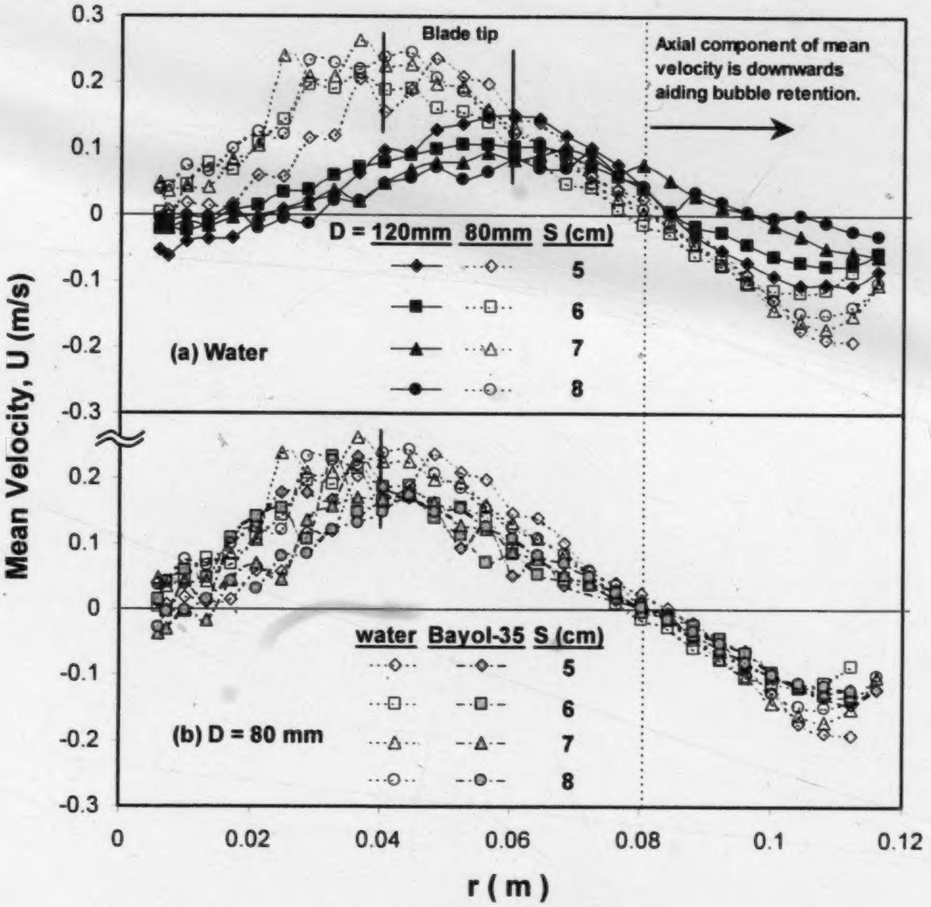

Figure 5.9 Radial profiles of the vertical component of mean velocity when the impeller speed is close to N_E. Beyond r ~ 0.08m the flow is downwards. The downward moving fluid pulls any bubbles formed at the surface downwards into the tank. This is the region of air entrainment. (a) Comparison of profiles with water for two impeller sizes (b) Comparison for water and Bayol-35 for D = 80 mm.

along the tank wall with the demarcation between the upwards and downwards streams being at r ~ 0.08m (0.67T/2) for both impeller sizes. Beyond r > 0.1m (0.83T/2) wall effects become dominant and the fluid velocity is drastically reduced. The downflow in the outer region of the tank (0.08m ≤ r ≤ 0.1m) is important in trapping the bubbles formed at the surface and pulling them down into the main circulation within the tank. There are some variations in the magnitude of the mean flow with submergence, particularly for the larger impeller. The radial position where the mean velocity is at its maximum is close to the blade tip (D/2) for both impeller sizes. The peak velocity is closer to the center than expected for a discharge stream angled at its theoretical value of 45° to the impeller. This is mainly due to the deflection of the discharge stream towards the center by the downflow in the outer region of the tank. Figures (5.9a and b) also show that the mean velocity is smaller for the larger impeller and to a lesser extent for Bayol-35. This is due to the lower N_E for the two cases as seen in Figure 5.8a.

5.5.3.2. Root Mean Square Velocity

In Figure 5.10a, the vertical component of the RMS velocity is scaled with the impeller tip speed and is shown as a function of the dimensionless radial distance (2r/D) for both impeller sizes and S = 4 to 8 cm. The figure shows that when scaled with the tip speed and the impeller diameter the vertical component of the RMS velocity collapses in the region of interest for both impeller diameters and all submergences. Although this curve is useful for representing the general relationship between the RMS velocity, impeller tip speed and the radial position, it shifts the data in the region of air entrainment and masks an important result.

Figures 5.10b and 5.10c show un-scaled RMS velocities. The radial and the vertical components of the RMS velocity in water are compared to each other in Figure 5.10b. In the inner region of the tank the radial component is small because the flow is predominantly vertical and the gradients are mainly in the axial direction. The flow has a larger radial component further out from the center. In the region of air entrainment the two components are remarkably similar in magnitude.

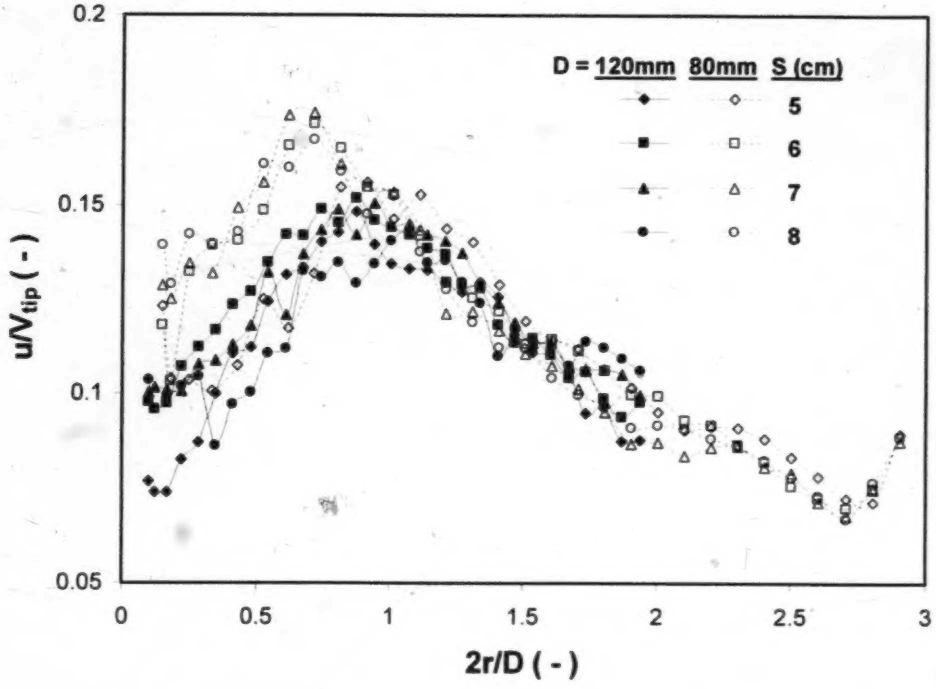

Figure 5.10a The axial component of the root mean square fluctuation (RMS) velocity when the impeller speed is 0.97N$_E$. The turbulence in the outer part of the tank scales with the impeller speed and diameter.

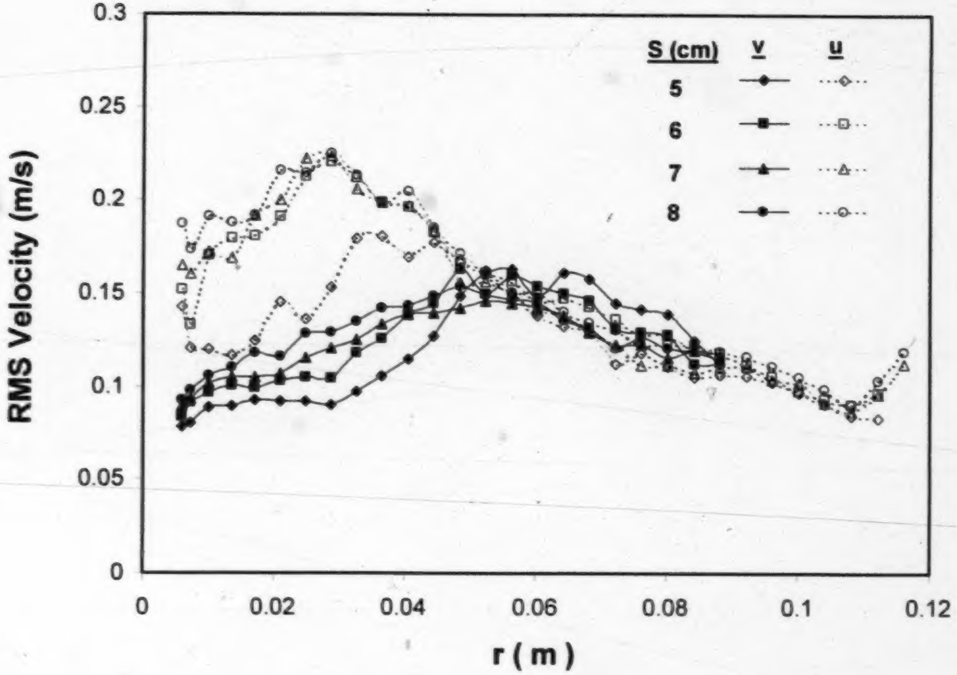

Figure 5.10b The axial and radial components of the RMS velocity near the surface are equal in the region of air entrainment.

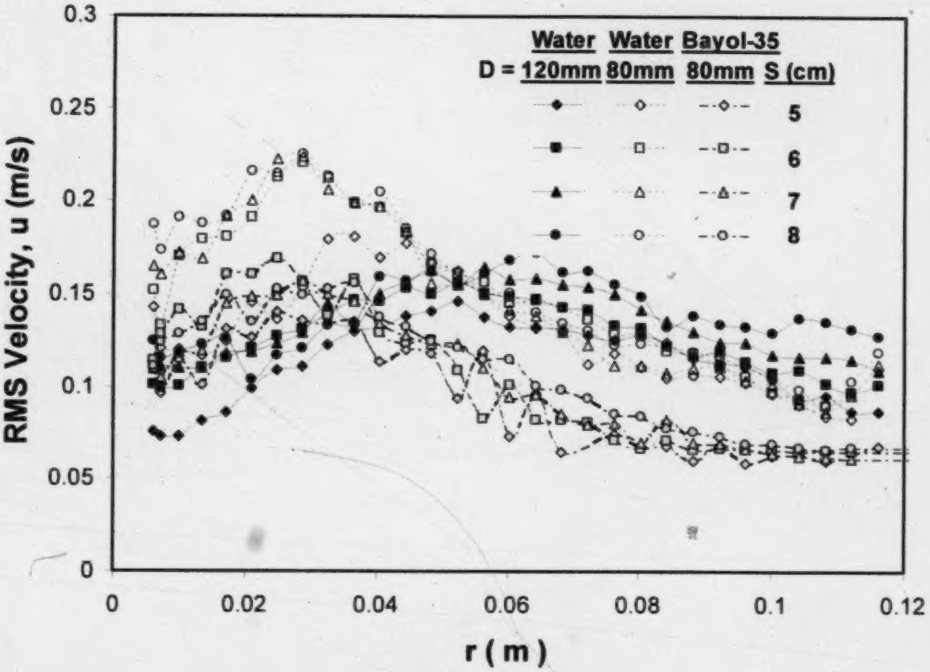

Figure 5.10c The absolute value of the RMS velocity is nearly constant in the region of air entrainment. There is a requirement for a minimum level of turbulence near the surface for air entrainment to occur. Once entrainment has occurred, mean down flow is necessary to pull the bubble into the tank. The amount of turbulence required however depends on the fluid properties.

The un-scaled axial component of the RMS velocity is shown in Figure 5.10c. In the inner part of the tank, turbulence is very dependent on impeller diameter although it is nearly independent of submergence. In the region of air entrainment the magnitude of the RMS velocity is bunched close together for all submergences and both impeller sizes when compared for the same fluid (water). The similarity of the RMS velocities in the outer region of the tank for the same fluid, irrespective of submergence and impeller diameter, agrees with observations by the authors in an earlier work (Bhattacharya and Kresta, 2004). When a different fluid (Bayol-35) is used, the amount of turbulence needed to form bubbles at the surface changes due to a change in fluid properties. The RMS velocity however remains independent of submergence. This is consistent with the mechanism of air entrainment proposed in section 5.2. The RMS velocity alone cannot sustain air entrainment. The mean velocity in the outer region of the tank ($0.08\text{m} \leq r \leq 0.1\text{m}$) shown in Figure 5.9 is needed to convect bubbles downwards.

5.6. Analysis of Theoretical versus Measured Velocity Field

Equation 5.11, or its equivalent Equation 5.16, provide the critical relation between the RMS and the mean velocity at the onset of air entrainment. When the left hand side of the equation is larger than the right hand side the RMS and mean velocities are balanced in such a way that the bubbles formed at the surface are of the right size to be dragged into the tank by the mean flow. From the proposed mechanism (Equation 5.11) it is expected that the term $u\left(U/\phi\right)^{0.25}$ will be constant irrespective of the fluid used. In Figure 5.11 this functional term is calculated from the absolute value of the measured mean and RMS velocities for the full radial span of the tank ($0.15 < 2r/D < 2.8$) for all submergences ($S = 5$ to 8) and two liquids with different properties (water and Bayol-35). The data for the various submergences and for both fluids collapse onto each other in the region of air entrainment which is highlighted in the figure. In the region of interest the downward mean flow is developed having passed through the point of inflection at $2r/D = 2$, and is also unaffected by the tank wall. The collapse of data in this region of air entrainment provides support for the proposed mechanism but there is need for direct comparison of critical and sub-critical conditions to further evaluate the model. This is

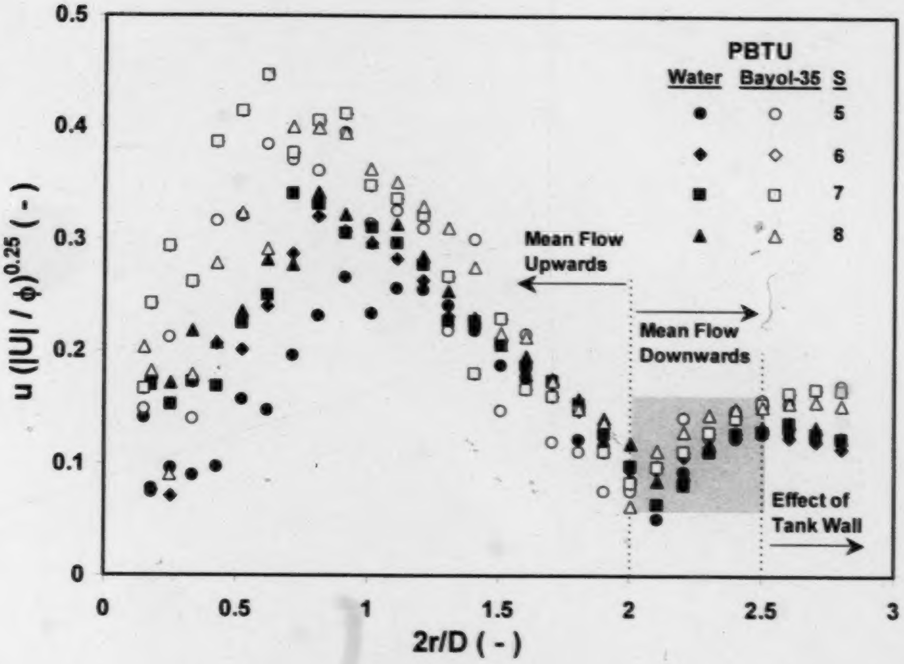

Figure 5.11 Comparison of the constant of proportionality in Equations 5.11 and 5.16 for Bayol-35 and Water. In the region of air entrainment, where the downward mean flow is fully formed and unaffected by the wall ($2.2 < 2r/D < 2.5$) the data collapse for both water and Bayol-35. The critical value of the constant [$u\ (|U|/\phi)^{0.25}$] is between 0.075 and 0.15.

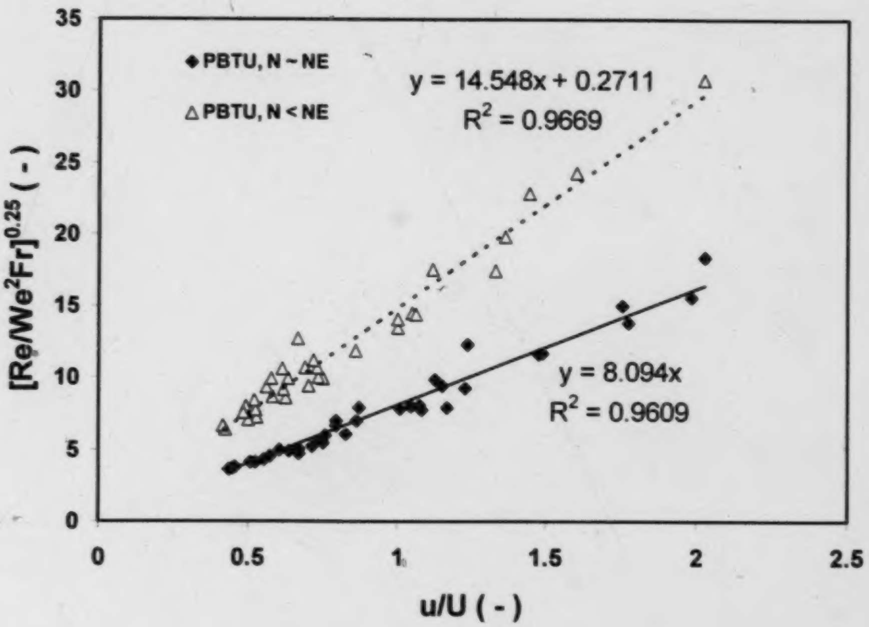

Figure 5.12a Relation between the RMS and mean velocity at the surface at critical and sub critical conditions. For the PBTU, the velocity data comes from Figures 5.9 and 5.10c in the air entrainment region (shown in Figure 5.11). The data is for a PBTU with D = T/3 and includes all submergences (S = 4 to 8cm). The functional relation between u/U and $[Re/We^2Fr]^{0.25}$ is different for the sub critical condition ($N < N_E$) than for the onset of air entrainment ($N \sim N_E$).

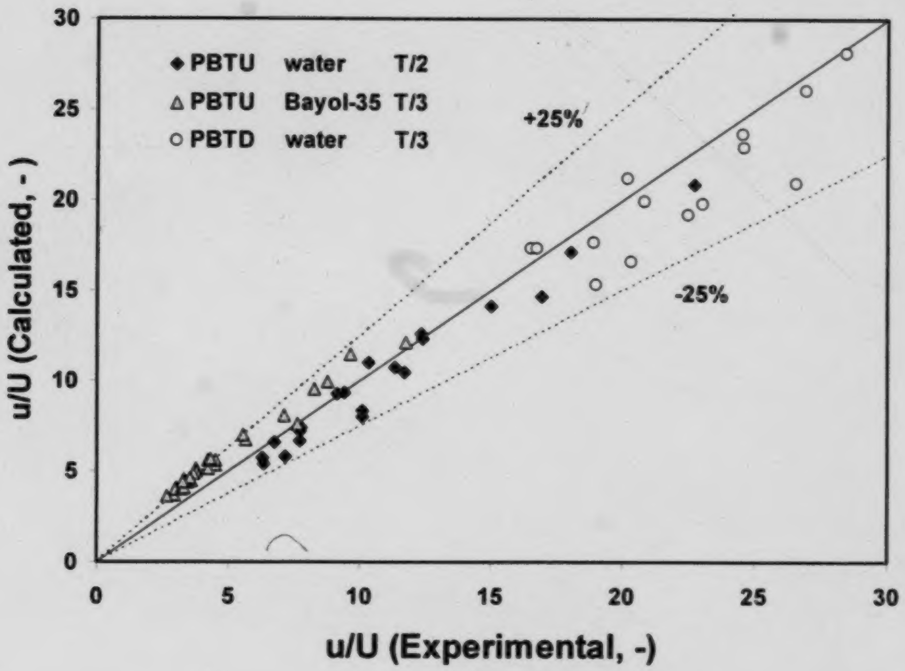

Figure 5.12b u/U calculated using Equation 5.20 is compared to the values measured with LDV.

done in Figure 5.12a, where the right hand side (RHS) of Equation (5.16) is compared to the measured intensity (u / U) for the region of air entrainment, using measured velocity data for the two conditions. Under critical conditions ($N = 0.98N_E$) the data for all submergences collapse into a linear relation as proposed by the model:

$$\left(\frac{u}{U}\right)_{NE,surf} = 1.235\left[\frac{Re}{We^2 Fr}\right]_{surf}^{0.25} \tag{5.20}$$

When $N < N_E$ the available intensity is expected to be less than what is required by the RHS. This is observed to be the case in Figure 5.12a for sub-critical condition. Not only is the available intensity less than what is required but the relation between the mean and RMS velocities fails to follow the relation given in Equation 5.20.

Equation (5.20) provides a relation between u and U at critical conditions for a given fluid property. A final test of the model is to provide the mean velocity and the fluid conditions and determine if the relation can correctly predict the turbulence intensity required to entrain air under these conditions. Equation (5.20) was used to calculate the intensity for the remaining runs in which experiments were conducted at the onset of air entrainment and a comparison between the measured values and calculated values is shown in Figure 5.12b. There is good match between estimated and calculated values not only for a larger impeller size but also for a different fluid and even for a PBTD with a flow field which is altogether different. The agreement is very good given the difficulties in measurement of velocity at the turbulent surface, the importance of keeping the fluids uncontaminated across experimental sets and the simplifying assumptions used in the model. Prediction of the conditions near the surface at the onset of air entrainment is more successful across a range of conditions than attempts to develop parametric models based on the impeller characteristics.

5.7. Conclusions

At high impeller speeds the PBTU starts ingesting air bubbles through the open surface of the vessel which can be detrimental to some industrial processes. The impeller speed N_E at which entrainment of air bubbles commences is therefore an important operational limit of the PBTU and needs to be properly defined.

Many previous studies have been conducted with the objective of developing parametric models relating the impeller speed for the onset of entrainment to a variety of experimental conditions, but the resulting correlations fail when used under conditions which differ from the original experiments. In this work, it was shown that air entrainment into a liquid thorough the open surface of a stirred tank is caused by subtle and complex interactions between the interface and the turbulent flow-field below it. These interactions cause surface deformations, the nature and magnitude of which are determined by the relative strength of gravity, surface tension and the turbulent kinetic energy reaching the surface. The deformations lead to the formation of bubbles which are trapped by the mean flow and dragged down into the tank, giving rise to sustained air entrainment. Since the turbulent flow field generated by an impeller is a complex function of parameters such as the impeller geometry, the impeller position and the tank geometry, it is to be expected that air entrainment is very sensitive to experimental conditions. There is therefore a requirement first to better understand the processes occurring at and below the surface that lead to bubble formation and entrapment and second to determine how changes at the impeller affect the turbulent flow field near the surface. This study successfully addressed the first step in this mechanistic approach. The result of this study is well suited for use in combination with accurate CFD simulations of the flow field.

The critical impeller speed for air entrainment, N_E was measured for various conditions (Table 2) to obtain the general relation between the operating variables (S, D and fluid properties) and air entrainment. It was found that simple relations could not relate N_E to the operating conditions. Quantities related to the impeller (N, D) cannot be used directly to explain the mechanism of air entrainment occurring far from the impeller near the tank surface. In order to better understand the process, velocity measurements were also made locally with an LDV, 1.5 cm below the liquid surface. The raw relation between N_E and the manipulated variables and the surface flow field measured with the LDV together give an insight into the mechanism of air entrainment. The present study therefore (i) presents a new set of data for the PBTU for which there is only one previous study (Tanaka and Izumi, 1987) and (ii) it also provides a simple model for the formation and entrainment of bubbles using force balances at the surface which was validated by velocity measurements near the surface. The relationship between the impeller and the turbulent flow-field near the surface has not been addressed. The suggested model is well suited for implementation with computational fluid dynamic simulations, which may allow prediction of the mean velocities and fluctuating velocities at the surface for a wide range of complex geometries, and thus to the ability to predict the point of air entrainment.

Chapter 6

Conclusions

6.1. Summary of Investigation

The primary objective of this study was to improve the performance of the stirred tank reactor with surface feed of reagents. Product quality in a mixing sensitive reaction is dependent on the turbulence level in the reaction zone close to the feed pipe, which in turn can be affected by the conditions of the feed stream, the ambient flow field or a combination of both. Based on this observation, two feed/impeller configurations were explored to determine their ability to reduce mixing limitations and thence improve performance:

1. High velocity surface feed.
2. Up-pumping impeller.

In the first configuration, the ambient flow field in the tank was kept unchanged but the feed conditions were modified. The objective here was threefold (a) generate additional turbulence in the feed stream (b) entrain reactants thus inducing additional mixing and (b) transport the reactants rapidly to the turbulent impeller region. The combined effect of higher turbulence levels in the jet and fast transport down to the impeller has the potential to offset the lack of ambient turbulence near the surface and improve performance. In the second configuration, the feed condition was unchanged but the flow field in the tank was altered by changing the pumping direction of the impeller. Now the impeller discharge was pointing upwards towards the surface and the turbulence level near the surface was increased manifold.

The ability of these configurations to suppress mixing limitations and improve product quality was studied in a glass stirred tank operated in the semi-batch mode using the third Bourne reaction. This reaction is a standardized competitive scheme widely used in mixing studies with well-established reaction kinetics and is perfectly suited for the turbulence levels existing in a stirred tank. During experiments, samples were collected at initial and final stages of operation and analyzed in a gas chromatograph to accurately obtain the amounts of product and byproducts formed and thence the yield of the byproducts.

6.2. *Observations*

Experiments showed that operation was very unstable with the high velocity feed jet and sufficient improvement in performance could not be obtained. One of the main difficulties was the inability to obtain fully turbulent conditions and operation remained confined to the transitional flow regime. A simple analysis confirmed that it was very difficult to obtain a fully turbulent feed jet ($Re_{jet} > 1x10^4$) without either (i) encountering stoichiometric limitations due to the molar flow rate of feed reagent being too high (ii) reaching very high nozzle pressure drop due to the nozzle diameter being too small or (iii) overshooting/impinging on the impeller due to very high jet velocities. This mode of operation does not provide a feasible solution to the problems encountered with surface feed.

Operation with an up-pumping pitched blade turbine showed significantly improved performance because of the higher levels of turbulence at the surface. Byproduct levels reduced with increasing impeller speed. However, at very high impeller speeds air bubbles were entrained into the tank. Since the presence of air can be detrimental to many industrial processes, N_E, the impeller speed at which air starts to entrain into the tank is a probable upper limit of operation. Reactive experiments showed that for the third Bourne reaction the product quality for surface feed matched the best results obtained with the submerged feed pipe when the up-pumping impeller was operated at N_E. Moreover, the product quality was independent of impeller submergence as long as the impeller was operated at the $N = N_E$ corresponding to that submergence. Experiments further confirmed that there was very little effect of the radial position of the feed or even the nozzle size on product quality. An up-pumping impeller is a stable and robust alternate configuration for minimizing byproduct yield where surface feed is required.

The fact that similar amounts of byproduct are obtained when $N = N_E$ indicates that (i) the liquid surface has similar levels of turbulence at $N = N_E$ irrespective of impeller location and (ii) air entrainment is a turbulence driven phenomenon. Additional experiments were conducted to study the effect of impeller configuration and fluid properties on N_E. The turbulent (RMS) and the mean components of velocity close to the surface were measured with a Laser Doppler Velocimeter (LDV) operated in the forward scatter mode. Based on the observed flow field a simple, two-step mechanism of air entrainment is proposed. In this mechanism, a bubble first forms at the surface when the turbulent kinetic energy is able to overcome surface energy and deform the surface. The mean down-flow then drags the newly formed bubble into the tank where it joins the mean circulation. Velocity measurements close to the surface were used to validate this model. While it is possible to describe the process of air entrainment with the surface flow field, results showed that it is very difficult to directly relate the surface flow conditions to macroscopic quantities measured near the impeller. The propagation of the flow from the impeller to the surface is complicated by its dependence on the tank and impeller geometry and is effectively unknown. This makes the task of correlating the observations at the surface to properties/conditions at the impeller very difficult.

Bibliography

Albal, R.S., Y.T., Shah, and A. Schumpe, 1983, Mass Transfer in Multiphase Agitated Contactors, Chem Eng J., **27**, 61-80

Anthieren, G.L., Eulerian-Lagrangian Model of Turbulent Mixing for Silver Halide Precipitation, M.S. Thesis, University of Alberta, Edmonton, Alberta

Aubin, J., P., Mavros, D.F., Fletcher, J., Bertrand, and C., Xuereb, 2001, Effect of Axial Agitator Configuration (Up-pumping, Down-pumping, Reverse Rotation) on Flow Patterns Generated in Stirred Vessels, Chem Eng Res Des, **79**, no. A8, 845-856

Aubin, J., N. Le, Sauze, J., Bertrand, D.F., Fletcher, and C., Xuereb, 2004, PIV Measurements of Flow in an Aerated Tank Stirred by a Down- and Up-Pumping Axial Flow Impeller, Expt Thermal Fluid Sci, **28**, no. 5, 447-456

Bakker, A., K.J., Myers, R.W., Ward, and C.K., Lee, 1996, The Laminar and Turbulent Flow Pattern of a Pitched Blade Turbine, Chem Eng Res Des, **74**, no. 4, 485-491

Baldi, S., and M., Yianneskis, 2003, On the Direct Measurement of Turbulence Energy Dissipation in Stirred Vessels with PIV, Ind Eng Chem Res, **42**, 7006-7016

Baldi, S., and M., Yianneskis, 2004, On the Quantification of Energy Dissipation in the Impeller Stream of a Stirred Vessel From Fluctuating Velocity Gradient Measurements, Chem Eng Sci, **59**, 2659-2671

Baldyga, J., and J.R., Bourne, 1988, Calculation of Micromxing in Inhomogeneous Stirred Tank Reactors, Chem Eng Res Des, **66**, 33-38

Baldyga, J., and J.R., Bourne, 1989, Simplification of Micromixing Calculations. I. Derivation and Application of New Model, Chem Eng J., **42**, 83-92

Baldyga, J., and J.R., Bourne, 1990, The Effect of Micromixing on Parallel Reactions, Chem Eng Sci, **45**, No. 4, 907-916

Baldyga, J., and J.R., Bourne, 1992, Interactions Between Mixing on Various Scales in Stirred Tank Reactors, Chem Eng Sci, **47**, No. 8, 1839-1848

Baldyga, J., and J.R., Bourne, Turbulent mixing and chemical reaction, John Wiley and Sons Ltd, Chichester, England (1999)

Baldyga, J., and Pohorecki, R., 1995, Turbulent micromixing in chemical reactors – a review, Chem. Eng. J., **58**, 183-195

Baldyga, J., J.R., Bourne, and Y., Yang, 1993, Influence of Feed Pipe Diameter on Mesomixing in Stirred Tank Reactors, Chem Eng Sci, **48**, No. 19, 3383-3390

Baldyga, J., Bourne, J.R., and S.J., Hearn, 1997, Interaction between chemical reactions and mixing on various scales, Chem Eng Sci, **52**, no. 4, 457-466

Baldyga, J., J.R. Bourne, and B. Zimmermann, 1994, Investigation of mixing in jet reactors using fast, competitive-consecutive reactions, Chem Eng Sci, **49**, no. 12, 1937-1946

Baldyga, J., J.R., Bourne, and B., Walker, 1998, Non-isothermal Mixing in Turbulent Liquids, Theory and Experiments, Can J. Chem Eng, **76**, 641-649

Banerjee, S, 1994, Upwelling, Downdrafts and Whirlpools: Dominant Structures in Free Surface Turbulence, Appl Mech Rev, **47**, 6, part 2, S166-S172

Batchelor, G.K., The Theory of Homogeneous Turbulence, Cambridge University Press, Cambridge, UK (1953)

Batchelor, G.K., 1959, Small Scale Variations of Convected Quantities Like Temperature in Turbulent Fluid. Part 1. General Discussions and the Case of Small Conductivity, J. Fluid Mech., **5**, 113-134

Bhattacharya, S., and S.M., Kresta, 2002, CFD Simulations of Three-Dimensional Wall Jets in a Stirred Tank, Can J. Chem Eng, **80**, 695-709

Bhattacharya, S., and S.M., Kresta, 2004, Surface Feed with Minimum By-product Formation for Competitive Reactions, Chem Eng Res Des, **82**, no. A9, 1153-1160

Bittorf, K.J., 2000, The Application of Wall Jets in Stirred Tanks with Solids Distribution, Ph.D. Thesis, University of Alberta, Edmonton, Alberta

Bittorf, K. and S.M., Kresta, 2000, Active Volume of Mean Circulation for Stirred Tanks Agitated with Axial Impellers, Chem Eng Sci, **55**, 1325-1335

Bittorf, K., and S.M., Kresta, 2001, 3-D Wall Jets: Axial Flow in a Stirred Tank, AIChE J., **47**, 1277-1284

Boersma, B.J., Brethouwer, G., and F.T.M., Nieuwstadt, 1998, A numerical investigation on the effect of the inflow conditions on the self-similar region of a round jet, Phys Fluid, **10**, no. 4, 899-909

Bourne, J.R., and P., Dell'Ava, 1987, Micro- and Macro-Mixing in Stirred Tank Reactors of Different Sizes, Chem Eng Res Des, **65**, 180-186

Bourne, J.R., and C.P., Hilber, 1990, The Productivity of Micromixing-Controlled Reactions: Effect of Feed Distribution in Stirred Tanks, Chem Eng Res Des, **68**, no. A , 51-56

Bourne, J.R., and S.A., Thoma, 1991, Some Factors Determining the Critical Feed Time of a Semi-Batch Reactor, Shorter Communication, Trans I Chem E, **69**, Part A, 321-323

Bourne, J.R., and S., Yu, 1994, Investigation of Micromixing in Stirred Tank Reactors Using Parallel Reactions, Ind Eng Chem Res, **33**, 41-55

Bourne, J.R., F., Kozicki, U., Moergeli, and P., Rys, 1981, Mixing and Fast Chemical Reactions: III. Model-experiment comparisons, Chem Eng Sci, **36**, 1655-1663

Brocchini, M., and D.H. Peregrine, 2001, The Dynamics of Strong Turbulence at Free Surface. Part 1. Description, J Fluid Mech., **449**, 225-254

Calderbank, P.H., 1958, Physical Rate Processes in Industrial Fermentation. Part I: The Interfacial Area in Gas-Liquid Contacting with Mechanical Agitation, Trans Instn Chem Engrs, **36**, 443-463

Chanson, H., 1993, Self-Aerated Flows in Chutes and Spillways, J Hydraulic Eng, **119**, no. 2, 220–243

Chapman, C.M., A.W., Nienow, and J.C., Middleton, 1980, Surface Aeration in a Small, Agitated and Sparged Vessel, Biotech Bioeng, **22**, 981-993

Chapman, C.M., A.W., Nienow, M., Cooke, and J.C., Middleton, 1983, Particle-Gas-Liquid Mixing in Stirred Vessels. 2. Gas-Liquid Mixing, Chem Eng Res Des, **61**, no. A , 82-95

Chapple, D., S.M., Kresta, A., Wall and A., Afacan, 2002, The Effect of Impeller and Tank Geometry on Power Number for a Pitched Blade Turbine, Chem Eng Res Des, **80**, no. A4, 364-372

Ciofalo, M., A. Brucato, F. Grisafi and N. Torraca, 1996, Turbulent Flow in Closed And Free-Surface Unbaffled Tanks Stired By Radial Impeller, Chem Eng Sci, **51**, no. 14, 3557-3573

Corrisin, S., 1964, The Isotropic Turbulent Mixer: Part II. Arbitrary Schmidt number, AIChE J., **10**, No. 6, 870-877

Cooper, R.G., and D., Wolf, 1968, Velocity Profiles and Pumping Capacities For Turbine Type Impellers, Can J Chem Eng, **46**, 94-100

Coustes, J., and J.P., Coudrec, 1988, Study by Laser Doppler Anemometry of The Turbulent Flow Induced by a Rushton Turbine in a Stirred Tank: Influence of Size of the Units – 1. Mean Flow and Turbulence, Chem Eng Sci, **43**, no. 10, 2751-2764

Cutter, L.A., 1966, Flow and Turbulence in a Stirred Tank, AIChE J., **12**, no. 1, 35-45

Danckwerts, P.V., 1958, The Effect of incomplete mixing on homogeneous reactions, Chem Eng Sci., **8**, 93-99

Davies, J.T., 1972, Turbulence Phenomena, An Introduction to Eddy Transfer of Momentum, Mass and Heat, Particularly at Interfaces, Academic Press, New York

Dean, G.B. and M.D. Stokes, 2002, Scale Dependence of Bubble Creation Mechanism in Breaking Waves, Nature, **418**, 839-844

Dyster, K.N., E., Koutsakos, Z., Jaworski, and A.W., Nienow, 1993, An LDA Study of the Radial Discharge Velocities Generated by a Rushton Turbine: Newtonian Fluids, Re ≥ 5, Chem Eng Res Des, **71**, no. A1, 11-23

Eggers, J., 2001, Air Entrainment Through Free-Surface Cusps, Phy Rev Letters, **86**, no. 19, 4290-286

Ervine, D.A. and H.T. Falvey, 1987, Behaviour of Turbulent Water Jets in Atmosphere and in Plunge Pools, Proc Inst Civ Engrs., Part 2, **83**, 295-314

Farge, M, and E. Guyon, 1999, A Philosophical and Historical Journey Through Mixing and Fully-developed Turbulence, in Mixing: Chaos and Turbulence, Eds: Chaté, H., E., Villermaux and J.-M., Chomaz, NATO ASI Series, Series B, 373, Kluwer Academic, New York

Fokema, M.D., S.M., Kresta, and P.E., Wood, 1994, Importance of Using the Correct Boundary Conditions for CFD Simulations of Stirred Tanks. Can J Chem Eng, **72**, 177-183.

Fossett, H., 1951, The Action of Free Jets in the Mixing of Fluids, Trans. Inst Chem Engrs., **29**, 322-332

Fox, E.A., and V.E. Gex, 1956, Single-phase blending of fluids, AIChE J., **2**, 539-544

Fukushima, C., Aanen, L., and J., Westerweel, 2002, Investigation of the mixing process in an axisymmetric turbulent jet using PIV and LIF, Laser Techniques for Fluid Mechanics, Eds. R.J. Adrian et al., Springer, Berlin, 339-356

Gangadharaiah, T, N.S. Lakshmana Rao, and K. Seetharamiah, 1970, Inception and Entrainment in Open Channel Flows, J Hydraulic Div, ASCE, **96**, 1549-1565

George, W.K., Chapter: X: Self-preservation of turbulent flows and its relation to initial conditions and coherent structures, Advances in Turbulence, Eds. George, W.K., and R., Arndt, Springer, New York (1989)

Govinda Rao, N.S., and N. Rajaratnam, 1961, On the Inception of Air-Entrainment in Open Channel Flows, Proc 9th IAHR Congr, Dubrovnik, 9-12

Greaves, M., and K.A.H., Kobbacy, 1981, Surface Aeration in Agitated Vessels, I. Chem Sym Series No. 64, Yorkshire Branch and Fluid Mixing Processes Group of the Inst Chem Engs, H1-H22, Rugby, Warks, UK

Grenville, R.K., 1992, Blending of Viscous Newtonian and Pseudo-Plastic Fluids, PhD Thesis, Cranfield Institute of Technology, Cranfield, Bedfordshire, England

Grenville, R., Ruszkowski, S., and E., Garred, 1995, Blending of miscible liquids in the turbulent and transitional regimes, Mixing XV, June 20-25, Alberta, Canada

Grenville, R.K., and J.N. Tilton, 1996, A new theory improves the correlation of blend time data from turbulent jet mixed vessels, Trans Inst Chem Engrs., **74**, Part A, 390-396

Grgic, B., 1998, Influence of the Impeller and Tank Geometry on Low Frequency Phenomena and Flow Stability, MSc Thesis, University of Alberta, Edmonton, Alberta

Gunkel, A.A., and M.E., Weber, 1975, Flow Phenomena in Stirred Tanks: Part 1: The Impeller Stream, AIChE J., **21**, 931-949

Hall, C. W., Laws and Models: Science, Engineering and Technology, CRC Press, Boca Raton (2000)

Hammoumi, M. E., Achard, J.L., and L., Davoust, 2002, Measurements of air entrainment by vertical plunging jets, Exp Fluids, **32**, 624-638

Harvey III, A.D., and S.E., Rogers, 1996, Steady and Un-steady Computations of Impeller-Stirred Reactors, AIChE J., **42**, 2701-2712

Hazuku, T., T. Takamasa, and K. Okamoto, 2003, Simultaneous Measuring System for Free Surface and Liquid Velocity Distributions Using PIV and LFD, Expt Thermal Fluid Sci, **27**, 677-684

Hemrajani, R.R., and G.B., Tatterson, 2004, Mechanically Stirred Vessels, Chapter 6 in the Handbook of Industrial Mixing, Eds Paul, E., V.A. Atiemo-Obeng, S.M. Kresta, John Wiley and Sons, New Jersey

Heywood, N.I., Madhvi, P., and McDonagh, M., 1985, Design of Ungassed Baffled Mixing Vessel to Minimize Surface Aeration of Low Viscosity Liquids, paper 26, Papers Presented at the 5th European Conference on Mixing, Würzburg, Germany, June 10-12, 1985, BHRA, The Fluid Engineering Center, Cranfield, Bedford, England, 243-261

Hinch, E.J., Mixing: Turbulence and Chaos – An Introduction, in Mixing: Chaos and Turbulence, Eds: Chaté, H., E., Villermaux and J.-M., Chomaz, NATO ASI Series, Series B, 373, Kluwer Academic, New York (1999)

Hino, M., 1961, On the Mechanism of Self-Aerated Flows on Steep Slope Channels. Applications of the Statistical Theory of Turbulence, Proc 9th IAHR Congr, Dubrovnik, 123-132

Hinze, O., Turbulence, Mc-Graw Hill (1975)

Hsu, Y.-C., C.-J., Huang, W.-H., Yen and R.Y., Peng, 1998, Onset of Gas Induction and Power Consumption in an Agitated Tank Having Shortened Narrower Baffles, J. Chem Tech Biotech, **71**, 187-186

Hussein, H.J., Capp, S.P., and W.K., George, 1994, Velocity measurements in a high-Reynolds-number momentum-conserving, axisymmetric, turbulent jet, J. Fluid Mech, **258**, 31-75

Jaworski, Z., A.W., Nienow, K.N., Dyster and W., Bujalski, 1991; An LDA Study of Turbulent Flow in a Baffled Vessel Agitated by a Pitched Blade Turbine, Chem Eng Res Des, **69**, no. 4, 313-320

Jaworski, Z., K.N., Dyster, and A.W., Nienow, 2001, The Effect of Size, Location and Pumping Direction of Pitched Blade Turbine Impellers on Flow Patterns: LDA Measurements and CFD Predictions, Chem Eng Res Des, **79**, no. A8, 887-894

Jo, M.C., W.R., Penny, and J.B., Fasano, 1994, Backmixing Into Reactor Feed Pipes Caused by Turbulence in an Agitated Vessel, AIChE Symp. Series no. 299, **90**, 41-49

Joshi, J.B., A.B., Pandit, and M.M., Sharma, 1982, Mechanically Agitated Gas-Liquid Reactors, Chem Eng Sci, **37**, no. 6, 813-844

Khan, F.R., Rielly, C.D., and Hargrave, G.K., 2003, A multi-block approach to obtain angle-resolved PIV measurements of the mean flow and turbulence fields in a stirred vessel. Session 1: Turbulence Characteristics in Stirred Systems, 11th European Conference on Mixing, Bamberg, Germany, 14-17 Oct, 47–54.

Kolar, V., P., Filip, and A.G. Curev, 1984, Hydrodynamics of a Radially Discharging Impeller Stream in Agitated Vessels, Chem Eng Comm, **27**, 313-

Kolar, V., P., Filip, and A.G. Curev, 1985, The Swirling Jet Model and its Application to a Radial Impeller Stream, Papers Presented at the 5th European Conference on Mixing, Würzburg, Germany, June 10-12, 1985, BHRA, The Fluid Engineering Center, Cranfield, Bedford, England, 483-490

Kresta, 1991, Characterization, Measurement and Prediction of the Turbulent Flow in Stirred Tanks, PhD Thesis, Mc Master University, Hamilton, Ontario

Kresta, S.M., 1998, Turbulence in Stirred Tanks: Anisotropic, Approximate and Applied, Can J. Chem Eng, **76**, 563-576

Kresta, S.M., 2004, Mixing as a Mechanism: Moving Beyond the Stirred Tank to Modelling and Control of the Scales of Segregation, 2004 NAMF Award Winner Presentation, AIChE Annual Meeting, Austin, Texas, Nov. 7-12

Kresta, S.M., and P.E., Wood, 1993, The Mean Flow Produced by a 45° Pitched Blade Turbine: Changes in Circulation Pattern Due to Off Bottom Clearance, Can J. Chem Eng, **71**, 42-53

Kresta, S.M., and R.S., Brodkey, Turbulence in Mixing Applications, Chapter 2 in the Handbook of Industrial Mixing, Eds Paul, E., V.A. Atiemo-Obeng, S.M. Kresta, John Wiley and Sons, New Jersey (2004)

Kresta, S.M., Bittorf, K.J., and D.J., Wilson, 2001, Internal Annular Wall Jets: Radial Flow in a Stirred Tank, AIChE J, **47**, 2390 - 2401

Lane, E.W., 1939, Entrainment of Air in Swiftly Flowing Water, Civ. Eng., ASCE, **9**, no. 2, 89-91

Laufhutte, H.D., and A., Mersmann, 1985, Dissipation of Power in Stirred Vessels, Papers Presented at the 5th European Conference on Mixing, Würzburg, Germany, June 10-12, 1985, BHRA, The Fluid Engineering Center, Cranfield, Bedford, England, 331-340

Leisure, M., Turbulence in Fluids, Kluwer, Dordrecht (1990)

Lee, K.C., and M., Yianneskis, 1998, Turbulence Properties of The Impeller Stream of a Rushton Turbine, AIChE J, **44**, no. 1, 13-24

Markopoulos J., and E., Kontogeorgaki, 1995, Vortex Depth in Unbaffled Single and Multiple Agitated Vessels, Chem Eng Tech, **18**, 68-74

Mavros, P., C., Xuereb, I., Fort and J., Bertrand, 2002, Investigation by Laser Doppler Velocimetry of the Effects of Liquid Flow Rates and Feed Positions on the Flow Patterns Induced in a Stirred Tank by an Axial-Flow Impeller, Chem Eng Sci, **57**, 3939-3952

Nagata, S., Mixing: Principles and Applications, Kodansha, Tokyo (1975)

Micheletti, M., S., Baldi, S.L., Yoeh, A., Ducci, G., Papadakis, K.C., Lee and M., Yianniskis, 2004, On Spatial and Temporal Variations And Estimates of Energy Dissipation in Stirred Reactors, Chem Eng Res Des, **82**, no. A9, 1188-1198

Nienow, A.W., and K., Inoue, 1993, A study of precipitation micromixing, macromixing, size distribution, and morphology, Paper 9.4 presented at CHISA, Prague, Czech Republic

Nienow, A.W., and W., Bujalski, 2004, The Versatility of Up-pumping Hydrofoil Agitators, Chem Eng Res and Des, **82**, no. A9, 1073-1081

Nienow, A.W., C.M., Chapman and J.C., Middleton, 1979, Gas Recirculation rate Through Impeller Cavities and Surface Aeration in Sparged Agitated Vessels, Chem Eng J., **17**, 111-118

Nienow, A.W., R., Kuboi, C.M., Chapman and K., Allsford, 1983, The Dispersion of Gases into Liquids by Mixed Flow Impellers, Proceeding of the Inter Conf

Physical Modelling of Multi-Phase Flow, Coventry, BHRA Fluid Engg, U.K., 417-437

Ng, K., and M., Yianneskis, 2000, Observations on The Distribution of Energy Dissipation in Stirred Vessels, Chem Eng Res Des, **78**, no. A3, 334-341

Okamato, K. and H. Madarame, 1998, Fluid Dynamics of a Free Surface in Liquid Metal Fast Breeder Reactors, Prog Nuclear Energy, **32**, ½, 195-207

Panchapakesan, N.R., and J.L., Lumley, 1993a, Turbulence measurements in axisymmetric jets of air and helium. Part 1. Air jet, J. Fluid Mech, **246**, 197-223

Panchapakesan, N.R., and J.L., Lumley, 1993b, Turbulence measurements in axisymmetric jets of air and helium. Part 2. Helium jet, J. Fluid Mech, **246**, 225-247

Patterson, G.K., E.L., Paul, S.M., Kresta and A.W., Etchells II, Mixing and Chemical Reactions, Chapter 13 in the Handbook of Industrial Mixing, Eds Paul, E., V.A. Atiemo-Obeng, S.M. Kresta, John Wiley and Sons, New Jersey (2004)

Patwardhan, A., and J.B., Joshi, 1998, Design of Stirred Vessels with Gas Entrained From Free Liquid Surface, Can J. Chem Eng, **76**, 339-364

Paul, E.L., and R.E., Treybal, 1971, Mixing and Product Distribution for a Liquid-Phase Second-Order, Competitive-Consecutive Reaction, AIChE J., **17**, 718-731

Paul, E., V.A. Atiemo-Obeng, S.M. Kresta, Introduction in the Handbook of Industrial Mixing, Eds Paul, E., V.A. Atiemo-Obeng, S.M. Kresta, John Wiley and Sons, New Jersey (2004)

Pope, S.B, Turbulent Flows, Cambridge University Press, Cambridge, U.K. (2000)

Rajaratnam, N, Turbulent Jets, Elsevier Scientific Pub., Amsterdam (1976)

Ranade, V.V., and J.B., Joshi, 1989, Flow Generated By Pitched Blade Turbines I: Measurements Using Laser Doppler Anemometer, Chem Eng Comm, **81**, 197-224

Ranade, V.V., and J.B., Joshi, 1990, Flow Generated by a Disc Turbine: Part I Experimental, Chem Eng Res Des, **68**, no. 1, 19-33

Reiger, F., P., Ditl and V. Novak, 1979, Vortex Depth in Mixed Unbaffled Vessels, Chem Eng Sci, **34**, 397-403

Rein, M., 1993, Phenomena of liquid Drop Impact on Solid and Liquid Surfaces, Fluid Dyn Res, **12**, 61-93

Rein, M., 1998, Turbulent Open-Channel Flows: Drop Generation and Self-Aeration, J Hydraulic Eng, **124**, 1, 98-102

Roussinova, V., S.M., Kresta, and R., Weetman, 2003, Low Frequency Macroinstabilities in a Stirred Tank: Scale-up and Prediction Based on Large Eddy Simulation, Chem Eng Sci, **58**, 2297-2311

Rushton, J.H., E.W., Costich, and H.J., Everett, 1950, Power Characteristics of Mixing Impellers, Chem Eng Prog, **46**, no. 8, 395-476

Sachs, J.P., and Rushton, J.H., 1954, Discharge Flow From Turbine-Type Mixing Impellers, Chem Eng Prog, **50**, 597-603

Schäffer, M., M., Höfken, and F., Durst, 1997, Detailed LDV Measurements for Visualization of Flow Field Within A Stirred-Tank Reactor Equipped With a Rushton Turbine, Chem Eng Res Des, **75**, no. A8, 729-736

Scähffer, M., M., Yianneskis, P. Wätcher, and F., Durst, 1998, Trailing Vortices around a 45^o Pitched-Blade Impeller, AIChE J., **44**, no. 6, 1233-1246

Stephenson, R., and J., Stuart, 1986, Mutual Binary Solubilities: Water-Alcohol and Water-Esters, J. Chem Eng. Data, **51**, 56–70.

Stokes, G.G., 1851, On the Effect of the Internal Friction of Fluids on the Motion of Pendulums, Trans Cambridge Phil Soc, **9**, 8–106.

Sverak, S., and Hrubý, M., 1981, Gas Entrainment From the Liquid Surface of vessels With Mechanical Agitators, Int Chem Eng, **21**, no. 3, 519-526

Tanaka, M., S. Noda, and E., O'shima, 1986, Effect of Location of a Submerged Impeller on the Enfoldment of Air Bubbles From the Free Surface in a Stirred Vessel, Int Chem Eng, **26**, n. 2, 314-318

Tanaka, M., and T., Izumi, 1987, Gas Entrainment in Stirred-Tank Reactors, Chem Eng Res Des, **65**, 195-198

Taylor, G.I., 1935, Statistical Theory of Turbulence, Proc of Royal Soc London. Series A, Math and Phy Sci, **151**, No. 873, 421-444

Tennekes, H. and J.L., Lumley, A First Course in Turbulence, MIT Press, Cambridge, Massachussets (1989)

Thoma, S., V.V., Ranade, and J.R., Bourne, 1991, Interaction Between Micro- and Macro-mixing During Reaction in Agitated Tanks, Can J. Chem Eng, **69**, 1135-1141

Van der Molen, K., and H.R.E., Van Maanen, 1978, Laser Doppler Measurements of the Turbulent Flow in Stirred Vessels to Establish Scaling Rules, Chem Eng Sci, **33**, no. 9, 1161-1168

Van't Riet, K., and J.M., Smith, 1975, The Trailing Vortex System Produced by Rushton Turbine Agitators, Chem Eng Sci, **30**, 1093-1105

Veljković, V.B., K.M., Bicok, and D.M., Simonović, 1991, Mechanism, Onset and Intensity of Surface Aeration in Geometrically Similar, Sparged, Agitated Vessel, Can J. Chem Eng, **69**, 916-926

Verschuren, I.L.M., Wijers, J.G., and J.T.F., Keurentjes, 2002, Large-Scale Oscillations of a Feedstream Inside a Stirred Tank reactor, AIChE J, **48**, no 9, 1888-1895

Villermaux, J. and R. David, 1987, Interpretation of Micromixing Effects on Fast Consecutive Competitive Reactions in Semi-Batch Stirred Tanks By a Simple Interaction Model, Chem Eng Commun, **54**, 333-352

Volkart, P., 1980, The Mechanism of Air Bubble Entrainment in Self-Aerated Flow, Int J Multiphase Flow, **6**, 411-423

Wygnanski, I., and H.E. Fiedler, 1969, Some Measurements in a Self-Preserving Jet, J. Fluid Mech., **38**, 577-612

Young, D.F., Munson, B.R., and T.H., Okiishi, Chapter 8: Viscous Flow in Pipes, A Brief Introduction to Fluid Mechanics, John Wiley, New York (2001)

Yu, S., 1993, Micromixing and Parallel Reactions, PhD Thesis, Swiss Federal Inst. Of Tech., Zurich

Zhou, G., 1997, Characteristics of Turbulence Energy Dissipation and Liquid-Liquid Dispersions in an Agitated Tank, PhD Thesis, University of Alberta, Edmonton, Alberta

Zhou, G., and S.M., Kresta, 1996, Impact of Tank Geometry on Maximum Energy Dissipation Rate for Impellers, AIChE J., **42**, 2476-2490

Zwietering, T.N., 1959, The degree of mixing in continuous flow systems, Chem Eng Sci., **11**, 1-15

Appendix A
Mean Flow Characteristics in a Stirred Tank

A.1. Rushton Turbine (RT)

Investigations on the flow field in stirred tanks are usually geared towards measurement of velocities in either the highly turbulent impeller region or the less active bulk region of the tank. Many of the studies on the mean flow in tanks stirred with RT have been directed towards the flow in the *impeller discharge* stream. The velocity profile at the impeller tip is parabolic with an initial spread roughly equal to the blade width as shown in Figure 2.7b. As the stream moves away from the impeller, the profile become flatter and broadens as the mean centreline velocity decays. This decay of the mean, radial component of the centerline velocity is often reported in the form:

$$\frac{\overline{V}(\text{impeller centerline})}{V_{Tip}} = \varphi\left(\frac{r}{R}\right)^{-\gamma} \qquad (A.1)$$

Velocity profiles similar to Equation (A.1) has been observed by numerous researchers who presented various values[6] for the constants, φ and γ. The decay and the spread of the mean velocity field in the impeller discharge stream suggest that it has a self-similar profile that is established only a short distance from the impeller. Kolar et al. (1984, 1985) modeled the impeller discharge stream as a swirling radial jet (SRJ) and the velocity profiles predicted by their SRJ model show very good match to the experimental data. This idea was carried forward by Kresta and Wood (1991) who used the SRJ model and the k-ε turbulence model to generate boundary conditions at the impeller and thence simulated the turbulent flow field in the whole tank. They also determined that the SRJ leaves the impeller blade at an angle of about 45 ° to the radial direction and their data show that the jet decay is inversely proportional to r, and the spreading half-angle of the jet is about 9.6°.

---

[6] For example, Lee and Yianneskis (1998) reported $\varphi = 0.74$ and $\gamma = 0.99$ and Dyster et al., 1993 reported similar values, while Van der Moolen and van Maanen, 1978 reported $\varphi = 0.85$ and $\gamma = 1.17$.

As the impeller discharge impinges the tank wall it splits into upwards and downwards-moving streams and the baffles damp out any remaining tangential motion. Kresta et al. (2001) modeled the *bulk* flow along the wall as two internal annular wall jets as shown in Figure 2.7c. The flow along the wall is mainly axial and Kresta et al. (2001) showed that experimental data agreed very well with their annular wall jet model in which the radial profiles of the axial velocity at different axial locations along the wall is compressed into a single similarity profile:

$$\frac{U}{U_m} = 1 - 1.75\tanh^2\left[0.702\left(\frac{y}{b} - 0.15\right)\right] \tag{A.2}$$

The notation 'y' is used to denote the radial distance from the wall, 'U_m' is the maximum axial velocity at any axial location and 'b' is the jet half-width defined as y at which $U = U_m/2$. Kresta et al. (2001) showed further that

$$\frac{U_m}{U_{core}} \propto \frac{1}{\sqrt{(z+z_0)/T}} \tag{A.3}$$

and $$\frac{b}{T} \propto \frac{(z+z_0)}{T} \tag{A.4}$$

U_{core}, the core velocity, is the maximum velocity existing in the jet and z_o, the virtual origin, is an imaginary point at which the width of the jet shrinks to zero. Experimental results from Kresta et al. (2001) show that U_m scales with V_{Tip}, and both U_m and z_0 are sensitive to impeller/tank geometry. A big attraction of this model is that the bulk motion in the tank can be completely defined simply through Equation (A.2). The free stream counter flow near the center is driven by the wall jet, and a single velocity and length scale completely define the bulk flow: the core velocity in the jet, U_{core}, and the virtual origin, z_0.

A.2. Pitched Blade Turbine (PBT)

In general the observations from previous studies on PBT can be divided into two groups based on the part of the flow field under considerations: (i) the impeller discharge stream and (ii) bulk flow. Observations on the impeller discharge stream are described first.

For relatively low clearances, the *discharge from the impeller* leaves at an angle of about 45° to the horizontal and moves downwards. The discharge velocity increases from very low values near the hub, to reach a peak of about $0.45V_{Tip}$ at a radial position of about 2r/D = 0.8 and then reduces sharply (Figure 2.9c). This was observed in numerous studies including those by Jaworski et al. (1991) and Kresta and Wood (1993). The angle of the discharge stream can however be affected by its interaction with the vessel wall. Kresta and Wood (1993) noted that if the impeller clearance was raised above a certain value (C/D ~ 0.67 for D = T/2) then the impeller discharge stream starts impinging on the tank wall and a secondary loop forms in the bottom of the tank as shown in Figure 2.9b. Similar reversal of flow near the bottom of the tank for high clearances was also noted by Jaworski et al. (1991). In the case of a small impeller, e.g. D = T/3, this loop is relatively weak, but for larger impeller sizes (D = T/2) the loop can be sufficiently strong to deflect the impeller discharge stream away (towards the wall) from its normal path. This interaction between the impeller discharge stream and the tank wall has consequences for simulation of the flow field generated by a PBT. For e.g. Fokema et al. (1994) showed that using velocity data at the suction and discharge of an impeller to start simulations could lead to significant errors for a PBT. Employing a steady-state simulation based on the Multiple Reference Frame (MRF) approach, earlier validated by Harvey and Rogers (1996), Bhattacharya and Kresta (2002) were able to determine the influence of the impeller clearance on the impingement point of the discharge and the formation of the secondary loop. They showed that the point of impingement is dependent on the impeller size and is $C/D_{Impingement}$ ~ 0.7 for D = T/2 and $C/D_{Impingement}$ ~ 1.4 for D = T/3.

An important feature of *bulk flow-field* generated by pitched blade turbines, first reported by Kresta and Wood (1991), is the fact that the velocity vectors in the top one-third of the tank are very small. This has been confirmed by many other studies. The Computational Fluid Dynamic (CFD) simulations by Bhattacharya and Kresta (2002) showed that the top one-third of the tank remained outside the active zone even when the impeller was placed at extraordinarily high clearances (C/D ~ 1.4 for T/3 impeller). Bittorf and Kresta (2001) explained this in terms of the formation of three-dimensional wall jets shown in Figure 2.9d. The figure shows one of the wall jets formed between the baffle and the tank wall. The expansion of the jet and decay of axial velocity in a vertical plane close to the baffle are shown for different axial positions in the tank. At any axial location, the axial velocity (U) increases rapidly from the no slip condition at the wall to its maximum value (U_m) and then decreases with a smaller gradient. At $y \sim 1.7b$ the axial velocity reverses direction due to recirculation and asymptotically approaches the recirculating velocity (U_R). In Figure (2.9d, D = T/3 and C/D ~ 1.0) the global maximum velocity along the tank wall, U_{core} occurs at z/T ~ 0.2. As the jet moves upwards, it expands in the y direction with a simultaneous decay in U_m. The jet finally collapses near the top of the tank (z/T ~ 0.7 for D = T/3 and C/D ~ 1.0). The section of the tank beyond the reach of the wall jet remains relatively quiescent.

Between the two limits of formation and disintegration, the three-dimensional wall jet is self-similar. Bittorf and Kresta (2001) extended the Goertler solution to include the effect of the recirculating flow outside the jet region and obtained a similarity profile similar to Equation (A.2):

$$\frac{U}{U_m} = 1 - 1.58\tanh^2[0.78(\eta - 0.15)] \qquad \text{(A.5)}$$

This equation in conjunction with expressions for the maximum velocity decay and jet expansion provides a complete characterization of the vertical flow. Bittorf and Kresta (2001) relate U_m and b in two regions of the jet. In the characteristic decay region a classical wall jet is still responding to the geometry of the nozzle. In the stirred tank the wall jet is responding to the combined effects of the tangential flow and circulation.

$$\frac{U_m}{U_{core}} = 1.35\left(\frac{z}{T}\right)^{-0.49} \quad \text{(characteristic decay)} \qquad \text{(A.6)}$$

In radial decay, the jet is fully formed and has no recollection of the initial effects of geometry. In cross-section it forms a quarter circle with expansion in the radial direction. The maximum velocity U_m is inversely proportional to the distance traveled:

$$\frac{U_m}{U_{core}} = 0.57\left(\frac{z}{T}\right)^{-1.15} \quad \text{(radial decay)} \qquad \text{(A.7)}$$

The jet half-width expands as:

$$\frac{b}{T} = 0.38\left[\frac{z - z_o}{T}\right] \qquad (A.8)$$

Bittorf and Kresta (2001) found that Equations (A.5), (A.6), (A.7) and (A.8) are valid for a range of axial impeller: PBT, HE3 and A310 impellers. This point is important because it means that the vertical flow field for all of these commonly used impellers can be characterized by simply using these three equations.

Appendix B
Fully Turbulent Flows

The instantaneous velocity ($\tilde{U}_i$) at any spatial location in the flow can be deconstructed into its constituent mean and fluctuating parts:

$$\tilde{U}_i = \overline{U}_i + u'_i \tag{B.1}$$

where, i takes the values 1, 2 and 3 representing the three axes of symmetry. u'_i are the turbulent fluctuations and the overbar represents an average defined as:

$$\overline{U}_i(x_{i,O}) = \lim_{T\to\infty} \frac{1}{2T} \int_{-T}^{T} \tilde{U}_i(x_{i,O}, t')dt' \tag{B.2}$$

Note that by their very definitions, Equations (B.1) and (B.2) imply that $\overline{u'_i} = 0$. When estimating the average in Equation (B.2), T can take only finite values but it should be large enough to keep errors within prescribed limits. On the other hand, if there is some slow time dependence in the flow then T should be short enough so that the temporal dynamics is not averaged out. In this case, an ensemble averaging is often preferred. If N macroscopically identical experiments are carried out to get N velocity measurements ($\tilde{U}_i^n$ being the velocity measured in the n^th^ experiment) then the ensemble average is obtained as:

$$\langle U_i \rangle = \lim_{N\to\infty} \frac{1}{N} \sum_{n=1}^{N} \tilde{U}_i^n \tag{B.3}$$

For stationary or quasi-stationary flows, Equations B.2 and B.3 are equivalent to each other. The definitions for fluctuating velocity and the turbulent kinetic energy have been provided in section 2.4.1.1 of Chapter 2. Turbulent kinetic energy is generated at the largest scales of the flow while it is dissipated at the smallest. The transfer of energy between the scales is often explained using the concepts of an energy cascade developed by Kolmogoroff. A schematic representation of the model is shown in Figure 2.11. The definitions of the rate of dissipation of turbulent kinetic energy, ε has been provided in section 2.4.1.2 of Chapter 2:

$$\varepsilon = \frac{\text{kinetic energy per unit mass}}{\text{decay time}} \sim \frac{3u_S^2/2}{\ell/u_S} \alpha \frac{u_S^3}{\ell} \tag{B.4}$$

Experiments have shown that the proportionality constant in Equation (B.4) is of the order of unity (~ 0.8). Instead of using the hypothetical characteristic scale, ℓ (obtained by volume averaging the scale of the largest, most energetic eddies) a more rigorous estimate of ε can be obtained by relating it to the better-defined integral length scale Λ_g (cross-stream, or its equivalent Λ_f in the stream wise direction). Taylor (1935) defined the cross-stream integral length scale as

$$\Lambda_g = \int_0^\infty g(\xi)d\xi \tag{B.5}$$

where the cross-stream (assuming flow in the x and the cross-stream to be in the y-directions) correlation function g(ξ) is defined as,

$$g(\xi) = \frac{\overline{u'(x, y+\xi)\cdot u'(x, y)}}{\overline{u'^2}} \tag{B.6}$$

For isotropic turbulence, Hinze (1975, pages 248 and 255) show that for a particular range of the energy spectrum (the –5/3, inertial subrange) the relation between ε and Λ_g is as follows

$$\varepsilon \sim 0.31\frac{u_S^3}{\Lambda_g} \tag{B.7}$$

The forms of Equations (2.20) and (B.7), especially the former, are very useful and have been used by numerous researchers to relate ε to the measured velocity fluctuations in a stirred tank.

The multitude of scales in turbulent flows is best illustrated by the distribution of the turbulent kinetic energy at the various scales. Different size of eddies have their own energy transfer characteristics that can be depicted by the energy spectrum. The later is obtained from the time evolution of the second order, two-point correlation tensor, Q_{ij} and its Fourier transform. This tensor is a fundamental, statistical quantity of a turbulent flow field and contains detailed information about the three-dimensional structure of the flow. Q_{ij} is defined by the correlation in the turbulent fluctuations between two points separated by the vector r_m (x_m and x_m+r_m, m takes the values of 1,2 and 3) as follows:

$$Q_{ij}(r_m)=\langle u'_i(x_m,t)\cdot u'_j(x_m+r_m,t)\rangle \tag{B.8}$$

The spectrum tensor, ϕ_{ij}, is obtained by Fourier transform of the correlation tensor Q_{ij}:

$$\phi_{ij}(k_m)=\frac{1}{(2\pi)^3}\int\int_{-\infty}^{\infty}\int \exp(-ik_jr_j)Q_{ij}(r_m)dr_1dr_2dr_3 \tag{B.9}$$

$$\text{with,}\quad Q_{ij}(r_m)=\int\int_{-\infty}^{\infty}\int \exp(ik_jr_j)\phi_{ij}(k_m)dk_1dk_2dk_3 \tag{B.10}$$

In Equations (B.9) and (B.10), $i=\sqrt{-1}$ and k_m is the wave vector ($k_i = 2\pi/r_i$). Of particular interest to this discussion is the fact that the trace of the spectrum tensor ($\phi_{ii} = \phi_{11} + \phi_{22} + \phi_{33}$) is equal to the kinetic energy at a given wave-number vector, k_m. This is seen from the value of $Q_{ii}(r_m)$ for $|r_m| = 0$ (Equations B.8 and B.10):

$$Q_{ii}(0)=\langle u'_i\cdot u'_i\rangle = u_i^2 = \int\iint_{-\infty}^{\infty}\phi_{ii}(k_m)dk_1dk_2dk_3 \tag{B.11}$$

Integration of ϕ_{ii} over a spherical shell of radius $|k|$, therefore gives the total amount of kinetic energy associated with the wave-number k:

$$E(k)=\frac{1}{2}\oiint \phi_{ii}(k_m)dS \tag{B.12}$$

E(k) is called the 'three dimensional spectrum of turbulence'. Equation (B.12) can be integrated using Equation (B.9) and properly defining dS (surface element in terms of spherical co-ordinates as shown on pages 159-160 of Baldyga and Bourne, 1999):

$$E(k)=\frac{1}{\pi}\int_0^{\infty}\sin(kr)krQ(r)dr \tag{B.13}$$

The inverse Fourier transform of Equation (B.13) leads to

$$Q_{ii}(r)=2\int_0^{\infty}\frac{\sin(kr)}{kr}E(k)dk \tag{B.14}$$

Finally, for r → 0, we have from Equations (B.11) and (B.14)

$$\int_0^{\infty}E(k)dk=\frac{u_i^2}{2} \tag{B.15}$$

Equation (B.15) shows that integrating the three dimensional energy spectrum over the full range of wave numbers (from 0 to ∞) gives the total turbulent kinetic energy per unit mass of the fluid. Figure 2.12 depicts a typical three-dimensional spectrum of turbulent kinetic energy for a fully turbulent flow with very high local Reynolds number. It is seen that eddies in a range of lower wave numbers, contribute most to the total turbulent kinetic energy. This 'range of energy containing eddies', is characterized by the wave number $k_o \sim 1/\ell$, also shown in the figure. Of course, the size of the energy containing large eddies depend on the scale of the system, since ℓ is dependent on the elements generating turbulent kinetic energy. As the wave number increases, the eddy size decreases and the energy content of the eddies reduces, i.e. $\int_{k_1}^{k_2} E(k)dk$ decreases as $[k_1, k_2]$ moves down the energy spectrum. On the other end of the energy spectrum, the energy content in the eddies with wave numbers comparable to k_K is the least but, as discussed earlier, the viscous dissipation of turbulent kinetic energy is the highest. In fact, the dissipation spectrum, related to the energy spectrum through the relation[7]:

$$D(k) = 2\nu k^2 E(k) \tag{B.16}$$

shows a maximum at a wave number comparable to k_K. The eddies in between these two extremities ($k_o << k << k_K$) are involved in a transfer of energy from the large energy containing eddies to the small dissipative ones. Additionally, when the local Reynolds number (defined in terms of ℓ, Equation B.29) is large, and the Kolmogoroff scale, η, is sufficiently small (Equation B.28), there exist a range of wave numbers where the eddy size is sufficiently large so that viscosity effects are negligible and the amounts of energy dissipated is small compared to the energy transported by inertial effects. Kolmogoroff hypothesized that the energy spectrum in this range of wave numbers is independent of ν and solely dependent on ε. The region is called the 'inertial subrange' and a dimensional analysis shows that for this region:

$$E(k) = \alpha\varepsilon^{2/3} k^{-5/3} \quad \text{for } k_O << k << k_K \tag{B.17}$$

---

[7] Rate of dissipation of turbulent kinetic energy is related to the dissipation and energy spectrums through the relations: $\varepsilon = \int_0^\infty D(k)dk = 2\nu\int_0^\infty E(k)k^2 dk$

The inertial subrange is shown in Figure 2.12 with the slope of –5/3.

Unlike the inertial subrange, E(k) in the range of wave numbers comparable to k_K show a dependence on ν because of the enhanced viscous dissipation in this region. Figure 2.12 also shows the spectrum of concentration fluctuations G(k), which is defined such that:

$$\int_0^\infty G(k)dk = \overline{c'^2_\infty} \tag{B.18}$$

Differences in the shapes of the concentration and the energy spectrum arise because of the differences in the momentum (ν) and scalar ($\mathcal{D}$) diffusivities.

B.1. Length Scales in Turbulent Mixing

In this section, the turbulent energy and concentration spectrums in Figures 2.12 and 2.14a and 2.14b are used to define some of the length scales characteristic to fully turbulent flows. This is followed by a brief discussion on the corresponding time scales.

Kolmogoroff scale (η). This is the smallest scale occurring in turbulent flows. Dissipation of turbulent energy at this scale results primarily from viscous deformation of the fluid elements and the mechanism is completely laminar. Equation (2.17) can be used to define a characteristic rate of strain at this scale:

$$s_K = \left(\frac{\varepsilon}{\nu}\right)^{1/2} \tag{B.19}$$

The corresponding characteristic time scale for viscous dissipation is

$$\tau_K = \frac{1}{s_K} = \left(\frac{\nu}{\varepsilon}\right)^{1/2} \tag{B.20}$$

If u_K is defined as the velocity scale of dissipation so that the turbulent kinetic energy per unit mass is u_K^2, then the rate of dissipation of turbulent kinetic energy per unit mass is:

$$\varepsilon = \frac{u_K^2}{\tau_K} \tag{B.21}$$

From Equations B.20 and B.21

$$u_K = (\nu \cdot \varepsilon)^{1/4} \tag{B.22}$$

The length scale of dissipation, the Kolmogoroff length scale, is then obtained as:

$$\eta = u_K \tau_K = \left(\frac{\nu^3}{\varepsilon}\right)^{1/2} \tag{B.23}$$

The Reynolds number at this length scale is

$$Re_K = \frac{u_K \eta}{\nu} = 1 \tag{B.24}$$

Equation (B.24) confirms that the mechanism of energy dissipation is indeed completely laminar. Although η is the smallest scale of turbulent motion, it is not necessarily the scale at which dissipation is maximum, λ_d (e.g. pages 270 and 271 in Tennekes and Lumley, 1989). The later is however, of the same order of magnitude as η ($\lambda_d \sim 5\eta$) and the wave number for which dissipation is at its peak is often approximated by

$$k_d \sim \frac{1}{\eta} \tag{B.25}$$

The Kolmogoroff scale marks the end of the inertial subrange where $E(k) \propto k^{-5/3}$:

$$k_O \le k \le \frac{1}{\eta} \quad (\text{inertial subrange}) \tag{B.26}$$

k_O denotes the wave number at the integral scale. If $[u_S, \ell]$ and $[u_K, \eta]$ both belong to the inertial subrange, then

$$\varepsilon \approx \frac{u_S^3}{\ell} \approx \frac{u_K^3}{\eta} \tag{B.27}$$

Equation (B.27) can be rewritten using Equation (B.22) to relate η to the large scale Reynolds number

$$\eta \approx \frac{\ell}{Re_\ell^{3/4}} \tag{B.28}$$

where

$$Re_\ell = \frac{u_S \ell}{\nu} \tag{B.29}$$

Equation (B.28) shows that η reduces in size with an increase in the large scale Reynolds number. In order to have a distinct inertial subrange, with the demarcation given by

Equation (2.32), ℓ has to be much larger than η, the later needs to be very small and therefore Re_ℓ has to sufficiently large.

Corrisin (η_C) and Batchelor (η_B) Scales. Figure 2.12 shows that the concentration spectrum, G(k), although similar in shape to the energy spectrum, E(k), is spread out over a different range of wave numbers due to differences in the momentum (ν) and scalar ($\mathcal{D}$) diffusivities. The spread of the concentration spectrum depends on the Schmidt number (Sc) of the fluid. Figures 2.14a and 2.14b shows the concentration spectrum at high Reynolds number for a gas with Sc ~ 1 and a liquid with Sc >> 1. When Sc ~ 1 (typical for gases) diffusivity starts affecting the concentration spectrum in the inertial subrange even *before* viscous effects have started. The wave number at which this happens is smaller than the wave number corresponding to the Kolmogoroff scale ($k_K = 2\pi/\eta$). Thus, molecular diffusion competes with inertial convection and the time scale for diffusion (τ_D) is comparable to the time scale for turbulent convection (τ_U). It is possible to define the length scale characteristic to this regime, the Corrisin scale of turbulence, η_C, using the similarity between the two time scales (see page 346, Baldyga and Bourne, 1999):

$$\eta_C = \left(\frac{D^3}{\varepsilon}\right)^{1/4} \qquad \text{(B.30)}$$

$k_C = 1/\eta_C$ is shown in Figure 2.14a where it demarcates the *inertial-diffusive subrange*:

$$k_C = \frac{1}{\eta_C} \le k \le \frac{1}{\eta} = k_K \quad (\text{inertial}-\text{diffusive subrange}) \qquad \text{(B.31)}$$

In this subrange, the spectral flux of concentration variance (see section 2.4.2) is no longer equal to ε_C but decreases due to molecular diffusion. The mechanism of mixing in liquids is very different from that in gases due to the absence of this subrange. For Sc ~ 1 (typical in most liquids) molecular diffusivity does not yet affect the concentration spectrum even when the wave number has reached k_K. The scales of concentration fluctuations therefore have to be reduced further (wave number increases) by viscous deformations. This region extending beyond k_K is the viscous-convective subrange, which ends when the scale of the concentration fluctuations becomes so small that diffusion can compete with deformation. This happens at a wave number comparable to the Batchelor scale, η_B, defined as:

$$\eta_B = \left(\frac{D^2 \nu}{\varepsilon}\right)^{1/4} = \eta \cdot Sc^{-1/2} \tag{B.32}$$

Like the Corrisin scale, η_B can be obtained by equating the diffusion time (τ_D at η_B) to the characteristic time for viscous deformation (τ_K). The argument behind this procedure, equating τ_D at η_B to τ_K, is that the concentration striations disappear only when the lamella can diffuse at the same rate as the viscous dissipation scale. The wave number corresponding to the Batchelor scale is used to demarcate the viscous-convective and the viscous-diffusive subranges, as seen in Figure 2.14b:

$$\begin{aligned} &\frac{1}{\eta} \le k \le \frac{1}{\eta_B} && (\text{viscous} - \text{convective subrange}) \\ &k \ge \frac{1}{\eta_B} && (\text{viscous} - \text{diffusive subrange}) \end{aligned} \tag{B.33}$$

The concentration spectrums for the inertial-diffusive and the viscous-convective subranges were developed by Corrisin (1964) and Batchelor (1959). Note that the energy spectrum remains unaffected by the diffusivities of the scalar.

Integral (Λ_g) and Characteristics (ℓ) length scales. Both length scales (for velocity) have already been defined earlier. It was seen that Λ_g is obtained rigorously from the correlation between velocities while ℓ is a hypothetical characteristic length scale obtained by volume averaging the size of the large eddies in the turbulent flow. In the case of isotropic turbulence, it is possible to find a relation between ℓ and Λ_g (Hinze, 1975)

$$\ell = 2.66 \Lambda_g \tag{B.34}$$

For engineering solutions, experimental data on dissipation is often reported in terms of Equation (2.20) and a characteristic length scale, which is related to a characteristic length of the turbulence generating mechanism. In these equations, the characteristic length scale is often denoted as 'L'. This notation will be used later while reporting previous studies on turbulence in stirred tanks.

Similar to the integral length scale derived for velocity fluctuations, the integral length scale for concentration fluctuations (Λ_C) can also be defined to describe the size of the concentration eddies. This is done as follows:

$$\Lambda_C = \int_0^{\infty} R_{CC}(r,t)dr \tag{B.35}$$

where,

$$R_{CC}(r_i) = \frac{\overline{c'_\alpha(x_i)\cdot c'_\alpha(x_i + r_i)}}{\overline{c'^2_\alpha}} \tag{B.36}$$

$c'_\alpha(x_i)$ and $c'_\alpha(x_i + r_i)$ are the concentration fluctuations of species 'α' at two locations separated by the vector r_i. Λ_C is a measure of the largest concentration eddies, or spots of tracer, present in the turbulent mixture. The notation L_C is often used to denote the characteristic length scale (comparable to Λ_C) associated with the large concentration eddies.

B.2. Time Scales in Turbulent Mixing

As progressively smaller eddies are encountered in the energy spectrum, the energy transfer characteristics of the eddies and the characteristic time scales change. The time scales of particular importance to turbulent mixing are described in this section, starting with the blend time, a macro-scale not directly related to turbulence but nonetheless important for mixing in a stirred tank.

Blend time (θ_B). The blend time is a macroscopic time scale that is described as the time taken to achieve homogeneity of an added contaminant or tracer over the bulk of a stirred tank. It is quantified in terms of the variance of the mean contaminant concentration ($\overline{c^2}$) obtained from instantaneous measurements of probes placed at different spatial locations in the tank, and is formally defined as the time required to reduce down to 5% of its initial value. The Grenville (1992) correlations for blend times are extensively used for design and scale-up. They are dependent on the flow regime (turbulent, transitional or laminar) as determined by the impeller Reynolds number (Re_I):

$$N\theta_B = \frac{5.4}{P_O^{1/3}}\left(\frac{T}{D}\right)^2 \qquad \text{(turbulent)}$$

$$N\theta_B = \frac{1}{Re_I}\,\frac{184.2}{P_O^{2/3}}\left(\frac{T}{D}\right)^2 \qquad \text{(transitional)} \qquad \text{(B.37)}$$

Laminar blending is based on completely different mechanism (cutting and folding) hence blend time for that regime is not presented here. In small tanks (up to about 0.001 m^3) blend times are typically about 2 seconds but can be as high as 20 seconds for larger vessels (20 m^3) for low viscosity liquids.

Kolmogoroff (τ_K) and Batchelor (τ_B) time scale. The Kolmogoroff (η) and Batchelor (η_B) length scales have already been described in section 2.4.2. The discussion also included a description of the respective time scales. Equation (B.20) gives τ_K while the Batchelor time scale is by definition equal to τ_K. Since Batchelor and Kolmogoroff time scales are equal, mixing time proportional to τ_K is often referred to as Batchelor scale mixing (page 769, Patterson et al., 2004).

Corrsin mixing time (τ_C): Corrsin (1964) developed an expression for the time constant (τ_C) for decay of the mean of the concentration variance of a contaminant added in homogeneous, isotropic, stationary turbulence with high Reynolds number. Expressions were developed both for $Sc \sim 1$ and $Sc >> 1$ by (i) simplifying the real concentration spectrum, G(k) into linear parts, the inertial subrange and viscous convective subrange and neglecting the viscous diffusive subrange (ii) developing an expression for the concentration microscale (λ_C) using this spectrum and following the methods used for Taylor's microscale (λ_C, Taylor, 1935) and (iii) finally substituting the expression for λ_C into the transport equation for $\overline{c'^2}$ and integrating. The expression for the Corrisin mixing time is:

$$\tau_C = 2\left(\frac{L_S^2}{\varepsilon}\right)^{1/3} + \frac{1}{2}\left(\frac{\nu}{\varepsilon}\right)^{1/2} \ln(Sc) \qquad \text{for } Sc >> 1$$

$$\tau_C = 1.36\left(\frac{L_S^2}{\varepsilon}\right)^{1/3} \qquad \text{for } Sc \sim 1 \qquad (B.38)$$

The first part of the Corrsin mixing time for Sc >> 1 (in liquids) identifies the time scale for mesomixing, while the second part gives the time scales at the smallest eddies, i.e. micromixing. Mesomixing is an intermediate scale mixing occurring in the inertial subrange, while micromixing occurs at the smallest concentration scales of the order of η_B and η. In terms of turbulent reactive mixing, the initial scale in Equation (B.38 for Sc >> 1), L_S is often set by the inlet conditions, e.g. feed pipe diameter and not by the local turbulence.

Complex models for turbulent mixing have been developed using the concentration and energy spectrums and the characteristic scales described above.

Appendix C
Models for Turbulent Mixing

C.1. Micromixing – EDD model:

The basic features of this mechanistic interpretation of micromixing have already been discussed in section (2.4.3) of Chapter 2. The process consists of engulfment of fluid from the surrounding (E), deformation of these elements (D) and final homogenization by means of diffusion and reaction (D). Unsteady diffusion and reaction occurring in the shrinking fluid lamellae is obtained from the species mass balance:

$$\frac{\partial C_\alpha}{\partial t} + u\frac{\partial C_\alpha}{\partial x} = D_\alpha \frac{\partial^2 C_\alpha}{\partial x^2} + r_\alpha \tag{C.1}$$

This equation is valid for the region $-\delta < x < \delta$ in Figure 2.15d, 'α' denotes the reactive species A, B, C etc. and u is the local rate of shrinkage given by:

$$u = -\frac{dx}{dt} = sx \tag{C.2}$$

's' is the rate of deformation of the vortex. Baldyga and Bourne (page 569, 1999) describe some of the relevant mechanism from which the rate of deformation can be estimated. The boundary conditions for Equation (C.1) are:

$$x = \pm\delta, \text{ and } \frac{\partial c_\alpha}{\partial x} = 0 \tag{C.3}$$

The mean lifetime of an energy-dissipating vortex is defined as the time required for the vortex fluid to return to a hydrodynamically isotropic state under the action of viscosity, in the absence of strain and is given by τ_ω (see Equation 2.36). Engulfment, deformation, diffusion and reaction continues with a frequency, τ_ω^{-1}, until the fluid is completely homogenized. Several generations of vortices are therefore needed to completely homogenize the added 'blob' of fluid. The set of parabolic, partial equations in Equation (C.1) need to be solved multiple times until the end of the process. Because these equations are stiff, computations are very costly. Baldyga and Bourne (1989) proposed a simplification of the EDD model for Sc < 4000 when the diffusion term is neglected. The simplified E-model is discussed below.

C.2. *Micromixing – E model*

When Sc < 4000 the role of molecular diffusion is very small compared to fluid engulfment even at scales equivalent to or smaller than η (Baldyga and Bourne, 1989). For this Schmidt number, the rate of engulfment is the limiting process and the main consideration is the rate of increase of the mixing or reaction volume (V_m):

$$\frac{dV_m}{dt} = EV_m \qquad \text{(C.4)}$$

E is the engulfment parameter, defined by Baldyga and Pohorecki (1995) which also leads to the definition of the characteristic time for micromixing (τ_E). V_m is the reaction or mixing volume under consideration and is initially equal to the volume of B added, V_{B0}. The mass balance (without diffusion effects) coupled with the equation for growth of the mixing volume by engulfment (Equation 2.37) gives the evolution equation for the concentration:

$$\frac{dc_\alpha}{dt} = E\left[\langle C_\alpha \rangle - C_\alpha\right] + r_\alpha \qquad \text{(C.5)}$$

r_α is the reaction rate for species 'α' and $\langle c_\alpha \rangle$ denote the concentration of species α in the local environment of the growing eddy or reaction volume. When the volume of B is not small, so that self-engulfment of B cannot be ruled out, a probability of engulfment, P, is added in Equations (2.37) and (2.40) to account for the later:

$$\frac{dV_m}{dt} = E\,P\,V_m \qquad \text{(C.6)}$$

$$\frac{dc_\alpha}{dt} = E\,P\left[\langle C_\alpha \rangle - C_\alpha\right] + r_\alpha \qquad \text{(C.7)}$$

where P is related to the volume fraction of B, X_B:

$$P = 1 - X_B \qquad \text{(C.8)}$$

Quantitatively this micromixing model involves simultaneous solution of Equations (C.6), (C.7) and (C.8) for all species involved in the reaction. The integration is done by (i) discretizing the feed volume in many parts and allowing each part to be added into the reactor one at a time (ii) solving Equations (C.6), (C.7) and (C.8) simultaneously using a proper numerical scheme until all B in the added part is used up, and (iii) finally updating the concentration in the tank, $\langle C_\alpha \rangle$, before the next part is added. Example calculations for competitive-consecutive reactions with an instantaneous first step are given in pages 616-632, Baldyga and Bourne (1999) for semibatch and CSTR.

C.3. Mesomixing – Mechanisms and Models

Concentration gradients in the microscale (micromixing) have a direct influence on the chemical reaction as outlined above. Inhomogeneity on a coarser scale, involving macro and mesomixing can also have a significant influence on the overall yield and selectivity of a complex reaction. Macromixing is linked to the overall flow-field/circulation in the mixing equipment and is quantified by the blend time. Mesomixing on the other hand occurs at a relatively smaller scale of the feed-pipe, and involves turbulent exchange between fresh feed and its surroundings. Two mechanisms have been identified for mesoscale limitations (Baldyga et al., 1997): turbulent dispersion and inertial convective disintegration. These processes have already been described in Chapter 2, here we will look at the mathematical constructs of the models.

C.3.1. Model based on turbulent dispersion:

For a point source with homogenous turbulence, when D_T = constant and $\overline{U}$ = constant, the radial distribution of the volume-fraction of species α, being fed, is given as:

$$X_{\alpha}^{0}(r,x)=\frac{\dot{V}_{\alpha}}{4\pi D_T x}\exp\left(-\frac{\overline{U}r^2}{4D_T x}\right) \tag{C.9}$$

Equation (C.9) gives the concentration field formed by dispersion of the feed stream (B-rich) radially, traverse to the flow by the action of turbulent dispersion. Micromixing proceeds within this B-rich fluid. The distribution of volume fraction for a finite source (as defined by Equation 2.42) is:

$$X_{\alpha}^{0}(r,x)=\frac{\dot{V}_{\alpha}}{2\pi d_f^2 D_T x}\exp\left(-\frac{\overline{U}r^2}{4D_T x}\right)\cdot\int_0^{d_f}\exp\left(-\frac{\overline{U}r^2}{4D_T x}\right)I_0\left(\frac{\overline{U}rr'}{2D_T x}\right)r'dr' \tag{C.10}$$

where, I_0 is a modified Bessel function of the first kind of order zero. Micromixing occurs within the concentration field of the expanding plume. While implementing this model for reaction calculations, micromixing equations (Equation 2.37 to 2.40) are solved while updating the local environment of the vortices using Equations (C.9) or (C.10).

Other methods of representing the traverse growth of the B-rich feed stream by turbulent dispersion have also been proposed. For a pulse input of a reactant (B) into a system containing another pure reactant (A), Villermaux and David (1987) proposed that the rate of growth of the reaction volume as:

$$\frac{1}{V_C}\frac{dV_C}{dt} = \frac{D_T}{V_C^{2/3}} \qquad \text{(C.11)}$$

where, V_C is the cloud or reaction volume. When the input is a continuous stream, instead of a pulse, concentration gradients in the radial direction are much greater than the gradient in the axial direction. In this case, the governing equation is obtained as:

$$\frac{1}{A_C}\frac{dA_C}{dt} \approx \frac{D_T}{A_C} \qquad \text{(C.12)}$$

Baldyga and Bourne (1999) point out that inhomogeneity in the turbulent field as well as the effects of converging or diverging flow significantly effect dispersive mesomixing and hence Equations (C.11) and (C.12).

C.3.2. Model based on inertial-convective disintegration:

Figure 2.17 shows a schematic representation of the process of inertial-convective disintegration. A large spot of contaminant is disintegrated by turbulence to η. Baldyga and Bourne (page 596, 1999) describe this process as "a cascade in concentration spectrum where decreasing concentration scale conveys material towards scales of molecular diffusion". Molecular diffusion causes local homogenization of concentration forming a new spot on which the disintegration-micromixing process is repeated. This process of reduction in concentration fluctuations has been interpreted either as (i) breakup of blobs of pure, unmixed solution resulting in *erosive mixing* or as (ii) formation of small eddies within larger eddies, giving the *eddies in eddies* interpretation. Baldyga et al. (1997), Baldyga, and Bourne (page 597, 1999) give a list of references for these interpretations. Both interpretations of the inertial-convective mesomixing process give the same time constant, τ_S, described above. It should be noted that the processes of convective disintegration and micromixing proceed simultaneously and not in series.

If the eddies in eddies interpretation is chosen as the representative mechanism of inertial-convective mesomixing, a mathematical model can be developed on the basis of the mechanism shown in Figure 2.18, reproduced from Baldyga et al. (1997). The figure shows segregated regions of reactant B in reactant A in a macroscopically well-mixed system, so that the average concentration of B in the system, X_{Bm}, is present uniformly throughout the reactor. The segregated regions or "islands" of B each have a composition X_B^e and the total volume fraction of the islands in the reactor is X_U, such that

$$X_{Bm} = X_U X_B^e \qquad \text{(C.13)}$$

When the reactant B is added into the reactor, the islands are purely B, so the initial volume fraction of the islands, X_U, is equal to the volume fraction of reactant B, X_{B0}. As mixing proceeds, A is mixed into the islands because of which the island volume increases, even as X_B^e reduces. The rate of growth of the island volume can be obtained as follows: (i) the variance of the structure shown in the figure can be expressed in terms of X_U, X_B^e and X_{Bm}, (ii) coupled with an expression for the rate of decay of variance in the inertial-convective subrange (Corrsin, 1964) and (iii) simplified with Equation (2.46) to obtain an expression for the rate of increase in the island volume:

$$\frac{dX_u}{dt} = \frac{X_u(1 - X_u)}{\tau_S} \qquad \text{(C.14)}$$

If τ_S is constant then Equation (2.47) can be integrated to give $X_U = f(t)$, using the initial volume fraction of the islands, X_{B0}, which is equal to the volume fraction of pure B in the reactor.

Equation (2.47) gives the rate of increase in the total volume of islands of B but the reaction takes place only in a small region within each island, where the A and B molecules are micromixed. Expressions are therefore needed to account for the change in the micromixed volume (within the growing islands) and the mass transfer within this region to be able to calculate the final product composition. If V_M is the total volume of micromixed, B-rich fluid in the system, the growth of V_M can be obtained from the Engulfment model of micromixing (Equation C.6):

$$\frac{dV_M}{dt} = EV_M(1 - X_{BU}) \tag{C.15}$$

where X_{BU}, is the volume fraction of the micromixed, B rich regions within the islands. If V_U is the total volume of all the islands, V_{Tank} is the total volume of the system and X_B is the volume fraction of micro-mixed regions with respect to the total system, then X_{BU} is obtained as:

$$X_{BU} = \frac{V_B}{V_U} = \frac{V_B}{V_{Tank}} \frac{V_{Tank}}{V_U} = \frac{X_B}{X_U} \tag{C.16}$$

Equations (C.15) and (C.16) allow the calculation of the rate of growth of the micromixed region with respect to the total system (here the tank):

$$\frac{dV_M}{dt} = EV_M\left(1 - \frac{X_B}{X_U}\right) \tag{C.17}$$

At time $t = 0$, $X_U = X_B = X_{B0}$, implying that the initial rate of growth of the micromixed volume (V_M) is zero. As eddy breakup increases, X_U becomes larger, the constraint of self-engulfment ($1 - X_{BU}$) is eased and micromixing can start. Equation (C.17) also shows that mesomixing retards micromixing when mesomixing is incomplete ($X_U < 1$). In the limit of complete mesomixing ($X_U \sim 1$), Equation (C.17) reduced to the engulfment Equation (C.6). Reaction can occur only within the micromixed region, hence the rate of change in concentration of any species, α, can be calculated from the unsteady-state mass-balance within the micromixed region as before (Equation C.6):

$$\frac{dc_\alpha}{dt} = E\left(1 - \frac{X_B}{X_u}\right)\left(\langle c_\alpha \rangle - c_\alpha\right) + r_\alpha \tag{C.18}$$

If $\tau_E < \tau_S$, i.e. micromixing takes place only within regions formed by mesomixing, Equations (2.47), (C.17) and (C.18) are integrated to obtain the concentration of each species. Baldyga et al. (1997) estimated yields of fast complex reactions in plug flow static mixers and semi-batch reactors when neither macromixing nor micromixing is limiting using this model. They reported satisfactory agreement between simulations and experimental results.

Appendix D
Velocity and Scalar Profiles in a Round Jet

The following is a review of the derivation of similarity solution for a fully turbulent, axisymmetric jet adapted mainly from the works of Hinze (1975) and Rajaratnam (1976). New arguments against the assumption of a universal solution (George, 1989; Hussein et al., 1994; Boersma et al., 1998) are also discussed.

D.1. Boundary layer equations

The continuity equation for an incompressible fluid in cylindrical co-ordinates[#] is:

$$\frac{\partial V_r}{\partial r}+\frac{V_r}{r}+\frac{1}{r}\frac{\partial V_\theta}{\partial \theta}+\frac{\partial V_x}{\partial x}=0 \qquad \text{(D.1a)}$$

In the same co-ordinate system, the ensemble averaged Reynolds equations for turbulent flows are:

Axial (x) direction:

$$\frac{\partial V_x}{\partial t}+V_r\frac{\partial V_x}{\partial r}+\frac{V_\theta}{r}\frac{\partial V_x}{\partial \theta}+V_x\frac{\partial V_x}{\partial x}=-\frac{1}{\rho}\frac{\partial P}{\partial x}+\frac{\mu}{\rho}\left(\frac{\partial^2 V_x}{\partial r^2}+\frac{1}{r}\frac{\partial V_x}{\partial r}\ldots\right.$$
$$\left.\ldots+\frac{1}{r^2}\frac{\partial^2 V_x}{\partial \theta^2}+\frac{\partial^2 V_x}{\partial x^2}\right)-\left(\frac{\partial \overline{v_x v_r}}{\partial r}+\frac{\overline{v_x v_r}}{r}+\frac{1}{r}\frac{\partial \overline{v_x v_\theta}}{\partial \theta}+\frac{\partial \overline{v_x^2}}{\partial x}\right) \qquad \text{(D.1b)}$$

Radial (r) direction:

$$\frac{\partial V_r}{\partial t}+V_r\frac{\partial V_r}{\partial r}+\frac{V_\theta}{r}\frac{\partial V_r}{\partial \theta}-\frac{V_\theta^2}{r}+V_x\frac{\partial V_r}{\partial x}=-\frac{1}{\rho}\frac{\partial P}{\partial r}+\frac{\mu}{\rho}\left(\frac{\partial^2 V_r}{\partial r^2}+\frac{1}{r}\frac{\partial V_r}{\partial r}\ldots\right.$$
$$\left.\ldots-\frac{V_r}{r^2}+\frac{1}{r^2}\frac{\partial^2 V_r}{\partial \theta^2}-\frac{2}{r^2}\frac{\partial V_\theta}{\partial \theta}+\frac{\partial^2 V_r}{\partial x^2}\right)-\left(\frac{\partial \overline{v_r^2}}{\partial r}+\frac{1}{r}\frac{\partial \overline{v_r v_\theta}}{\partial \theta}-\frac{\overline{v_\theta^2}}{r}+\frac{\partial \overline{v_x v_r}}{\partial x}+\frac{v_r^2}{r}\right) \qquad \text{(D.1c)}$$

Tangential (θ) direction:

[#] Capital letters are used for mean quantities, while small letters are for fluctuating quantities. Thus the actual ith component velocity $\widetilde{V}_i$, is given as $\widetilde{V}_i = V_i + v_i$ and the pressure $\widetilde{P}$, as $\widetilde{P} = P + p$

$$\frac{\partial V_x}{\partial t}+V_r\frac{\partial V_x}{\partial r}+\frac{V_\theta}{r}\frac{\partial V_x}{\partial \theta}+V_x\frac{\partial V_x}{\partial x}=-\frac{1}{\rho}\frac{\partial P}{\partial x}+\frac{\mu}{\rho}\left(\frac{\partial^2 V_x}{\partial r^2}+\frac{1}{r}\frac{\partial V_x}{\partial r}\dots\right.$$

$$\left.\dots+\frac{1}{r^2}\frac{\partial^2 V_x}{\partial \theta^2}+\frac{\partial^2 V_x}{\partial x^2}\right)-\left(\frac{\partial \overline{v_x v_r}}{\partial r}+\frac{\overline{v_x v_r}}{r}+\frac{1}{r}\frac{\partial \overline{v_x v_\theta}}{\partial \theta}+\frac{\partial \overline{v_x^2}}{\partial x}\right) \tag{D.1d}$$

Scalar transport:

$$\frac{\partial V_x}{\partial t}+V_r\frac{\partial V_x}{\partial r}+\frac{V_\theta}{r}\frac{\partial V_x}{\partial \theta}+V_x\frac{\partial V_x}{\partial x}=-\frac{1}{\rho}\frac{\partial P}{\partial x}+\frac{\mu}{\rho}\left(\frac{\partial^2 V_x}{\partial r^2}+\frac{1}{r}\frac{\partial V_x}{\partial r}\dots\right.$$

$$\left.\dots+\frac{1}{r^2}\frac{\partial^2 V_x}{\partial \theta^2}+\frac{\partial^2 V_x}{\partial x^2}\right)-\left(\frac{\partial \overline{v_x v_r}}{\partial r}+\frac{\overline{v_x v_r}}{r}+\frac{1}{r}\frac{\partial \overline{v_x v_\theta}}{\partial \theta}+\frac{\partial \overline{v_x^2}}{\partial x}\right) \tag{D.1e}$$

Assuming steady, $\frac{\partial V_x}{\partial t}=\frac{\partial V_r}{\partial t}=\frac{\partial V_\theta}{\partial t}=0$, axisymmetric flow, $\frac{\partial}{\partial \theta}=0$, without swirl, $V_\theta=0$, the continuity equation reduces to:

$$\frac{\partial V_r}{\partial r}+\frac{V_r}{r}+\frac{\partial V_x}{\partial x}=0\text{, which is equivalent to }\frac{\partial (rV_r)}{\partial r}+\frac{\partial (rV_x)}{\partial x}=0 \tag{D.2a}$$

and with similar assumptions the Reynolds equations reduce to:

Axial (x) direction:

$$\frac{\partial V_x}{\partial t}+V_r\frac{\partial V_x}{\partial r}+\frac{V_\theta}{r}\frac{\partial V_x}{\partial \theta}+V_x\frac{\partial V_x}{\partial x}=-\frac{1}{\rho}\frac{\partial P}{\partial x}+\frac{\mu}{\rho}\left(\frac{\partial^2 V_x}{\partial r^2}+\frac{1}{r}\frac{\partial V_x}{\partial r}\dots\right.$$

$$\left.\dots+\frac{1}{r^2}\frac{\partial^2 V_x}{\partial \theta^2}+\frac{\partial^2 V_x}{\partial x^2}\right)-\left(\frac{\partial \overline{v_x v_r}}{\partial r}+\frac{\overline{v_x v_r}}{r}+\frac{1}{r}\frac{\partial \overline{v_x v_\theta}}{\partial \theta}+\frac{\partial \overline{v_x^2}}{\partial x}\right) \tag{D.2b}$$

Radial (r) direction:

$$\frac{\partial V_x}{\partial t}+V_r\frac{\partial V_x}{\partial r}+\frac{V_\theta}{r}\frac{\partial V_x}{\partial \theta}+V_x\frac{\partial V_x}{\partial x}=-\frac{1}{\rho}\frac{\partial P}{\partial x}+\frac{\mu}{\rho}\left(\frac{\partial^2 V_x}{\partial r^2}+\frac{1}{r}\frac{\partial V_x}{\partial r}\dots\right.$$

$$\left.\dots+\frac{1}{r^2}\frac{\partial^2 V_x}{\partial \theta^2}+\frac{\partial^2 V_x}{\partial x^2}\right)-\left(\frac{\partial \overline{v_x v_r}}{\partial r}+\frac{\overline{v_x v_r}}{r}+\frac{1}{r}\frac{\partial \overline{v_x v_\theta}}{\partial \theta}+\frac{\partial \overline{v_x^2}}{\partial x}\right) \tag{D.2c}$$

Scalar transport:

$$\frac{\partial V_x}{\partial t}+V_r\frac{\partial V_x}{\partial r}+\frac{V_\theta}{r}\frac{\partial V_x}{\partial \theta}+V_x\frac{\partial V_x}{\partial x}=-\frac{1}{\rho}\frac{\partial P}{\partial x}+\frac{\mu}{\rho}\left(\frac{\partial^2 V_x}{\partial r^2}+\frac{1}{r}\frac{\partial V_x}{\partial r}\dots\right.$$

$$\left.\dots+\frac{1}{r^2}\frac{\partial^2 V_x}{\partial \theta^2}+\frac{\partial^2 V_x}{\partial x^2}\right)-\left(\frac{\partial \overline{v_x v_r}}{\partial r}+\frac{\overline{v_x v_r}}{r}+\frac{1}{r}\frac{\partial \overline{v_x v_\theta}}{\partial \theta}+\frac{\partial \overline{v_x^2}}{\partial x}\right) \tag{D.2d}$$

Dividing Equations (D.2b) and (D.2c) by V_xL, the terms containing μ/ρ become negligible at high Reynolds number ($Re = V_x L \mu / \rho \rightarrow \infty$). Thus, for highly turbulent flows, Equations (D.2a), (D.2b) and (D.2c) become:

$$\frac{\partial(rV_r)}{\partial r} + \frac{\partial(rV_x)}{\partial x} = 0 \tag{D.3a}$$

$$V_r \frac{\partial V_x}{\partial r} + V_x \frac{\partial V_x}{\partial x} = -\frac{1}{\rho}\frac{\partial P}{\partial x} - \left(\frac{\partial \overline{v_x v_r}}{\partial r} + \frac{\overline{v_x v_r}}{r} + \frac{\partial \overline{v_x^2}}{\partial x}\right) \tag{D.3b}$$

$$V_r \frac{\partial V_r}{\partial r} + V_x \frac{\partial V_r}{\partial x} = -\frac{1}{\rho}\frac{\partial P}{\partial r} - \left(\frac{\partial \overline{v_r^2}}{\partial r} - \frac{\overline{v_\theta^2}}{r} + \frac{\partial \overline{v_x v_r}}{\partial x} + \frac{\overline{v_r^2}}{r}\right) \tag{D.3c}$$

In highly turbulent flows $\overline{v_i c} \sim D_{Ti}\frac{\partial C}{\partial x_i} >> D_i\frac{\partial C}{\partial x_i}$, where D_{Ti} and D_i are respectively the turbulent and molecular diffusivities. As a result, Equation (D.2d) takes the form:

$$\frac{1}{r}\frac{\partial(rCV_r)}{\partial r} + \frac{\partial(CV_x)}{\partial x} = -\frac{1}{r}\frac{\partial}{\partial r}\left(r\overline{v_r c}\right) - \frac{\partial}{\partial x}\left(\overline{v_x c}\right) \tag{D.3d}$$

For the case of axisymmetric jets, these equations can be further simplified by employing an order of magnitude analysis, giving the so-called boundary layer equations. The following scales can be assumed:

$$\begin{array}{lll} V_x \sim U & \overline{v_x^2} \sim \overline{v_r^2} \sim \overline{v_\theta^2} \sim u^2 & \overline{v_i v_j} \sim R_{ij}u^2\,[R_{ij} \sim O(1)] \\ r \sim \delta & x \sim L & \end{array}$$

Using the above velocity and length scales in the continuity equation, equation (D.3a), the velocity scale for V_r (U_r) can be obtained:

$$\begin{array}{c} \dfrac{\partial(rV_r)}{\partial r} + \dfrac{\partial(rV_x)}{\partial x} = 0 \\ \dfrac{\delta U_r}{\delta} \qquad \dfrac{\delta U}{L} \end{array} \qquad \text{giving, } U_r \sim \frac{\delta U}{L} \tag{D.4}$$

Equation (D.3c) can be analyzed term by term to determine the order of magnitude of each term in the equation. This leads to simplification of the equation as follows:

$$
\begin{array}{cccccc}
V_r \dfrac{\partial V_r}{\partial r} & + \; V_x \dfrac{\partial V_r}{\partial x} = & -\dfrac{1}{\rho}\dfrac{\partial P}{\partial r} & -\left(\dfrac{\partial \overline{v_r^2}}{\partial r} \right. & + \; \dfrac{\partial \overline{v_x v_r}}{\partial x} & + \; \dfrac{\overline{v_r^2}}{r} \; - \; \left. \dfrac{\overline{v_\theta^2}}{r} \right) \\
\hline
\dfrac{\delta U}{L}\dfrac{\delta U}{L}\dfrac{1}{\delta} & U\dfrac{\delta U}{L}\dfrac{1}{L} & & \dfrac{u^2}{\delta} & \dfrac{R_{ij}u^2}{L} & \dfrac{u^2-u^2}{\delta}=0 \\
\left(\dfrac{\delta}{L}\right)\dfrac{U^2}{L}<<1 & \left(\dfrac{\delta}{L}\right)\dfrac{U^2}{L}<<1 & & \dfrac{u^2}{\delta} & \dfrac{R_{ij}u^2}{L}\sim\dfrac{u^2}{\delta}\left(\dfrac{\delta}{L}\right)<<1 & \\
 & & & & \text{if } O\left(\dfrac{u^2}{\delta}\right)\sim O\left(\dfrac{U^2}{L}\right) &
\end{array}
$$

so that

$$0 = -\frac{1}{\rho}\frac{\partial P}{\partial r} - \frac{\partial \overline{v_r^2}}{\partial r}$$

On integration this equation gives:

$$P = P(0) - \rho \overline{v_r^2},$$

Thus, $\dfrac{\partial P}{\partial x} = -\dfrac{\partial\left(\rho \overline{v_r^2}\right)}{\partial x}$ when the external pressure gradient, $\dfrac{\partial P(0)}{\partial x} = 0$. Employing this relation for pressure gradient in Equation (D.3b) results in:

$$V_r \frac{\partial V_x}{\partial r} + V_x \frac{\partial V_x}{\partial x} = -\left(\frac{\partial \overline{v_x v_r}}{\partial r} + \frac{\overline{v_x v_r}}{r} + \frac{\partial \overline{v_x^2}}{\partial x} - \frac{\partial \overline{v_r^2}}{\partial x} \right)$$

which is further simplified:

$$
\begin{array}{cccccc}
V_r \dfrac{\partial V_x}{\partial r} & + \; V_x \dfrac{\partial V_x}{\partial x} & = -\left(\dfrac{\partial \overline{v_x v_r}}{\partial r} \right. & + \; \dfrac{\overline{v_x v_r}}{r} & + \; \dfrac{\partial \overline{v_x^2}}{\partial x} & - \; \left. \dfrac{\partial \overline{v_r^2}}{\partial x} \right) \\
\dfrac{\delta U}{L}\dfrac{U}{\delta} & U\dfrac{U}{L} & \dfrac{R_{ij}u^2}{\delta} & \dfrac{R_{ij}u^2}{\delta} & \dfrac{u^2-u^2}{L}=0 &
\end{array}
$$

Thus, the equation for flow of an axisymmetric jet *without external pressure gradient* is:

$$\boxed{V_r \frac{\partial V_x}{\partial r} + V_x \frac{\partial V_x}{\partial x} = -\frac{1}{r}\frac{\partial\left(r\,\overline{v_x v_r}\right)}{\partial r}} \qquad \text{(D.5)}$$

Equations (D.3a) and (D.5) constitute the equations for an axisymmetric jet. Equation (D.3d) can be multiplied throughout by 'r' and written in the form:

$$\frac{\partial(rCV_r)}{\partial r} + \frac{\partial(rCV_x)}{\partial x} = -\frac{\partial}{\partial r}\left(\overline{rv_r c}\right) - \frac{\partial}{\partial x}\left(\overline{rv_x c}\right)$$

Further using concentration scales C ~ Ω and c ~ ω:

$$
\begin{array}{ccccccc}
\dfrac{\partial(rCV_r)}{\partial r} & + & \dfrac{\partial(rCV_x)}{\partial x} & = & -\dfrac{\partial}{\partial r}\left(r\overline{v_r c}\right) & - & \dfrac{\partial}{\partial x}\left(r\overline{v_x c}\right) \\
\dfrac{\delta\Omega}{\delta}\dfrac{\delta U}{L} & & \dfrac{\delta\Omega U}{L} & & \dfrac{\delta u\omega}{\delta} & & \dfrac{\delta u\omega}{L} \\
\delta\dfrac{\Omega U}{L} & & \delta\dfrac{\Omega U}{L} & & u\omega & & \left(\dfrac{\delta}{L}\right)u\omega << 1 \\
 & & & & & & \text{if } O\left(\dfrac{\Omega U}{L}\right) \sim O\left(\dfrac{\omega u}{\delta}\right)
\end{array}
$$

Thus giving the scalar transport equation:

$$\frac{\partial(rCV_r)}{\partial r}+\frac{\partial(rCV_x)}{\partial x}=-\frac{\partial}{\partial r}\left(r\overline{v_r c}\right) \qquad \text{(D.6a)}$$

This equation can be further simplified using the continuity equation (Equation D.3a) to give:

$$\boxed{V_r\frac{\partial C}{\partial r}+V_x\frac{\partial C}{\partial x}=-\frac{1}{r}\frac{\partial}{\partial r}\left(r\overline{v_r c}\right)} \qquad \text{(D.6)}$$

D.2. Axisymmetric jet in a co-flowing stream

D.2.1. Momentum flux:

In the case of an axisymmetric jet discharging into a co-flowing stream with a uniform velocity, U_s, Equation (D.5) can be written as:

$$(Us+U)\frac{\partial(Us+U)}{\partial x}+V_r\frac{\partial(Us+U)}{\partial r}=-\frac{1}{r}\frac{\partial\left(r\,\overline{v_x v_r}\right)}{\partial r}$$

Since U_s is constant this equation can be further simplified to give:

$$(Us+U)\frac{\partial U}{\partial x}+V_r\frac{\partial U}{\partial r}=-\frac{1}{r}\frac{\partial\left(r\,\overline{v_x v_r}\right)}{\partial r} \qquad \text{(D.7)}$$

where, U, is the axial velocity in the jet. In the same notation, the continuity equation is simply:

$$\frac{\partial(rV_r)}{\partial r}+\frac{\partial(rU)}{\partial x}=0 \qquad \text{(D.8)}$$

Multiplying Equation (D.7) throughout by 'ρr' and then integrating with respect to 'r' from the centerline of the jet to infinity, gives an expression for the change of momentum in the jet along 'x'. Thus,

$$\int_0^\infty \rho r(U_s+U)\frac{\partial U}{\partial x}dr+\int_0^\infty \rho r V_r\frac{\partial U}{\partial r}dr=-\int_0^\infty \frac{\partial\left(r\,\rho\overline{v_x v_r}\right)}{\partial r}dr \qquad \text{(D.9a)}$$

The first term in equation (D.9a) can be expanded and reorganized to give:

$$\int_0^\infty \rho r(U_s+U)\frac{\partial U}{\partial x}dr=\int_0^\infty \frac{\partial(\rho r U_s U)}{\partial x}dr+\frac{1}{2}\int_0^\infty \frac{\partial\left(\rho r U^2\right)}{\partial x}dr$$

Which on integrating with the Leibniz formula* gives:

$$\int_0^\infty \rho r(U_s+U)\frac{\partial U}{\partial x}dr=\frac{d}{dx}\int_0^\infty \rho r U_s U dr+\frac{1}{2}\frac{d}{dx}\int_0^\infty \rho r U^2 dr \qquad \text{(D.9b)}$$

The second term in Equation (D.9a) can be integrated by parts to give:

$$\int_0^\infty \rho r V_r\frac{\partial U}{\partial r}dr=\rho r V_r U\Big|_0^\infty-\int_0^\infty \rho U\frac{\partial(rV_r)}{\partial r}dr \qquad \text{(D.9c)}$$

The first term on the right hand side of Equation (D.9b) is zero since $V_r = 0$ at $r = \infty$. Further, from the continuity equation:

$$\frac{\partial(rV_r)}{\partial r}=-\frac{\partial(rU)}{\partial x} \qquad \text{(D.9d)}$$

Combining Equations (D.9c) and (D.9d) give

$$\int_0^\infty \rho r V_r\frac{\partial U}{\partial r}dr=\int_0^\infty \rho U\frac{\partial(rU)}{\partial x}dr=\frac{1}{2}\int_0^\infty \frac{\partial\left(\rho r U^2\right)}{\partial x}dr$$

This on integration, again using the Leibniz rule, gives

$$\int_0^\infty \rho r V_r\frac{\partial U}{\partial r}dr=\frac{1}{2}\frac{d}{dx}\int_0^\infty \rho r U^2 dr \qquad \text{(D.9e)}$$

Combining Equations (D.9b) and (D.9e) give the expression for the left hand side of Equation (D.9a):

---

[*] The Leibniz formula gives: $\frac{d}{dt}\int_{\alpha(t)}^{\beta(t)} f(x,t)dx=\int_{\alpha(t)}^{\beta(t)}\frac{\partial[f(x,t)]}{\partial t}dx+\left[f(\beta,t)\frac{d\beta}{dt}-f(\alpha,t)\frac{d\alpha}{dt}\right]$

$$\int_0^\infty \rho r(U_s+U)\frac{\partial U}{\partial x}dr+\int_0^\infty \rho r V_r\frac{\partial U}{\partial r}dr=\frac{d}{dx}\int_0^\infty \rho r U_s U dr+\frac{d}{dx}\int_0^\infty \rho r U^2 dr$$
$$=\frac{d}{dx}\int_0^\infty \rho r U(U_s+U)dr \tag{D.9f}$$

The right hand side of Equation (D.9a) is:

$$-\int_0^\infty \frac{\partial\left(r\,\rho\overline{v_x v_r}\right)}{\partial r}dr=r\,\rho\overline{v_x v_r}\Big|_0^\infty=0 \tag{D.9g}$$

since, this term is obviously zero at r = 0, and $\overline{v_x v_r}=0$ at $r=\infty$. Thus, combining Equations (D.9f) and (D.9g) give the integrated form of Equation (D.9a):

$$\frac{d}{dx}\int_0^\infty \rho r U(U_s+U)dr=0 \quad\Rightarrow\quad 2\pi\frac{d}{dx}\int_0^\infty \rho r U(U_s+U)dr=0 \tag{D.9h}$$

The term within the integral is the momentum flux passing through any x-plane in the x-direction. Since the momentum passing through the plane of the nozzle is

$\rho U_0(U_0-U_s)\frac{\pi}{4}d^2$, integrating Equation (D.9h) finally gives:

$$2\pi\int_0^\infty \rho r U(U_s+U)dr=\rho U_0(U_0-U_s)\frac{\pi}{4}d^2 \tag{D.9}$$

D.2.2. Scalar flux

For a jet issuing into a co-flowing stream of velocity U_s, the scalar transport equation (Equation D.6) can be modified to:

$$(U_s+U)\frac{\partial C}{\partial x}+V_r\frac{\partial C}{\partial r}=-\frac{1}{r}\frac{\partial}{\partial r}\left(r\overline{v_r c}\right) \tag{D.10a}$$

Equation (D.10a) can be further modified using the continuity Equation (D.8) to the form:

$$\frac{\partial[rC(U_s+U)]}{\partial x}+\frac{\partial[rCV_r]}{\partial r}=-\frac{\partial}{\partial r}\left(r\overline{v_r c}\right) \tag{D.10b}$$

Equation (D.10b) can be integrated term by term, using the procedures described above:

$$\int_0^\infty \frac{\partial[rC(U_s+U)]}{\partial x}dr=\frac{d}{dx}\int_0^\infty rC(U_s+U)dr$$

$$\int_0^\infty \frac{\partial[rCV_r]}{\partial r}dr = rCV_r\Big|_0^\infty = 0$$

$$\int_0^\infty \frac{\partial}{\partial r}\left(r\overline{v_r c}\right)dr = r\overline{v_r c}\Big|_0^\infty = 0$$

Combining these equations with Equation (D.10b) yields:

$$\frac{d}{dx}\int_0^\infty rC(U_s + U)dr = 0 \quad \Rightarrow \quad 2\pi\frac{d}{dx}\int_0^\infty rC(U_s + U)dr = 0 \qquad \text{(D.10c)}$$

The flux of scalar in the plane of the nozzle is $\frac{\pi}{4}d^2U_o(C_0 - C_s)$. Hence integration of Equation (D.10c) gives:

$$2\pi\int_0^\infty rC(U_s + U)dr = \frac{\pi}{4}d^2U_0(C_0 - C_s) \qquad \text{(D.10)}$$

D.3. Similarity Solutions - Velocity

Dividing Equation (D.7) throughout by U_o^2, we obtain

$$\left(\frac{Us}{U_o} + \frac{U}{U_o}\right)\frac{\partial}{\partial x}\left(\frac{U}{U_o}\right) + \frac{V_r}{U_o}\frac{\partial}{\partial r}\left(\frac{U}{U_o}\right) = -\frac{1}{r}\frac{\partial}{\partial r}\left(r\frac{\overline{v_x v_r}}{U_o^2}\right) \qquad \text{(D.11a)}$$

If the flow is assumed to be self-similar at a certain distance from the nozzle (8 to 10d), and the following similarity variables are selected:

$$\frac{U}{U_m} = f(\eta) \qquad \frac{V_r}{U_m} = g(\eta) \qquad \frac{\overline{v_x v_r}}{U_m^2} = h(\eta) \qquad \frac{U_s}{U_o} = \mu$$

$$\frac{U_m}{U_o} = \psi(\xi) \qquad \eta = \frac{r}{d}\varphi(\xi)^* \qquad \xi = \frac{x - x_o}{d}$$

[Note: Recently doubts have been raised (Boersman et al., 1998) over the choice of velocity scale in the similarity variable 'h'. A short discussion on this issue is provided later.]

Equation (D.10a) can be written as:

---

* where the jet half-width is given as, $b = {}^{d}/_{\varphi(\xi)}$. The jet half-width, b, is the value of the radius, r, at which $U = U_m/2$

$$(\mu + f\psi)\frac{\partial}{\partial x}(f\psi) + g\psi\frac{\partial}{\partial r}(f\psi) = -\frac{\varphi}{\eta d}\frac{\partial}{\partial r}\left(\frac{\eta d}{\varphi}h\psi^2\right), \text{ i.e.}$$

$$(\mu + f\psi)\left[f\frac{d\psi}{d\xi}\frac{d\xi}{dx} + \psi\frac{df}{d\eta}\frac{d\eta}{d\varphi}\frac{d\varphi}{d\xi}\frac{d\xi}{dx}\right] + g\psi\left[f\frac{\partial\psi}{\partial r} + \psi\frac{df}{d\eta}\frac{\partial\eta}{\partial r}\right] = -\frac{\psi^2}{\eta}\frac{d(\eta h)}{d\eta}\frac{d\eta}{dr}$$

or, $$(\mu + f\psi)\left[f\frac{d\psi}{d\xi}\frac{1}{d} + \psi\frac{df}{d\eta}\frac{\eta}{\varphi}\frac{d\varphi}{d\xi}\frac{1}{d}\right] + g\psi\left[\psi\frac{df}{d\eta}\frac{\varphi}{d}\right] = -\frac{\psi^2}{\eta}\frac{d(\eta h)}{d\eta}\frac{\varphi}{d}.$$

i.e. $$(\mu + f\psi)\left[\frac{\psi}{\varphi}\frac{d\varphi}{d\xi}\left\{\eta\frac{df}{d\eta}\right\} + \frac{d\psi}{d\xi}\{f\}\right] + \psi^2\varphi\left\{g\frac{df}{d\eta}\right\} = -\psi^2\varphi\left\{\frac{1}{\eta}\frac{d(\eta h)}{d\eta}\right\} \quad \text{(D.11)}$$

The terms within curly brackets are functions of η, while the remaining terms are functions of ξ only. Hence for complete similarity, i.e. to obtain an equation, which is a function of only η, each of the remaining terms should be either individually constant or proportional to each other. Therefore, the proportionality needed are:

(a) $\frac{\psi}{\varphi}\frac{d\varphi}{d\xi} \,\alpha\, \frac{d\psi}{d\xi}$ (b) $\psi\frac{d\psi}{d\xi} \,\alpha\, \frac{d\psi}{d\xi}$ (c) $\psi^2\varphi \,\alpha\, \frac{d\psi}{d\xi}$

so that a function of the following form can be obtained:

$$\mu\left[C_1\eta\frac{df}{d\eta} + f\right] + C_2 f\left[C_1\eta\frac{df}{d\eta} + f\right] + C_3 g\frac{df}{d\eta} = -C_3\frac{1}{\eta}\frac{d(\eta h)}{d\eta}$$

However, the conditions (a), (b) and (c) can be satisfied only if ψ and φ are both zero implying that a full similarity solution of Equation (D.11) is impossible. Similarity solutions are however possible in the two limiting conditions given below:

$\mu >> \psi f$, when the proportionality needed are: $\frac{\psi}{\varphi}\frac{d\varphi}{d\xi} \,\alpha\, \frac{d\psi}{d\xi}$ and $\psi^2\varphi \,\alpha\, \frac{d\psi}{d\xi}$

$\psi f >> \mu$, when the proportionality needed are: $\frac{\psi}{\varphi}\frac{d\varphi}{d\xi} \,\alpha\, \frac{d\psi}{d\xi}$ and $\psi\varphi \,\alpha\, \frac{d\psi}{d\xi}$

Case A - High stream velocity ($\mu >> \psi f$)

The dimensionless form of the momentum Equation (D.9) is:

$$\int_0^\infty\left(\frac{U_s}{U_o}\frac{U}{U_o} + \frac{U^2}{U_o^2}\right)r\,dr = \int_0^\infty\frac{U_s}{U_o}\frac{U}{U_o}r\,dr + \int_0^\infty\frac{U^2}{U_o^2}r\,dr = \text{const.}$$

i.e., $\int_0^\infty \mu f \psi \frac{d^2}{\varphi^2} \eta \, d\eta + \int_0^\infty f^2 \psi^2 \frac{d^2}{\varphi^2} \eta \, d\eta = \text{const.}$

i.e., $\frac{\mu\psi}{\varphi^2}\left\{\int_0^\infty f \, \eta \, d\eta\right\} + \frac{\psi^2}{\varphi^2}\left\{\int_0^\infty f^2 \eta \, d\eta\right\} = \text{const.}$ (D.12)

Under the condition, $\mu >> \psi f$, equation (D.12) reduces to:

$$\frac{\mu\psi}{\varphi^2}\left\{\int_0^\infty f \, \eta \, d\eta\right\} = \text{const.} \quad \text{(D.13a)}$$

thus giving, $\psi = A_1\varphi^2$, where A_1 is a constant. Equation (D.11) on the other hand reduces to:

$$\mu \frac{\psi}{\varphi} \frac{d\varphi}{d\xi} \eta \frac{df}{d\eta} + \mu \frac{d\psi}{d\xi} f + \psi^2 \varphi g \frac{df}{d\eta} = -\psi^2 \varphi \frac{1}{\eta} \frac{d(\eta h)}{d\eta}$$

i.e., $\mu A_1 \varphi \frac{d\varphi}{d\xi} \eta \frac{df}{d\eta} + \mu A_1 \frac{d\varphi^2}{d\xi} f + A_1^2 \varphi^5 g \frac{df}{d\eta} = -A_1^2 \varphi^5 \frac{1}{\eta} \frac{d(\eta h)}{d\eta}$

or, $\mu A_1 \frac{d\varphi}{d\xi}\left(\eta \frac{df}{d\eta} + 2f\right) + A_1^2 \varphi^4 \left(g \frac{df}{d\eta} + \frac{1}{\eta} \frac{d(\eta h)}{d\eta}\right) = 0$

or, $\mu A_1 \frac{d\varphi}{d\xi}\left(\eta \frac{df}{d\eta} + 2f\right) + A_1^2 \varphi^4 \left(\frac{g}{\mu} \frac{df}{d\eta} + \frac{1}{\mu} \frac{1}{\eta} \frac{d(\eta h)}{d\eta}\right) = 0$ (D.13b)

Further, the condition $\mu >> \psi f$ implies that

$$\frac{\psi f}{\mu} << 1 \Rightarrow \frac{U}{U_s} << 1 \xrightarrow{\text{continuity}} \frac{V_r}{U_s} << 1 \Rightarrow \frac{g\psi}{\mu} << 1 \Rightarrow \frac{A_1 \varphi^2 g}{\mu} << 1$$

which leads to the simplification of equation (D.13b) to:

$$\frac{d\varphi}{d\xi}\left(\eta \frac{df}{d\eta} + 2f\right) + \varphi^4 \frac{A_1}{\mu}\left(\frac{1}{\eta} \frac{d(\eta h)}{d\eta}\right) = 0 \quad \text{(D.13c)}$$

or, $\frac{d\varphi}{d\xi} = \chi \varphi^4$, where χ is a constant with respect to ξ. (D.13d)

Since $\frac{1}{\varphi} = 0$ when $\xi = 0$, the solution for equation (D.13d) is:

$\varphi \, \alpha \, \xi^{-1/3}$ i.e. $\varphi \, \alpha \left(\frac{d}{x - x_0}\right)^{1/3}$, thus implying $b = \frac{d}{\varphi} \, \alpha \, d^{2/3} (x - x_0)^{1/3}$

Also, since $\psi = A_1\varphi^2$, $$\psi = \frac{U_m}{U_o}\alpha\left(\frac{d}{x-x_0}\right)^{2/3}$$

From equations (D.13c) and (D.13d):

$$\eta\frac{df}{d\eta} + 2f = -\left(\frac{A_1}{\chi\mu}\right)\frac{1}{\eta}\frac{d(\eta h)}{d\eta} = -B_1\frac{1}{\eta}\frac{d(\eta h)}{d\eta}$$

or, $$\frac{d(\eta^2 f)}{d\eta} = -B_1\frac{d(\eta h)}{d\eta}$$

Since $h = 0$ at $\eta = 0$, integration of the above equation gives:

$$\eta f = -B_1 h \qquad \text{(D.13e)}$$

Further, assuming that the transport of turbulent momentum is by gradient type of diffusion, and that the eddy diffusion coefficient, ε_T, is isotropic, we have:

$$\tau_{xr} = -\rho\overline{v_x v_r} = \rho\varepsilon_T\frac{\partial U}{\partial r}$$

Thus,

$$h = \frac{\overline{v_x v_r}}{U_m^2} = -\frac{\varepsilon_T}{U_m^2}\frac{\partial U}{\partial r} = -\frac{\varepsilon_T}{U_m}\frac{\varphi}{d}\frac{d}{d\eta}\left(\frac{U}{U_m}\right) = -\frac{\varepsilon_T}{U_m}\frac{C_1}{\left[d^2(x-x_o)\right]^{1/3}}\frac{d}{d\eta}\left(\frac{U}{U_m}\right) \qquad \text{(D.13f)}$$

Combining equations (D.13e) and (D.13f)

$$\eta\frac{U}{U_m} = B_1\frac{\varepsilon_T}{U_m}\frac{C_1}{\left[d^2(x-x_o)\right]^{1/3}}\frac{d}{d\eta}\left(\frac{U}{U_m}\right)$$

C_1 being the constant of proportionality between φ and x. After some rearrangement, the above equation gives:

$$\frac{\varepsilon_T}{U_m\left[d^2(x-x_o)\right]^{1/3}} = \frac{1}{D_1}\frac{\eta U/U_m}{\frac{d}{d\eta}\left(\frac{U}{U_m}\right)}$$ (D_1 being a constant)

or, $$\frac{\varepsilon_T}{U_o d} = \frac{1}{D_1}\frac{\eta f}{\frac{df}{d\eta}}\left(\frac{d}{x-x_o}\right)^{1/3} = \phi(\eta)\,\xi^{-1/3} \qquad \text{(D.13g)}$$

$\phi(\eta)$ being a function only of η. Note that ε_T is a function not only of η but also of ξ. If it is assumed that $\phi(\eta)$ is constant (Hinze, 1959), the last two terms in equation (D.13g) can be integrated to yield an expression for the velocity, U:

$$\frac{1}{D_1}\eta d\eta = \phi\frac{df}{f}$$

i.e. $$f = \frac{U}{U_m} = \exp\left(\frac{\eta^2}{D_1\phi}\right) \qquad \text{(since } f(0) = 1\text{)}$$

Moreover, from equation (11g), $\phi(\eta) = \frac{\varepsilon_T}{U_o d}\left(\frac{x - x_0}{d}\right)^{-1/3}$. Hence

$$\frac{U}{U_m} = \exp\left(D'\frac{U_0 d^{4/3}}{\varepsilon_T(x - x_0)^{1/3}}\eta^2\right) \tag{D.13h}$$

Hinze (1959) assigned D' = -1/6, in the above equation.

Goertler solution: If it is assumed that $\varepsilon_T \,\alpha\, U_m b$, then we obtain:

$$\varepsilon_T \,\alpha \left\{U_o\left(\frac{d}{x - x_o}\right)^{2/3}\right\}\left\{d^{2/3}(x - x_0)^{1/3}\right\} = U_o\frac{d^{4/3}}{(x - x_o)^{1/3}}$$

Plugging this expression for ε_T in Equation (13h) gives:

$$\frac{U}{U_m} = \exp\left(D'\eta^2\right) \tag{D.13}$$

Case B) ~ Stagnant ambient fluid ($U_s \sim 0$) $\psi f >> \mu$

Under this condition, Equation (D.9) assumes the form:

$$\frac{\psi^2}{\varphi^2}\left\{\int_0^\infty f^2\eta d\eta\right\} = \text{const.} \tag{D.14a}$$

giving, $\psi = A_2\varphi$, where A_2 is a constant. The equation of motion (Equation D.11), reduces to:

$$\frac{\psi^2}{\varphi}\frac{d\varphi}{d\xi}\left\{\eta f\frac{df}{d\eta}\right\} + \psi\frac{d\psi}{d\xi}\left\{f^2\right\} + \psi^2\varphi\left\{g\frac{df}{d\eta}\right\} = -\psi^2\varphi\left\{\frac{1}{\eta}\frac{d(\eta h)}{d\eta}\right\}$$

i.e, $$A_2^2\varphi\frac{d\varphi}{d\xi}\left[\eta f\frac{df}{d\eta}+f^2\right]+A_2^2\varphi^3\left\{g\frac{df}{d\eta}+\frac{1}{\eta}\frac{d(\eta h)}{d\eta}\right\}=0 \qquad \text{(D.14b)}$$

i.e., $$\frac{d\varphi}{d\xi}=X\varphi^2 \text{ where X is a constant with respect to } \xi. \qquad \text{(D.14c)}$$

As before, since $\frac{1}{\varphi}=0$ when $\xi=0$ the solution for equation (D.14c) is:

$\varphi\,\alpha\,\frac{1}{\xi}$ i.e. $\varphi\,\alpha\,\frac{d}{x-x_0}$, thus implying $\quad b=\frac{d}{\varphi}\,\alpha\,(x-x_0)$

Also, since $\psi = A_2\varphi$, $\quad \psi=\frac{U_m}{U_o}\,\alpha\,\frac{d}{x-x_0}$

From equations (D.14b) and (D.14c):

$$X\left(\eta f\frac{df}{d\eta}+f^2\right)=-g\frac{df}{d\eta}-\frac{1}{\eta}\frac{d(\eta h)}{d\eta} \qquad \text{(D.14d)}$$

From the continuity equation (Equation D.8):

$$\frac{\partial}{\partial r}\left(r\frac{V_r}{U_o}\right)+\frac{\partial}{\partial x}\left(r\frac{U}{U_o}\right)=0$$

i.e., $$\frac{\partial}{\partial r}(g\psi)+\frac{g\psi}{r}+\frac{\partial}{\partial x}(f\psi)=0$$

or, $$\left[g\frac{\partial\psi}{\partial r}+\psi\frac{dg}{d\eta}\frac{\partial\eta}{\partial r}\right]+\frac{\psi\varphi}{d}\frac{g}{\eta}+\left[f\frac{d\psi}{d\xi}\frac{d\xi}{dx}+\psi\frac{df}{d\eta}\frac{d\eta}{d\varphi}\frac{d\varphi}{d\xi}\frac{d\xi}{dx}\right]=0$$

i.e., $$\psi\varphi\frac{1}{\eta}\frac{d(\eta g)}{d\eta}+\frac{d\psi}{d\xi}f+\frac{\psi}{\varphi}\frac{d\varphi}{d\xi}\eta\frac{df}{d\eta}=0$$

Since $\psi = A_2\varphi$ and using equation (D.14c) the above equation transforms to:

$$A_2\varphi^2\frac{1}{\eta}\frac{d(\eta g)}{d\eta}+A_2X\varphi^2\left(f+\eta\frac{df}{d\eta}\right)=0$$

i.e., $$\frac{1}{\eta}\frac{d(\eta g)}{d\eta}=-X\frac{d(\eta f)}{d\eta}$$

which on integration gives:

$$g=-X\left(\eta f-\frac{F}{\eta}\right), \text{ where } F=\int_0^\eta \eta f d\eta$$

and hence,

$$f=\frac{1}{\eta}\frac{dF}{d\eta}\text{ and }g=-X\left(\frac{dF}{d\eta}-\frac{F}{\eta}\right) \tag{D.14e}$$

Using equation (D.14e) in equation (D.14d):

$$X\left[\frac{1}{\eta}\frac{dF}{d\eta}\frac{d^2F}{d\eta^2}-\frac{1}{\eta^2}\left(\frac{dF}{d\eta}\right)^2+\frac{1}{\eta^2}\left(\frac{dF}{d\eta}\right)^2\right]-X\left[\frac{1}{\eta}\frac{dF}{d\eta}\frac{d^2F}{d\eta^2}-\frac{1}{\eta^2}\left(\frac{dF}{d\eta}\right)^2\right.$$

$$\left.-\frac{F}{\eta^2}\frac{d^2F}{d\eta^2}+\frac{F}{\eta^3}\frac{dF}{d\eta}\right]=-\frac{1}{\eta}\frac{d(\eta h)}{d\eta}$$

i.e., $$\frac{F}{\eta}\frac{d^2F}{d\eta^2}+\frac{1}{\eta}\left(\frac{dF}{d\eta}\right)^2-\frac{F}{\eta^2}\frac{dF}{d\eta}=-\frac{1}{X}\frac{d(\eta h)}{d\eta}$$

or, $$-\frac{d}{d\eta}\left(\frac{F}{\eta}\frac{dF}{d\eta}\right)=\frac{1}{X}\frac{d(\eta h)}{d\eta}$$

which on integration gives:

$$\frac{\eta h}{X}=-\frac{dF}{d\eta}\frac{F}{\eta}=-f\int_0^\eta \eta f d\eta$$

i.e., $$h=-\frac{X}{\eta}\frac{U}{U_m}\int_0^\eta\frac{U}{U_m}\eta d\eta$$

Combining this equation with equation (D.13f) and the relation between φ and x:

$$\frac{\varepsilon_T}{U_m}\frac{C_2}{(x-x_o)}\frac{d}{d\eta}\left(\frac{U}{U_m}\right)=\frac{X}{\eta}\frac{U}{U_m}\int_0^\eta\frac{U}{U_m}\eta d\eta \tag{D.14f}$$

i.e., $$\frac{\varepsilon_T}{U_m}\frac{1}{(x-x_o)}=D_2\frac{\dfrac{U}{U_m}\displaystyle\int_0^\eta\frac{U}{U_m}\eta d\eta}{\eta\dfrac{d}{d\eta}\left(\dfrac{U}{U_m}\right)}=\kappa(\eta) \tag{D.14g}$$

C_2 being the constant of proportionality between φ and x and D_2 is another constant equal to X/C_2. Note also that unlike the previous case, ε_T is a function only of η, since $U_m(x - x_0)$ is constant. Equation (D.14g) can be written in terms of F(η):

$$F\frac{dF}{d\eta}=\left[\frac{1}{D_2}\frac{\varepsilon_T}{U_m}\frac{1}{(x-x_o)}\right]\eta^2\frac{d}{d\eta}\left(\frac{1}{\eta}\frac{dF}{d\eta}\right)$$

which on integration gives:

$$\frac{F^2}{2} = \Phi\left(\eta\frac{dF}{d\eta} - 2F\right), \text{ with } \Phi = \frac{1}{D_2}\frac{\varepsilon_T}{U_m}\frac{1}{(x - x_o)}$$

In the above equation, the constant of integration is zero, since $F = 0$ at $\eta = 0$. The equation can be rearranged to give:

$$\frac{2\Phi dF}{F(F + 4\Phi)} = \frac{d\eta}{\eta}$$

and further simplified using the method of partial fractions, yielding:

$$\frac{dF}{F} - \frac{dF}{F + 4\Phi} = 2\frac{d\eta}{\eta}$$

This equation can be easily integrated to give:

$$\ln\left(\frac{F}{F + 4\Phi}\right) = \ln\left(\eta^2 C\right)$$

Which on rearranging finally yields:

$$F = \frac{4\Phi\eta^2 C}{1 - \eta^2 C} \qquad \text{(D.14h)}$$

From equations (D.14e) and (D.14h) an expression for f is obtained:

$$f = \frac{8\Phi C}{\left(1 - \eta^2 C\right)^2}$$

Since $f = 1$ at $\eta = 0$, the constant of integration is obtained as $C = {}^{1}\!/_{8\Phi}$. Putting the value of Φ:

$$f = \frac{U}{U_m} = \frac{1}{\left\{1 + \left(\frac{D_2' U_m (x - x_0)}{8\varepsilon_T}\right)\eta^2\right\}^2}, \qquad \text{where } D_2' = -D_2 \qquad \text{(D.14i)}$$

It is easily shown that

$$U_m(x - x_o) = U_o\psi(x - x_o) = U_o A_2 C_2 d = E_2 U_o d \quad (E_2 \text{ is a constant}) \quad \text{(D.14j)}$$

Combining (D.14i) and (D.14j) an expression for U is obtained:

$$\frac{U}{U_m} = \frac{1}{\left\{1 + \frac{D'' U_o d}{\varepsilon_T}\eta^2\right\}^2} \qquad \text{where, } D'' \text{ is a new constant} \quad \text{(D.14k)}$$

Goertler solution: Again assuming $\varepsilon_T \; \alpha \; U_m b$, we obtain:

$$\varepsilon_T \; \alpha \left\{ U_o \frac{d}{x - x_o} \right\} \{x - x_0\} = U_o d$$

Which gives an expression for U/U$_m$:

$$\frac{U}{U_m} = \frac{1}{\{1 + D''\eta^2\}^2} \qquad \text{(D.14)}$$

D.4. Similarity Solutions - Scalar

Modifying the scalar transport Equation (D.6) by introducing $V_x = U_s + U$ and dividing throughout by $U_o C_o$ results in:

$$\left(\frac{U_s}{U_o} + \frac{U}{U_o} \right) \frac{\partial}{\partial x} \left(\frac{C}{C_o} \right) + \frac{V_r}{U_o} \frac{\partial}{\partial r} \left(\frac{C}{C_o} \right) = -\frac{1}{r} \frac{\partial}{\partial r} \left[r \frac{\overline{v_r c}}{U_o C_o} \right] \qquad \text{(D.15a)}$$

Where, U_s and U_o are the stream and nozzle velocities as described earlier and C_o is the concentration of the scalar at the nozzle. Assuming similarity in concentration and scaling the concentration and correlation terms as follows:

$$\frac{C}{C_m} = k(\eta_1) \qquad \frac{C_m}{C_o} = \Psi(\xi) \qquad \frac{\overline{v_r c}}{U_m C_m} = z(\eta_1) \qquad \eta_1 = \frac{r\varphi_1}{d}$$

Equation (15a) is reduced to:

$$(\mu + f\psi) \frac{\partial}{\partial x} (k\Psi) + g\psi \frac{\partial}{\partial r} (k\Psi) = -\frac{1}{r} \frac{\partial}{\partial r} \left[r \frac{\partial}{\partial r} (\psi \Psi z) \right]$$

$$(\mu + f\psi) \left[k \frac{d\Psi}{d\xi} \frac{d\xi}{dx} + \Psi \frac{dk}{d\eta_1} \frac{d\eta_1}{d\varphi} \frac{d\varphi}{d\xi} \frac{d\xi}{dx} \right] + g\psi \left[k \frac{\partial \Psi}{\partial r} + \Psi \frac{dk}{d\eta_1} \frac{\partial \eta_1}{\partial r} \right] = -\frac{\psi \Psi}{r} \frac{\partial (rz)}{\partial \eta_1} \frac{\partial \eta_1}{\partial r}$$

$$(\mu + f\psi) \left[\frac{d\Psi}{d\xi} \{k\} + \frac{\Psi}{\varphi_1} \frac{d\varphi_1}{d\xi} \left\{ \eta_1 \frac{dk}{d\eta_1} \right\} \right] + \psi \Psi \varphi_1 \left\{ g \frac{dk}{d\eta_1} \right\} = -\psi \Psi \varphi_1 \left\{ \frac{1}{\eta_1} \frac{\partial (\eta_1 z)}{\partial \eta_1} \right\} \qquad \text{(D.15)}$$

Using the method discussed in section C) it can be shown that a complete similarity solution of Equation (D.15) is impossible. However, there are two conditions under which similarity solutions exist, as was the case for equation (D.11). As before these are (i) $\mu >> \psi f$ and (ii) $\psi f >> \mu$.

Case A) $\mu >> \psi f$:

For this condition Equation (D.15) simplifies to:

$$\mu\frac{d\Psi}{d\xi}k+\mu\frac{\Psi}{\varphi_1}\frac{d\varphi_1}{d\xi}\eta_1\frac{dk}{d\eta_1}+\psi\Psi\varphi_1 g\frac{dk}{d\eta_1}=-\psi\Psi\varphi_1\frac{1}{\eta_1}\frac{d(\eta_1 z)}{d\eta_1} \qquad \text{(D.16a)}$$

On the other hand, the scalar flux balance (Equation D.9h) in the dimensionless form is:

$$\int_0^\infty\frac{C}{C_o}\left(\frac{U_s}{U_o}+\frac{U}{U_o}\right)rdr=\int_0^\infty\frac{C}{C_o}\frac{U_s}{U_o}rdr+\int_0^\infty\frac{C}{C_o}\frac{U}{U_o}rdr = \text{const.}$$

$$\text{i.e.,} \qquad \frac{\mu\Psi}{\varphi_1^2}\left\{\int_0^\infty k\eta_1 d\eta_1\right\}+\frac{\Psi\psi}{\varphi_1^2}\left\{\int_0^\infty kf\eta_1 d\eta_1\right\}=\text{const.} \qquad \text{(D.16b)}$$

Under the condition $\mu >> \psi f$, equation (D.16b) reduces to

$$\frac{\mu\Psi}{\varphi_1^2}\left\{\int_0^\infty k\eta d\eta\right\}=\text{const.} \qquad \text{(D.16)}$$

giving, $\Psi = A_3\varphi_1^2$. If it is further assumed that $\varphi_1 \propto \varphi$, i.e. $\varphi_1 = K_1\varphi$, and hence $\eta_1 = K_1\eta$, Equation (D.16a) can be expressed as:

$$\frac{d\Psi}{d\xi}k+\frac{\Psi}{\varphi_1}\frac{d\varphi_1}{d\xi}\eta_1\frac{dk}{d\eta_1}+\left(\frac{\psi g}{\mu}\right)\Psi\varphi_1 g\frac{dk}{d\eta_1}=-\frac{\psi\Psi\varphi_1}{\mu}\frac{1}{\eta_1}\frac{d(\eta_1 z)}{d\eta_1}$$

Since $(\psi g)/\mu << 1$, the above equation simplifies to:

$$\mu A_3\varphi_1\frac{d\varphi_1}{d\xi}\left[2k+\eta_1\frac{dk}{d\eta_1}\right]+A_1A_3\varphi_1^5\left[\frac{1}{\eta_1}\frac{d(\eta_1 z)}{d\eta_1}\right]=0 \qquad \text{(D.17a)}$$

$$\text{giving, } \frac{d\varphi_1}{d\xi}=\Theta\varphi_1^4 \qquad \text{(D.17b)}$$

Expressions for the concentration half-width (b_1) and Ψ are therefore similar to those of b and ψ developed previously:

$$\varphi_1\alpha\left(\frac{d}{x-x_o}\right)^{1/3} \qquad b_1=\frac{d}{\varphi_1}\alpha\, d^{2/3}(x-x_0)^{1/2} \qquad \Psi=\frac{C_m}{C_o}\alpha\left(\frac{d}{x-x_0}\right)^{2/3}$$

Combining equations (D.17a) and (D.17b) and rearranging gives:

$$\frac{d(\eta_1^2 k)}{d\eta_1}=-B_3\frac{d(\eta_1 z)}{d\eta_1} \qquad \text{(where, } B_3 \text{ is a constant)}$$

Integration of this equation results in:

$$\eta_1 k = -B_3 z,\ \text{since}\ z = 0 \quad \text{at} \quad \eta_1 = 0 \qquad \text{(D.17c)}$$

If it is assumed that turbulence transport of the scalar is by a gradient diffusion type of mechanism, then the coupled fluctuating velocity-concentration term can be expressed as:

$$-\overline{v_r c} = D_T \frac{\partial C}{\partial r} \qquad \text{(D.17d)}$$

so that

$$-z = -\frac{\overline{v_r c}}{U_m C_m} = \frac{D_T}{U_m}\frac{\partial}{\partial r}\left(\frac{C}{C_m}\right) = \frac{D_T}{U_o A_3 d}\left(\frac{x - x_o}{d}\right)^{1/3}\frac{dk}{d\eta_1}$$

Combining equations (D.17c) and (D.17d) gives:

$$\eta_1 k = \left\{\frac{D_T \xi^{1/3}}{U_o A_3 d}\right\}\frac{dk}{d\eta_1} \qquad \text{(D.17e)}$$

Assuming the bracketed term to be constant equation (D.17e) can be integrated to obtain

$$k = \frac{C}{C_m} = \exp\left(A_3 \frac{U_o d}{D_T \xi^{1/3}} \eta_1^2\right)$$

$$\text{i.e.,} \quad \frac{C}{C_m} = \exp\left(D''' \frac{U_o d}{D_T \xi^{1/3}} \eta^2\right) \quad \text{(D''' being a constant)} \qquad \text{(D.17)}$$

Therefore, for $\mu >> \psi f$, both the dimensionless velocity and scalar concentration profiles have Gaussian radial distributions.

Case A) $\psi f >> \mu$

Using the concept of turbulent transport by gradient diffusion, Equation (D.6) can be written in the form

$$\left(U_s + U\right)\frac{\partial C}{\partial x} + V_r \frac{\partial C}{\partial r} = \frac{1}{r}\frac{\partial}{\partial r}\left(r D_T \frac{\partial C}{\partial r}\right) \qquad \text{(D.18a)}$$

which yields the dimensionless equation:

$$\left(\frac{U_s}{U_o} + \frac{U}{U_o}\right)\frac{\partial}{\partial x}\left(\frac{C}{C_o}\right) + \frac{V_r}{U_o}\frac{\partial}{\partial r}\left(\frac{C}{C_o}\right) = -\frac{1}{r}\frac{\partial}{\partial r}\left[r \frac{D_T}{U_o}\frac{\partial}{\partial r}\left(\frac{C}{C_o}\right)\right]$$

$$(\mu + f\psi)\left[\frac{d\Psi}{d\xi}\{k\} + \frac{\Psi}{\varphi_1}\frac{d\varphi_1}{d\xi}\left\{\eta_1 \frac{dk}{d\eta_1}\right\}\right] + \psi\Psi\varphi_1\left\{g\frac{dk}{d\eta_1}\right\} = \Psi\varphi_1{}^2\left\{\frac{1}{\eta_1}\frac{\partial}{\partial\eta_1}\left[\eta_1 \frac{D_T}{U_o d}\frac{\partial k}{\partial\eta_1}\right]\right\}$$

Under the condition $\psi f >> \mu$, this equation further reduces to:

$$\psi\frac{d\Psi}{d\xi}\{fk\} + \frac{\Psi}{\varphi_1}\psi\frac{d\varphi_1}{d\xi}\left\{f\eta_1 \frac{dk}{d\eta_1}\right\} + \psi\Psi\varphi_1\left\{g\frac{dk}{d\eta_1}\right\} = \Psi\varphi_1{}^2\left\{\frac{1}{\eta_1}\frac{\partial}{\partial\eta_1}\left[\eta_1 \frac{D_T}{U_o d}\frac{\partial k}{\partial\eta_1}\right]\right\}$$

(D.18b)

On the other hand, for this condition, equation (D.16b) reduces to the form:

$$\frac{\Psi\psi}{\varphi_1^2}\left\{\int_0^\infty kf\eta_1 d\eta_1\right\} = \text{const.}$$

Thus giving $\Psi = A_4\varphi$. This and the fact that $\varphi_1 \propto \varphi$, can be combined with equation (D.16b) to yield:

$$\varphi_1\frac{d\varphi_1}{d\xi}\left[fk + f\eta_1\frac{dk}{d\eta_1}\right] + \varphi_1^3\left[g\frac{dk}{d\eta_1} - \frac{K_1}{A_2}\frac{1}{\eta_1}\frac{d}{d\eta_1}\left(\eta_1\frac{D_T}{U_o d}\frac{dk}{d\eta_1}\right)\right] = 0 \quad \text{(D.18c)}$$

$$\text{i.e.,}\quad \frac{d\varphi_1}{d\xi} = \Lambda\varphi_1^2 \Rightarrow \varphi_1 \alpha \xi^{-1} \quad \text{(D.18d)}$$

therefore giving $b_1 = \frac{d}{\varphi_1}\alpha(x - x_0)$ $\Psi = \frac{C_m}{C_o}\alpha\frac{d}{x - x_0}$

Combining equation (D.18d) with the result in equation (D.18c) gives the following equation after some rearrangement:

$$f\frac{d(\eta k)}{d\eta_1} + \frac{1}{\Lambda}g\frac{dk}{d\eta_1} = \frac{K_1}{A_2\Lambda}\frac{1}{\eta_1}\frac{d}{d\eta_1}\left(\eta_1\frac{D_T}{U_o d}\frac{dk}{d\eta_1}\right) \quad \text{(D.18e)}$$

From section D.3,

$$f = \frac{1}{\eta}\frac{dF}{d\eta} \text{ and } g = -X\left(\frac{dF}{d\eta} - \frac{F}{\eta}\right) \quad \text{i.e.} \quad f = \frac{K_1^2}{\eta_1}\frac{dF}{d\eta_1} \text{ and}$$

$$g = -XK_1\left(\frac{dF}{d\eta_1} - \frac{F}{\eta_1}\right)$$

Thus, equation (D.18e) can be written solely in terms of F and η_1:

$$\frac{1}{\eta_1}\frac{dF}{d\eta_1}\frac{d(\eta_1 k)}{d\eta_1} - \frac{X}{\Lambda K_1}\left(\frac{dF}{d\eta_1} - \frac{F}{\eta_1}\right)\frac{dk}{d\eta_1} = \frac{1}{\Lambda}\frac{1}{\eta_1}\frac{d}{d\eta_1}\left(\eta_1\frac{D_T}{U_o A_2 d}\frac{dk}{d\eta_1}\right)$$

It can be easily shown that $\frac{X}{\Lambda K_1} = 1$, and hence the above equation simplifies to:

$$\frac{dF}{d\eta_1}\frac{dk}{d\eta_1} + \frac{dF}{d\eta_1}\frac{k}{\eta_1} - \frac{dF}{d\eta_1}\frac{dk}{d\eta_1} + \frac{F}{\eta_1}\frac{dk}{d\eta_1} = \frac{1}{\Lambda}\frac{1}{\eta_1}\frac{d}{d\eta_1}\left(\eta_1 \frac{D_T}{U_o A_2 d}\frac{dk}{d\eta_1}\right)$$

or, $$\frac{d(Fk)}{d\eta_1} = \frac{1}{\Lambda}\frac{d}{d\eta_1}\left(\eta_1 \frac{D_T}{U_o A_2 d}\frac{dk}{d\eta_1}\right) \qquad \text{(D.18f)}$$

Integrating equation (D.18f) with the boundary condition, F = 0 at $\eta_1 = 0$, gives:

$$Fk = \frac{\eta_1}{\Lambda}\frac{D_T}{U_o A_2 d}\frac{dk}{d\eta_1} \qquad \text{(D.18g)}$$

The next integration yields:

$$k = \frac{C}{C_m} = \exp\left(\int_0^{\eta}\frac{U_o A_2 d}{D_T} F \frac{d\eta_1}{\eta_1}\right). \qquad \text{(D.18h)}$$

Since $F = \int_0^{\eta} f\eta d\eta$, and f is a function of ε_T, the dependence of ε_T on η has to be known before equation (D.18h) can be solved.

Goertler solution: From section D.3 we find that an expression for f is given by equation (14). Using this expression, F is obtained as

$$F = \int_0^{\eta}\frac{\eta d\eta}{\left(1 + D''\eta^2\right)^2} = -\frac{1}{2D''(1 + D''\eta)}\Bigg|_0^{\eta} = \frac{\eta D''}{1 + D''\eta} = \frac{\eta_1 D_1''}{1 + D_1''\eta_1}$$

Putting this expression in equation (18h)

$$\frac{C_1 d\eta_1}{1 + D_1''\eta_1} = \frac{D_T}{U_o A_2 d}\frac{dk}{k}$$

D.5. Arguments against universal solution

Dividing equation (D.7) throughout by U_o^2, we obtain

$$\left(\frac{Us}{U_o} + \frac{U}{U_o}\right)\frac{\partial}{\partial x}\left(\frac{U}{U_o}\right) + \frac{V_r}{U_o}\frac{\partial}{\partial r}\left(\frac{U}{U_o}\right) = -\frac{1}{r}\frac{\partial}{\partial r}\left(r\frac{\overline{v_x v_r}}{U_o^2}\right) \qquad \text{(D.19)}$$

If the flow is assumed to be self-similar at a certain distance from the nozzle (8 to 10d_f), and the following similarity variables are selected:

$$\frac{U}{U_1} = f(\eta) \qquad \frac{V_r}{U_1} = g(\eta) \qquad \frac{\overline{v_x v_r}}{U_2^2} = h(\eta) \qquad \frac{U_s}{U_o} = \mu$$

$$\frac{U_1}{U_o} = \psi_1(\xi) \qquad \frac{U_2}{U_o} = \psi_2(\xi) \qquad \eta = \frac{r}{d}\varphi(\xi) \qquad \xi = \frac{x - x_o}{d}$$

Equation (D.10a) can be written as:

$$(\mu + f\psi_1)\frac{\partial}{\partial x}(f\psi_1) + g\psi_1\frac{\partial}{\partial r}(f\psi_1) = -\frac{\varphi}{\eta d}\frac{\partial}{\partial r}\left(\frac{\eta d}{\varphi}h\psi_2^2\right)$$

i.e.
$$(\mu + f\psi_1)\left[\frac{\psi_1}{\varphi}\frac{d\varphi}{d\xi}\left\{\eta\frac{df}{d\eta}\right\} + \frac{d\psi_1}{d\xi}\{f\}\right] + \psi_1^2\varphi\left\{g\frac{df}{d\eta}\right\} = -\psi_2^2\varphi\left\{\frac{1}{\eta}\frac{d(\eta h)}{d\eta}\right\} \qquad \text{(D.20)}$$

Using the arguments given in section D.3 it can again be shown that similarity is possible only in the limiting conditions of:

$\mu >> \psi_1 f$,

$\psi f >> \mu$

Case B) ~ Stagnant ambient fluid ($U_s \sim 0$) $\psi f >> \mu$

Under this condition, Equation (D.9) assumes the form:

$$\frac{\psi_1^2}{\varphi^2}\left\{\int_0^\infty f^2 \eta d\eta\right\} = \text{const.} \qquad \text{(D.21)}$$

giving, $\psi_1 = A_2\varphi$, where A_2 is a constant. The equation of motion reduces to:

$$\frac{\psi_1^2}{\varphi}\frac{d\varphi}{d\xi}\left\{\eta f\frac{df}{d\eta}\right\} + \psi_1\frac{d\psi_1}{d\xi}\{f^2\} + \psi_1^2\varphi\left\{g\frac{df}{d\eta}\right\} = -\psi_2^2\varphi\left\{\frac{1}{\eta}\frac{d(\eta h)}{d\eta}\right\}$$

i.e,
$$A_2^2\varphi\frac{d\varphi}{d\xi}\left[\eta f\frac{df}{d\eta} + f^2\right] + A_2^2\varphi^3 g\frac{df}{d\eta} + \psi_2^2\varphi\frac{1}{\eta}\frac{d(\eta h)}{d\eta} = 0 \qquad \text{(D.22)}$$

For a similarity solution to be possible:

$\frac{d\varphi}{d\xi} = X_1\varphi^2$, and

$$\frac{d\varphi}{d\xi} = \psi_2^2 \quad \Rightarrow \quad \frac{1}{\psi_2^2}\frac{d\varphi}{d\xi} = \text{const.}$$

Using the definition of φ, ψ_1, ψ_2 and the fact that $b = d/\varphi$, the second condition implies that:

$$\frac{\psi_1^2}{\psi_2^2}\frac{db}{dx} = \text{const.} \Rightarrow \frac{U_1^2}{U_2^2}\frac{db}{dx} = \text{const.} \Rightarrow U_2^2 \propto U_1^2\frac{db}{dx} \tag{D.23}$$

Thus, to obtain a similarity solution, it is not needed that $U_1 = U_2$ or even that $\frac{db}{dx} = \text{const.}$ Fixing, $U_1 = U_2$ forces the spreading rate of the jet to be a universal constant, while this is strictly not required.

Appendix E
Data from Reactive Experiments

Table E.1 Experimental Data for PBTD. Feed is through a 3mm nozzle placed at the surface. 2r/D = 1.75 and N = 252 rpm

Feed time (s)	Feed Velocity (m/s)	Conc. of Ester (mol/m^3)	Conc. of NaOH (mol/m^3)	$X_{Q,Ester}$ (-)	$X_{Q,Ethanol}$ (-)	Δ[8] (%)	ε[9] (%)
19.8	1.56	92.54	88.53	0.304	0.317	2.11	4.3
30	1.03	91.49	88.74	0.279	0.302	4.09	3.0
40	0.77	89.45	88.77	0.269	0.299	5.29	0.8
50	0.62	105.28	89.29	0.279	0.459	24.44	15.2
50	0.62	95.52	88.39	0.275	0.353	12.48	7.5
50	0.63	90.18	90.08	0.266	0.268	0.37	0.1
60	0.52	90.75	89.46	0.279	0.289	1.75	1.4
70	0.44	86.54	89.05	0.286	0.239	8.90	2.9
70	0.444	95.17	89.35	0.279	0.347	10.92	6.1
70	0.444	87.26	89.35	0.286	0.205	16.54	2.4
80	0.388	88.17	89.15	0.281	0.257	4.56	1.1
80	0.388	92.05	89.29	0.305	0.282	3.89	3.0
90	0.344	88.59	89.01	0.282	0.276	1.04	0.5
90	0.345	86.45	89.22	0.275	0.290	2.72	3.2
100	0.310	85.33	89.08	0.278	0.213	13.18	4.4
100	0.313	85.90	87.75	0.288	0.311	3.81	2.2
110	0.284	88.87	87.65	0.288	0.311	3.94	1.4
120	0.260	91.58	87.48	0.286	0.327	6.56	4.5
150	0.207	87.58	87.01	0.273	0.293	3.58	0.7
150	0.207	87.25	87.01	0.279	0.270	1.61	0.3

---

[8] Δ is the deviation between byproduct yield calculated from Ester and Ethanol concentrations (Yu, 1993): $\Delta = \frac{\mathrm{abs}\left(X_{Q,\mathrm{Ethanol}} - X_{Q,\mathrm{Ester}}\right)}{\left(X_{Q,\mathrm{Ethanol}} + X_{Q,\mathrm{Ester}}\right)} \times 100$

[9] ε is the deviation from the required equimolar amounts of Ester and NaOH:

$$\varepsilon = \frac{\mathrm{abs}\left(C_{\mathrm{Ester}} - C_{\mathrm{NaOH}}\right)}{C_{\mathrm{Ester}}} \times 100$$

Table E.1 Continued

Feed time (s)	Feed Velocity (m/s)	Conc. of Ester (mol/m^3)	Conc. of NaOH (mol/m^3)	$X_{Q,Ester}$ (-)	$X_{Q,Ethanol}$ (-)	Δ (%)	ε (%)
250	0.123	87.33	86.68	0.271	0.285	2.57	0.7
300	0.103	87.56	90.96	0.261	0.258	0.41	3.9
318.6	0.097	88.64	90.85	0.260	0.251	1.72	2.5
514.2	0.061	88.63	91.52	0.254	0.265	2.12	3.3
969.6	0.032	86.46	91.17	0.254	0.257	0.74	5.4
1206	0.026	87.79	91.27	0.252	0.252	0.12	4.0
2232	0.014	87.08	91.06	0.249	0.247	0.55	4.6
3006	0.010	88.57	91.13	0.250	0.278	5.29	2. 9

Table E.2 **Experimental Data for PBTD. Feed is through a 0.762 mm nozzle placed at the surface. 2r/D = 1.75 & N = 252 rpm**

Feed time (s)	Feed Velocity (m/s)	Conc. of Ester (mol/m^3)	Conc. of NaOH (mol/m^3)	$X_{Q,Ester}$ (-)	$X_{Q,Ethanol}$ (-)	Δ (%)	ε (%)
19.8	25.02	88.29	93.38	0.219	0.240	4.63	5.8
30	16.06	90.84	86.81	0.266	0.298	5.70	4.48
40	12.19	86.54	87.85	0.253	0.264	2.11	1.58
50	9.741	87.78	87.75	0.275	0.281	1.05	0.03
60	8.098	88.29	87.55	0.282	0.276	1.10	0.88
70	6.952	87.05	87.68		0.273		
80	6.119	85.83	88.19	0.293			
90	5.410	86.89	87.72	0.286	0.283	0.54	1.0
100	4.869	90.00	87.72	0.291	0.301	1.61	2.5
110	4.419	88.80	87.58	0.292	0.310	3.04	1.4
120	4.068	87.56	87.95	0.287	0.307	3.42	0. 4
150	3.250	86.02	87.82	0.281	0.295	2.49	2.1
200	2.411	91.53	90.92	0.277	0.284	1.21	0.7
250	1.943	87.61	91.59	0.299	0.287	2.01	4.5
300	1.607	86.26	90.92	0.290	0.299	1.41	5.4
350	1.382	87.00	91.24	0.296	0.313	2.91	4.9
450	1.062	87.25	90.15	0.281	0.273	1.41	3.3
537	0.900	87.00	91.10	0.275	0.287	2.25	4.7

Table E.3 **Experimental Data for PBTD with the feed stream added 1.4cm above the liquid surface to form a plunging jet. Feed is through a 3 mm nozzle. 2r/D = 1.75 and N = 252 rpm**

Feed time (s)	Feed Velocity (m/s)	Conc. of Ester (mol/m^3)	Conc. of NaOH (mol/m^3)	$X_{Q,Ester}$ (-)	$X_{Q,Ethanol}$ (-)	Δ (%)	ε (%)
10	3.098	87.38	91.03	0.318	0.285	5.57	4.2
20	1.565	87.48	91.03	0.264	0.250	2.84	4.0
30	1.020	88.57	89.97	0.261	0.257	0.90	1.6
40	0.769	88.91	90.36	0.277	0.274	0.58	1.6
50	0.622	87.48	91.41	0.274	0.265	1.53	4.5
60	0.516	88.82	90.92	0.287	0.278	1.48	2.4
70	0.441	88.96	90.81	0.276	0.288	2.15	2.1
80	0.386	89.78	90.85	0.292	0.301	1.48	1.2

Table E.4 **Experimental Data for PBTD with the feed stream added 1.4cm above the liquid surface to form a plunging jet. Feed is through a 0.762 mm nozzle. 2r/D = 1.75 and N = 252 rpm.**

Feed time (s)	Feed Velocity (m/s)	Conc. of Ester (mol/m^3)	Conc. of NaOH (mol/m^3)	$X_{Q,Ester}$ (-)	$X_{Q,Ethanol}$ (-)	Δ (%)	ε (%)
40**	12.010	88.76	90.60	0.270	0.288	3.21	2.1
40	12.171	89.62	91.80	0.275	0.300	4.38	2.4
19.8	24.339	89.46	90.88	0.208	0.206	0.32	1.6
30	15.722	88.12	88.99	0.280	0.268	2.27	1.0
39	12.060	87.14	88.74	0.249	0.274	4.83	1.8
50	9.665	88.63	91.13	0.291	0.306	2.57	2.8
60	8.019	89.00	90.74	0.300	0.315	2.35	2.0
70	6.876	87.37	90.78	0.299	0.293	0.91	3.9
80	6.017	87.28	90.78	0.282	0.281	0.09	4.0
90	5.374	87.87	91.20	0.284	0.297	2.25	3.8
100	4.821	87.67	90.92	0.296	0.288	1.34	3.7

Note: ** This data point was collected for feed at 3.4 cm above the surface of the liquid

Table E.5 Experimental Data for PBTD with feed added at the surface. Feed is through a 3 mm nozzle. 2r/D = 1.75 and N = 375 rpm

Feed time (s)	Feed Velocity (m/s)	Conc. of Ester (mol/m^3)	Conc. of NaOH (mol/m^3)	$X_{Q,Ester}$ (-)	$X_{Q,Ethanol}$ (-)	Δ (%)	ε (%)
10	3.088	86.69	91.62	0.282	0.277	0.94	5.7
20	1.543	86.05	90.67	0.258	0.262	0.93	5.4
24	1.295	86.26	91.34	0.259	0.256	0.62	5.9
30	1.026	86.37	90.50	0.259	0.262	0.63	4.8
40	0.775	87.05	91.06	0.264	0.277	2.31	4.6
50	0.619	87.51	90.99	0.262	0.274	2.19	4.0
60	0.516	87.34	91.03	0.260	0.251	1.70	4.2
70	0.444	86.67	91.34	0.260	0.255	1.01	5.4
80	0.388	86.26	91.20	0.255	0.244	2.25	5.7
90	0.344	85.80	90.96	0.245	0.249	0.85	6.0
110	0.281	86.46	90.74	0.248	0.251	0.55	5.0

Table E.6 Experimental Data for PBTD with feed added at the surface. Feed is through a 3 mm nozzle. 2r/D = 1.75 and N = 500 rpm

Feed time (s)	Feed Velocity (m/s)	Conc. of Ester (mol/m^3)	Conc. of NaOH (mol/m^3)	$X_{Q,Ester}$ (-)	$X_{Q,Ethanol}$ (-)	Δ (%)	ε (%)
10	3.063	85.98	90.04	0.240	0.232	1.74	4.7
20	1.550	87.55	91.10	0.227	0.249	4.49	4.1
30	1.029	88.68	90.74	0.243	0.247	0.85	2.3
40	0.777	91.13	91.27	0.248	0.239	1.76	0.2
50	0.619	87.23	90.99	0.247	0.250	0.70	4.3
60	0.516	87.21	91.03	0.240	0.246	1.35	4.4
70	0.442	86.80	90.96	0.241	0.236	0.99	4.8
80	0.388	87.07	91.20	0.249	0.230	4.08	4.7
90	0.345	84.36	91.20	0.238	0.208	6.78	8.1
110	0.283	85.87	91.52	0.233	0.245	2.44	6.6

Table E.7 Experimental Data for PBTD with feed added 2.1cm above the nozzle with a dip tube. Feed is through a 3 mm nozzle. 2r/D = 0.8 and N = 252 rpm

Feed time (s)	Feed Velocity (m/s)	Conc. of Ester (mol/m^3)	Conc. of NaOH (mol/m^3)	$X_{Q,Ester}$ (-)	$X_{Q,Ethanol}$ (-)	Δ (%)	ε (%)
30	1.030	88.34	90.78	0.194	0.208	3.25	2.8
40	0.770	86.78	90.46	0.176	0.147	9.06	4.2
60	0.513	87.76	90.53	0.145	0.153	2.62	3.2
80	0.386	86.89	90.71	0.133	0.126	2.74	4.4
102	0.305	86.68	91.66	0.126	0.133	2.77	5.7
311	0.100	86.75	91.41	0.106	0.089	8.96	5.4
554	0.056	87.32	91.17	0.115	0.112	1.56	4.4
557	0.056	85.75	91.06	0.114	0.093	10.15	6.2
869	0.036	86.54	91.20	0.121	0.118	1.52	5.4
996	0.031	85.97	91.31	0.128	0.124	1.55	6.2
1183	0.026	86.54	91.10	0.133	0.120	5.14	5.3
1828	0.017	87.56	91.06	0.130	0.132	0.77	4.0
2951	0.010	86.81	91.03	0.134	0.139	1.55	4.9
4260	0.007	87.20	90.96	0.144	0.112	12.37	4.3
5340	0.006	88.87	90.99	0.141	0.157	5.56	2.4

Table E.8 **Experimental Data for PBTD with feed added 2.1cm above the nozzle with a dip tube. Feed is through a 0.762 mm nozzle. 2r/D = 0.8 and N = 252 rpm**

Feed time (s)	Feed Velocity (m/s)	Conc. of Ester (mol/m^3)	Conc. of NaOH (mol/m^3)	$X_{Q,Ester}$ (-)	$X_{Q,Ethanol}$ (-)	Δ (%)	ε (%)
40	0.769	87.72	90.39	0.170	0.159	3.44	3.0
60	0.514	87.00	90.64	0.149	0.146	1.00	4.2
80	0.386	86.15	90.81	0.131	0.117	5.80	5.4
101	0.308	86.90	91.45	0.123	0.109	6.04	5.2
310	0.100	86.99	91.13	0.106	0.096	4.73	4.8
552	0.056	86.87	91.31	0.101	0.096	2.69	5.1
1119	0.028	87.79	91.06	0.108	0.112	1.50	3.7
2931	0.011	86.94	91.03	0.110	0.124	6.20	4.7
3840	0.008	88.66	90.99	0.110	0.121	4.43	2.6
6432	0.005	88.30	91.03	0.123	0.166	14.67	3.1
3068**	0.010	86.31	91.03	0.085	0.092	4.10	5.5
1122**	0.028	87.05	90.92	0.087	0.078	5.90	4.4

Note: ** These data point were collected with a Rushton turbine. The feed was in the plane of the impeller disc at 2r/D = 1.125. N = 188 rpm.

Table E.9 **Experimental Data for a combination of PBTU and PBTD with feed at the surface. Feed is through a 3 mm nozzle. 2r/D = 0.8 and N = 252 rpm**

Feed time (s)	Feed Velocity (m/s)	Conc. of Ester (mol/m^3)	Conc. of NaOH (mol/m^3)	$X_{Q,Ester}$ (-)	$X_{Q,Ethanol}$ (-)	Δ (%)	ε (%)
10	3.083	85.85	90.60	0.276	0.296	3.47	5.5
20	1.542	86.19	90.60	0.295	0.308	2.04	5.1
30	1.028	85.07	90.64	0.296	0.290	1.01	6.5
40	0.774	88.60	90.99	0.290	0.284	1.00	2.7
50	0.619	87.49	90.92	0.285	0.272	2.31	3.9
60	0.518	86.03	91.27	0.265	0.255	1.95	6.1
70	0.443	86.43	91.20	0.254	0.243	2.13	5.5
80	0.388	86.71	91.27	0.235	0.245	2.21	5.3
90	0.345	89.69	91.17	0.245	0.279	6.60	1.6
100	0.311	85.46	91.27	0.230	0.209	4.90	6.8
110	0.281	85.65	90.96	0.228	0.244	3.44	6.2
130	0.238	86.09	90.99	0.224	0.243	4.09	5.7
150	0.206	89.11	90.67	0.205	0.223	4.12	1.8
200	0.155	85.39	90.85	0.201	0.199	0.57	6.4
250	0.124	87.78	90.85	0.193	0.178	4.05	3.5
300	0.105	85.30	90.74	0.190	0.187	0.81	6.4
350	0.088	86.93	92.25	0.158	0.162	1.05	6.1
450	0.069	86.93	91.48	0.162	0.153	2.78	5.2

Table E.10 **Experimental Data for PBTU with feed at surface. Feed is through a 3 mm nozzle. 2r/D = 1.75 and N = 252 rpm**

Feed time (s)	Feed Velocity (m/s)	Conc. of Ester (mol/m^3)	Conc. of NaOH (mol/m^3)	$X_{Q,Ester}$ (-)	$X_{Q,Ethanol}$ (-)	Δ (%)	ε (%)
10	3.083	87.40	90.60	0.324	0.325	0.12	3.7
20	1.539	85.64	90.46	0.321	0.308	2.12	5.6
30	1.033	89.94	91.03	0.310	0.316	0.98	1.2
40	0.774	84.58	91.03	0.291	0.260	5.50	7.6
50	0.620	85.76	91.13	0.268	0.272	0.78	6.3
60	0.519	86.25	91.41	0.265	0.259	1.26	6.0
70	0.442	85.58	90.92	0.247	0.250	0.72	6.2
80	0.388	86.61	91.13	0.239	0.253	2.93	5.2
90	0.346	84.71	91.41	0.241	0.220	4.52	7.9
100	0.312	86.72	91.62	0.234	0.237	0.61	5.6
120	0.260	84.54	91.55	0.219	0.208	2.63	8.3
150	0.206	85.91	90.78	0.211	0.198	3.13	5.7
250	0.124	86.36	90.96	0.194	0.174	5.28	5.3
350	0.088	87.09	90.96	0.177	0.159	5.10	4.4
450	0.069	85.74	91.31	0.165	0.144	6.97	6.5
555	0.057	86.93	93.62	0.167	0.160	2.17	7.7
867	0.036	86.78	91.24	0.145	0.136	3.49	5.1
961	0.032	83.14	91.17	0.129	0.143	5.31	9.7
1349	0.023	86.99	91.10	0.128	0.142	5.41	4.7
2828	0.011	87.97	91.06	0.129	0.154	8.64	3.5
4169	0.007	86.08	91.03	0.135	0.184	15.39	5.7
5710	0.005	85.32	90.99	0.122	0.168	15.82	6.6
9840	0.003	85.53	90.99	0.128	0.189	19.28	6.4

Table E.11 Experimental Data for PBTU with feed at surface. Feed is through a 3 mm nozzle. $2r/D = 0.8$ and $N = 252$ rpm

Feed time (s)	Feed Velocity (m/s)	Conc. of Ester (mol/m^3)	Conc. of NaOH (mol/m^3)	$X_{Q,Ester}$ (-)	$X_{Q,Ethanol}$ (-)	Δ (%)	ε (%)
30	1.033	86.25	91.03	0.247	0.256	1.87	5.5
40	0.783	85.48	92.04	0.254	0.252	0.34	7.7
50	0.621	85.71	91.17	0.232	0.224	1.55	6.4
60	0.516	81.33	90.96	0.205	0.178	6.87	11.8
70	0.443	86.29	91.20	0.201	0.203	0.48	5.7
80	0.389	86.25	91.34	0.210	0.201	2.31	5.9
90	0.346	87.01	91.55	0.205	0.201	1.21	5.2
100	0.310	87.72	91.10	0.193	0.197	0.84	3.9
120	0.259	84.89	91.45	0.193	0.175	4.86	7.7
130	0.251	85.46	95.73	0.189	0.192	0.76	12.0
140	0.224	87.11	92.25	0.183	0.174	2.57	5.9
150	0.214	85.83	94.08	0.184	0.176	2.30	9.6
250	0.124	86.50	91.27	0.169	0.130	12.81	5.5
350	0.089	86.08	91.69	0.158	0.154	1.31	6.5
408	0.076	85.87	91.27	0.156	0.124	11.17	6.3
538	0.058	85.18	91.17	0.145	0.146	0.47	7.0
702	0.044	86.20	91.13	0.143	0.151	2.83	5.7
915	0.034	86.43	91.13	0.138	0.148	3.40	5.4
1157	0.027	86.49	91.10	0.139	0.154	5.20	5.3
2415	0.013	84.98	91.06	0.136	0.151	5.36	7.2
3444	0.009	86.83	91.06	0.139	0.148	3.13	4.9
4750	0.007	87.52	91.03	0.144	0.179	10.80	4.0
6347	0.005	84.94	91.03	0.144	0.197	15.69	7.2

Table E.12 Experimental Data for PBTU with feed at surface. Feed is through a 0.762mm nozzle. 2r/D = 0.8 and N = 252 rpm

Feed time (s)	Feed Velocity (m/s)	Conc. of Ester (mol/m^3)	Conc. of NaOH (mol/m^3)	$X_{Q,Ester}$ (-)	$X_{Q,Ethanol}$ (-)	Δ (%)	ε (%)
20	24.638	84.82	92.89	0.162	0.161	0.25	9.5
30	16.121	86.98	91.20	0.203	0.219	3.88	4.9
40	12.053	85.63	90.92	0.192	0.171	5.78	6.2
50	9.646	87.11	90.96	0.200	0.216	3.95	4.4
60	8.035	85.97	90.92	0.193	0.204	2.90	5.8
70	6.936	86.71	91.55	0.198	0.210	3.01	5.6
80	6.024	86.01	90.88	0.195	0.187	1.94	5.7
90	5.342	85.61	90.67	0.198	0.178	5.28	5.9
100	4.855	86.56	91.55	0.198	0.185	3.43	5.8
110	4.388	85.80	91.03	0.191	0.184	2.02	6.1
130	3.710	85.80	90.96	0.192	0.184	2.01	6.0
150	3.241	87.21	91.66	0.187	0.196	2.30	5.1
250	1.935	86.73	91.20	0.175	0.179	1.20	5.2
350	1.398	85.76	92.25	0.172	0.160	3.69	7.6
442	1.101	86.40	91.76	0.159	0.168	2.72	6.2
530	0.914	85.81	91.38	0.147	0.155	2.55	6.5

Table E.13 Experimental Data for PBTU with different impeller positions. Feed is through a 3mm feed pipe at the surface of the tank at 2r/D = 0.8.

S/D (-)	N_E (rpm)	Feed time (s)	Feed Velocity (m/s)	Conc. of Ester (mol/m^3)	Conc. of NaOH (mol/m^3)	$X_{Q,Ester}$ (-)	$X_{Q,Ethanol}$ (-)
0.125	210	2968	0.010	87.72	91.06	0.107	0.151
0.25	240	2936	0.011	86.37	91.24	0.106	0.142
0.375	260	3016	0.010	85.60	90.99	0.100	0.136
0.625	280	3103	0.010	85.97	91.03	0.109	0.139
1	330	3127	0.010	86.12	91.03	0.122	0.146

Appendix F
Vortex Data In Un-Baffled Vessel

Table F.1 **Vortex Data From an Un-Baffled Tank Stirred with a Rushton Turbine. Experimental Fluid was R.O. Water.**

Impeller Type	Rushton Turbine		Rushton Turbine		Rushton Turbine	
D (cm)	8.1		7.7		12.1	
Blade Type	Thin		Thick		-	
Data	N (rpm)	h_l (cm)	N (rpm)	h_l (cm)	N (rpm)	h_l (cm)
	200	3.9	200	3.4	100	2.1
	250	5.7	250	4.9	150	4.4
	300	8.1	300	6.6	200	7.9
	350	10.9	350	9	250	11.8
	395	13.5	400	11.8	290	14.1

Table F.2 **Vortex Data From an Un-Baffled Tank Stirred with a Down-Pumping Pitched Blade Turbine. Experimental Fluid was R.O. Water.**

Impeller Type	PBTD		PBTD	
D (cm)	8		12	
Blade Type	-		-	
Data	N (rpm)	h_l (cm)	N (rpm)	h_l (cm)
	200	2.0	100	1.4
	250	3.3	150	2.9
	300	4.9	200	5.7
	350	6.8	250	8.9
	400	9.3	300	12.3
	450	11.8		

Table F.3 **Vortex Data From an Un-Baffled Tank Stirred with an Up-Pumping Pitched Blade Turbine. Experimental Fluid was R.O. Water.**

Impeller Type	PBTU		PBTU	
D (cm)	8		12	
Blade Type	-		-	
Data	N (rpm)	h_l (cm)	N (rpm)	h_l (cm)
	150	1.1	100	1.3
	200	2.4	110	1.5
	250	3.5	120	1.7
	300	5.1	130	2.3
	350	6.9	140	2.7
	400	8.8	150	3.0
	450	11.4	160	3.3
	480	12.7	170	3.7
			180	4.1
			190	4.7
			200	5.3
			210	5.6
			220	6.1
			230	6.8
			240	7.3
			250	8.3
			260	8.9
			270	9.8
			280	10.5
			290	11.1
			300	12.0

Appendix G
Data from Air Entrainment Experiments

Table G.1 **Impeller speed at the onset of air entrainment, N_E. Data is presented here for water for various baffle configurations.**

a) Standard Baffles

S (cm)	D (cm)	Ncrit (rpm)				Ncrit (rpm) (Average)
		1	2	3	4	
8	8	325	330	330	325	328
7	8	310	310	315	310	311
6	8	295	300	300	290	296
5	8	280	285	285	270	280
4	8	270	265	265	260	265
3	8	255	255	255	250	254
2	8	230	235	240	230	234
1	8	210	215	215		213
0.5	8	195	195	200		197
8	12	195	200		190	195
7	12	180	180	180	170	178
6	12	170	170	167	160	167
5	12	165	163	160	150	160
4	12	157	157		145	153
3	12	153	153		140	149
2	12	142	145		130	139
1	12	115	113			114

b) Liquid Surface T/10 Above Baffle

S (cm)	D (cm)	Ncrit (rpm)
8	8	335
7	8	320
6	8	310
5	8	300
4	8	285
3	8	270
2	8	250
1	8	240

S (cm)	D (cm)	Ncrit (rpm)
8	12	210
7	12	195
6	12	185
5	12	180
4	12	170
3	12	160
2	12	140
1	12	120

c) Notched Baffles

S (cm)	D (cm)	Ncrit (rpm)
9	8	340
8	8	330
7	8	320
6	8	310
5	8	290
4	8	275
3	8	260
2	8	250
1	8	230

S (cm)	D (cm)	Ncrit (rpm)
9	12	250
8	12	185
7	12	170
6	12	160
5	12	155
4	12	145
3	12	135
2	12	120
1	12	110

Table G.2 Impeller speed at the onset of air entrainment, N_E. Data is presented here for triethylene glycol (TEG) for two baffle configurations.

a) Standard Baffles

S (cm)	D (cm)	Ncrit (rpm)				Ncrit (rpm) (Average)
		1	2	3	4	
12	8	625		635		630
11	8	550		550		550
10	8	500		500		500
9	8	460		460		460
8	8	425	410	420		418
7	8	380	380	385		382
6	8	350	350	350		350
5	8	320	315	320		318
4	8	300	290	300		297
3	8	280	275	280		278
2	8	275	265	265		268
1	8	250		245		248
0.5	8	230				230
11	12	360	365	365		363
10	12	325	325	325		325
9	12	295	295	295		295
8	12	265	265	265		265
7	12	240	235	240		238
6	12	220	220	215		218
5	12	200	200	200		200
4	12	190	190	190		190
3	12	175	170	175		173
2	12	155	155	155		155
1	12	145	145	145		145
0.5	12	140				140

b) Liquid Surface T/10 Above Baffles

S (cm)	D (cm)	Ncrit (rpm)
10	8	500
9	8	455
8	8	410
7	8	380
6	8	350
5	8	310
4	8	290
3	8	275
2	8	265
1	8	250

S (cm)	D (cm)	Ncrit (rpm)
10	12	325
9	12	300
8	12	270
7	12	240
6	12	215
5	12	200
4	12	190
3	12	180
2	12	160
1	12	145

Table G.3 Impeller speed at the onset of air entrainment, N_E. Data is presented here for Bayol-35 for two baffle configurations.

a) Standard Baffles

S (cm)	D (cm)	Ncrit (rpm)				Ncrit (rpm) (Average)
		1	2	3	4	
12	8		355	360		358
11	8		340	340		340
10	8		325	325		325
9	8		300	300		300
8	8	270	275	275		273
7	8	250	255	255		253
6	8	235	245	245		242
5	8	220	230	230		227
4	8	210	215	215		213
3	8	200	205	205		203
2	8	190	195	200		195
1	8		185	190		188
10	12		245	245		245
9	12		200	205		203
8	12	150	160	170		160
7	12	140	145	145		143
6	12	130	135	135		133
5	12	120	125	125		123
4	12	115	120	120		118
3	12	105	115	115		112
2	12	100	110	105		105
1	12		100	100		100

b) Liquid Surface T/10 Above Baffles

S (cm)	D (cm)	Ncrit (rpm)
10	8	320
9	8	300
8	8	285
7	8	270
6	8	255
5	8	240
4	8	220
3	8	210
2	8	200
1	8	185

S (cm)	D (cm)	Ncrit (rpm)
10	12	230
9	12	205
8	12	175
7	12	165
6	12	155
5	12	145
4	12	140
3	12	130
2	12	115
1	12	100

Appendix H
Experimental Data From LDV Measurements

Table H.1a **Velocity data for an up-pumping pitched blade turbine of size D = T/3 which was placed 8 cm below the surface and operated at N = 0.98N$_E$ (321 rpm). Velocity was measured 1.5 cm below the liquid level in a vertical plane 6 mm upstream of the baffle. The experimental fluid is water.**

2r/D (-)	RMS-Axial m/s	Mean-Axial m/s	Data Rate Hz	Valid Count -
0.150	0.187	-0.037	825	59589
0.180	0.173	-0.042	825	59616
0.250	0.191	-0.075	823	59637
0.335	0.188	-0.066	810	59641
0.427	0.192	-0.100	817	59614
0.522	0.216	-0.126	175	59607
0.619	0.215	-0.122	815	59590
0.716	0.225	-0.233	870	59606
0.814	0.214	-0.229	841	59629
0.912	0.198	-0.221	833	59621
1.012	0.205	-0.239	817	59622
1.110	0.185	-0.246	795	59679
1.209	0.172	-0.208	714	59703
1.309	0.160	-0.187	653	59733
1.408	0.151	-0.155	610	59756
1.508	0.151	-0.124	596	59749
1.607	0.140	-0.108	623	59781
1.707	0.134	-0.084	589	59793
1.806	0.130	-0.060	562	59780
1.906	0.123	-0.037	526	59814
2.006	0.123	-0.010	505	59787
2.106	0.122	0.013	483	59810
2.205	0.118	0.043	457	59799
2.305	0.116	0.066	420	59860
2.405	0.111	0.090	401	59858
2.505	0.105	0.126	369	59887
2.604	0.098	0.147	332	59878
2.704	0.090	0.149	290	59904
2.804	0.103	0.137	264	59865
2.904	0.119	0.102	296	59822

Table H.1b Velocity data for an up-pumping pitched blade turbine of size D = T/3 which was placed 7 cm below the surface and operated at $N = 0.98N_E$ (306 rpm). Velocity was measured 1.5 cm below the liquid level in a vertical plane 6 mm upstream of the baffle. The experimental fluid is water.

2r/D (-)	RMS-Axial m/s	Mean-Axial m/s	Data Rate Hz	Valid Count -
0.150	0.165	-0.049	731	59607
0.180	0.160	-0.035	732	59610
0.250	0.172	-0.043	742	59672
0.335	0.169	-0.043	723	59678
0.427	0.191	-0.084	748	59671
0.522	0.200	-0.106	757	59658
0.619	0.223	-0.240	809	59664
0.716	0.223	-0.210	779	59624
0.814	0.206	-0.210	786	59683
0.912	0.199	-0.263	811	59669
1.012	0.197	-0.226	751	59701
1.110	0.184	-0.227	720	59716
1.209	0.156	-0.198	664	59735
1.309	0.156	-0.195	605	59758
1.408	0.150	-0.161	558	59788
1.508	0.142	-0.133	536	59784
1.607	0.138	-0.109	546	59696
1.707	0.130	-0.085	564	59693
1.806	0.122	-0.051	584	59699
1.906	0.111	-0.025	605	59690
2.006	0.112	-0.004	608	59735
2.106	0.107	0.014	622	59717
2.205	0.110	0.043	625	59673
2.305	0.111	0.075	654	59753
2.405	0.104	0.103	665	59743
2.505	0.102	0.142	684	59769
2.604	0.092	0.160	691	59816
2.704	0.087	0.171	697	59853
2.804	0.096	0.150	690	59793
2.904	0.112	0.104	374	59708

Table H.1c Velocity data for an up-pumping pitched blade turbine of size D = T/3 which was placed 6 cm below the surface and operated at $N = 0.98N_E$ (290 rpm). Velocity was measured 1.5 cm below the liquid level in a vertical plane 6 mm upstream of the baffle. The experimental fluid is water.

2r/D (-)	RMS-Axial m/s	Mean-Axial m/s	Data Rate Hz	Valid Count -
0.150	0.152	-0.003	729	59582
0.180	0.133	0.004	769	59569
0.250	0.170	-0.046	776	59625
0.335	0.179	-0.078	741	59597
0.427	0.181	-0.068	725	59579
0.522	0.191	-0.108	736	59609
0.619	0.213	-0.144	747	59603
0.716	0.220	-0.196	760	59613
0.814	0.212	-0.192	740	59574
0.912	0.199	-0.215	726	59619
1.012	0.196	-0.189	689	59584
1.110	0.182	-0.190	672	59634
1.209	0.167	-0.161	624	59660
1.309	0.161	-0.156	601	59657
1.408	0.157	-0.140	539	59661
1.508	0.146	-0.090	498	59680
1.607	0.147	-0.080	474	59664
1.707	0.143	-0.048	434	59679
1.806	0.137	-0.043	398	59715
1.906	0.128	-0.009	354	59698
2.006	0.128	0.015	322	59714
2.106	0.120	0.028	289	59692
2.205	0.118	0.059	247	59690
2.305	0.111	0.075	221	59679
2.405	0.106	0.101	187	59668
2.505	0.097	0.113	151	59636
2.604	0.093	0.117	128	59711
2.704	0.090	0.113	103	59696
2.804	0.097	0.086	79	10066

Table H.1d **Velocity data for an up-pumping pitched blade turbine of size D = T/3 which was placed 5 cm below the surface and operated at N = 0.98N_E (277 rpm). Velocity was measured 1.5 cm below the liquid level in a vertical plane 6 mm upstream of the baffle. The experimental fluid is water.**

2r/D (-)	RMS-Axial m/s	Mean-Axial m/s	Data Rate Hz	Valid Count -
0.150	0.143	-0.041	811	59470
0.180	0.121	-0.007	797	59522
0.250	0.120	-0.018	765	59533
0.335	0.117	-0.015	751	59551
0.427	0.125	-0.016	754	59598
0.522	0.145	-0.059	758	59631
0.619	0.136	-0.058	757	59569
0.716	0.153	-0.117	743	59652
0.814	0.180	-0.119	741	59646
0.912	0.181	-0.205	771	59624
1.012	0.170	-0.156	722	59637
1.110	0.177	-0.189	693	59633
1.209	0.167	-0.237	671	59665
1.309	0.163	-0.209	608	59734
1.408	0.150	-0.199	565	59732
1.508	0.138	-0.148	560	59719
1.607	0.133	-0.140	528	59717
1.707	0.130	-0.102	536	59687
1.806	0.112	-0.059	546	59715
1.906	0.118	-0.041	567	59758
2.006	0.111	-0.025	562	59753
2.106	0.105	-0.002	557	59719
2.205	0.106	0.025	572	59743
2.305	0.106	0.052	573	59714
2.405	0.102	0.089	577	59778
2.505	0.097	0.127	585	59792
2.604	0.091	0.173	596	59837
2.704	0.084	0.187	594	59838
2.804	0.083	0.191	607	59847
2.904	0.104	0.155	265	59770

Table H.2a Velocity data for an up-pumping pitched blade turbine of size D = T/2 which was placed 8 cm below the surface and operated at $N = 0.98N_E$ (191 rpm). Velocity was measured 1.5 cm below the liquid level in a vertical plane 6 mm upstream of the baffle. The experimental fluid is water.

2r/D (-)	RMS-Axial m/s	Mean-Axial m/s	Data Rate Hz	Valid Count -
0.100	0.124	0.005	982	59345
0.120	0.115	0.009	973	59324
0.167	0.119	0.001	180	59268
0.224	0.122	0.003	994	59260
0.285	0.126	-0.010	974	59263
0.348	0.103	0.019	979	59370
0.412	0.117	0.005	991	59308
0.477	0.121	0.013	180	59406
0.543	0.133	-0.022	179	59348
0.608	0.134	-0.022	943	59372
0.674	0.159	-0.048	939	59407
0.740	0.157	-0.056	917	59450
0.806	0.162	-0.072	876	59416
0.872	0.155	-0.054	855	59457
0.939	0.161	-0.065	174	59419
1.005	0.169	-0.085	174	59489
1.071	0.172	-0.072	871	59500
1.138	0.162	-0.071	852	59482
1.204	0.163	-0.094	847	59535
1.271	0.155	-0.061	797	59538
1.337	0.149	-0.043	778	59551
1.404	0.132	-0.005	743	59548
1.470	0.139	-0.034	710	59564
1.537	0.133	-0.021	691	59572
1.603	0.133	-0.006	655	59595
1.670	0.129	0.004	615	59543
1.736	0.137	0.000	570	59556
1.803	0.135	0.011	528	59541
1.869	0.131	0.023	506	59571
1.936	0.127	0.030	458	59623

Table H.2b **Velocity data for an up-pumping pitched blade turbine of size $D = T/2$ which was placed 7 cm below the surface and operated at $N = 0.98N_E$ (174 rpm). Velocity was measured 1.5 cm below the liquid level in a vertical plane 6 mm upstream of the baffle. The experimental fluid is water.**

2r/D (-)	RMS-Axial m/s	Mean-Axial m/s	Data Rate Hz	Valid Count -
0.100	0.110	0.007	961	59373
0.120	0.111	0.021	956	59334
0.167	0.110	0.008	947	59313
0.224	0.110	0.016	933	59328
0.285	0.118	0.004	932	59410
0.348	0.119	0.000	179	59398
0.412	0.123	-0.006	944	59395
0.477	0.129	-0.017	991	59387
0.543	0.145	-0.038	961	59412
0.608	0.132	-0.022	929	59403
0.674	0.150	-0.050	179	59493
0.740	0.157	-0.070	177	59469
0.806	0.163	-0.081	956	59522
0.872	0.155	-0.079	897	59501
0.939	0.164	-0.095	844	59582
1.005	0.158	-0.083	837	59546
1.071	0.158	-0.091	916	59593
1.138	0.156	-0.099	914	59550
1.204	0.154	-0.087	885	59598
1.271	0.150	-0.064	876	59592
1.337	0.142	-0.075	882	59637
1.404	0.136	-0.052	866	59596
1.470	0.130	-0.029	841	59636
1.537	0.124	-0.012	853	59635
1.603	0.124	-0.005	818	59617
1.670	0.118	0.014	777	59602
1.736	0.116	0.030	703	59559
1.803	0.116	0.049	652	59594
1.869	0.115	0.055	641	59650
1.936	0.109	0.062	614	59619

Table H.2c Velocity data for an up-pumping pitched blade turbine of size D = T/2 which was placed 6 cm below the surface and operated at $N = 0.98N_E$ (164 rpm). Velocity was measured 1.5 cm below the liquid level in a vertical plane 6 mm upstream of the baffle. The experimental fluid is water.

2r/D (-)	RMS-Axial m/s	Mean-Axial m/s	Data Rate Hz	Valid Count -
0.100	0.101	0.022	167	59613
0.120	0.099	0.018	630	59657
0.167	0.100	0.024	588	59665
0.224	0.110	0.013	584	59694
0.285	0.116	-0.007	567	59656
0.348	0.120	-0.015	538	59691
0.412	0.127	-0.035	492	59684
0.477	0.131	-0.039	470	59691
0.543	0.139	-0.060	458	59705
0.608	0.147	-0.072	419	59728
0.674	0.146	-0.080	389	59714
0.740	0.153	-0.091	350	59737
0.806	0.150	-0.099	323	59747
0.872	0.157	-0.107	289	59714
0.939	0.150	-0.107	245	59702
1.005	0.149	-0.104	222	59744
1.071	0.147	-0.104	693	59821
1.138	0.143	-0.094	690	59782
1.204	0.141	-0.075	693	59784
1.271	0.133	-0.058	699	59786
1.337	0.132	-0.040	695	59791
1.404	0.122	-0.006	688	59819
1.470	0.117	0.016	666	59788
1.537	0.118	0.026	669	59789
1.603	0.114	0.044	634	59774
1.670	0.108	0.062	616	59797
1.736	0.109	0.072	591	59794
1.803	0.102	0.077	563	59812
1.869	0.097	0.075	533	59813
1.936	0.101	0.056	519	59859

Table H.2d **Velocity data for an up-pumping pitched blade turbine of size D = T/2 which was placed 5 cm below the surface and operated at N = 0.98N_E (157 rpm). Velocity was measured 1.5 cm below the liquid level in a vertical plane 6 mm upstream of the baffle. The experimental fluid is water.**

2r/D (-)	RMS-Axial m/s	Mean-Axial m/s	Data Rate Hz	Valid Count -
0.100	0.076	0.054	705	59607
0.120	0.073	0.062	737	59633
0.167	0.073	0.040	737	59600
0.224	0.082	0.036	171	59628
0.285	0.086	0.035	759	59609
0.348	0.099	0.008	770	59647
0.412	0.109	-0.009	762	59657
0.477	0.111	-0.023	722	59661
0.543	0.123	-0.031	696	59696
0.608	0.130	-0.064	647	59682
0.674	0.132	-0.097	586	59724
0.740	0.139	-0.096	544	59697
0.806	0.141	-0.130	505	59759
0.872	0.146	-0.138	462	59737
0.939	0.138	-0.149	412	59705
1.005	0.133	-0.152	394	59761
1.071	0.132	-0.146	743	59788
1.138	0.131	-0.120	737	59779
1.204	0.128	-0.102	736	59771
1.271	0.125	-0.076	750	59783
1.337	0.128	-0.044	746	59767
1.404	0.124	-0.004	738	59777
1.470	0.116	0.030	734	59772
1.537	0.113	0.053	712	59762
1.603	0.112	0.072	714	59705
1.670	0.105	0.091	688	59770
1.736	0.094	0.105	659	59799
1.803	0.095	0.104	612	59772
1.869	0.086	0.105	605	59800
1.936	0.087	0.084	571	59815

Table H.3a Repeatability of velocity data for a PBTU. Second set of data for a D = T/3 impeller operated at a submergence of 8 mm and a speed of 321 rpm. Velocity was measured in a vertical plane 6mm upstream of the baffle, 1.5 cm below the liquid surface. The experimental fluid is water.

2r/D (-)	RMS-Axial m/s	Mean-Axial m/s	Data Rate Hz	Valid Count -
0.150	0.151	0.002	682	59579
0.180	0.141	0.019	688	59579
0.250	0.166	-0.011	730	59592
0.335	0.181	-0.027	726	59574
0.427	0.175	-0.044	722	59535
0.522	0.214	-0.111	782	59571
0.619	0.201	-0.097	781	59568
0.716	0.211	-0.127	790	59572
0.814	0.210	-0.209	840	59532
0.912	0.203	-0.224	870	59554
1.012	0.193	-0.224	862	59520
1.110	0.186	-0.205	847	59535
1.209	0.184	-0.183	801	59582
1.309	0.170	-0.194	812	59576
1.408	0.161	-0.149	773	59571
1.508	0.156	-0.129	732	59585
1.607	0.142	-0.077	692	59666
1.707	0.142	-0.052	670	59640
1.806	0.137	-0.035	644	59677
1.906	0.132	-0.008	633	59633
2.006	0.120	0.022	606	59661
2.106	0.124	0.029	600	59642
2.205	0.116	0.047	585	59647
2.305	0.112	0.101	596	59663
2.405	0.102	0.116	583	59726
2.505	0.098	0.130	565	59698
2.604	0.094	0.143	554	59745
2.704	0.098	0.127	527	59736
2.804	0.114	0.075	244	59730

Table H.3b Repeatability of velocity data for a PBTU. Third set of data for a D = T/3 impeller operated at a submergence of 8 mm and a speed of 321 rpm. Velocity was measured in a vertical plane 6mm upstream of the baffle, 1.5 cm below the liquid surface. The experimental fluid is water.

2r/D (-)	RMS-Axial m/s	Mean-Axial m/s	Data Rate Hz	Valid Count -
0.180	0.164	-0.035	808	59306
0.250	0.167	-0.030	775	59324
0.335	0.161	-0.029	751	59336
0.427	0.177	-0.047	702	59362
0.522	0.165	-0.029	667	59353
0.619	0.201	-0.102	648	59346
0.716	0.202	-0.111	598	59394
0.814	0.197	-0.175	566	59387
0.912	0.195	-0.170	512	59340
1.012	0.190	-0.166	460	59299
1.110	0.185	-0.158	403	59252
1.209	0.174	-0.161	360	59374
1.309	0.170	-0.139	319	59322
1.408	0.157	-0.120	267	59268
1.508	0.145	-0.089	241	59313
1.607	0.147	-0.090	721	59736
1.707	0.145	-0.065	678	59748
1.806	0.131	-0.028	628	59727
1.906	0.133	-0.014	588	59745
2.006	0.128	0.011	542	59742
2.106	0.123	0.043	505	59784
2.205	0.116	0.078	457	59777
2.305	0.115	0.096	413	59732
2.405	0.107	0.126	370	59774
2.505	0.100	0.129	312	59803
2.604	0.091	0.127	263	59779
2.704	0.088	0.124	213	59851
2.804	0.087	0.109	156	59834
2.904	0.095	0.080	84	59893

Table H.4a Velocity data for an up-pumping pitched blade turbine. Measurements were made in a vertical mid-baffle plane. Velocity was measured 1.5 cm below the liquid surface for a D = T/3 impeller operated at a submergence of 8 mm and a speed of 321 rpm. The experimental fluid is water.

2r/D (-)	RMS-Axial m/s	Mean-Axial m/s	Data Rate Hz	Valid Count -
0.150	0.140	0.029	728	59674
0.180	0.162	-0.006	731	59665
0.250	0.172	-0.027	753	59677
0.335	0.175	-0.029	744	59678
0.427	0.169	-0.020	741	59707
0.522	0.195	-0.091	784	59703
0.619	0.220	-0.134	817	59673
0.716	0.211	-0.112	811	59679
0.814	0.212	-0.173	832	59702
0.912	0.211	-0.213	850	59677
1.012	0.207	-0.189	831	59646
1.110	0.193	-0.213	851	59679
1.209	0.172	-0.209	833	59701
1.309	0.172	-0.168	801	59719
1.408	0.168	-0.140	752	59659
1.508	0.154	-0.115	734	59712
1.607	0.156	-0.096	652	59668
1.707	0.151	-0.084	635	59680
1.806	0.136	-0.053	621	59652
1.906	0.132	-0.037	613	59657
2.006	0.132	0.017	601	59633
2.106	0.119	0.047	608	59646
2.205	0.113	0.066	591	59673
2.305	0.110	0.096	570	59654
2.405	0.105	0.123	580	59694
2.505	0.098	0.139	574	59648
2.604	0.098	0.126	572	59691
2.704	0.109	0.117	556	59746
2.804	0.112	0.069	149	59657

Table H.4b **Velocity data for an up-pumping pitched blade turbine. Measurements were made in a vertical mid-baffle plane. Velocity was measured 1.5 cm below the liquid surface for a D = T/3 impeller operated at a submergence of 6 mm and a speed of 290 rpm. The experimental fluid is water.**

2r/D	RMS-Axial	Mean-Axial	Data Rate	Valid Count
(-)	m/s	m/s	Hz	-
0.150	0.150	-0.014	747	59517
0.180	0.135	-0.001	733	59551
0.250	0.129	-0.003	709	59573
0.335	0.144	-0.002	695	59559
0.427	0.134	0.008	681	59589
0.522	0.163	-0.035	662	59565
0.619	0.174	-0.055	663	59634
0.716	0.214	-0.133	695	59593
0.814	0.224	-0.189	702	59592
0.912	0.213	-0.195	675	59560
1.012	0.212	-0.222	670	59609
1.110	0.189	-0.234	650	59576
1.209	0.176	-0.197	608	59546
1.309	0.168	-0.184	566	59573
1.408	0.159	-0.143	512	59613
1.508	0.152	-0.103	481	59603
1.607	0.141	-0.079	455	59638
1.707	0.137	-0.046	420	59619
1.806	0.129	-0.025	406	59648
1.906	0.126	-0.007	391	59643
2.006	0.119	0.012	375	59649
2.106	0.116	0.046	351	59649
2.205	0.109	0.060	336	59667
2.305	0.107	0.095	134	59654
2.405	0.100	0.121	339	59644
2.505	0.093	0.130	309	59694
2.604	0.086	0.131	288	59671
2.704	0.093	0.094	272	59645
2.804	0.093	0.059	134	59610

Table H.5a Velocity data for an up-pumping pitched blade turbine of size D = T/3 which was placed 8 cm below the surface and operated at $N = 0.98N_E$ (265 rpm). Velocity was measured 1.5 cm below the liquid level in a vertical plane 6 mm upstream of the baffle. The experimental fluid is Bayol-35.

2r/D (-)	RMS-Axial m/s	Mean-Axial m/s	Data Rate Hz	Valid Count -
0.150	0.111	0.028	784	58838
0.180	0.124	0.004	749	58889
0.250	0.128	0.003	780	58830
0.335	0.135	-0.015	737	58837
0.427	0.150	-0.043	757	58854
0.522	0.135	-0.031	170	58838
0.618	0.153	-0.081	795	58869
0.716	0.149	-0.084	738	58858
0.814	0.152	-0.122	749	58861
0.912	0.156	-0.132	770	59028
1.011	0.138	-0.149	170	58965
1.110	0.132	-0.175	757	58984
1.209	0.125	-0.149	704	58967
1.309	0.121	-0.155	169	59059
1.408	0.115	-0.127	699	58967
1.507	0.115	-0.109	665	58938
1.607	0.100	-0.084	657	58955
1.707	0.098	-0.070	632	58998
1.806	0.094	-0.050	166	59207
1.906	0.085	-0.025	156	59035
2.006	0.084	-0.005	541	59018
2.105	0.078	0.014	518	58998
2.205	0.075	0.033	501	58889
2.305	0.073	0.052	483	58922
2.405	0.069	0.080	150	58951
2.504	0.069	0.100	461	58807
2.604	0.067	0.112	148	58869
2.704	0.066	0.116	447	58976
2.804	0.067	0.123	422	58904
2.904	0.069	0.098	87	59094

Table H.5b **Velocity data for an up-pumping pitched blade turbine of size $D = T/3$ which was placed 7 cm below the surface and operated at $N = 0.98N_E$ (246 rpm). Velocity was measured 1.5 cm below the liquid level in a vertical plane 6 mm upstream of the baffle. The experimental fluid is Bayol-35.**

2r/D (-)	RMS-Axial m/s	Mean-Axial m/s	Data Rate Hz	Valid Count -
0.150	0.110	0.037	636	58871
0.180	0.105	0.029	660	58889
0.250	0.119	0.001	163	58931
0.335	0.119	0.016	163	58924
0.427	0.145	-0.044	679	58932
0.522	0.149	-0.070	705	58993
0.618	0.149	-0.046	674	58980
0.716	0.157	-0.136	690	59032
0.814	0.150	-0.159	747	59070
0.912	0.146	-0.171	702	59060
1.011	0.134	-0.169	747	59119
1.110	0.128	-0.182	720	59148
1.209	0.123	-0.164	720	59104
1.309	0.123	-0.129	702	59135
1.408	0.110	-0.123	647	59121
1.507	0.095	-0.087	651	59088
1.607	0.096	-0.077	649	59057
1.707	0.086	-0.054	606	59111
1.806	0.079	-0.040	159	59068
1.906	0.080	-0.028	553	59061
2.006	0.070	0.002	571	59073
2.105	0.082	0.011	590	59034
2.205	0.070	0.036	526	58851
2.305	0.069	0.059	478	58885
2.405	0.066	0.080	148	58925
2.504	0.064	0.100	474	58950
2.604	0.063	0.114	482	59003
2.704	0.062	0.125	150	58914
2.804	0.061	0.122	438	59082
2.904	0.067	0.109	231	59080

Table H.5c **Velocity data for an up-pumping pitched blade turbine of size $D = T/3$ which was placed 6 cm below the surface and operated at $N = 0.98N_E$ (234 rpm). Velocity was measured 1.5 cm below the liquid level in a vertical plane 6 mm upstream of the baffle. The experimental fluid is Bayol-35.**

2r/D (-)	RMS-Axial m/s	Mean-Axial m/s	Data Rate Hz	Valid Count -
0.150	0.114	-0.014	762	58922
0.180	0.129	-0.040	747	58916
0.250	0.142	-0.058	747	58938
0.335	0.132	-0.049	744	58895
0.427	0.160	-0.108	170	58969
0.522	0.160	-0.142	786	59059
0.618	0.169	-0.154	740	59026
0.716	0.157	-0.106	170	58941
0.814	0.138	-0.234	802	59133
0.912	0.158	-0.149	759	59052
1.011	0.129	-0.167	725	59051
1.110	0.124	-0.174	736	58994
1.209	0.125	-0.139	668	59068
1.309	0.109	-0.114	648	59065
1.408	0.083	-0.071	621	58936
1.507	0.101	-0.085	594	59047
1.607	0.082	-0.053	551	58973
1.707	0.082	-0.045	545	58935
1.806	0.081	-0.038	586	59105
1.906	0.071	-0.018	516	58991
2.006	0.067	-0.007	467	58894
2.105	0.071	0.011	151	58923
2.205	0.066	0.025	63	58902
2.305	0.066	0.044	446	58910
2.405	0.066	0.066	427	58794
2.504	0.066	0.095	424	58850
2.604	0.065	0.121	144	58828
2.704	0.065	0.131	410	58773
2.804	0.065	0.132	369	58833
2.904	0.069	0.109	87	59020

Table H.5d **Velocity data for an up-pumping pitched blade turbine of size $D = T/3$ which was placed 5 cm below the surface and operated at $N = 0.98N_E$ (220 rpm). Velocity was measured 1.5 cm below the liquid level in a vertical plane 6 mm upstream of the baffle. The experimental fluid is Bayol-35.**

2r/D (-)	RMS-Axial m/s	Mean-Axial m/s	Data Rate Hz	Valid Count -
0.150	0.109	-0.010	708	58959
0.180	0.096	0.001	164	58870
0.250	0.114	-0.038	168	59019
0.335	0.101	-0.011	167	58949
0.427	0.131	-0.108	778	59080
0.522	0.127	-0.130	813	59122
0.618	0.140	-0.179	860	59203
0.716	0.136	-0.179	734	59197
0.814	0.134	-0.168	732	59169
0.912	0.135	-0.234	824	59253
1.011	0.113	-0.187	840	59187
1.110	0.120	-0.171	736	59196
1.209	0.118	-0.150	743	59135
1.309	0.094	-0.095	664	59199
1.408	0.119	-0.128	758	59146
1.507	0.073	-0.052	656	58994
1.607	0.097	-0.078	654	59249
1.707	0.064	-0.037	157	58956
1.906	0.074	-0.016	538	59124
2.006	0.067	-0.005	486	58990
2.105	0.068	0.005	150	58983
2.205	0.060	0.020	436	58961
2.305	0.069	0.056	464	58953
2.405	0.059	0.062	471	58830
2.504	0.063	0.095	419	58927
2.604	0.063	0.117	429	58975
2.704	0.060	0.133	420	58951
2.804	0.064	0.144	394	58876
2.904	0.068	0.122	203	59063

Table H.6a First set of velocity data for a down-pumping pitched blade turbine. Velocity was measured 4 mm below the impeller (D = T/3) operated at a speed of 400 rpm in a vertical plane 6mm upstream of the baffle. The experimental fluid is water.

2r/D (-)	RMS-Axial m/s	Mean-Axial m/s	Data Rate Hz	Valid Count -
0.1	0.114	-0.057	500	5655
0.15	0.145	0.036	461	7749
0.2	0.175	0.250	904	12229
0.25	0.157	0.375	949	56939
0.3	0.146	0.417	1034	26519
0.35	0.138	0.501	1092	65533
0.4	0.139	0.543	1185	71083
0.45	0.136	0.603	1205	72312
0.5	0.142	0.659	1316	78948
0.55	0.138	0.695	1382	82904
0.6	0.147	0.733	1359	81536
0.65	0.155	0.752	1413	84800
0.7	0.192	0.800	1378	82653
0.75	0.239	0.798	1388	83258
0.8	0.293	0.758	1228	73704
0.85	0.369	0.587	1132	67906
0.9	0.392	0.399	970	50731
0.95	0.370	0.193	991	55993
1	0.326	0.085	753	19955
1.05	0.262	0.108	759	10455
1.1	0.175	0.100	724	13739
1.15	0.156	0.125	764	22093
1.2	0.117	0.137	653	32001
1.25	0.115	0.132	601	14676
1.3	0.108	0.157	615	11311
1.35	0.101	0.110	641	16122
1.4	0.106	0.126	676	14630
1.45	0.107	0.117	567	25940
1.5	0.107	0.122	555	20337
1.55	0.110	0.100	554	23460
1.6	0.109	0.067	515	30907
1.65	0.112	0.048	493	10072
1.7	0.113	0.062	381	11536
1.75	0.114	0.034	407	20586
1.8	0.119	0.007	421	10177
1.85	0.117	-0.023	374	17622
1.9	0.123	-0.013	329	11719
1.95	0.120	-0.036	336	20151
2	0.113	-0.068	333	11255
2.05	0.123	-0.064	344	14026
2.1	0.115	-0.131	355	21310

Table H.6b **Second set of velocity data for a down-pumping pitched blade turbine. Velocity was measured 4 mm below the impeller (D = T/3) which was operated at a speed of 400 rpm. Measurements were made in a vertical plane 6mm upstream of the baffle. The experimental fluid is water.**

2r/D (-)	RMS-Axial m/s	Mean-Axial m/s	Data Rate Hz	Valid Count -
0.1	0.105	-0.050	390	4441
0.15	0.146	0.054	388	14080
0.2	0.172	0.283	499	7719
0.25	0.159	0.372	517	21963
0.3	0.147	0.421	571	14196
0.35	0.145	0.493	639	38310
0.4	0.139	0.542	724	43451
0.45	0.136	0.604	748	44887
0.5	0.147	0.644	773	46400
0.55	0.137	0.666	772	46332
0.6	0.151	0.742	786	47129
0.65	0.143	0.730	785	47091
0.7	0.184	0.803	772	46319
0.75	0.231	0.808	763	45807
0.8	0.245	0.773	687	41221
0.85	0.332	0.655	620	37194
0.9	0.403	0.367	503	30178
0.95	0.375	0.197	495	29700
1	0.321	0.077	423	25370
1.05	0.248	0.078	393	21735
1.1	0.191	0.102	355	20320
1.15	0.149	0.134	384	10331
1.2	0.118	0.124	336	8069
1.25	0.111	0.135	348	15882
1.3	0.106	0.142	321	10679
1.35	0.104	0.127	353	21151
1.4	0.111	0.121	344	6465
1.45	0.113	0.118	321	5831
1.5	0.111	0.094	329	5686
1.55	0.110	0.089	323	19365
1.6	0.113	0.095	312	7489

Table H.6c **Third set of velocity data for a down-pumping pitched blade turbine. Velocity was measured 4 mm below the impeller (D = T/3) which was operated at a speed of 400 rpm. Measurements were made in a vertical plane 6mm upstream of the baffle. The experimental fluid is water.**

2r/D (-)	RMS-Axial m/s	Mean-Axial m/s	Data Rate Hz	Valid Count -
0.1	0.114	-0.063	368	6106
0.15	0.145	0.047	291	4592
0.2	0.180	0.220	438	14956
0.25	0.150	0.410	396	23763
0.3	0.148	0.434	523	31367
0.35	0.144	0.515	573	34399
0.4	0.138	0.549	592	35545
0.45	0.139	0.605	620	37179
0.5	0.136	0.623	627	34223
0.55	0.139	0.676	678	40701
0.6	0.152	0.734	707	42417
0.65	0.171	0.786	725	43522
0.7	0.185	0.803	711	42682
0.75	0.236	0.817	694	41613
0.8	0.272	0.782	609	36545
0.85	0.324	0.686	591	35432
0.9	0.391	0.410	467	28043
0.95	0.381	0.174	384	23064
1	0.313	0.097	381	11244
1.05	0.256	0.101	306	18354
1.1	0.192	0.104	318	10007
1.15	0.144	0.122	307	18239
1.2	0.119	0.126	308	18467
1.25	0.110	0.135	273	15298
1.3	0.104	0.125	260	14012
1.35	0.111	0.136	281	11605
1.4	0.107	0.129	274	16469
1.45	0.109	0.127	248	8014
1.5	0.116	0.090	266	9179
1.55	0.110	0.096	276	16530
1.6	0.120	0.053	244	6089

Appendix I
Byproduct Yield as a Function of RMS Velocity

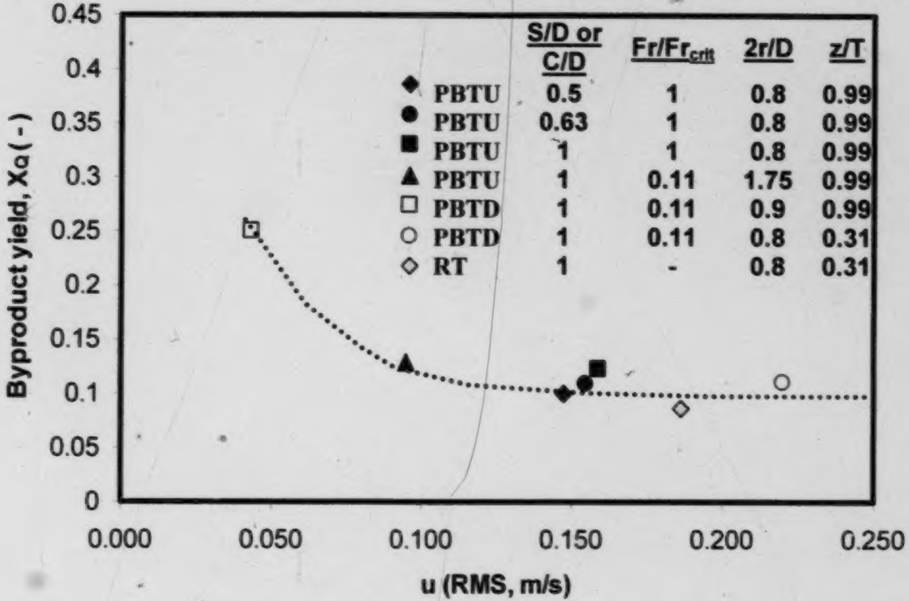

Table of Data for the Figure:

Impeller Type	S or C (cm)	N (rpm)	2r/D (-)	z_{feed} -	X_Q (-)	u m/s	
PBTU	8	252	1.75	surface	0.129	0.095	
PBTU	4	260	0.8	surface	0.1	0.147	
PBTU	5	280	0.8	surface	0.109	0.155	
PBTU	8	330	0.8	surface	0.122	0.159	
PBTD	8	252	0.875	surface	0.25	0.043	
PBTD	8	252	0.875	0.5cm from impeller	0.11	0.220	
PBTD	8	252	0.875	2.1cm from impeller	0.136		*
RT	8	189	1.65	0	0.086	0.186	**

Notes: * No measurements are available

** Radial component estimated from Lee and Yianneskis (1998) and Dyster et al. (1993)